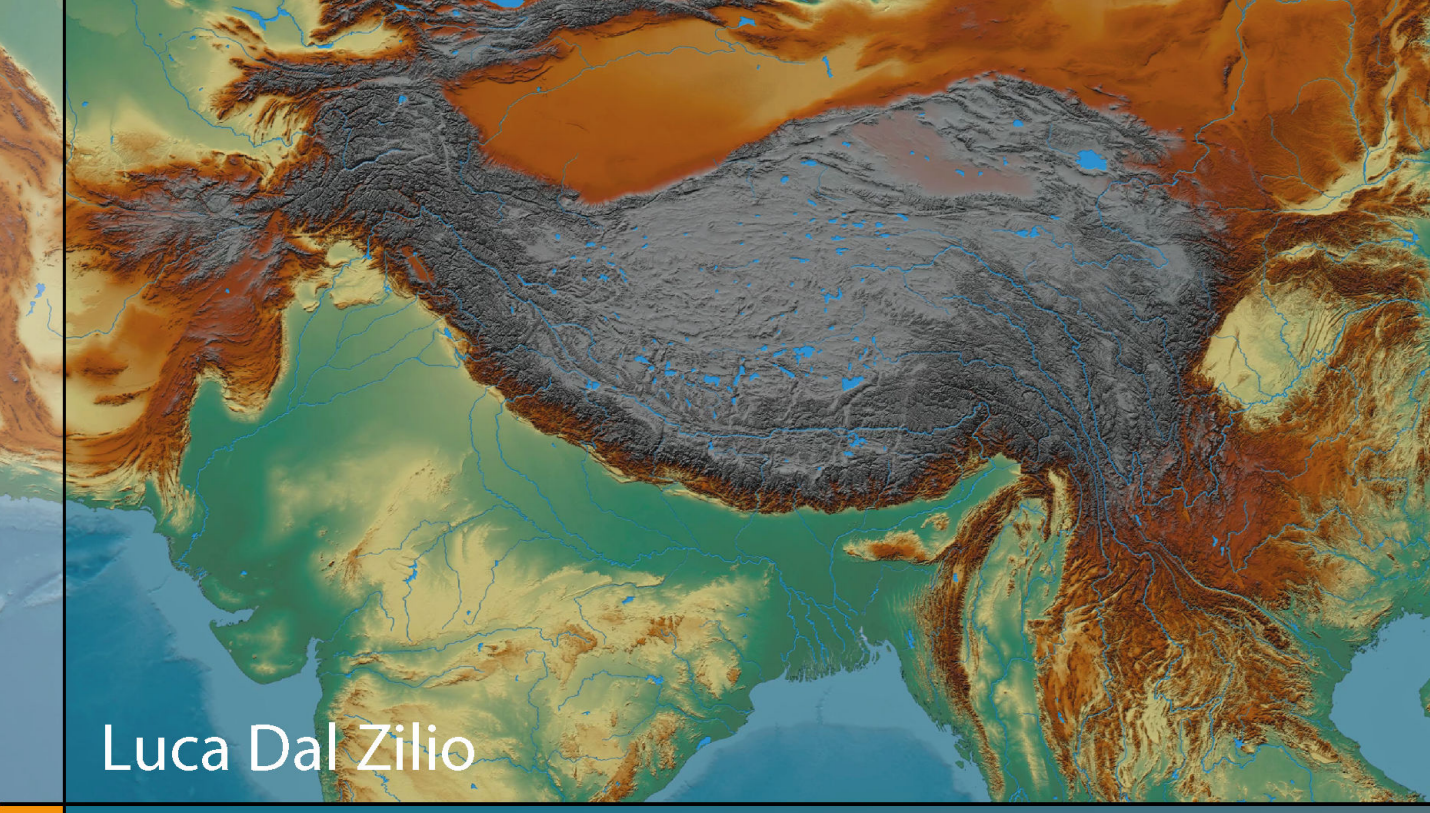


Luca Dal Zilio

Cross-scale modeling of mountain building and the seismic cycle:

From Alps to Himalaya

ETH zürich

Swiss Federal Institute of Technology
Department of Earth Sciences
Institute of Geophysics

DISS. ETH NO. 25709

CROSS-SCALE MODELING OF MOUNTAIN BUILDING AND THE SEISMIC CYCLE: FROM ALPS TO HIMALAYA

A dissertation submitted to
ETH ZURICH

for the degree of
DOCTOR OF SCIENCES

presented by

LUCA DAL ZILIO

M.Sc. in Geology, University of Padova, Italy
Born on January 25th 1989
citizen of Italy

accepted on the recommendation of

Prof. Taras V. Gerya	ETH Zürich	Examiner
Prof. Ylona van Dinther	Utrecht University	Co-Examiner
Prof. Edi Kissling	ETH Zürich	Co-Examiner
Prof. Stefan Wiemer	ETH Zürich	Co-Examiner
Prof. Romain Jolivet	ENS Paris	Co-Examiner
Prof. Onno Oncken	GFZ Potsdam	Co-Examiner

2019

Luca Dal Zilio
Department of Earth Sciences
Institute of Geophysics
Swiss Federal Institute of Technology (ETH Zürich)
Switzerland
luca.dalzilio@erdw.ethz.ch

Cross-scale modeling of mountain building and the seismic cycle:
From Alps to Himalaya

ETH Zürich, © 2019
Diss. ETH No. 25709

This thesis is subject to copyright. All rights are reserved, whether the whole or part of the material is concerned, specifically the rights of reprinting, reuse of illustrations, or in any other way. Duplication of this publication or parts thereof is permitted only under the provisions of ETH Zürich, in its current version, and permission for use must always be obtained from the author.

Cover image: Zoom into Himalayas mountain range. Relief map Motion Background — @storyblocks.com

Predicting earthquake is
"A game of chance of which we still don't know all the rules"
— Cinna Lomnitz, 1989.

Abstract

Orogenesis—the process of mountain building—forms some of the most spectacular features of the Earth's surface. This complex geological process operates on a wide range of time and length scales and is characterized by fold-and-thrust-belts that grow through sequential stacking of thrust sheets. These faults trigger large earthquakes, often close to densely populated areas. Understanding the dynamics and deformation of collisional orogens thus constitutes an important and challenging step towards improving seismic hazard assessment. By integrating the approaches of numerical modeling, seismology, geodesy, and tectonophysics, this thesis provides a thorough and advanced analysis to improve our understanding of the seismotectonics evolution of collisional mountain ranges. Generic models as well as specific examples—from the Alps to the Himalayas—are explored to evaluate the relation between long-term mountain building processes and short-term seismogenesis.

First, I present a novel model to investigate the partitioning between tectonic and kinematic processes and assess seismic behaviour of mountain belts. These models obtain a Gutenberg–Richter frequency magnitude distribution due to spontaneous events occurring throughout the orogen. I propose that both the corresponding slope (*b* value) and maximum earthquake magnitude correlate linearly with plate convergence rate through a rheological feedback with temperature and strain rate. This is in agreement with earthquakes recorded across the Alps, Apennines, Zagros and Himalaya.

I then explore the self-driven evolution of a convergent margin, from subduction to collisional orogeny and spontaneous slab breakoff. I show how slow—but persistent—bending of a post-collisional residual slab controls the latest evolution of the orogen, including crustal delamination, the construction of the foreland basin, and the seismicity pattern throughout the orogen. Based on these new insights, I argue that tectonic processes across the Central Alps are related to vertical forces driven by a *Slab Rollback Orogeny* model.

To facilitate a comparison to natural settings, I develop a tool for the design of realistic and accurate model setups. By including a number of tectonic constraints, I use this tool to set a rigorous setup of the present-day lithospheric structure of the Nepal Himalaya. This model allows me to explore the conditions that could explain the bimodal seismicity ($\mathrm{M_w}$≤7.8 vs. M8+) of large Himalayan earthquakes. Results reproduce realistic earthquake sequence of irregular magnitude—including events similar to the 2015 $\mathrm{M_w}$ 7.8 Gorkha earthquake—and provides an excellent match to the interseismic observations. Most importantly, this model shows that fault frictional and non-planar geometry of the Himalayan megathrust introduce a shallow region of large strength excess, which can only be activated once enough stress is transferred by partial (blind) ruptures.

Finally, I use a Bayesian sampling method to propose a new coupling model of the Himalayan megathrust. This inversion benefits from an objective weighting of the various datasets by combining observational and modelling errors. In particular, this approach does not include any contamination from the smoothing regularization used in standard approaches. The impact of this model is distinct, as it shows three potential barriers of low coupling separating discrete and large highly coupled patches. These new findings raise the possibility of a heterogeneous coupling distribution of the Himalayan megathrust, both along-strike and down-dip.

Overall, this thesis provides a better understanding of the interaction between mountain building processes and seismicity, and a valuable improvement to this fast-moving cross-field of seismotectonics, seismology and geodynamics.

Riassunto

L'orogenesi—il processo di costruzione delle montagne—forma alcune delle caratteristiche più spettacolari della superficie terrestre. Questo complesso processo geologico opera su una vasta gamma di scale di tempo e lunghezza ed è caratterizzato da un impilamento sequenziale di pieghe e faglie. Queste faglie innescano grandi terremoti, spesso vicini ai grandi centri abitati. Comprendere le dinamiche e la deformazione degli orogeni collisionali costituisce quindi un problema importante e impegnativo per valutare meglio il rischio sismico. Integrando gli approcci di modellistica numerica, sismologia, geodesia e tettonofisica, questa tesi fornisce un'analisi approfondita e avanzata per migliorare la nostra comprensione dell'evoluzione sismotettonica delle catene montuose collisionali. Modelli generici ed esempi specifici—dalle Alpi all'Himalaya—sono esplorati per valutare la relazione tra i processi di formazione delle montagne e i meccanismi sismogenetici.

Per prima cosa, presento un nuovo modello per indagare la ripartizione tra i processi tettonici e cinematici e valutare il comportamento sismico delle catene montuose. Attraverso eventi spontanei che si verificano in tutto l'orogene, questi modelli ottengono una distribuzione della magnitudine e frequenza di Gutenberg-Richter. Questa distribuzione indica che sia la corrispondente pendenza (valore *b*) che la magnitudo massima dei terremoti sono linearmente correlate con la velocità di convergenza delle placche attraverso un feedback reologico con la temperatura e la velocità di deformazione. Questo risultati sono in accordo con i terremoti registrati nelle Alpi, gli Appennini, Zagros e l'Himalaya.

Esamino poi l'evoluzione auto-guidata di un margine convergente, dalla subduzione all'orogenesi collisionale e alla rottura spontanea della placca in subduzione. Mostro come il lento—ma persistente—piegamento della placca in subduzione controlla l' evoluzione terminale dell'orogene, compresa la delaminazione crostale, la formazione del bacino di avampaese e la sismicità in tutto l'orogene. Sulla base di queste nuove intuizioni, sostengo che i processi tettonici attraverso le Alpi Centrali sono legati alle forze verticali guidate da un modello di affondamento della placca in subduzione.

Per facilitare il confronto con gli ambienti geologici, propongo uno strumento per la configurazione di modelli realistici e accurati. Includendo una serie di vincoli tettonici, questo strumento è utilizzato per una configurazione rigorosa dell'attuale struttura litosferica del Nepal–Himalaya. Questo modello consente di esplorare le cause che controllano la sismicità bimodale (magnitudo $\mathrm{M_w}\leq$7.8 vs. M8+) dei grandi terremoti Himalayani. I risultati riproducono una sequenza realistica di terremoti con magnitudo irregolare—compresi eventi simili al terremoto $\mathrm{M_w}$ 7.8 di Gorkha del 2015—e forniscono un ottimo combaciamento con le osservazioni interseismiche. In particolare, questo modello mostra che la frizione e la geometria non planare della faglia portano alla formazione di una regione superficiale ad eccesso

di forza, la quale può essere attivata solo dopo che una sufficiente sollecitazione è stata trasferita dalle rotture parziali più profonde.

Infine, utilizzo un metodo di campionamento Bayesiano per proporre un nuovo modello di accoppiamento del margine di placca Himalayano. Questa modellizzazione inversa beneficia di una ponderazione oggettiva dei vari set di dati combinando errori di osservazione e di modellazione. In particolare, questo modello non include alcuna contaminazione proveniente dalla regolarizzazione utilizzata negli approcci standard. L'impatto di questo modello è distinto, poiché mostra zone discrete ad alto accoppiamento intersismico separate da tre potenziali barriere. Queste nuove scoperte sollevano la possibilità di una distribuzione eterogenea dell'accoppiamento intersismico nel margine di placca Himalayano, sia in profondità che lungo l'arco.

Nel complesso, questa tesi fornisce una migliore comprensione dell'interazione tra i processi di costruzione delle montagne e la sismicità, oltre che un prezioso miglioramento di questo campo trasversale in rapida evoluzione.

Contents

1 INTRODUCTION 1
1.1 Collision and mountain building . . . 2
1.2 Shortcomings of the observational record . . . 10
1.3 Why numerical modeling? . . . 12
1.4 Thesis objectives . . . 16
2 SEISMIC BEHAVIOUR OF MOUNTAIN BELTS CONTROLLED BY PLATE CONVERGENCE RATE 19
2.1 Abstract . . . 19
2.2 Introduction . . . 20
2.3 Methods . . . 22
2.3.1 Seismo-Thermo-Mechanical Modeling . . . 22
2.3.2 Model setup . . . 23
2.3.3 Modeling procedure . . . 25
2.3.4 Evaluating the Gutenberg-Richter distribution and *b* value . 26
2.4 Results . . . 28
2.4.1 Set A: Long-term mountain building . . . 28
2.4.2 Set A: Short-term seismicity . . . 30
2.4.3 Set A: Gutenberg–Richter parameters . . . 30
2.4.4 Set B: Role of mountain ranges architecture . . . 32
2.5 Discussion . . . 35
2.5.1 How does convergence rate control seismicity? . . . 36
2.5.2 Comparison to natural examples . . . 39
2.5.3 On the differential stress dependence of the *b* value . . . 41
2.5.4 Limitations and uncertainties . . . 42
2.5.5 Seismic hazard implications . . . 44
2.6 Conclusions . . . 45
3 SLAB ROLLBACK OROGENY MODEL 49
3.1 Abstract . . . 49
3.2 Introduction . . . 50
3.3 Initial model design . . . 52
3.3.1 Numerical code description . . . 52
3.3.2 Rheological model . . . 54
3.3.3 Eclogitization . . . 58
3.3.4 Estimation of Moment Magnitude (M_W) . . . 59
3.3.5 Setup . . . 59
3.4 Numerical model results . . . 61
3.4.1 Rollback subduction, collision, and slab breakoff . . . 62
3.4.2 Post slab breakoff evolution of the orogen . . . 64
3.4.3 Regional stresses and seismicity distribution . . . 66
3.5 Discussion and Conclusions . . . 68

4 BIMODAL SEISMICITY IN THE HIMALAYA CONTROLLED BY FAULT FRICTION AND GEOMETRY 71
4.1 Abstract . . . 71
4.2 Introduction . . . 72
4.3 Methods . . . 75
4.3.1 Seismo-Thermo-Mechanical methodology . . . 75
4.3.2 Rheological model . . . 77
4.4 Model setup . . . 79
4.4.1 Model configuration and boundary conditions . . . 79
4.4.2 Initial geometry . . . 80
4.4.3 Friction properties on the Main Himalayan Thrust . . . 82
4.4.4 Temperature distribution . . . 83
4.5 Modelling procedure . . . 84
4.6 Modelling limitations . . . 84
4.7 Results . . . 85
4.7.1 Consistency with interseismic deformation . . . 85
4.7.2 Bimodal earthquake behaviour of the reference model . . . 87
4.7.3 Effect of fault friction and geometry on seismic ruptures . . . 92
4.8 Discussion and conclusions . . . 96
5 SEGMENTATION OF THE MAIN HIMALAYAN THRUST INFERRED FROM GEODETIC OBSERVATIONS OF INTERSEISMIC COUPLING 101
5.1 Abstract . . . 101
5.2 Introduction . . . 102
5.3 Methods . . . 105
5.3.1 Geodetic Observations . . . 105
5.3.2 Bayesian analysis . . . 107
5.4 Results . . . 110
5.5 Interseismic coupling distribution . . . 110
5.6 Discussion . . . 114
5.6.1 Segmentation of the Himalayan megathrust and seismicity . 114
5.6.2 Coupling vs. topography . . . 117
6 CONCLUSIONS AND PERSPECTIVES 123
6.1 Thesis conclusions . . . 123
6.2 Application of the STM approach in collisional orogens . . . 124
6.3 Development of observationally constrained models . . . 126
6.4 Exploring the potential of GeoMAC . . . 127
6.5 Inverse modeling: Bayesian sampling method . . . 128
6.6 Future perspectives . . . 129
A TECTONICS AND SEISMICITY IN THE NORTHERN APENNINES DRIVEN BY SLAB RETREAT AND CRUSTAL DELAMINATION 135
A.1 Abstract . . . 135
A.2 Introduction . . . 136
A.3 Methodology and setup . . . 139
A.3.1 Seismo-thermo-mechanical modeling . . . 139

A.3.2 Model setup and observational constraints 140
A.3.3 Model settings 142
A.3.4 Modeling procedure 144
A.3.5 Evaluation of model seismicity 144
A.4 Results and analysis 145
A.4.1 Lithospheric and crustal dynamics 145
A.4.2 Seismicity and surface displacement 146
A.4.3 Surface velocities 146
A.4.4 Seismicity and stresses 147
A.4.5 Slab pull controlling the distribution of seismicity 150
A.4.6 Effect of lithospheric mantle stiffness on seismicity 151
A.4.7 Effect of rock strength on earthquake distribution 153
A.5 Discussion 154
A.5.1 Surface deformation and GPS observations 154
A.5.2 Geodynamics 155
A.5.3 Seismicity 156
A.5.4 Implications of deeper processes on upper crustal seismicity 157
A.5.5 Limitations 158
A.6 Conclusions 159
CURRICULUM VITAE 189
ACKNOWLEDGMENTS 195

1

Introduction

The destructive nature associated with convergent tectonics is manifested by large earthquakes that occur along subduction zones and within fold-and-thrust belts. Seismogenic faults in convergent margins pose some of the most significant natural hazards to human life and property. While the threats of subduction zone earthquakes are well-known, the hazards posed by seismic ruptures in continental mountain belts are repeatedly underestimated in regional hazard assessments. Recent events in these geologic settings (e.g. 1999 $\mathrm{M_w}$ 7.6 Chi-Chi, Taiwan; 2008 $\mathrm{M_w}$ 7.9 Wenchuan, China; 2012 $\mathrm{M_w}$ 6.1 Emilia-Romagna, Italy; 2015 $\mathrm{M_w}$ 7.8 Gorkha, Nepal; 2016 $\mathrm{M_w}$ 6.2 Central Italy) have led to tens of thousands of deaths and tens of billions of dollars in damage to infrastructure. When no accurate information is available on recent damaging earthquakes, seismic hazard assessment (SHA) studies must rely on extrapolating the occurrence frequency of smaller events, and on field observations of paleo-earthquakes. Numerical models of earthquake physics is a unique tool to artificially lengthen the observation window of local seismicity, and thus add to the SHA toolbox.

This thesis integrates a wide spectrum of scientific disciplines ranging from geodynamics and tectonics to earthquake physics, geodesy and seismology. This allows a detailed investigation of the deformation and seismicity associated with mountain building processes and fault activity in the Earth's upper, brittle crust. New insights into these deformational processes on both earthquake cycle and geologic timescales are combined to improve our physical understanding of seismicity in mountain belts, which have a breadth of potential applications in active tectonics studies and seismic hazard assessment.

This introductory Chapter 1 presents the most important concepts relating to mountain building processes, tectonics and seismicity in orogenic mountain belts and their relevance (Section 1.1), including a description of two specific tectonic settings: the Alps and the Himalayas. This overview then introduces the current limitations on recurrence times of damaging earthquakes due to our very limited

observation span (Section 1.2) and why numerical simulation is an essential tool in earthquake physics research and how it improves our physical understanding of these destructive events (Section 1.3). In particular, it explains why we need to combine recent scientific advances in different fields and integrate them into new composite numerical modeling approaches, which is the main goal of this thesis. Finally, the objectives and final remarks are outlined in Section 1.4.

1.1 Collision and mountain building

The process of building an orogen, or $orogenesis$, occurs when two tectonic plates collide—either forcing material upwards to form mountain belts such as the Alps or the Himalayas or causing one plate to be subducted below the other, resulting in mountain chains such as the Andes. Orogenic belts are commonly long, arcuate tracts of highly deformed rocks and are the clearest manifestations of long-term deformation of the continental crust. The processes that control orogenesis vary considerably depending on the tectonic setting and the type of lithosphere involved in the deformation. $Non–collisional$ or Andean-type orogens result from ocean–continent convergence where plate motions and other factors controlling subduction lead to compression within the overriding plate (e.g., Oncken *et al.* , 2006). $Collisional$ orogens, which are those addressed in this thesis, develop where a continent collides with a continental margin as a result of subduction (e.g., Handy *et al.* , 2010; Schmid *et al.* , 1996) (Fig. 1.1). In these latter belts, the thickness and positive buoyancy of the colliding material inhibits its descent into the mantle and leads to compression and orogeny (Kissling & Schlunegger, 2018).

Much of the internal variability displayed by collisional orogens can be explained by differences in the strength and rheology of the continental lithosphere and by physical processes that influence these properties during orogenesis. For example, where the continental lithosphere is relatively cool and strong, orogens tend to be comparatively narrow, ranging between 100- and 400-km-wide. The Southern European Alps exhibit these characteristics (e.g., Rosenberg *et al.* , 2017). Conversely, where the continental lithosphere is relatively hot and weak, strain tends to delocalize and is distributed across zones that can be over a thousand kilometers

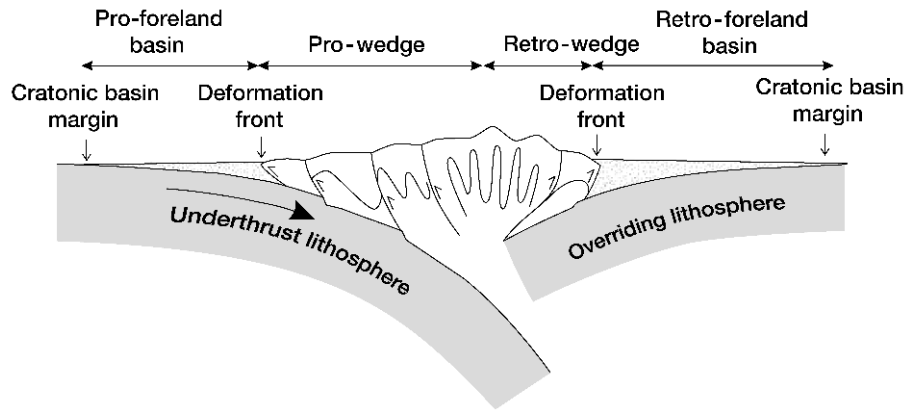


Figure 1.1.: Cartoon of a doubly vergent $collisional$ orogen. The pro-foreland basin lies in the flexural depression over the subducting slab, which advances towards the orogen at the regional convergence rate. The retro-foreland basin lies in the flexural depression above the overriding slab which is predominantly stationary with respect to the orogen.

wide. The Himalayan–Tibetan orogen displays these latter features (e.g., Avouac, 2015).

The dynamics of mountain building combines multiple processes across a wide spectrum of spatiotemporal scales, such as crustal shortening, thickening, and intense erosion (e.g., Willett, 2010). Most importantly, mountain ranges and their piedmonts are also a primary locus of earthquakes. They have therefore been the focus of a variety of investigations that have addressed various aspects of mountain building processes. Geological and geophysical studies give some idea of the structure of the range and physical properties at depth (e.g., Nábělek *et al.* , 2009; Fry *et al.* , 2010). The long-term geological history of mountain ranges—from several millions to a few tens of millions of years—have been documented by structural, thermo-barometric, and thermo-chronological studies (e.g., Avouac, 2015, and references therein). Morpho-tectonic studies have revealed the evolution over the past several thousands or tens of thousands of years (e.g., Hinderer *et al.* , 2013). Finally, geodetic measurements and seismological monitoring have revealed the pattern of strain and stress buildup over several years (e.g., Stevens & Avouac, 2015; Houlie *et al.* , 2018). All together, these studies show that processes that affect the strength and rheology of continental lithosphere act at different spatiotemporal scales throughout the orogenesis. Like all other major zones of continental deformation, the evolution of collisional orogens is governed by the

balance among large-scale, regional forces, and small-scale, local forces, as well as the strength and rheology of the continental lithosphere and by physical processes that change these parameters over time.

The European Alps and the Himalayan–Tibetan belt represent two ideal examples of complex orogens formed by continent–continent collision following the closure of a major ocean basin, and they have long served as a field laboratory for testing geological ideas (e.g., Willett, 2010). The Alpine orogeny is one of the best-studied orogenic arcs in the world and constitutes a challenge for a great number of geoscientists due to the intricate processes involved in the collision of the Adria and the European plates. On the other hand, the Himalayan–Tibetan orogen is one of the most spectacular examples of a plate convergence event on Earth followed by the collision and subsequent formation of the Tibetan plateau (e.g., Capitanio *et al.* , 2010). The active tectonics, diverse structure, and relatively well-known plate boundary history of this belt allows for the direct measurements of many tectonic relationships and provide important constraints on the driving mechanisms of deformation and the manner in which deformation is accommodated (e.g., Yin & Harrison, 2000). In addition, the immense size, high elevations and recent earthquakes of this orogen illustrate how mountain building and seismicity are interrelated. These interactions form important elements of orogenesis and seismotectonics in most, if not all, tectonic settings.

The Alps—an untypical but classic orogen example

The Alps can rightly be termed the classic orogen because they have been intensely investigated for more than two hundred years and many fundamental concepts and basic facts on mountain building came from these studies.

In principle, the Alps are the product of a classical Wilson cycle that begun with the opening of the Alpine Tethys between Eurasia in the north and Africa and Adria in the south in mesozoic times (Handy *et al.* , 2010). However, contradicting interpretations and serious problems concerning the understanding of the tectonic evolution of this orogen continued to arise—these are the possible reasons "*why plate tectonics was not invented in the Alps*" (Trümpy, 2001).

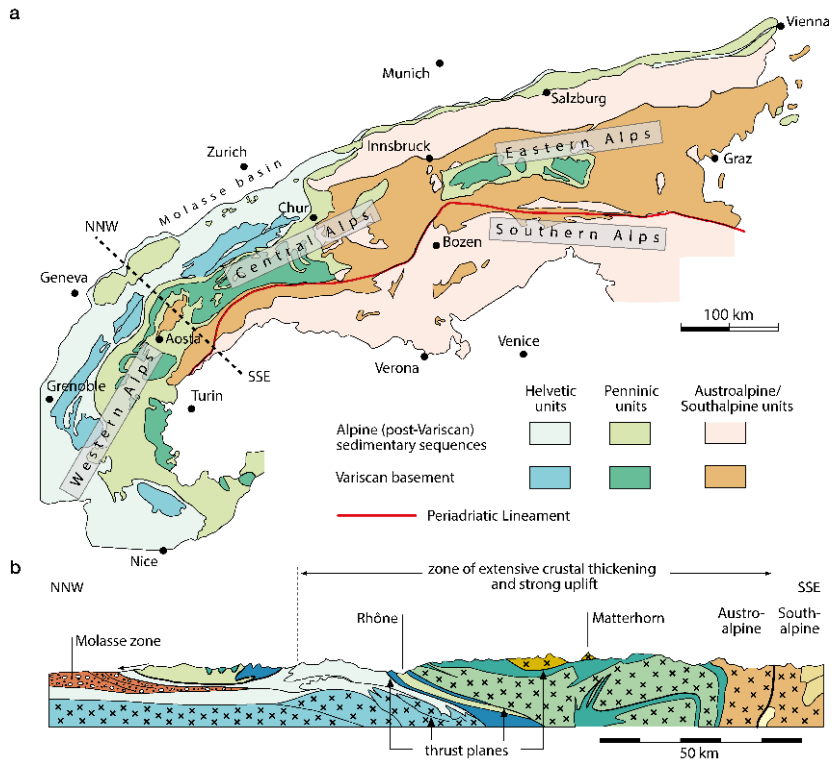


Figure 1.2.: (**a**) Tectonic map of the Alps showing the three mega-units that comprise the nappe systems. The Austroalpine unit was thrust over the Penninic unit, which in turn was thrust over the Helvetic unit. The Periadriatic Lineament is a large-scale fault zone that borders the northern margin of the Southern Alps. (**b**) Cross section of the western Swiss Alps showing present relations of major tectonic elements, modified after Trumpy (1980). The Austroalpine unit overlies the South Penninic unit that is composed of ocean floor material. The Middle Penninic unit, a continental fragment rifted from Europe is in the foreground.

The Alps represent a double-vergent collisional belt resulting from the Cretaceous to Eocene eastward subduction of the European continental crust beneath the Adria upper plate followed by continental collision (Coward & Dietrich, 1989; Pfiffner *et al.* , 2002). The suture zone between the two plates is marked by slices of ophiolitic materials representing the Liguria-Piedmont Ocean, which separated the European continental margin from the Adriatic margin in the Mesozoic (e.g., Stampfli *et al.* , 1998) (Fig. 1.2).

The present convergence rate in the Central Alps is relatively small (1–2 mm/yr) (Calais *et al.* , 2002; Sue *et al.* , 2007; D'agostino *et al.* , 2008) and comparable to the isostatic uplift rate (Champagnac *et al.* , 2007; Serpelloni *et al.* , 2013). These

low convergence rates indicate a mostly locked subduction–collision zone in the Central Alps and not an ongoing dominant convergence (Singer *et al.* , 2014). The stress field derived from focal mechanism of local earthquakes (Sue *et al.* , 1999) in the western Alps shows compression in the northern foreland and southern hinterland and extension in the core of the orogen. This peculiar stress distribution through the orogen may be interpreted as the result of the slow, but constant, convergence of Europe and Adria in combination with isostatic rebound due to erosional unloading of topography (Fig. 1.3) (Kissling, 2009).

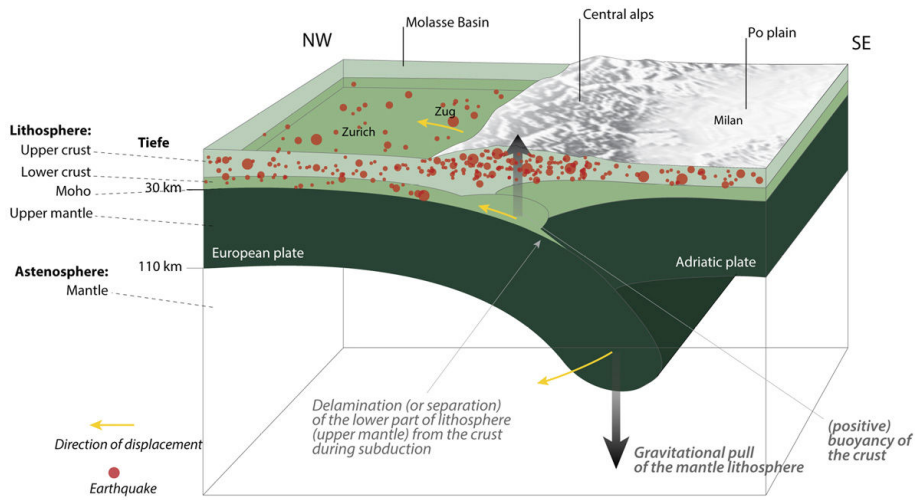


Figure 1.3.: Cross section through the lithosphere schematically showing the various forces acting at depth on the Alps. The hanging European slab (mantle lithosphere) causes a downward force, while the lower crust detaches from the slab and the large crustal root generates buoyancy to compensate for loads by topography and by the slab (Singer *et al.* , 2014).

The Alps have been the locus of relatively strong ($\mathrm{M} > 6$) earthquakes in the past. Information from historical sources and modern earthquake catalogues show that there were at least 12 earthquakes with a magnitude ≥ 6 in the past thousand years (Fig. 1.4). The last one took place in 1976 in northern Italy ($\mathrm{M_w}$ 6.46, Rovida *et al.* (2011)), followed by two aftershocks with magnitudes > 6 within a few months (Pondrelli *et al.* , 2001). This earthquake sequence claimed 989 lives and injured 2'400 people. As a consequence, approximately 45'000 people were left homeless. Although the extent of damage for historical events can sometimes be difficult to

estimate, it is likely that at least three of the earthquakes caused more than 10'000 deaths.

While for some of these earthquakes authors generally agree that the fault sources belong to the Eastern Southern Alps thrust fault system, emerging at the boundary between the Venetian plane and the mountain front in northeastern Italy (e.g., Benedetti *et al.* , 2000; Cheloni *et al.* , 2012), for others, the fault sources are still uncertain. This is the case of the 1117 (M6.7) Verona earthquake, the 1348 (M7) Carinzia earthquake and the 1511 Slovenia (M~6.9) earthquake (Rovida *et al.* , 2011; Stucchi *et al.* , 2013). Uncertainties on the location, geometry and seismic potential of active faults in the Eastern Alps persists due to: (1) the complex structural framework of the region, inherited by the geodynamic evolution of this area and resulting in deformation distributed over a vast area, (2) slow deformation rates at mainly blind faults, (3) sparse instrumental seismicity, causing some areas where strong historical earthquakes occurred to appear presently almost aseismic.

In this scenario, Global Positioning System (GPS) data provide fundamental constraints on the kinematics of continental deformation. GPS observations, in fact, have provided increasingly more details on the kinematics of this area (e.g., Grenerczy *et al.* , 2005; Caporali *et al.* , 2013), fault slip-rates (e.g., Bechtold *et al.* , 2009; Barba *et al.* , 2013), seismic potential (e.g., Cheloni *et al.* , 2014), and geodynamics (e.g., Metois *et al.* , 2015).

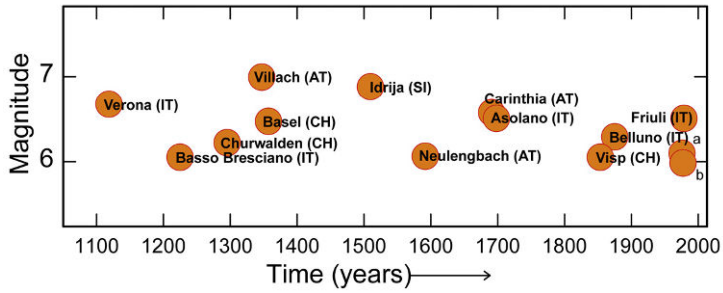


Figure 1.4.: Time series of the largest earthquakes in the last millennium in the Alpine region. The aftershocks of the 1976 Friuli earthquake are labeled "a" and "b". Credit: *Swiss Seismological Service*.

For example, the kinematic boundary conditions in the Eastern Southern Alps of Italy are well known, with ~N–S convergence rates increasing from west to east as resulting from the counterclockwise rotation of the Adriatic microplate around a pole

of rotation located in the western Po Plain (Nocquet & Calais, 2003; Battaglia *et al.* , 2004; Serpelloni *et al.* , 2005; D'agostino *et al.* , 2008). Deformation indicators from geodesy and seismotectonics are in fairly good agreement in the Southeastern Alps, making assumptions on the kinematics and location of active faults there more robust. On the contrary, at the boundary between Italy, Austria and Slovenia, where different tectonic regimes coexist (e.g., Bressan *et al.* , 2003; Poli & Renner, 2004; Herak *et al.* , 2009) and GPS stations are sparser, uncertainties on the location and kinematics of major active faults are larger.

The Himalaya—the world's highest mountain ranges

The Himalayan arc and the Tibetan Plateau formed as a result of the collision between India and Asia (e.g., Molnar & Tapponnier, 1975). The two continents were once separated by the Tethys Sea, which was subducted beneath the southern margin of Asia (Fig. 1.5). The present-day structure of the Himalayas is formed by

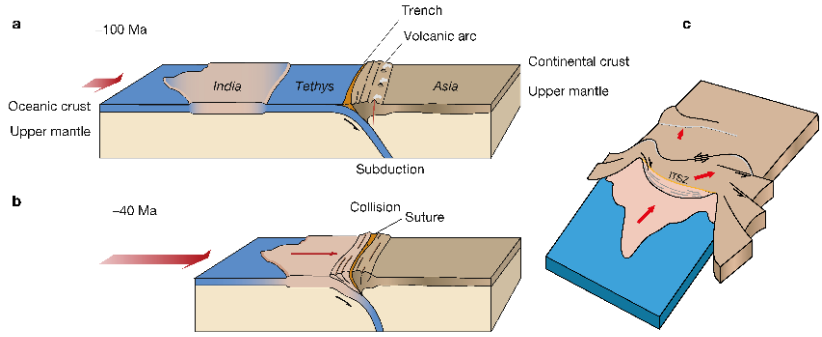


Figure 1.5.: Convergence and collision between India and Asia, modified after Avouac (2015). (**a-b**) Prior to the collision, an ocean, the Tethys Sea, used to separate the northern margin of India and Eurasia. The southern margin of Asia was an active margin with a subduction zone similar, for example, to the Andean subduction zone bordering the western margin of South America. (**c**) Sketch showing how indentation of India into Eurasia since the onset of the collision has been absorbed by a combination of crustal thickening and lateral escape.

a stack of thrust sheets (Le Fort, 1975). Two major thrusts, from north to south, are the Main Central Thrust (MCT) and Main Boundary Thrust (MBT), which are passively displaced above the basal Main Himalayan Thrust (MHT) (Fig. 1.6). They

form, respectively, the southern limits of the High Himalaya and Lesser Himalaya domains, while the Lesser Himalaya domain thrusts over the Sub-Himalaya.

The lithospheric structures beneath Nepal and Southern Tibet have been locally imaged by geophysical data (e.g., Nábělek *et al.* , 2009) and a crustal ramp has been deduced from balanced cross-sections and indirect models which associate: (1) the clustering of micro-seismicity with stress increase in the vicinity of the ramp (Pandey *et al.* , 1995); (2) the increase in topography and fluvial incision with increasing dip of the MHT (Lavé & Avouac, 2001); (3) the present-day velocity field with the mechanical behavior of the crust in the vicinity of the ramp (Berger *et al.* , 2004); and (4) the thermo-chronological data with thermo-kinematic models (Herman *et al.* , 2010).

The MHT absorbs about 20 mm/yr of convergence in Nepal, which is nearly half of the present convergence between India and Eurasia (e.g., Bilham *et al.* , 1997; Bettinelli *et al.* , 2006) (Fig. 1.6). Great earthquakes of $\mathrm{M}8+$ have episodically ruptured segments of the brittle upper part of the MHT several hundred kilometers long. Historical archives in the Kathmandu Valley and the surrounding Himalayan foothills indicate that several earthquakes have occurred during the last millennium (e.g., Mugnier *et al.* , 2013). The brittle upper part of the MHT is usually locked but sometimes ruptures producing great earthquakes (Bilham *et al.* , 2001; Stevens & Avouac, 2015); this is a great threat to communities as it is only a matter of time until the next great earthquake occurs in this densely populated area where many hydroelectric dams have been built (Mugnier *et al.* , 2013). Recently, the moment magnitude ($\mathrm{M_w}$) 7.8 Gorkha earthquake—which struck Nepal in April 2015—resulted in more than 8'700 deaths, destroyed 490'000 houses and 30'000 classrooms, and rendered 3.5 million homeless. The emerging view is that, although the mainshock nucleated near the anticipated location, also known as "seismic gap", it was not the long-awaited "big one" in western Nepal. Thus, several questions remain open: (1) does a great earthquake ($M > 7$) release all the strain stored by the Tibet–India convergence during the preceding interseismic period, or (2) does it only release a portion of the stored energy, or (3) can it release all the energy not released during one or more preceding earthquakes (Feldl & Bilham, 2006)? In the first case, it would be possible to infer a rather regular seismic cycle, but in the other two cases, the remaining elastic energy would drive a more random or

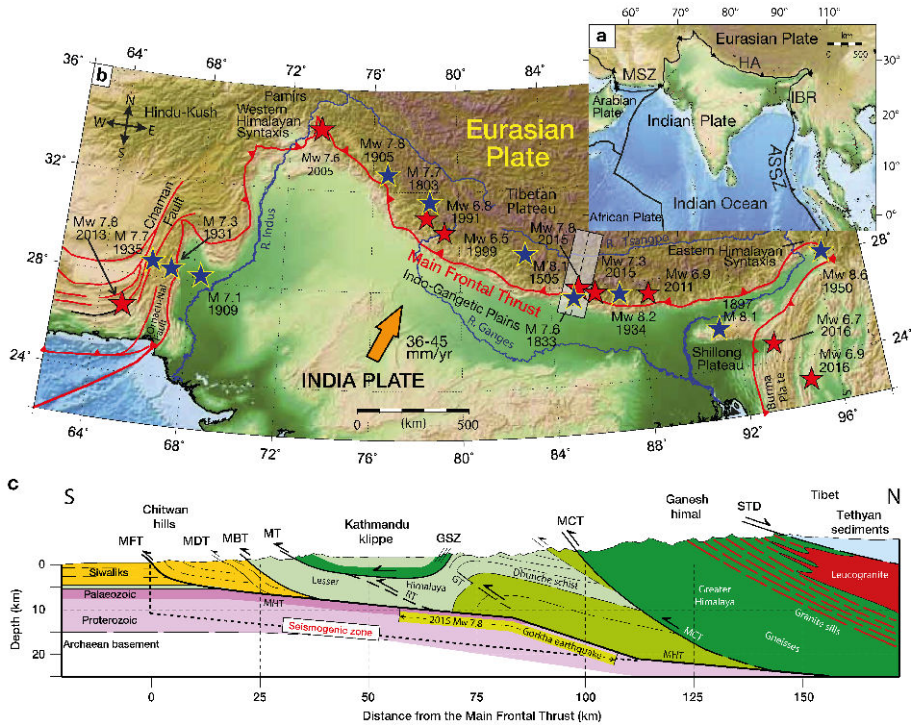


Figure 1.6.: The Himalayan arc. (**a**) India-Eurasia plate boundary showing Makran Subduction Zone (MSZ), Himalayan Arc (HA), Indo-Burman Ranges (IBR), and Andaman-Sumatra Subduction Zone (ASSZ). (**b**) Map showing significant earthquakes in the Himalaya, modified after Rajendran *et al.* (2017). Red stars: Modern-day events ($M_w \geq 6.5$). Blue stars: Historic earthquakes ($M \geq 7$). Thick red line with triangles shows the convergent plate boundary and major fault systems. (**c**) Generalized cross section of the central Himalaya, modified after Elliott *et al.* (2016), showing the Main Central Thrust (MCT), the Main Boundary Thrust (MBT), the Main Frontal Thrust (MFT), the South Tibetan Detachment (STD), and the Indo-Tsangpo Suture Zone (ITSZ). Detachment plane coincides with the Main Himalayan Thrust (MHT).

clustered sequence of events. Furthermore, in the second case, and as observed after the 2005 Kashmir earthquake (Jouanne *et al.* , 2011), significant postseismic deformation might occur, and in the third case, giant earthquakes (M9+) cannot be excluded (Stevens & Avouac, 2016).

1.2 Shortcomings of the observational record

Our instrumental record dates back to ~1900, while thousands of years of data are required to cover several complete seismic cycles and reveal the earthquake

characteristics of a typical subduction zone (e.g., McCaffrey, 2008). Unfortunately, paleoseismological studies (e.g., Sieh *et al.* , 2008) do not provide enough spatiotemporal coverage to extend the global analysis that far back in time. Additionally, contemporary variations of several geodynamic parameters within tens of convergent margins make it difficult to identify one-to-one correlations and cause-effect relationships (e.g., Heuret *et al.* , 2011).

Seismologists have attempted to tie the history of earthquakes over the past century to various properties of seismogenic faults, such as convergence rate, temperature, and others (e.g., Uyeda & Kanamori, 1979; Ruff & Kanamori, 1980), in order to understand what might limit earthquake size. On the other hand, traditional seismic hazards assessment methodologies can estimate the coseismic slip along ancient ruptures and thus constrain paleo-earthquake magnitude and total fault slip rates (see Galli *et al.* , 2008, for a review). However, deformation associated with seismic faulting can be multifaceted, often involving a set of tectonic and physical characteristics. Also, many active thrust faults—or portions of these faults—are blind. Thus, estimating fault slip rate and moment magnitude exclusively from uplift measures across surface ruptures is inadequate to measure the slip budget at depth. For blind faults and other structures with limited fault exposures, geologic structure provide the most direct means of constraining fault activity. Hence, the observed seismicity is the result of the combined effect of various parameters, whose isolated roles remains unknown.

Assessing earthquake hazard is an ambitious enterprise. Given the complexities of the earthquake process and our limited knowledge of it, many subjective choices are needed. For example, earthquake hazard maps depend heavily on their makers' preconceptions about how the earth works. When these preconceptions prove correct, a map fares well. When they prove incorrect or inadequate, a map does poorly. The 20 May 2012 $\mathrm{M_w}$=6.1 earthquake that struck the Emilia region of northern Italy illustrates a common problem afflicting earthquake hazard assessment (Peresan & Panza, 2012). It occurred in an area classified as "low seismic hazard" based on the current national seismic hazard map. The 2011 Tohoku earthquake is another striking example—after the 2008 Wenchuan and 2010 Haiti earthquakes—of highly destructive earthquakes that occurred in areas predicted by earthquake hazard maps to be relatively safe (Stein *et al.* , 2012).

Predicting earthquake hazard has been described as playing a game of chance (Lomnitz, 1989). As in any game of chance, the best we can do is to maximize our expectation value by understanding the game as well as possible. The better we understand the physics of earthquakes and the limitations of the hazard maps, the better we can use and improve these maps.

Over the past two decades, earthquake science has entered a new era with the development of space-based technologies to measure surface deformation at the boundaries of tectonic plates and large faults. In particular, the launch of the Global Positioning System (GPS) revolutionized crustal deformation measurements. Since the early 1990s, GPS measurements, either in campaign style or as continuous monitoring, have delineated patterns of co-, post- and inter-seismic deformation for many seismic zones with unprecedented clarity (e.g., Moreno *et al.* , 2010; Avouac, 2015b). Developments in satellite radar interferometry and satellite gravimetry further improved the situation (e.g., Elliott *et al.* , 2016). However, the short time span of modern measurements necessitates comparative studies of different zones that are at different stages of the deformation cycle. In particular, the observed seismicity is the result of the joint effect of various parameters, whose isolated role remains hidden. So far we have not yet observed a complete seismic cycle with reasonable spatio-temporal resolution and thus need to paste the inherently different snapshots together. This short and sparse instrumental and historical record of megathrust earthquakes (McCaffrey, 2008) makes it virtually impossible to understand the governing physics and isolate the role of a single tectonic parameter.

1.3 Why numerical modeling?

Natural fault systems are typically remote and hardly accessible, and data are in most cases sparse and expensive to acquire. Access to active faults requires drilling and/or dedicated field campaigns, which are rare and expensive, and extreme conditions (e.g., high temperatures) in existing boreholes inhibit long-term data acquisition. Besides that, rock mechanics experiments are often not fully representative. The spatial and temporal scales of natural fault systems exceed those that are experimentally accessible by orders of magnitude, and their typ-

ical pressure, temperature, and compositional ranges are difficult to deal with experimentally.

Other approaches have been employed, including (1) scaled laboratory experiments, (2) analytical techniques and (3) numerical experiments. Laboratory experiments make use of analogue materials like sandpaper, honey, silicon putty or sand to simulate the rheology of the mantle and crust, thereby taking care that key non-dimensional parameters of the experiments are as close as possible to natural values. Although much insight has been obtained by these experiments, it is difficult to incorporate physical processes acting at different spatiotemporal scales or temperature dependent rheologies. Analytical techniques can be used to derive solutions to the governing mechanical equations, but are typically limited to small deformations and/or relatively simple rheologies. Numerical experiments do not suffer from these drawbacks but have the disadvantage of being computational expensive, especially in three dimensions. Moreover, it is sometimes not easy to understand results of numerical experiments in terms of the controlling parameters, since typically many different (nonlinear) processes are incorporated and act simultaneously in these models. Thus, the more a model resembles nature, the harder it becomes to understand. It is clear, for example, that orogeny would not exist without horizontal compression. At the same time, gravity may also influence its formation. But what are their respective roles in tectonic processes? How do they affect the seismic behaviour of mountain belts? What is the nature of the thermo-mechanical connection between crust and mantle? In this thesis such questions are addressed by a combination of forward and inverse modeling techniques.

Forward modeling: Seismo-Thermo-Mechanical (STM) approach

Recent progress in computing technology has enabled numerical models of the seismic cycle that more accurately represent the physics of earthquakes and aseismic slip. However, even for the more pragmatic goal of understanding only the behavior of destructive large dynamic events, it is still important to consider the entire spatiotemporal scales of mountain building and seismic cycle processes. This is because the long-term tectonic deformation may determine where large

earthquakes would nucleate as well as modify stress and other initial conditions before and after earthquakes (e.g., Lapusta & Barbot, 2012).

Ideally, a model of earthquake cycles should account for long-term tectonic stress, fault growth, stress relaxation of the rock medium in response to previous earthquakes, fault rupture as a frictional instability, as well as the effects on evolving fault structure (Wang, 2007). However, such a comprehensive model is not yet available, despite solid attempts (Aagaard *et al.* , 2013). To approach such an ideal model, a new two-dimensional (2D) seismo-thermo-mechanical (STM) modeling approach has been developed by Ylona van Dinther at ETH Zürich (van Dinther, 2013, *PhD thesis*). To bridge long-term tectonic and short-term seismicity time scales, the STM modeling approach aims to merge the strengths of geodynamic models (e.g., Gerya, 2011; Dal Zilio *et al.* , 2018a) and classical seismic cycle simulations (e.g., Lapusta & Liu, 2009). State-of-the-art seismic cycle simulations efficiently and accurately simulate cycles of fast and slow slip earthquakes resulting from tectonic loading (yr-kyr). They are, however, limited to fault motion along a single, infinitely thin planar fault embedded in an elastic half space (Lapusta & Barbot, 2012). In contrast, geodynamic models take care of the spontaneously evolving complex fault geometry and visco-elastic deformation, but ignore short time scales as they focus on long-term processes (kyr–Myr).

The basis of the 2D STM modeling approach is the continuum-based, visco-elasto-plastic model I2ELVIS, which was originally designed for long-term geodynamic simulations (Gerya & Yuen, 2007). It solves for the conservation of mass, momentum and energy using a finite-difference scheme with a marker-in-cell technique. The implementation of a strongly rate-dependent friction formulation and inertial term allowed for the simulation of spontaneously developing frictional instabilities along variable rupture paths, which were validated against analogue earthquakes (Corbi *et al.* , 2013; van Dinther *et al.* , 2013a). In a more realistic subduction zone setting, a reasonable agreement with a range of seismological, geodetic, and geological observations was obtained both for megathrust earthquakes (van Dinther *et al.* , 2013b), and off-megathrust earthquakes (van Dinther *et al.* , 2014).

This PhD thesis aims to continue this existing and intriguing research avenue, by applying the STM approach to unravel the cause–effect relationship between

governing characteristics of continent-continent collisional plate boundaries, related seismicity, and interseismic processes. This includes the application of generic setups to investigate the first-order factors of seismic behaviour in mountain belts.

A major contribution of this thesis is the development of a tool that integrates geological and geophysical data for the design of present-day model setups. This approach accounts for correct far-field boundary conditions (e.g., plate convergence rates and primary plate driving forces), consistent rheological data, rigorous crustal and lithospheric structures, and accurate fault geometries. Outcome from these models can be used for a direct comparison with existing observations from present-day, seismically active, mountain belts.

Inverse modeling: Bayesian approach accounting for prediction uncertainty when inferring interseismic coupling

Modern geodetic observations in seismogenic plate boundaries enable exploration of the kinematics of active faults during the interseismic, coseismic, and postseismic phases of the earthquake cycle (e.g., Thatcher, 1975). During the interseismic phase of seismic cycle, plate movements and their relative interactions generate a displacement on the fault system that varies with the fault geometry, crust rheology and intensity of plates relative motion (Bürgmann & Dresen, 2008; Thatcher, 2009). This deformation is detectable by geodetic techniques and provide large amounts of measurements with millimeter precision, thereby allowing for the study of interseismic deformation at local fault scale. Such studies lead to the identification of regions where faults are locked, or coupled, accumulating elastic strain that can drive future earthquakes (e.g., Jolivet *et al.* , 2015), and those where faults are slipping aseismically during the interseismic (e.g., Perfettini *et al.* , 2010).

To perform an inversion, we assume that the system can be described by a set of physical laws, expressed in the form of mathematical equations. When the equations accurately describe the real physics, inversion may yield the best geophysical solution. However, for problems like interseismic deformation, the processes are much less well understood (Wang, 2007). The problem of determining fault slip from surface deformation data thus suffers from sources of *non-uniqueness* (Taran-

tola & Valette, 1982). Also, source inversion algorithms usually do not include realistic error analyses and their results are generally not accompanied by reliable estimates of uncertainty. These limitations reduce the utility of inferred interseismic models and associated by-products. Furthermore, uncertainty in both data and model predictions can cause current source models to be significantly biased due to overfitting of seismic and geodetic observations. The reliability of any source inversion depends on many factors including the size and complexity of a fault, the amount and quality of data, the prior information, and the way in which data sample the source region.

To overcome these limitations, this thesis adopts an newly developed algorithm based on a fully Bayesian approach, which allows for the derivation of the Probability Density Function (PDF) of slip during the interseismic period. By combining the available information from observations and prior information on the model parameters, the Bayesian source inversion constructs a posterior distribution for the source model parameters. The general formalism provided by this approach is used to (1) explicitly quantify the impact of uncertainties in our models and (2) rigorously incorporate such uncertainties in potential ill-posed inverse problems.

1.4 Thesis objectives

The main objectives of this thesis are accomplished in five subsequent steps, which were either published or are in preparation for publication as independent peer-reviewed articles. The body of this thesis consists of the following chapters:

- **Chapter** 2 focuses on the partitioning between tectonic and kinematic processes to seismic behaviour of mountain belts in a generic two-dimensional (2D) continental collision setting. It quantifies the effect of plate convergence rate in terms of both frequency and magnitude distribution of earthquakes due to spontaneous events occurring throughout the orogen.

- **Chapter** 3 presents results of post-slab breakoff orogenic evolution in terms of both long-term dynamics and short-term seismicity. This so-called "*Slab Rollback Orogeny model*" identifies the first-order mechanism responsible

for the latest stage of the Alpine orogeny and, in particular, the evolution of foreland (Molasse) basin and the relatively deep lower crust seismicity.

- **Chapter** 4 explores the conditions that could explain the bimodal seismicity ($\mathrm{M_w}$≤7.8 vs. M8+) of large Himalayan earthquakes. By including a number of tectonic constraints, we design an accurate setup of the present-day lithospheric structure and geometry of the Main Himalayan thrust (MHT) fault. It explains how that a bimodal seismicity emerges as a result of relatively higher friction and a non-planar geometry of the MHT.

- **Chapter** 5 proposes a new coupling model of the Himalayan megathrust, obtained from the joint inversion of a recent compilation of interseismic GPS velocities and leveling data in a fully Bayesian framework. This approach allows for the evaluation of the population of plausible coupling models given geodetic data and forward problem uncertainties. The results obtained in this chapter, combined with the size, location and frequency of large historical earthquakes, provide new insights on where pre-seismic locking is taking place, and what fraction of the long-term slip rate it accounts for.

The final achievements of the aforementioned chapters are evaluated in a concluding **Chapter** 6. After summarizing the main results, I discuss some future perspectives in terms of future developments and methodological improvements, open problems, and new potential avenues of application. The appendix A contains a co-authored paper (in preparation) that investigates the role of lithospheric-scale driving forces and crustal rheology in controlling both large-scale dynamics and small-scale tectonics and seismicity of the Northern Apennines orogen.

In general, the models presented in this thesis give insight into various mountain building processes acting at different spatiotemporal scales. Any model, whether forward or inverse, has the drawback of being a simplification of nature. Ultimately, whether the simplifications are justified can only be tested through close collaboration between the different fields of geosciences. From my perspective, the duty of modelers is to provide a thorough understanding of processes that happen in their highly idealized world. The examples presented in this thesis realize this

philosophy through combined application of forward and inverse modeling methods and integration of geological and geophysical constraints.

2

Seismic behaviour of mountain belts controlled by plate convergence rate

This chapter is published as:
Dal Zilio L., van Dinther, Y., Gerya, T. V., Casper C. Pranger
Seismic behaviour of mountain belts controlled by plate convergence rate
Earth and Planetary Science Letters 482 (2018): 81-92.

2.1 Abstract

The relative contribution of tectonic and kinematic processes to seismic behaviour of mountain belts is still controversial. To understand the partitioning between these processes we developed a model that simulates both tectonic and seismic processes in a continental collision setting. These 2D seismo-thermo-mechanical (STM) models obtain a Gutenberg-Richter frequency-magnitude distribution due to spontaneous events occurring throughout the orogen. Our simulations suggest that both the corresponding slope (*b* value) and maximum earthquake magnitude ($\mathrm{M_{max}}$) correlate linearly with plate convergence rate. By analyzing 1D rheological profiles and isotherm depths we demonstrate that plate convergence rate controls the brittle strength through a rheological feedback with temperature and strain rate. Faster convergence leads to cooler temperatures and also results in more larger seismogenic domains, thereby increasing both $\mathrm{M_{max}}$ and the relative number of large earthquakes (decreasing *b* value). This mechanism also predicts a more seismogenic lower crust, which is confirmed by a transition from uni- to bi-modal hypocenter depth distributions in our models. This transition and a linear relation between convergence rate and *b* value and $\mathrm{M_{max}}$ is supported by our comparison of earthquakes recorded across the Alps, Apennines, Zagros and Himalaya. These results imply that deformation in the Alps occurs in a more ductile manner compared to the Himalayas, thereby reducing its seismic hazard. Furthermore, a second

set of experiments with higher temperature and different orogenic architecture shows the same linear relation with convergence rate, suggesting that large-scale tectonic structure plays a subordinate role. We thus propose that plate convergence rate, which also controls the average differential stress of the orogen and its linear relation to the *b* value, is the first-order parameter controlling seismic hazard of mountain belts.

2.2 Introduction

Mountain building is the most spectacular manifestation of continental dynamics. The fact that mountain ranges are able to maintain their topography over tens of millions of years, is the evidence of how tectonic forces deform the continental crust (Avouac, 2015). Frequent earthquakes are the physical response of such crustal deformation, driven by convergence of continental plates.

Mitigating the impact of these earthquakes in mountain belts is crucial as part of these regions are densely populated. Moreover, understanding the partitioning of seismic and aseismic fault slip is central to seismotectonics, as it ultimately determines the seismic potential of faults. Although we cannot predict when and where the next earthquake will occur, we may forecast the maximum credible size and frequency of future events using the Gutenberg-Richter law (Gutenberg & Richter, 1944). This power law describes the frequency-magnitude distribution of earthquakes and its slope, the so-called *b* value, is commonly used to describe the relative occurrence of small and large events (e.g., Schorlemmer *et al.* , 2005). From a physical mechanism perspective, local spatial variability of *b* and corresponding seismic hazard have been interpreted to relate to differences in the rheology of the crust (e.g., Pasquale *et al.* , 2010), tectonic regime (e.g., Gulia & Wiemer, 2010; Doglioni *et al.* , 2015), differential stress (e.g., Spada *et al.* , 2013b; Scholz, 2015), style-of-faulting (e.g., Schorlemmer *et al.* , 2005), and degree of heterogeneity (e.g., Singh *et al.* , 2009). On a larger regional scale, studies over the past decades have suggested that variations in seismicity of the mountain chains are related to variations in geologic structure (e.g., Bollinger *et al.* , 2004; Grenerczy *et al.* , 2005;

Tatar *et al.* , 2002). However, the preeminent physical parameter in controlling the seismic behaviour in orogenic mountain belts is still unclear.

Mountain building processes acting on a time-scale of millions of years have been widely studied both using numerical models (e.g., Faccenda *et al.* , 2008) and analogue experiments (e.g., Davis *et al.* , 1983). These models have been used to investigate the effect of different physical characteristics on the evolving geometry and dynamics of a collisional margin. However, because of the relatively large computational time step (Δ_t =1000 yr), transient features and short-term processes, such as earthquakes, are not included. On the other hand, dynamic rupture simulations physically consistently model the propagation and arrest of a rupture for a set of unknown initial conditions—such as the stresses—and strength and the fault geometry (e.g., Dalguer, 2012). Alternatively, seismic cycle models simulate cycles of recurring interseismic and coseismic periods, either by kinematically defining slip or stress drop or by dramatically allowing rupture nucleation and propagation (e.g., Lapusta & Barbot, 2012). However, these models can only assume planar faults and they not account for anelastic deformation. Consequently, such models cannot address the complex fold-and-thrust belt structures and the long-term mountain building processes. Therefore, to improve our physical understanding of how mountain belts behave in terms of seismicity, we need an orogen-scale approach that takes into account the evolution of complex mountain belt architectures from the long-term tectonic history.

To overcome these modelling limitations we use a physics-based self-consistent seismo-thermo-mechanical (STM) modelling approach, which captures the dynamics of both long-term orogen-scale deformation and short-term seismic behaviour. We analyze results of a series of numerical models of continent-continent collision where different plate convergence rates are systematically tested to study its effects on seismicity style. We characterize this style by analysing the Gutenberg–Richer distribution and corresponding *b* value obtained from the synthetic catalog of each numerical simulation. To understand these results we analyze the rheological feedback between plate convergence rate and the brittle strength of crustal rocks. Then, we verify our numerical hypothesis calculating similar quantities for natural examples of collisional orogens (i.e., Alps, Apennines, Zagros and Himalaya).

2.3 Methods

2.3.1 Seismo-Thermo-Mechanical Modeling

The employed numerical STM code (van Dinther *et al.* , 2013b) combines conservative finite differences on a fully staggered grid and marker-in-cell techniques (Gerya & Yuen, 2003). The momentum, mass and heat conservation equations are implicitly solved using a visco-elasto-plastic rheology (Gerya & Yuen, 2007) on the non-deforming Eulerian grid. The advection of physical properties including viscosity, plastic strain and temperature is performed with the displacement of Lagrangian markers. The momentum equations include the inertial term to stabilize high-coseismic slip rates at small time steps. The employed visco-elasto-plastic rheology is based on a constitutive relationship between deviatoric stresses and strain rates $\dot{\varepsilon}_{ij}$ applying linear elasticity and non-Newtonian viscosity (Gerya & Yuen, 2007)

$$\dot{\varepsilon}_{ij} = \frac{1}{2G}\frac{D\sigma'_{ij}}{Dt} + \frac{1}{2\eta}\sigma'_{ij} + \begin{cases} 0 & \text{for } \sigma'_{II} < \sigma_{yield} \\ \chi\frac{\partial\sigma'_{II}}{\partial\sigma'_{ij}} = \chi\frac{\partial\sigma'_{ij}}{2\sigma'_{II}} & \text{for } \sigma'_{II} = \sigma_{yield} \end{cases} \tag{2.1}$$

where G is shear modulus and η is effective viscosity. $D\sigma'_{ij}/Dt$ is the objective co-rotational time derivative solved using a time explicit scheme and $\sigma'_{II} = \sqrt{{\sigma'_{xx}}^2 + {\sigma'_{xz}}^2}$ is the square root of the second invariant of the deviatoric stress tensor, and χ is a plastic multiplier connecting plastic strain rates and stresses (Gerya & Yuen, 2007). Viscous creep is computed in terms of deformation invariants and depends on strain rate, temperature, and pressure (Ranalli, 1995). The viscous component of the deformation is then calculated as a combination of diffusion and dislocation creep. Plastic behaviour is taken into account assuming a non-associative Drucker-Prager yield criterion. Evaluated at each Lagrangian marker, plasticity sets in when the square root of the second invariant of the deviatoric stress tensor reaches the local pressure-dependent yield strength (σ'_{II}=σ_{yield})

$$\sigma_{yield} = C + \mu_{eff}\ \ P, \tag{2.2}$$

where C is the cohesion. An important component in the yield criterion is the friction coefficient. Following the approach in van Dinther *et al.* (2013a), we apply a strongly rate-dependent friction formulation (e.g., Ampuero & Ben-Zion, 2008) in which the effective friction coefficient μ_{eff} depends on the visco-plastic slip velocity $V = (\sigma_{yield}/\eta_m)\Delta x$. Here η_m is the local viscosity, σ_{yield}/η_m is the square root of the second invariant of the visco-plastic strain rate ($\dot{\varepsilon}_{II}$) and Δx is the Eulerian grid size. This allows us to calculate the effective steady-state friction (μ_{eff}) coefficient at every marker as a function of slip rate V as

$$\mu_{eff} = \mu_s(1-\gamma) + \mu_s \frac{\gamma}{1+\frac{V}{V_c}} \tag{2.3}$$

$$\gamma = 1 - (\mu_d/\mu_s) \tag{2.4}$$

where μ_s and μ_d are static and dynamic friction coefficients, respectively. V_c is the characteristic velocity at which half of the friction change has occurred, and γ represents the amount of slip velocity-induced weakening if γ is positive, or strengthening if γ is negative. For all lithologies, the velocity weakening frictional formulation is parameterized using $\gamma = 0.7$ and $V_c = 4.4$ cm/yr, following van Dinther *et al.* (2013b). Full details of this method are provided in Gerya & Yuen (2007) and van Dinther *et al.* (2013b).

2.3.2 Model setup

The initial 2D model setup consists in a 4000 x 250 km computational domain (Fig. 2.1). Two 1700-km-long continental plates were separated by a 600-km-long oceanic plate. Both continental plates and an oceanic are composed of an upper crust, lower crust and lithospheric mantle. The visco-elasto-plastic thermomechanical parameters of these lithologies are based on a range of laboratory experiments (Table 2.1).

The models use a grid resolution of 2041 x 401 nodes with variable grid spacing. This allow a minimum grid resolution of 400 m in the area subjected to largest deformation. More than 28 million Lagrangian markers carrying material properties

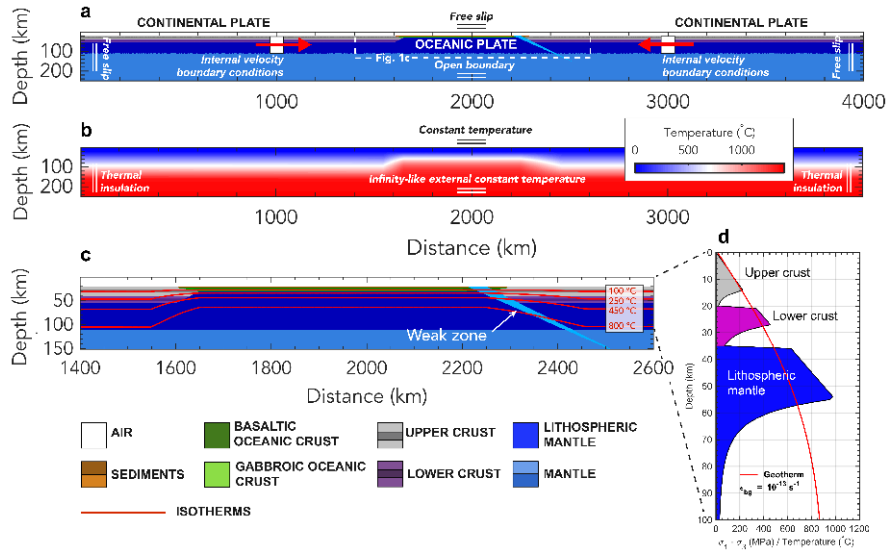


Figure 2.1.: 2D setup. (**a**) Initial composition map including boundary conditions. (**b**) Initial temperature distribution. (**c**) Zoom of oceanic plate with initial thermal structure in red. Plate convergence rate is applied at 1000 km for the left plate and 3000 km for the right plate. (**d**) 1D lithospheric strength profile and the corresponding initial geotherm.

were used in each experiment. The model has free slip boundary conditions and a permeable lower boundary with an infinity-like external free slip and external constant temperature conditions at 1670 km depth (Burg & Gerya, 2005). The free surface boundary condition atop the crust is implemented by using a "sticky air" layer (Schmeling *et al.* , 2008) with low density (1 kg/m^3) and viscosity (10^{17} Pa s). The model is kinematically driven using internal boundary conditions located at 1000 and 3000 km (Fig. 2.1), which allow to impose a initial convergence rate of 10 cm yr^{-1}. The thermal structure of the oceanic lithosphere was calculated from the half space cooling model (Turcotte & Schubert, 2002) for a given plate age of 70 Myr (Fig. 2.1b). The initial continental geotherm was set using values of 0 °C at the surface and 1300 °C at 142 km depth. The thermal gradient used within the mantle was quasi-adiabatic (0.5°C/km). Gravitational acceleration of 9.81 m s^{-2} was used in the model. To initiate subduction a weak zone was imposed on the right ocean-continent transition. The weak zone cuts through the whole lithospheric mantle with an angle of ~30° and is characterised by weak plastic strength (1 MPa) and wet olivine rheological parameters (Ranalli, 1995).

Material *flow law* [a]	ρ_0 [b] ($kg\,m^{-3}$)	E_a [a] ($kJ\,mol^{-1}$)	V_a [a] (J/bar)	n [a]	η_0 [a] ($Pa^n\,s$)	Hr [b,c] (μWm^{-3})	k [a] $Wm^{-1}K^{-1}$	G [d] (GPa)	μ_s [e,f]	λ
Sediments (Wet Qz)	2600	154	1.2	2.3	1.97 x 10^{17}	1.5	$[0.64+807/(T+77)]$ $exp(4\,10^{-5}P)$	25	0.35 [g]	0
Upper cont. crust (Wet Qz)	2750	154	0.8	2.3	1.97 x 10^{17}	0.25	$[0.64+807/(T+77)]$ $exp(4\,10^{-5}P)$	25	0.6	0
Lower cont. crust (Mafic Granulite)	3000	445	0.8	4.2	1.25 x 10^{21}	1.5-4.0	$[0.64+807/(T+77)]$ $exp(4\,10^{-5}P)$	25	0.6	0
Upper oc. crust (Wet Qz)	3000	154	0.8	2.3	1.97 x 10^{17}	0.25	$[1.18+974/(T+77)]$ $exp(4\,10^{-5}P)$	25	0.5	0.95 [h]
Lower oc. crust (Plg-An 75%)	3300	238	0.8	3.2	4.8 x 10^{22}	0.0022	$[1.18+974/(T+77)]$ $exp(4\,10^{-5}P)$	25	0.6	0
Mantle (Dry Olivine)	3300	532	0.8	3.5	3.98 x 10^{16}	0.0022	$[0.73+1293/(T+77)]$ $exp(4\,10^{-5}P)$	67	0.6	0

Table 2.1.: Rheological parameters. ρ_0 is the reference density, E_a is the activation energy, V_a is the activation volume, n is the stress exponent, η_0 is the reference viscosity, Hr is the radiogenic heat production, G is the shear modulus, μ_s is the static friction coefficient and λ is the pore-fluid pressure factor (P_{fluid}/P_{solid}). Other properties for all rock types: cohesion (C) is 1 MPa (Schultz, 1995), specific heat capacity (C_p) is 1000 $J\ kg^{-1}K^{-1}$, thermal conductivity (k) is in $Wm^{-1}K^{-1}$ at T_K and P_{MPa}, thermal expansion α_ρ= 3x10^{-5} K^{-1} and compressibility β_ρ=1x10^{-5} MPa^{-1}. [a] Ranalli (1995); [b] Turcotte & Schubert (2002); [c] Rudnick & Fountain (1995); [d] van Dinther *et al.* (2013b); [e] Di Toro *et al.* (2011); [f] Del Gaudio *et al.* (2009); [g] Den Hartog *et al.* (2012); [h] Seno (2009).

2.3.3 Modeling procedure

The modeling approach comprises two steps: (1) long-term evolution, namely the closure of the oceanic basin, the subsequent continent-continent collision and mountain building, which is followed by (2) short-term seismic cycle, which simulate cycles of reoccurring interseismic and coseismic periods. Prior to the first modeling stage we define the initial geometry, rock properties, and temperature distributions (Fig. 2.1). Then we simulate the long-term evolution of a generic convergent margin, from subduction to collisional orogeny using a time step of 1000 yr. In this stage the inertia is negligible and friction is constant. Typical model evolution leads to self-sustaining subduction of the oceanic plate beneath the continental plate, followed later by continent-continent collision. In the second (short-term) modeling stage, the simulation starts with the distribution of physical properties (e.g., stress distribution, temperature, viscosity, and other material properties) from the long-term simulation. The time step is progressively decreases to 5 years, while the inertia term and rate-dependent friction are activated (van Dinther *et al.* , 2013b). Stress build up occurs as elastic strain is accumulated. Differential loading due to rheological discontinuities, tectonic asperities, temperature, and viscosity distribution causes stresses to be concentrated in different regions. In a typical

seismic cycle, when the maximum strength is locally reached, the instability is fed through the feedback of decreasing viscosities. This increases slip velocities, which decreases the slip rate-dependent friction and strength, and in turn decreases viscosities even further. Spontaneous rupture propagation occurs because stresses are increased ahead of the rupture front to balance the dropping stresses within the rupture and to thereby maintain a static equilibrium. Finally, healing of strength occurs as slip velocities decrease.

2.3.4 Evaluating the Gutenberg-Richter distribution and b value

For each numerical experiment we analyze all rupture events to determine their downdip rupture width (W). These events occurring throughout the orogen are recognized using a Rupture Detector Algorithm (RDA), which analyzes each Lagrangian marker continuously. If its velocity exceeds a threshold of 9.0 x 10^{-9} m s^{-1}, while simultaneously stresses drop more than 0.4 MPa that marker's physical properties are stored in a synthetic data set. Subsequently markers are grouped into one event when they occur within 400 m of a marker that ruptured this or the previous time step. The rationale for choosing these thresholds comes from the minimally common stress drop (Allmann & Shearer, 2009) and our Eulerian grid size of 400 m, respectively. The sensitivity of these thresholds is tested and only introduces minimal variations in actual *b* values and number of events.

From these spontaneous rupture paths we measure the rupture width (W) to estimate the moment magnitude ($\mathrm{M_w}$) using the empirical scaling relations in Wells & Coppersmith (1994). This empirical relationship is available from regression analysis based on a large numbers of events in nature:

$$M_W = a + b\,log(W), \tag{2.5}$$

where a and b are coefficients that vary with the style-of-faulting (i.e., normal or reverse faulting). We chose Wells & Coppersmith (1994) because they include various types of faulting and different tectonic environments. From these spontaneous synthetic events, we determine a single Gutenberg-Richter distribution for

the entire orogen. The corresponding *b* values of these power law distributions are then estimated using the maximum curvature method (MAXC) (e.g., Marzocchi & Sandri, 2003). First, the completeness magnitude M_c is given by the probability density function of the magnitudes $M \geq M_c$

$$P(m) = b \;\; log(10)10^{b-(M-M_c)}. \tag{2.6}$$

Then, the *b* value is estimated with Aki's maximum likelihood method corrected for binned data (Tinti & Mulargia, 1987)

$$b = \frac{1}{log(10)\Delta m} \;\; log\,(1 + \frac{\Delta m}{\hat{u} - M_c}); \tag{2.7}$$

where $\hat{u}$ is the sampling average of the magnitudes and the event magnitudes are binned into magnitude bins of Δm=0.1-0.3. We want to point out that we use this formula rather than the commonly used (e.g., Utsu, 1966) corrections because it gives more accurate and stable results under varying sample sizes (Marzocchi & Sandri, 2003). To estimate the error of the *b* value we use (Marzocchi & Sandri, 2003)

$$\sigma_b = 2.30 \;\; \hat{b} \;\; \sqrt{\frac{\sum_{i=1}^{N}(M_i - \hat{u})^2}{N(N-1)}} \tag{2.8}$$

in which $\hat{b}$ is the *b* value that maximizes the likelihood function (Fisher, 1950), according to

$$\hat{b} = \frac{1}{log(10)(\hat{u} - M_{thresh})}, \tag{2.9}$$

where N is the number of earthquakes and M_{thresh} is the threshold magnitude, which corresponds to the minimum magnitude of completeness of the catalogue. These equations provide a reliable estimation in the presence of possible (time/spatial) variations of the *b* value (Marzocchi & Sandri, 2003).

2.4 Results

In this section, we outline the main results obtained from two sets of numerical experiments. The first set of numerical experiments (set A) were designed to cover systematically the same cumulated convergence (i.e., 1.8 km), assuming a range of convergence velocities from 10 to 50 mm yr^{-1}. A second set of numerical experiments (set B) is designed to study the importance of orogenic type and geometry on seismic behaviour with respect to the role of convergence rate. This is accomplished by increasing the radiogenic heat production of the lower crust of the upper plate, which changes the orogens geodynamic evolution and the resulting orogenic structure. For the reference model of each set of numerical experiment, we describe the general development of the post-subduction collisional orogeny from the long-term evolution; subsequently, a description of the short-term seismicity is given in order to characterize the seismicity style. Finally we quantify this seismicity using the Gutenberg-Richter distribution and the *b* value, which are used to evaluate the role that the plate convergence rate has in controlling the seismic behaviour of orogenic belts.

2.4.1 Set A: Long-term mountain building

In all experiments, a fixed convergence rate of 10 cm yr^{-1} is imposed during the early phases of the models, which consist of oceanic plate consumption and ocean closure. As the incipient phase of continent-continent collision starts, the convergence rate gradually steps down to a lower value (from 10 cm yr^{-1} to a value in the range between 5 and 1 cm yr^{-1}). Therefore, each model exhibits the same behaviour during the subduction stage. The collisional regime has very similar features for models with different convergence rates—no significant differences in shape and size of the orogen and subduction dip-angle are observed.

The collisional regime with a convergence rate of 50 mm yr^{-1} is greatly affected by the buoyant and rheologically weak materials scraped off and accreted at the overriding plate margin. At the onset of collision, rocks of the crustal root affect the base of the plates' contact, increasing the degree of rheological coupling. As

collision continues, more crustal material is accreted at the frontal margin, raising the topography and thus building up compressional stresses within the upper plate. The final structure of this collisional zone is characterized by an asymmetric fold-and-thrust belt structure, in which the stiff lithospheric edge of the right continental plate acts as a buttress, thus separating an orogenic wedge marked by different deformation styles (Fig. 2.2a). The pro-foreland basin and the orogenic wedge are dominated by simple shear deformation and nappe stacking. On the other side, the retro-foreland basin is characterized by pure shear shortening, thickening of the crust, back-thrusting and vertical exhumation of deep lithospheric mantle slices along the buttress. Approximately half of the 50 mm yr^{-1} convergence is absorbed by crustal shortening across the orogenic wedge (22 $\pm$4 mm yr^{-1}), while the remainder is accommodated through stable viscous shear along the deeper portion of the downgoing continent.

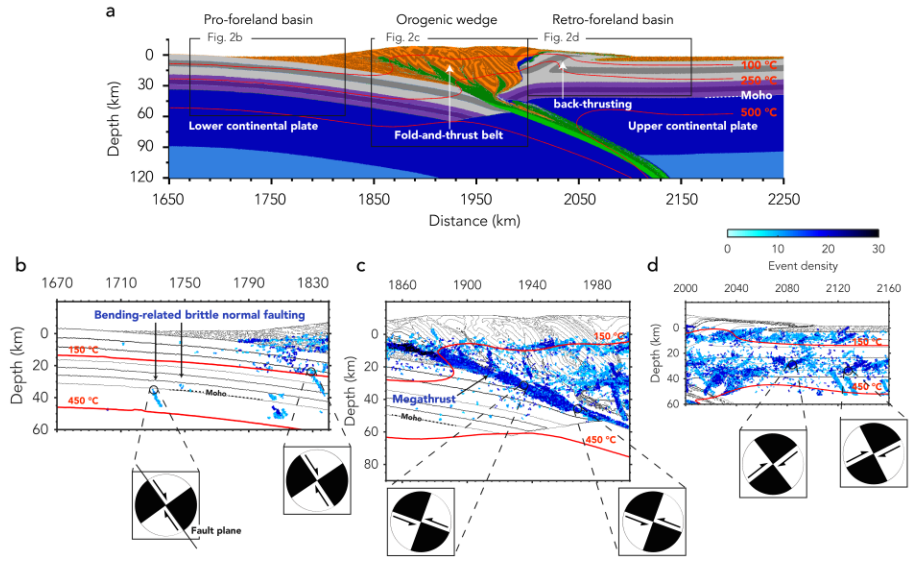


Figure 2.2.: Long-term (**a**) and short-term (**b-d**) characteristics of the Set A reference model for a plate convergence rate of 50 mm yr^{-1}. (**a**) Composition shows a broad orogen marked by nappe stacking in the pro-wedge and crustal shortening in the retro-wedge. The short-term spatial evolution of all rupture events within the (**b**) pro-wedge, (**c**) orogenic wedge, and (**d**) retro-wedge. The inferred focal mechanisms show a broad pattern of different style of faulting, which are consistent with the local tectonic regime.

2.4.2 Set A: Short-term seismicity

Results from the short-term seismicity shows a wide domain subjected to brittle-plastic faulting: beneath the pro-foreland basin, normal-faulting events propagating in the lower continental plate (Fig. 2.2b). Due to temperature-dependent mechanical properties of the lithosphere, such ruptures are mainly located in the brittle-plastic part of the upper/lower crust and sporadically nucleate in the lithospheric mantle, but never at temperatures greater than 500°C. Seismogenic deformation in the orogenic wedge (Fig. 2.2c) is largely driven by elastic strain accumulation along the main thrust, which is characterized by partially or fully locked interseismic periods and rapid coseismic rebound. Seismic energy release in this region is dominated by the largest events occurring on the megathrust, which nucleate at different depths and propagate both down- and upward. Within the retro-foreland basin we observe pervasive reverse faulting, which propagates from the deep crust up to the subsurface (Fig. 2.2d). Fault propagation is assisted by inherited lithospheric structures near the orogenic wedge, which promote localized deformation and coseismic faulting up to the subsurface. Beneath the retro-foreland basin, brittle faulting occurs on young faults that are marked by coseismic events.

2.4.3 Set A: Gutenberg–Richter parameters

The rupture width of these events is scaled according to empirical scaling relations (Wells & Coppersmith, 1994, Section 2.4) to plot the corresponding moment magnitude versus the number of events larger than each size (Fig. 2.3a). The resulting frequency-magnitude distribution follows a power-law, as earthquakes do in nature (e.g., Pasquale *et al.* , 2010). Most seismic cycle models, including our previous subduction zone models (van Dinther *et al.* , 2014), do not capture this important statistical feature of earthquake occurrence. Due to the occurrence of events on many smaller faults, throughout the orogen and the megathrust interface, these models do produce a Gutenberg-Richter distribution. We quantify the behaviour of seismicity through analyzing the parameters describing this Gutenberg-Richter distribution.

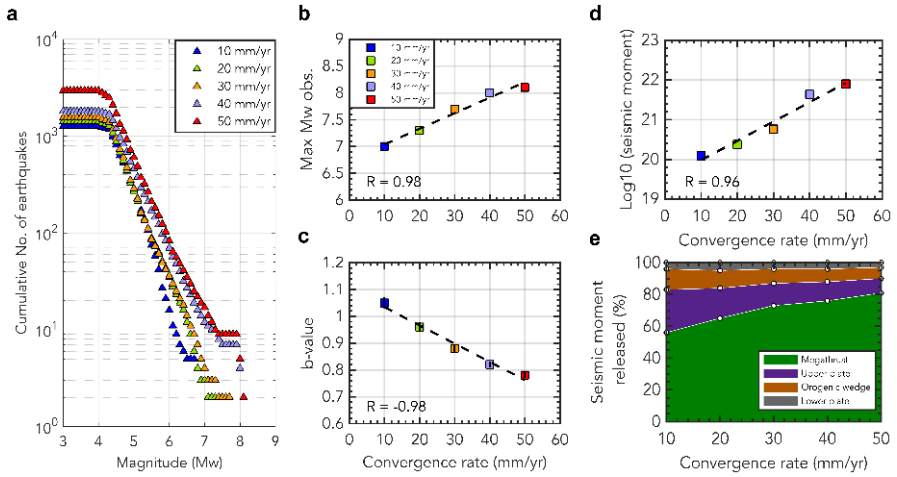


Figure 2.3.: Seismic behaviour of the reference models assuming the same amount of convergence (i.e., 1.8 km) and with plate convergence rate varying from 10 to 50 mm yr^{-1}. (**a**) Gutenberg-Richter distribution. (**b**) Relationship between plate convergence rate and estimated maximum magnitude. (**c**) Relationship between plate convergence rate and *b* value. (**d**) Relationship between plate convergence rate and cumulative seismic moment released. (**e**) Seismic moment released (in percentage) between the megathrust, upper plate, orogenic wedge and lower plate, as a function of plate convergence rate. Dashed lines indicate the regression line.

Comparing models with different convergence rates (varying from 10 to 50 mm yr^{-1}) but the same amount of convergence, we observe the following relationship: (i) the cumulative number of events increases for higher convergence rates (Fig. 2.3a) and (ii) $\mathbf{M_{max}}$ indicate a positive and linear correlation with plate convergence rate (from 7.0 to 8.1, Fig. 2.3b). Following the same line of reasoning, we compared *b* values and convergence rate and found a linear and negative correlation between these parameters (from 1.05 to 0.78, Fig. 2.3c). Moreover, the cumulative seismic moment released shows a linear and positive relations with plate convergence rate (Fig. 2.3d). The Pearson linear correlation coefficient (R) demonstrates a good linear fit between plate convergence rate and $\mathbf{M_{max}}$ (R= 0.98, Fig. 2.3b), *b* value (R= –0.98, Fig. 2.3c) and seismic moment released (R= 0.96, Fig. 2.3d). To evaluate the significance of these correlations we extracted the *p* value, which represents the significance level to reject the null hypothesis that these correlations occur randomly irrespective of convergence rate. The result of this analysis indicates that the correlations are highly significant between convergence rate and $\mathbf{M_{max}}$ (*p* value=0.013) and *b* value (*p* value=0.003), meaning that they

are significant at 97.7% (Fig. 2.3b, c) and 95.7% (Fig. 2.3d), respectively. To further understand where the seismic energy is released in different regions, we divided the domain in (1) megathrust, (2) upper plate, (3) orogenic wedge and (4) lower plate. Subsequently, we compare their distributions with respect to the convergence rate (Figure 2.3e). We observe a dominant role of the megathrust, which releases 81% of seismic moment for convergence rates of 50 mm yr^{-1}. This progressively decreases down to 56% when for convergence rate of 10 mm yr^{-1}. On the other hand, a decrease in the seismic moment released in the megathrust results in an increase in other regions, namely for the orogenic wedge and the upper plate, whereas the lower plate value remains almost constant. Overall, increasing convergence rate thus transfers seismic energy release from the megathrust into neighbouring regions.

2.4.4 Set B: Role of mountain ranges architecture

The geometry of tectonic structures is typically considered to be of first order importance in the control of seismic behaviour of orogenic mountain belts (e.g., Avouac, 2015; Bollinger *et al.* , 2004; Cheloni *et al.* , 2014; Chen *et al.* , 2016). To compare that importance with respect to the role of plate convergence rate we performed a second set of numerical experiments with a distinctly different orogenic architecture. In the models of set B the lower crust of the upper plate has higher concentration of radiogenic elements of 4 $\mu W/m^3$ (Table 1) with respect to the previous set A, as observed in the Sikkim Himalaya (Rudnick & Fountain, 1995).

The early stages of the long-term development of the orogen are very similar to the previous set of models (Fig. 2.4). Sediments are accreted in the orogenic prism and the lithospheric edge acts as a buttress, while the upper plate is only slightly ablated due to shearing between the two plates. At the onset of continental collision, however, the warm upper plate edge is warped up due to the push from the material of the accretionary prism. The present model hence, shows, yielding and crosscutting of the upper plate due to thermal softening at the indentation zone and in the retro-foreland basin. As collision continues, crustal stacking produces the progressive rightward migration of the suture zone and the development of an

elevated plateau. The final structure of this coupled collisional zone is characterized by a thick and hot crustal wedge overlying a subducting plate with a broad asymmetrical collisional zone (Fig. 2.4a). Also notable is the different deformation styles that characterized the retro-wedge (Fig. 2.4b): beneath the orogenic wedge the crustal detachment is dominated by simple shear, whereas far from wedge (in the retro-foreland basin) the plateau is characterized by pure shear thickening. The wide collisional zone thus leads to an asymmetric one-sided structure. As a result, stresses are mainly compressive with minor extension due to plate bending. Also notable is the difference in the thermal evolution of the pro- and retrowedge. This nicely underscores the significance of radiogenic material in controlling the rheological conditions that are attained by any given block of the crust.

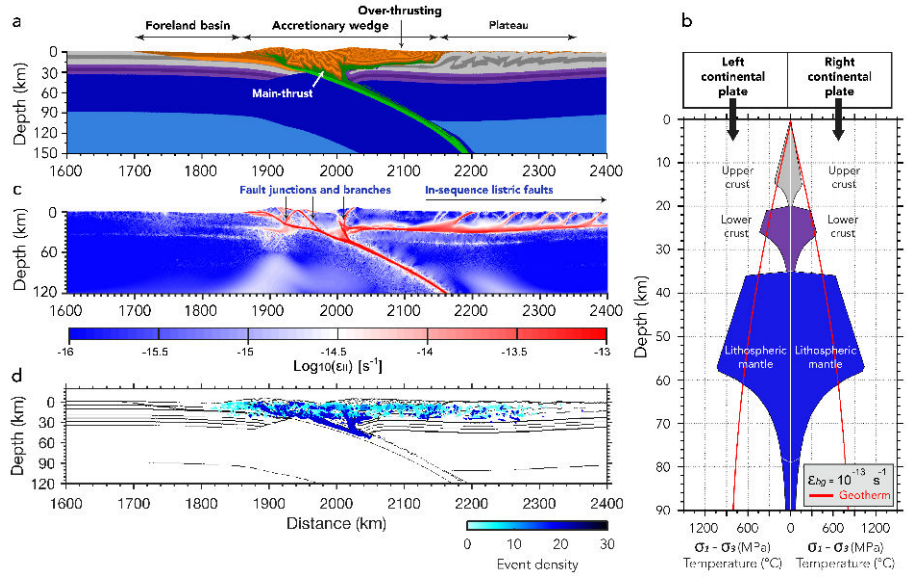


Figure 2.4.: Set B numerical experiments simulating a warmer and broader orogenic belt (plate convergence rate: 50 mm yr^{-1}). A higher radiogenic heat was applied in the upper continental plate with respect to the reference model (see Table 1). (**a**) Compositional map showing the orogenic wedge development, backthrusting and crustal shortening, overthrusting of the orogenic wedge, and broadening of the continental plateau. (**b**) 1D strength envelope profile of the left and right continental plates. (**c**) Strain rate map. Fault activation due to continent-continent collision occurs mainly at the main thrust, in the orogenic wedge, and in the upper plate. (**d**) Rupture event density map. Seismogenic faulting is in agreement with the strain rate field.

These different deformation styles lead to a distinctly different spatial distribution of seismicity (Fig. 2.4c). The large collision zone results in a compressional domain

in the frontal part of the orogenic wedge with some extensional areas due to the plate bending beneath the foreland basin, which are characterized by normal-faulting events. The megathrust geometry along the inherited subduction channel is comparable to the previous set of experiments, although it branches into several fault segments due to crustal softening in the upper plate. Because of the yielding of the warm upper plate, the orogenic wedge overthrusts the retro-foreland domain causing a sequence of back-thrusts far from the orogenic wedge (in the plateau). These results illustrate that thermal crustal properties affect the structure and geometry of collisional orogens and thereby their spatial distribution of seismicity.

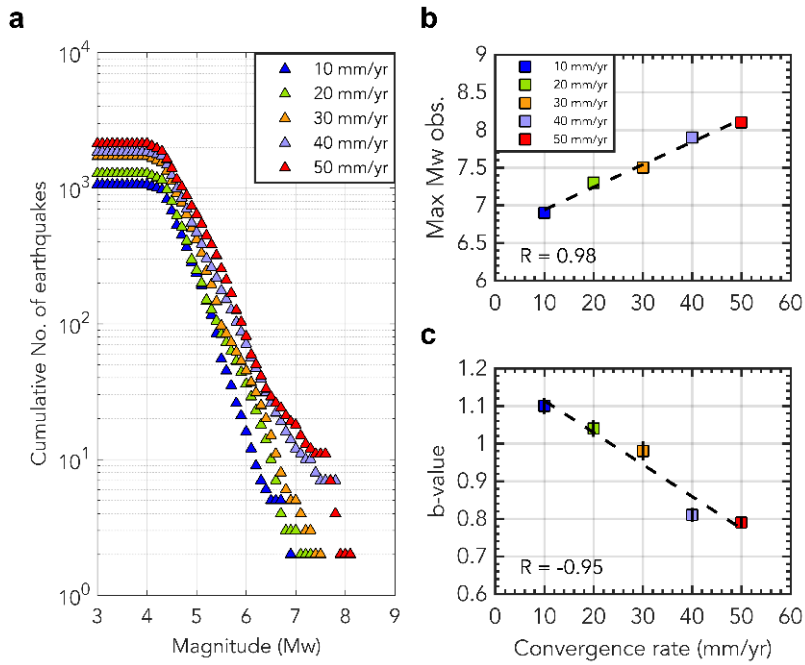


Figure 2.5.: Results from the model shown in Fig. 2.4 (set of experiments B) assuming the same amount of convergence (i.e., 1.8 km): Gutenberg-Richter distributions and dependence of *b* and maximum M_W observed on plate convergence rate. (**a**) Frequency-magnitude distribution for the five simulations. (**b**) Relationship between plate convergence rate and maximum magnitude estimated. (**c**) Relationship between plate convergence rate and *b* value estimated. Dashed line indicates the regression line.

The characterization of this distinctly different orogenic structure seismicity, through the Gutenberg-Richter distribution is, however, surprisingly similar with

respect to the previous set of numerical simulations (Fig. 2.5). Comparing these models with the previous set A of numerical experiments, we observe that the positive relations between plate convergence rate and the cumulative number of events (Fig. 2.5a) and the maximum magnitude $\mathbf{M_{max}}$ (from 6.9 to 8.1, Fig. 2.5b) are confirmed. Moreover, the resulting *b* values show a linear and negative trend for higher convergence rates, with values from 1.10 to 0.79 (Fig. 2.5c). Although the absolute values of $\mathbf{M_{max}}$ and *b* are slightly different compared to the previous set A (Fig. 2.3), the correlation coefficient confirms the linear relations between both of them and plate convergence rate.

These results therefore indicate that small variations in the radiogenic content of crustal rocks may have obvious effects on both the long-term formation of a collisional orogen and the short-term seismicity. Radiogenic heating increases the temperature of crustal rocks, producing a high and broad plateau and thus affecting the spatial distribution of seismicity. Despite the fact that this hot tectonic environment influences the location of seismogenic faults, we stress that the characterization of the seismic behaviour through the Gutenberg-Richter statistics is determined by the convergence rate acting in the subduction/collision system rather than by geometry of the orogen itself.

2.5 Discussion

These results shed light on the correlation between plate convergence rate and seismicity characteristics at continent-continent collisional margins and lead to several interesting implications. We first discuss the physical mechanisms responsible for the control of plate convergence rate on the seismic behaviour of orogenic belts. Subsequently, we make a comparison between the Alps, Apennines, Zagros and Himalaya and our numerical experiments. Finally, we discuss involved uncertainties and modeling limitations.

2.5.1 How does convergence rate control seismicity?

The seismic behaviour of mountain belts is determined by the location of elastic strain build up within strong elastic-brittle layers (Scholz, 2002), while weaker layers are presumed to creep and deform aseismically (e.g., Doglioni *et al.* , 2011; Pasquale *et al.* , 2010). The strength of the Earth's lithosphere depends on several rheological properties such as stress, strain rate, strain history, composition, and most importantly temperature (e.g., Chen & Yang, 2004; Maggi *et al.* , 2000). In our numerical experiments, as well as in nature, both the large-scale temperature field and the strain rate distribution are mainly controlled by the plate convergence rate. The subsequent control of temperature and background strain rate on the strength and rheology of the lithosphere can be visualized in a simplified manner using 1D lithospheric strength profiles (Fig. 2.6). These profiles are based on same lithological stratification of continental lithosphere and the same rheological properties as in the 2D simulations. To compose these, we used the Moho temperatures (T_{Moho}) reflecting the reference temperature of the lithosphere and a background strain rate ($\dot{\varepsilon}_{bg}$) as reference parameters. An increase in convergence rate, for instance, allows for deeper subduction of lower temperatures, thereby deepening the brittle extent of the crust (Fig. 2.6a). Thus, the brittle behaviour of the upper crust deepens, and the lower crust becomes more brittle. Similar behaviour can be found for the feedback through strain rate, because higher convergence rates lead to larger background strain rates, thereby extending the brittle failure depth (Fig. 2.6b and Fig. 5.6).

Consequently, the lower crust is to a larger extent seismogenic. To quantify in which form plastic strain is released throughout the orogen, we further analyzed the partitioning between seismic and aseismic deformation. Results show that within the seismogenic depth range, seismic/aseismic strain vary with plate convergence rate (Fig. 2.6c). For a range of convergence rate varying from 10 to 50 mm yr^{-1}, seismic strain increases (from 19% to 58%) when the rate of collision between the two continental plates rises. Also, seismicity is observed to migrate from the megathrust into the orogenic wedge as convergence rate decreases. This more distributed form of brittle deformation is also accompanied by a larger contribution of ductile deformation, thereby reducing the magnitude of the largest events.

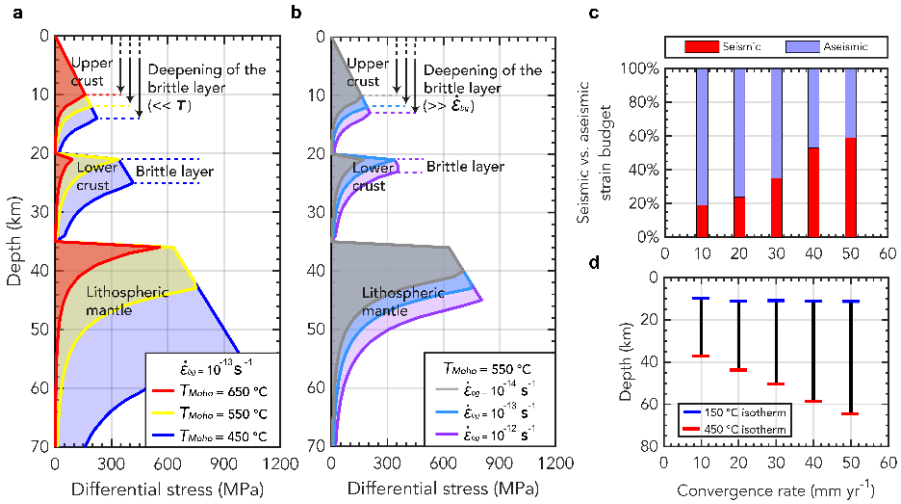


Figure 2.6.: 1D lithospheric strength profiles taken from the initial lithological sequence of the continental plate show the representative distribution of differential stress with depth, as a function of (**a**) temperature and (**b**) strain rate, which are both controlled by plate convergence rate. Note that the temperature distribution, and strain rate field, characterize the deepening of brittle behaviour within the upper crust and the brittle-ductile transition of the lower crust with increasing convergence rate. (**c**) Quantitative view of the relationship between seismic/aseismic strain and plate convergence rate throughout the orogen. Panel (**d**) shows the deepening of the megathrust seismogenic zone for higher convergence rates. The seismogenic downdip width is confined by the 150°C isotherm (where friction switches from velocity-strengthening to velocity-weakening) and the 450°C isotherm (thermally driven brittle-ductile transition).

These results thus demonstrate that the competition between seismic and aseismic strain has a strong influence on the seismic behaviour of mountain belts. Seismicity tends to localize on the megathrust when convergence rate increases, while a more distributed seismicity yields to seismic events of smaller sizes for slower convergent margins. This rheological feedback has important implications for the seismogenic response of the system. On the megathrust, temperatures (and stresses) increase with depth, whereas viscosities decrease beyond 60-70 km depth, reaching near upper mantle values at ~80-90 km depth. Consequently, thermally and stress driven creep governs a spontaneous, conditionally stable downdip transition zone between temperatures of 350–450°C. Ruptures initiate above it, propagate within it, and arrest below it as ductile shearing relaxes stresses. Results in Fig. 2.6d indicate that the location at depth of such brittle/ductile transition zone depends on the convergence rate. As a result, the rupture width (and the

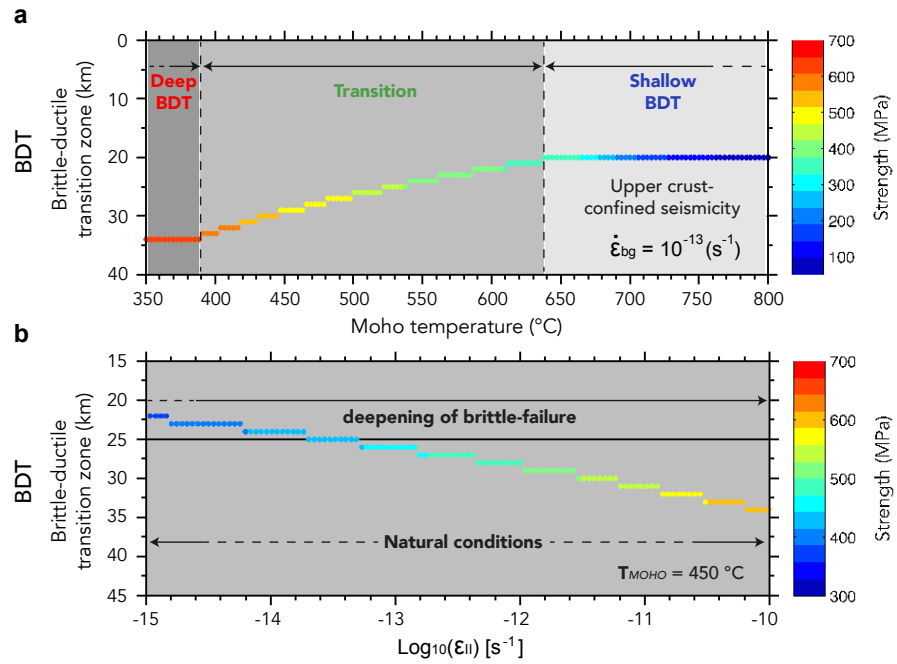


Figure 2.7.: Depth and strength evolution of the brittle-ductile transition (BDT) zone as a function of (**a**) temperature and (**b**) strain rate. Color scale denotes the rock strength at the corresponding BDT zone. (**a**) 1D simulation with an initial background strain rate of $10^{-13}s^{-1}$. Note the deepening of the BDT zone and the increasing of strength when the Moho temperature decreases. (**b**) 1D simulation assuming an increasing of strain rate for a constant temperature (T_{Moho} = 450°C). Results show the rheological feedback between the strain rate and the depth of BDT zone and the magnitude of strength.

corresponding maximum magnitude $\mathrm{M_{max}}$) changes according to this rheological feedback.

We next investigated the possible correlation between the increasing of convergence rate and the deepening of the brittle strength. To do so, we analyze the depth distribution of all rupture events of each model performed during the first set of experiment. These synthetic hypocenter distributions show that earthquakes nucleate over a larger depth extent when convergence rates are higher (Fig. 2.8a). The depth distribution gradually changes with increasing of plate convergence rate, from unimodal (i.e., upper crust confined) distributions for low convergence rates (10–30 mm yr^{-1}) to bimodal (i.e., upper and lower crust seismogenic) distributions for high convergence rates (40–50 mm yr^{-1}, Fig. 2.8a). The bimodal depth distribution of hypocenters for rapidly converging orogens thus confirms the predictions from the

simplified continental 1D strength profiles. Slowly converging orogens (i.e., with higher temperature and lower background strain rate) have a largely ductile lower crust, while rapidly converging orogens (i.e., with lower temperature and higher background strain rate) have a second brittle layer within the lower crust.

2.5.2 Comparison to natural examples

2.5.2 Relation between plate convergence rate and depth distribution of seismicity

To verify this physical mechanism we analyze whether earthquake data also show the conversion from a ductile lower crust to a more brittle one for rapidly converging orogens. Using the U.S. National Earthquake Information Center (NEIC) catalogue, we collected the distribution earthquakes with magnitude ≥4.5 occurring at depths from 0 to 70 km within four representative continent-continent orogenic regions differing in plate convergence rate: Alps (2.3±0.5 mm/yr), Apennines (5±1 mm yr^{-1}), Zagros (25±3 mm/yr), and Himalaya (38±2 mm/yr). As a result of the declustering procedure, the events that are closely related to each other spatially or temporally, and could be considered as aftershocks, are removed using the algorithm of Gardner & Knopoff (1974) included in the interactive software tool ZMAP (Wiemer, 2001). These natural data show a systematic difference in hypocenter locations between the Alpine and Apennine chains and the Zagros-Himalayan environments (Fig. 2.8b). The slowly converging Alpine-Apennine orogenic systems are dominated by an upper crust confined, unimodal distribution of earthquakes. The rapidly converging Zagros and Himalayan regions, however, also reveal many earthquakes nucleating within the lower crust. This change from unimodal to bimodal hypocenter distributions was independently suggested by our models (Fig. 2.8a). These natural data thus support our mechanical explanation that the seismogenic domain is extended as the lithosphere is colder and background strain rate is higher with increasing converging velocities.

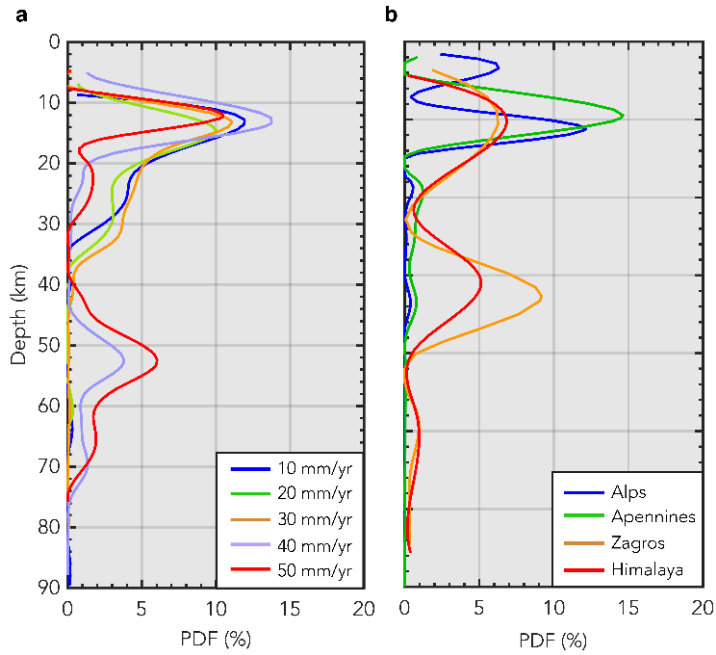


Figure 2.8.: Probability density distribution of hypocenters versus depth for (**a**) numerical experiments and (**b**) nature cases ($M_W > 2.5$). Modeling results in (**a**) indicate a unimodal, upper crust confined, distribution of earthquakes in the case of lower converging rates (10, 20, and 30 mm/yr). Highly converging mountain belts show instead a bimodal distributions of earthquakes, since both the upper and lower crust are seismogenetic. These results find agreement with the seismicity data from the four continent-continent mountain belts analyzed.

2.5.2 Relation between plate convergence rate and earthquake-size distribution

The same data sets are then used to analyze the relation between convergence rate and the Gutenberg-Richter parameters for each continent-continent collisional orogen studied (Fig. 2.9). To do so, earthquakes listed in the form of body wave (m_b) or local (M_L) magnitude are converted to moment magnitude ($\mathrm{M_w}$) using the empirical global relations provided in Hanks & Kanamori (1979) and Scordilis (2006). The four different continent-continent orogens reveal a distinctly different frequency-magnitude distribution in accordance with their known seismicity patterns (Fig. 2.9a). When we plot two of its governing Gutenberg-Richter parameters against each convergence rate from literature (Wang *et al.* , 2001; Grenerczy *et al.* , 2005;

Tatar *et al.* , 2002), we once again find a positive linear relationship with sufficient confidence (R= 0.91 in Fig. 2.9b and R= –0.92 in Fig. 2.9c, respectively). Therefore, these seismicity data support the hypothesis that an increasing in plate convergence rate leads to larger maximum moment magnitudes and smaller *b* values.

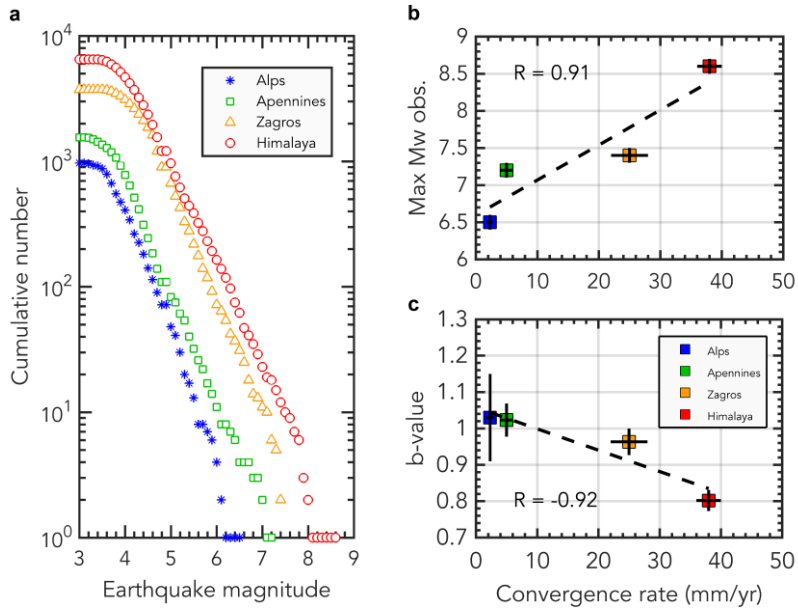


Figure 2.9.: (**a**) Frequency-magnitude distribution of earthquakes for events in the four orogenic belts considered. (**b**) Relationship between plate convergence rate and maximum magnitude observed in the NEIC catalogue. (**c**) Relationship between plate convergence rate and *b* value (see Methods). Dashed line indicates the regression line.

2.5.3 On the differential stress dependence of the b value

Several studies have suggested a relation between differential stress ($\Delta\sigma$) and the relative size distribution of earthquakes quantified by the *b* value. In the laboratory, acoustic emissions (AEs) from seismically active micro-cracks follow a power law analogous to the Gutenberg-Richter relation with decreasing *b* value for increasing $\Delta\sigma$ (e.g., Amitrano, 2003). More recently, other studies suggested this inverse and linear relation holds for tectonic earthquakes in continental areas (Spada *et al.* , 2013b; Scholz, 2015).

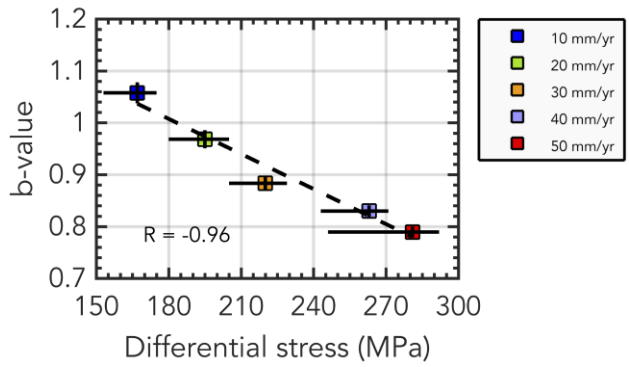


Figure 2.10.: *b* values versus average differential stress from the suite of reference simulations with different convergence rate (from 10 to 50 mm yr^{-1}). The differential stress is averaged over the whole orogenic belt domain over all interseismic periods. Black lines denote the range of *b* value error and the standard deviation of the differential stress, respectively. Dashed line indicates the regression line.

In our numerical experiments, the *b* value is also observed to decrease linearly as a function of the average differential stress (Fig. 2.10). This can likely result from the linear relation between stress and strain in the elastic constitutive equation (first part of eq. 1). Moreover, Scholz (2015) demonstrated that the dependences of *b* value on confining pressure (Amitrano, 2003), mechanical strength of the crust (Pasquale *et al.* , 2010) and focal mechanism (Schorlemmer *et al.* , 2005; Doglioni *et al.* , 2015) are in fact the result of the underlying differential stress. We propose that the convergence rate is in fact the ultimate first-order physical parameter governing the other physical parameters and thus the seismicity behaviour in mountain belts.

2.5.4 Limitations and uncertainties

2.5.4 Modeling limitations

The numerical model has the same limitations as the one previously applied to subduction zones (van Dinther *et al.* , 2013b). In nature, earthquake ruptures occur within a three-dimensional, geometrically complex fault system with various scales of downdip and along-strike variations in its seismogenic behaviour. The lateral, third dimension is absent in our numerical model. That means that our two-dimensional plane strain model ignores lateral variations in interseismic

stress buildup and rupture propagation. Compared to nature our model produces unrealistically long seismic events because of the large time step (i.e., 5 years). This means that a simulated event or earthquake refers to the occurrence of rapid threshold-exceeding slip during which permanent displacement and stress drop occur along a localized interface. On the other hand, the presented results generally demonstrate a satisfactory agreement with a wide range of long- and short-term natural observations. Events in our numerical model have reasonable downdip widths (which are used to estimate the moment magnitude), and similar behaviour to events in the laboratory model (van Dinther *et al.* , 2013a). However, is important to stress that the small-scale complexities of each natural system are difficult to reproduce in a self-consistent lithospheric-scale model. Moreover, even excluding expected along-strike variations of the orogen, details of individual orogens cannot be expected to be reproduced in general models such as the ones of this study. In spite of these potential pitfalls, however, the number of salient but enigmatic observed features of the real collision zones that our models do succeed in reproducing is highly encouraging and provides useful insights.

2.5.4 Consistency of results using the NEIC catalogue

The usage of the USGS National Earthquake Information Center (NEIC) catalogue for the period 1905–2016 also requires a note of caution. The NEIC catalogue is a composite catalogue, whose heterogeneity could affect the estimation of b values (e.g., Kamer & Hiemer, 2015). We ultimately selected—for each continent-continent collision zone—the whole study region, rather than splitting those regions into segments of different volumes. We made this arbitrary choice because for comparison with the results obtained from our numerical experiments. Despite the presence of several mountain belts worldwide (e.g., Pyrenees and Dinarides), we chose these four study regions (i.e., Alps, Apennines, Zagros and Himalaya) because (1) differ in the tectonic structure, (2) are tectonically active, (3) show different seismic behaviour and (4) have a wide and representative spectrum of convergence rates. To investigate the influence of sample size, we repeated the analysis using some study regions cut in half. The resulting b values were not strongly affected ($\Delta b \leq 0.04$), although the relative error increases due to lower

sample size. Since hypocenter depth is particularly difficult to estimate in these data sets, we integrated the analysis of local studies (e.g., Maggi *et al.* , 2000; Jackson, 2002; Pasquale *et al.* , 2010; Bragato & Slejko, 2005). This qualitative comparison shows that despite the uncertainties, our analysis remain sufficiently representative.

2.5.5 Seismic hazard implications

Despite inevitable modeling limitations and uncertainties from spatiotemporally limited data, the combination of the presented Gutenberg-Richter distribution results from numerical models and earthquake data in addition to a rheological analysis of the brittle strength supports the hypothesis that the seismicity in orogenic belts is fundamentally controlled by plate convergence rate. In profile view the tectonic structure of the orogen itself plays an important role for the spatial distribution of seismicity, although subordinate in terms of Gutenberg-Richter statistics. Plate convergence rate seems to control the forces driving seismic and aseismic deformation within these mountain belts. Low convergence rate in the Alps and Apennines is accommodated by moderate earthquakes and more ductile deformation, whereas a pervasive set of large earthquakes marks both the rapidly converging Zagros and Himalayan regions.

Probabilistic seismic hazard and risk assessment is determined by the ratio of large over small earthquakes (*b* value), $\mathrm{M}_{\mathrm{max}}$, and the seismicity rate (*a* value) (e.g., Wiemer *et al.* , 2009). Our results indicate that the seismicity rate is not the only hazard parameter affected by convergence rate. $\mathrm{M}_{\mathrm{max}}$ and the relative amount of large earthquakes (i.e., lower *b* value) increase as well with increased convergence rate due to a wider seismogenic zone resulting from the feedback of temperature and background strain rate on brittle strength. This result does not agree with previous studies that do not account for this feedback, such as in theoretical studies (e.g., Molnar, 1979) and more simple analog and numerical models of subduction zones (Corbi *et al.* , 2017). Moreover, global studies of earthquakes in subduction zones that do show large variability of *b* value, do not unequivocally support a correlation between convergence rate and *b* value

(Nishikawa & Ide, 2014, R = 0.22) and $\mathbf{M_{max}}$ (Marzocchi *et al.* , 2016). Although in similar studies a weak correlation between convergence rate and $\mathbf{M_{max}}$ has been proposed (Heuret *et al.* , 2011, R = 0.42). The absence of a robust correlation in observations of subduction zones over the last decades could be explained by a too limited observational time period (McCaffrey, 2008) or ambiguity introduced by other parameters influencing megathrust seismicity at the same time. However, taking into account longer time series and rheological feedback, we suggest that the seismic hazard in rapidly converging regions is increased even further than expected when only taking seismicity rate and corresponding increased likelihood into account. Considering that the same line of reasoning is expected to hold for subduction zones, we would also expect seismic hazard, or at least $\mathbf{M_{max}}$, to increase with increasing subduction velocity.

2.6 Conclusions

We systematically studied the influence of convergence rate on seismicity in active continent-continent collisional orogens through using numerical models and a comparison with earthquake data. The most important results can be summarized as follows:

1. Cycles of spontaneous earthquake-like ruptures on non a-priori defined faults are for the first time simulated in a generic continent-continent collision zone. Using the developed, innovative seismo-thermo-mechanical approach, we simulate the feedback between long-term continental orogeny and relating deformation and short-term seismicity. Our results show physically consistent emergence of complex rupture events, both on- and off-megathrust. These events lead to a Gutenberg-Richter frequency-magnitude distribution, a key observational feature of seismicity, which is typically not reproduced in seismic cycle models.

2. These Gutenberg-Richter distributions suggest an inverse, linear relationship between plate convergence rate and *b* value. Also, these results indicate a positive, linear relationship between $\mathbf{M_{max}}$ and plate convergence rate. This

means that plate convergence rate controls the seismic behaviour of mountain belts, both in terms of frequency and size of earthquakes. Collisional orogens with high convergence rates are manifested by pervasive seismicity, high magnitude of earthquakes and relative low *b* values. In contrast, decreasing convergence rates lead to relatively larger amounts of smaller earthquakes (i.e., increasing *b* value) and lower maximum magnitudes. Moreover, seismicity is observed to migrate from the main thrust into the orogenic wedge as convergence rate decreases. This more distributed form of brittle deformation is also accompanied by a larger contribution of ductile deformation, thereby additionally reducing seismic hazard for slower convergent margins.

3. High convergence rates reduce the average temperature of the orogen, thereby increasing the brittle portion of the crust at the expense of the ductile portion. Higher convergence rates, moreover, lead to larger background strain rates, which extend the brittle failure depth even further. This rheological feedback mechanism therefore suggests that for high collision rates the brittle strength is larger and, in turn, increases the capacity of seismogenic faults to store and release elastic strain energy.

4. Our analysis shows that the *b* value decreases linearly with differential stress for orogens with higher convergence rate, which agrees with laboratory experiments and natural data. Since differential stress in turn depends on the plate convergence rate, it supports our hypothesis that the convergence rate is in fact the ultimate first-order physical parameter governing the other physical parameters and thus the seismic behaviour of mountain belts.

5. These modeling results found a good agreement with general observations of seismicity patterns within the collisional orogens. Himalayan and Zagros orogens are mainly characterized by bimodal (i.e., upper and lower crust) distribution of earthquakes and a localized seismicity along the megathrust. The Alps and Apennines show instead an unimodal (i.e., upper crust confined) distribution of earthquakes and a more widespread, and less intense,

seismicity.

6. Warm collision zones are manifested by the development of a high and broad plateau overlying a thick crustal wedge formed by continuous accretion of crustal slices. Results show that the location of seismogenic faults may change according to the regional stresses and the main tectonic structures. However, the resulting seismic behaviour is dominated by plate convergence rate.

First-order agreement between our models and data support the implications of our results and contributes to fill the gap left in modeling seismicity of collisional margins. Even though second-order effects can come from the tectonic structure of the belt itself, our findings suggests that convergence rate is a critical parameter for the seismic behaviour of mountain belts. Therefore, hazard studies should pay attention to this critical parameter as it, besides seismicity rate, also affects $\mathrm{M}_{\max}$, *b* value, and is directly related to the distribution of stresses in the Earth's crust.

Acknowledgements
This study was funded by the SNF project Swiss-AlpArray SINERGIA. We thank E. Kissling, S. Wiemer and Y. Kamer for encouragement and for providing helpful background information. For constructive comments and discussions we thank G. Hetényi, J. Singer, S. Simuté and the STM–group. Numerical simulations were performed on ETH cluster Euler. We thank David Whipp and an anonymous reviewer for their constructive comments, which helped improve the paper considerably.

3

Slab Rollback Orogeny model for the evolution of the Central Alps—Seismo-Thermo-Mechanical proof

A similar version of this chapter is under review as:
Dal Zilio L., Kissling E., Gerya T. V., and van Dinther Y.
Slab Rollback Orogeny model for the evolution of the Central Alps: Seismo-Thermo-Mechanical test

3.1 Abstract

The role of mantle-lithosphere interactions in shaping mountain belts has long been debated. Several conceptual models implicate a key role for horizontal kinematic forces in sustaining mountain building processes. For the central European Alps, however, recent stratigraphic, palaeo-altimetry and lithosphere structural evidence suggest that dynamic vertical forces—provided by a *Slab Rollback Orogeny* (SRO) model—are the primary determinant of the latest construction of thick nappe successions, the large-scale tectonic evolution, and the present-day seismicity pattern. In this study we investigate this hypothesis by performing 2-D, high-resolution, rheologically consistent, visco-elasto-plastic seismo-thermo-mechanical numerical modeling, which simulates both tectonic and seismic processes in a subduction and continental collision setting. Our numerical experiments reproduce the self-driven stages of oceanic subduction, continent-continent collision, and spontaneous slab breakoff. The subsequent evolution of the orogen shows how slow, but persistent, flexural bending of post-collisional residual slab and crustal delamination control the latest evolution of the orogen. Bending-related slab suction leads to the coeval development of nappe stacking of the buoyant crustal root, widening of the orogen, and a distinctive seismicity pattern that implies the occurrence of extensional forces at work in the orogen and beneath the foreland basin. Our results thus suggest that a self-sustaining rollback mechanism is capable of explaining the post-collisional

evolution of the Central Alps, including the construction of thick sedimentary successions in the Molasse foreland basin and the most recent tectonic deformation of the Jura fold-and-thrust belt.

3.2 Introduction

The process of continent–continent collision in shaping mountain ranges and adjacent foreland basins has been discussed over many decades (e.g., Malinverno & Ryan, 1986; Beaumont *et al.* , 1996; Avouac, 2015). According to most commonly used concept, the evolution of mountain belts has largely been driven by the horizontal convergence between the two colliding plates (e.g., Schmid *et al.* , 1996; Handy *et al.* , 2010). This view is based on the perception in which a rigid indenter—frequently exemplified by a bulldozer—converts the kinematic convergence into the mountain building processes (Willett, 2010). For the central European Alps (Fig. 3.1A), however, this general concept is neither consistent with observations nor with isostatic mass balancing models (Schlunegger & Kissling, 2015).

The crustal root has been seismically determined to be ~60-km thick, and thus far out of conventional Airy-isostatic equilibrium with a mean surface topography of only about 2 km (Kissling, 1993). A more recent, alternative explanation suggests that the Central Alpine evolved in response to a slab rollback process, in which the dynamic vertical forces of a retreating subduction and crustal buoyancy forces are the major driving mechanisms of the orogenic system (Brun & Faccenna, 2008; Kissling & Schlunegger, 2018). This revised model on Alpine evolution, which we refer to as *Slab Rollback Orogeny* (SRO) model, consider the well-known concepts of slab pull and retreat, force balancing, and the principles of mass conservations. This SRO model provides a dynamically consistent mechanism to explain the construction of thick sedimentary successions in the Molasse basin where the extra slab load has maintained the Alpine surface at moderate, but persistent, elevations (Schlunegger & Kissling, 2015). This SRO model provides a dynamically consistent mechanism to explain the construction of thick sedimentary successions in the Molasse basin (Schlunegger & Kissling, 2015) and the imbricate stacking of the crustal root (Fry *et al.* , 2010).

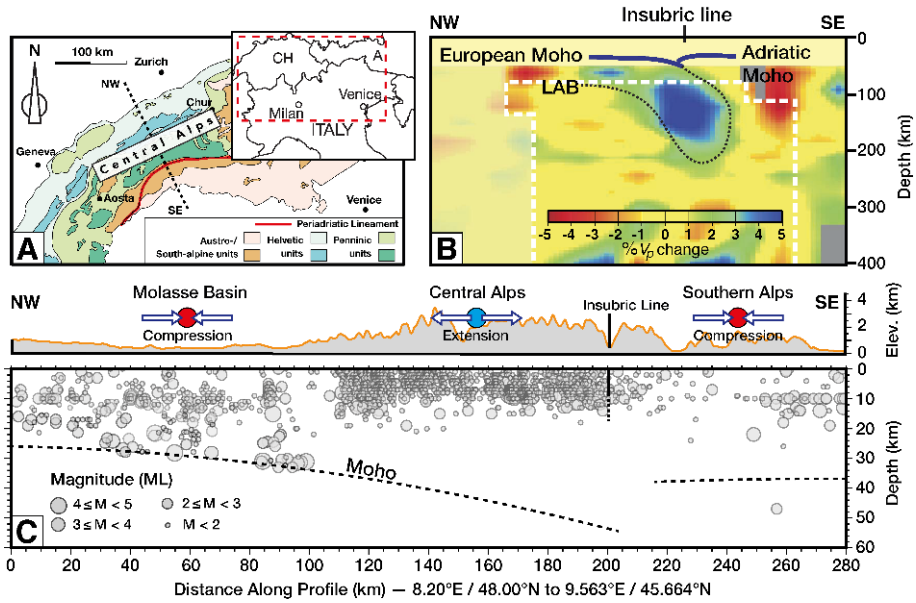


Figure 3.1.: **A**: Inset map illustrating the Alps and its foreland basin along with the section discussed in this paper. **B**: Teleseismic tomography cross-section illustrating European slab geometry beneath the central Alps. The figure shows lateral variations of P-wave velocity Vp beneath the Moho. **C**: Topographic signal and vertical cross-section approximately perpendicular to the strike of the Central Alps. Transparent gray circles represent hypocenters. Dashed black lines indicate the Moho with a minimum ±3 km uncertainty of the depth.

On a large-scale, teleseismic tomography cross-sections have shown that, along the NW–SE transect across the Central Alps, the slab dips with only ~60° (Fig. 3.1B), while along a N–S transect at ~10°E longitude the slab hangs in a sub-vertical position beneath the core of the Alps (Lippitsch *et al.* , 2003). Geological interpretations based on receiver function profile (Zhao *et al.* , 2015) and on teleseismic imaging (Zhao *et al.* , 2016) argue that the European mantle slab is still attached beneath southern Western Alps. In contrast, recent teleseismic full-waveform inversion by Beller *et al.* (2017) indicates a low-velocity zone in the lower lithosphere and they explicitly support the hypothesis of a slab tearing beneath the Western Alpine arc.

If the scenario proposed by Lippitsch *et al.* (2003) is correct, the SRO model provides a possible explanation for the current seismicity pattern across the Central Alps (Fig. 3.1C), which is characterized by bending-related faulting events beneath the Molasse Basin and within the subducting European plate (Singer *et al.* , 2014). This post-collisional slab rollback orogeny scenario thus suggests a mechanism

where tectonic processes related to a retreating collision regime conditioned the subduction processes, the accommodation of space in the Molasse Basin and the crustal accretion in the adjacent Alps. However, although well established, this new theory has never been tested through the use of physics-based numerical methods.

In this study, we employ a newly-developed, high-resolution (400 m), 2-D Seismo-Thermo-Mechanical (STM) model to simulate both the long-term tectonic of collisional orogens and the short-term seismicity (e.g., Dal Zilio *et al.* , 2018b) and to test whether the buoyancy forces of the postulated post-collisional rollback are sufficient to drive the evolution and to shape the Central Alps as we know them today.

3.3 Initial model design

3.3.1 Numerical code description

In order to simulate the dynamics of mountain building processes coupled to mantle dynamics, we employ the seismo-thermo-mechanical (STM) (van Dinther *et al.* , 2013b). This numerical code solves for the two-dimensional steady state momentum equations and heat conservation equation using the finite-difference/marker-in-cell method on a Eulerian grid Gerya & Yuen (2007):

$$\frac{\partial v_x}{\partial x} + \frac{\partial v_z}{\partial z} = 0 \tag{3.1}$$

$$\frac{\partial \sigma'_{xx}}{\partial x} + \frac{\partial \sigma'_{xz}}{\partial z} - \frac{\partial P}{\partial x} = \rho \frac{D v_x}{D t} \tag{3.2}$$

$$\frac{\partial \sigma'_{zz}}{\partial z} + \frac{\partial \sigma'_{zx}}{\partial x} - \frac{\partial P}{\partial z} = \rho \frac{D v_z}{D t} - \rho g \tag{3.3}$$

These equations are solved to obtain the horizontal and vertical velocities (v_x and v_z) and pressure (P, defined as the mean stress), whereas ρ is density, σ'_{ij} are

deviatoric stress tensor components, and g = 9.81 m/s^2 is the vertical component of the gravitation acceleration. The advection of transport properties including viscosity, plastic strain and temperature is performed with the displacement of Lagrangian markers.

The momentum equations include the inertial term to stabilize higher slip rates at low time steps. A time step of 1 year, however, reduces our formulation to a virtually quasi-static one. Ruptures during the resulting events hence represent the occurrence of rapid threshold-exceeding slip during which permanent displacement and stress drop occur along a localized interface.

The heat equation describes the balance of heat in a continuous medium and is solved in a Lagrangian manner and is expressed in the following way (Gerya, 2010):

$$\rho C_p \frac{DT}{Dt} = -\frac{\partial q_x}{\partial x} - \frac{\partial q_z}{\partial z} + H_\mathrm{r} + H_\mathrm{a} + H_\mathrm{s}; \tag{3.4}$$

$$q_x = -k(T,C)\frac{\partial T}{\partial x}; \tag{3.5}$$

$$q_z = -k(T,C)\frac{\partial T}{\partial z}; \tag{3.6}$$

$$H_a = T\alpha\frac{DP}{Dt} \tag{3.7}$$

$$H_\mathrm{s} = \sigma'_{ij}\ \dot{\varepsilon}_{ij,\ vp}; \tag{3.8}$$

Such a formulation takes into account the effect of radioactive heating (H_r), adiabatic heat production/consumption (H_a), and shear heating (H_s). DP/Dt represents the substantive time derivative of pressure, whereas α is the thermal expansion. Thermal conductivity $k(T,C)$ is a function of both temperature and composition (cf. Table 3.1). q_x and q_z are the horizontal and vertical components of the heat flux vector, $\dot{\varepsilon}_{ij,\ vp}$ is the visco-plastic component of the deviatoric strain rate tensor, and H is the rock enthalpy. The isobaric heat capacity (C_p) and isothermal compression

term are computed at each timestep and takes into account the effect of latent heat due to phase transformations (Faccenda & Dal Zilio, 2017). Evaluation of H_T and H_s terms requires information from the pressure and stress tensor components. These terms are thus computed after solving the Stokes equations. The heat equation can then be solved taking into account the effect of isothermal compression, phases changes and shear heating at the current timestep.

$Material$ $flow\ law$ [a]	ρ_0 [b] ($kg\ m^{-3}$)	E_a [a] ($kJ\ mol^{-1}$)	V_a [a] (J/bar)	n [a]	η_0 [a] ($Pa^n\ s$)	Hr [b,c] ($\mu W m^{-3}$)	k [a] $Wm^{-1}K^{-1}$	G (GPa)	μ_s [d,e,f]	λ [g,h]
Sediments (Wet Qz)	2600	154	1.2	2.3	1.97 x 10^{17}	1.5	$[0.64+807/(T+77)]$ $exp(4\ 10^{-5}P)$	25	0.35	0.4
Upper cont. crust (Wet Qz)	2750	154	0.8	2.3	1.97 x 10^{17}	0.25	$[0.64+807/(T+77)]$ $exp(4\ 10^{-5}P)$	34	0.6	0.4
Lower cont. crust (Mafic Granulite)	3000	445	0.8	4.2	1.25 x 10^{21}	1.5	$[0.64+807/(T+77)]$ $exp(4\ 10^{-5}P)$	34	0.6	0.4
Upper oc. crust (Wet Qz)	3000	154	0.8	2.3	1.97 x 10^{17}	0.25	$[1.18+974/(T+77)]$ $exp(4\ 10^{-5}P)$	38	0.6	0.95
Lower oc. crust (Plg-An 75%)	3300	238	0.8	3.2	4.8 x 10^{22}	0.0022	$[1.18+974/(T+77)]$ $exp(4\ 10^{-5}P)$	38	0.6	0.4
Mantle (Dry Olivine)	3300	532	0.8	3.5	3.98 x 10^{16}	0.0022	$[0.73+1293/(T+77)]$ $exp(4\ 10^{-5}P)$	67	0.6	0.4

Table 3.1.: Rheological parameters. ρ_0 is the reference density, E_a is the activation energy, V_a is the activation volume, n is the stress exponent, η_0 is the reference viscosity, Hr is the radiogenic heat production, G is the shear modulus, μ_s is the static friction coefficient and λ is the pore-fluid pressure factor (P_{fluid}/P_{solid}). Other properties for all rock types: cohesion (C) is 1 MPa (Schultz, 1995), specific heat capacity (C_p) is 1000 $J\ kg^{-1}K^{-1}$, thermal conductivity (k) is in $Wm^{-1}K^{-1}$ at T_K and P_{MPa}, thermal expansion α_ρ= 3x10^{-5} K^{-1} and compressibility β_ρ=1x10^{-5} MPa^{-1}. [a] Ranalli (1995); [b] Turcotte & Schubert (2002); [c] Rudnick & Fountain (1995); [d] Di Toro *et al.* (2011); [e] Del Gaudio *et al.* (2009); [f] Den Hartog *et al.* (2012); [g] Sibson (1994); [h] Seno (2009).

3.3.2 Rheological model

We consider that the strength of the lithosphere is controlled, at the different timescales of orogeny, by the combination of both brittle and ductile deformation mechanisms in a visco-elasto-plastic rheology. Viscous creep is computed in terms of deformation invariants and depends on strain rate, temperature, and pressure (Ranalli, 1995). The effective viscosity (η_{eff}) of the deformation is calculated as a combination of diffusion (η_{diff}) and dislocation creep (η_{dis}):

$$\frac{1}{\eta_{eff}} = \frac{1}{\eta_{diff}} + \frac{1}{\eta_{disl}} \tag{3.9}$$

The calculation of the viscosity associated with dislocation creep regime is formulated as follows:

$$\eta_{disl} = \frac{1}{2} A_d \, \sigma\prime_{II}^{1-n} \, exp\Big(\frac{E_a + PV_a}{nRT}\Big) \tag{3.10}$$

where $\sigma\prime_{II}$ is the second invariant of deviatoric stress tensor, A_d is the pre-exponential factor, E_a the activation energy, V_a is the activation volume, n the stress exponent, and R is the gas constant. Those material properties are determined from laboratory flow experiments and are given in Table 3.1.

Dislocation creep is dominant for high stress levels, while diffusion creep is a thermally activated mechanism and is the most convenient way to accommodate deformation at low stress conditions:

$$\eta_{diff} = \frac{1}{2} A_d \, \tau_{tr}^{1-n} \, exp\Big(\frac{E_a + PV_a}{nRT}\Big). \tag{3.11}$$

In this case, τ_{tr} defines the stress transition between diffusion creep and dislocation creep, which is assumed to occur at 30 kPa (Turcotte & Schubert, 2002).

Our rheological model takes into account a second semi-brittle deformation mechanism characterized by the exponential flow of olivine and also known as Peierls mechanism. As demonstrated in Duretz *et al.* (2011), Peierls creep in olivine is a key mechanism for slab breakoff, generally causing slabs to break earlier and at shallower depths. This flow mechanism has been put in evidence in a number experimental studies (Evans & Goetze, 1979; Katayama & Karato, 2008). Moreover, recent studies have shown that the existence of plate tectonics requires sufficiently lithospheric yield stress that are lower than Mohr–Coulomb stresses (Van Heck & Tackley, 2008). Such conditions necessitate the use of stress limiters such as Peierls creep which promotes the localization of deformation in the lithospheric mantle (Kameyama *et al.* , 1999; Lu *et al.* , 2011). The effective viscosity corresponding to the Peierls creep regime is characterized by an exponential dependance on the second stress invariant and is formulated as:

$$\eta_{peierls} = \frac{1}{2A_{peierls}\sigma_{II}} exp\left(\frac{E_a + PV_a}{nRT}\left(1 - \left(\frac{\sigma_{II}}{\sigma_{peierls}}\right)^p\right)^q\right); \tag{3.12}$$

for dry olivine, $A_{peierls} = 10^{7.8}\, 10^{-12}\ Pa^{-2}s^{-1}$ is the material constant for Peierls creep, $\sigma_{peierls}$ is the Peierls stress that limits the strength of the material and corresponds to 9.1 GPa (Evans & Goetze, 1979). Exponents p and q depend on the shape and geometry of obstacles that limit the dislocation motion and are equal to 1 and 2, respectively. The Peierls mechanism is a dominant deformation mechanism of the downgoing slab, where the temperature is low and stress is high (e.g. Karato *et al.* , 2001).

The 2-D steady state momentum equations are solved using constitutive relations that relate deviatoric stresses and strain rates in a nonlinear visco-elasto-plastic manner:

$$\dot{\varepsilon}_{ij} = \frac{1}{2G}\frac{D\sigma'_{ij}}{Dt} + \frac{1}{2\eta}\sigma'_{ij} + \begin{cases} 0 & \text{for } \sigma'_{II} < \sigma_{yield} \\ \chi \frac{\partial \sigma'_{II}}{\partial \sigma'_{ij}} = \chi \frac{\partial \sigma'_{ij}}{2\sigma'_{II}} & \text{for } \sigma'_{II} = \sigma_{yield} \end{cases} \tag{3.13}$$

where G is shear modulus and η is effective viscosity. $D\sigma'_{ij}/Dt$ is the objective co-rotational time derivative solved using a time explicit scheme (Gerya, 2010) and $\sigma_{II} = \sqrt{{\sigma'_{xx}}^2 + {\sigma'_{xz}}^2}$ is the second invariant of the deviatoric stress tensor, and χ is a plastic multiplier connecting plastic strain rates and stresses. Introducing a visco-plastic viscosity (η_{vp}), we can rewrite equation 3.13 as:

$$\sigma'_{ij} = 2\eta_{vp} Z \dot{\varepsilon}_{ij} + \sigma_{ij}(1 - Z) \tag{3.14}$$

where Z is the visco-elasticity factor:

$$Z = \frac{G\Delta t_{comp}}{G\Delta t_{comp} + \eta_{vp}} \tag{3.15}$$

where Δt_{comp} is the computational time step.

The brittle part of the lithosphere is controlled by Mohr–Coulomb (or non-associative Drucker-Prager) plasticity which expresses the linear dependence of the geomaterials resistance on the total pressure Prager & Drucker (1952). Mohr–Coulomb plasticity acts as a stress limiter in the regions where the second stress invariant (σ_{ii}) exceeds the material yield stress. The yield stress depends

on the pressure, the standard strength (i.e., cohesion) C (MPa), and the effective friction coefficient μ_{eff}:

$$\sigma_{yield} = C + \mu_{eff} P \tag{3.16}$$

where C is the cohesion.

An important component in the yield criterion is the friction coefficient. Following the approach of van Dinther *et al.* (2013b), we apply a strongly rate-dependent friction formulation (Ampuero & Ben-Zion, 2008), in which the effective friction coefficient μ_{eff} depends on the visco-plastic slip velocity $V = (\sigma_{yield}/\eta_m)\Delta x$, in which η_m is the local viscosity from the previous time step and Δx is the Eulerian grid size:

$$\mu_{eff} = \frac{V_c\,\mu_s + V\,\mu_d}{V_c + V} \tag{3.17}$$

$$\gamma = 1 - (\mu_d/\mu_s) \tag{3.18}$$

where μ_s and μ_d are static and dynamic friction coefficients, respectively, V_c is the characteristic velocity, namely the velocity at which half of the friction change has occurred, and γ represents the amount of slip velocity-induced weakening if $\gamma = 1 - (\mu_d/\mu_s)$ is positive, or strengthening if γ is negative.

When plastic yielding condition is locally reached we require a constant second invariant of deviatoric stresses (assuming the absence of elastic deformation)

$$\text{if} \quad \sigma'_{II} = \sigma_{yield} : \left\{ \quad \frac{D\sigma'_{II}}{Dt} = 0, \quad \dot{\varepsilon_{ij}}^{elastic} = 0 \right\}; \tag{3.19}$$

then the stress components are similarly (i.e., isotropically) corrected so that

$$\sigma'_{ij} = \sigma'_{ij} \cdot \frac{\sigma_{yield}}{\sigma'_{II}}. \tag{3.20}$$

Accordingly, the local viscosity-like parameter η_{vp} decreases to weaken the material and to localise deformation

$$\eta_{vp} = \eta \frac{\sigma'_{II}}{\eta\chi + \sigma'_{II}} \tag{3.21}$$

where

$$\chi = 2(\dot{\varepsilon_{II}} - \dot{\varepsilon_{II}}^{viscous}) = 2(\dot{\varepsilon_{II}} - \frac{1}{2\eta}\sigma'_{II}) \tag{3.22}$$

and

$$\dot{\varepsilon_{II}} = \sqrt{\dot{\varepsilon_{xx}}^2 + \dot{\varepsilon_{xz}}^2} \tag{3.23}$$

Finally the visco-plastic viscosity η_{vp} is corrected during plastic deformation:

$$\eta_{vp} = \frac{\sigma_{yield}}{2\dot{\varepsilon_{II}}} \tag{3.24}$$

On the other hand, if the plastic yielding condition is not satisfied, this means that the material is under elastic and/or viscous deformation (i.e., diffusion and/or dislocation creep), therefore $\eta_{vp} = \eta$.

3.3.3 Eclogitization

Eclogitization of the continental mafic crust can have major effects on the evolution of continental plates. With the progression of the reaction, the eclogitized continental root becomes denser than the surrounding mantle and thus it is prone to foundering (Kay & Kay, 1993). Numerical models predict that high-density eclogite affects the orogeny evolution (Doin & Henry, 2001; Li *et al.* , 2016) and, if sufficiently weak, can lead to delamination of the continental plate (Krystopowicz & Currie, 2013).

Therefore, eclogitization of subducted crust is here implemented in a relatively simplified manner (Faccenda & Dal Zilio, 2017). More specifically, for the basalts of the upper and lower mafic crust, a phase transition from basalt to garnet-granulite and then eclogite (Ito & Kennedy, 1971) is applied. Eclogitization of the crust is implemented as a linear density increase with pressure and temperature from 0% to 16% in the P–T region between the experimentally determined garnet-in and plagioclase-out phase transitions in basalt (Ito & Kennedy, 1971). For temperatures lower than $T_{ecl_{min}}$ = 673K no eclogitization is possible. For temperatures between $T_{ecl_{min}}$ and $T_{ecl_{max}}$= 873 K the maximum density increase due to eclogitization is linearly increasing with temperature from 0% to 16%.

3.3.4 Estimation of Moment Magnitude (M_W)

During the seismic cycle simulation we analyze all rupture events to determine their downdip rupture width (W). These events occurring throughout the orogen are recognized using a Rupture Detector Algorithm (RDA), which analyzes each Lagrangian marker in space and time throughout the simulation. If its velocity exceeds a threshold of 9.0 x 10^{-9} m s^{-1}, while simultaneously stresses drop more than 0.4 MPa that marker's physical properties are stored in a synthetic data set. Subsequently markers are grouped into one event when they occur within 400 m of a marker that ruptured this or the previous time step. The rationale for choosing these thresholds comes from the minimally common stress drop (Allmann & Shearer, 2009) and our Eulerian grid size of 400 m, respectively.

From these spontaneous rupture paths we measure the rupture width (W) to estimate the moment magnitude (M_W) using the empirical scaling relations in Wells & Coppersmith (1994). This empirical relationship is available from regression analysis based on a large numbers of events in nature:

$$M_W = a + b\,log(W), \tag{3.25}$$

where a and b are coefficients that vary with the style-of-faulting (i.e., normal or reverse faulting). We chose Wells & Coppersmith (1994) because they include various types of faulting and different tectonic environments.

3.3.5 Setup

The initial model domain consists of two continental plates separated by an oceanic basin (see Fig. 3.2A). The dimensions of the model box is 3000 x 1200 km^2 (1921 x 347 nodes), and all the mechanical boundaries are free slip. Variable grid spacing enables to reach a 400 m grid resolution in the central part of the domain where the continental collision takes place. Lithological structure are resolved with ~33 million markers. In order to study the interplay between subduction and orogenic evolution, we follow the semi-dynamic approach employed in Duretz *et al.* (2011). The initial

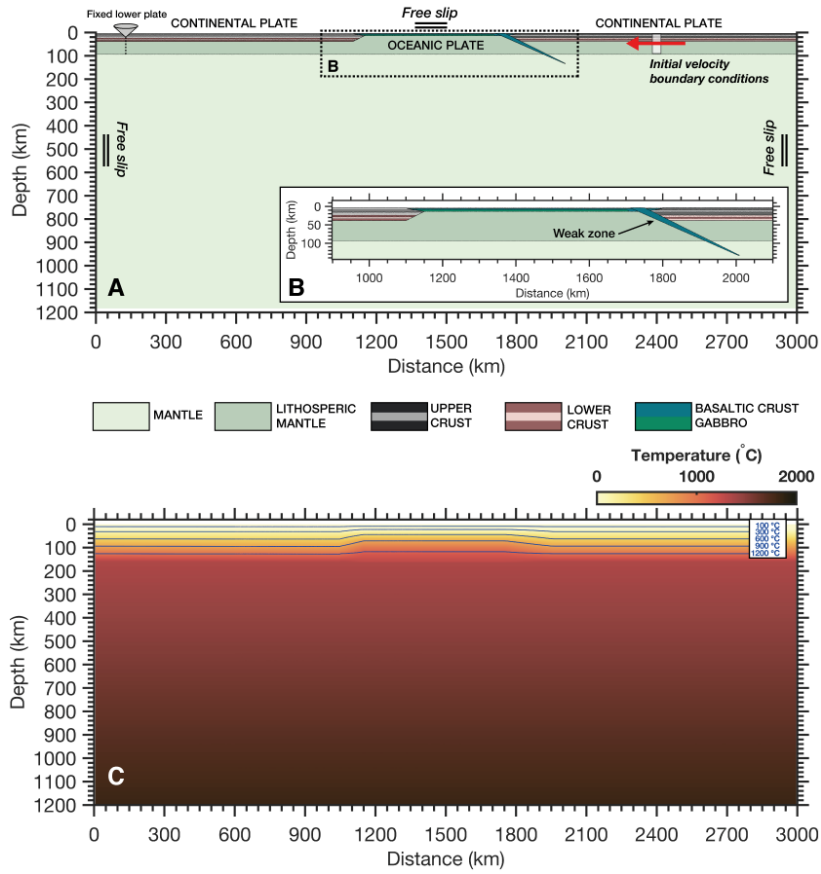


Figure 3.2.: 2-D initial setup. **A**: Initial composition map including boundary conditions. **B**: Zoom of oceanic plate and pre-imposed weak zone to initiate subduction. Using a similar approach of Duretz *et al.* (2011), the model simulates subduction initiation through the use of a fixed convergence rate on the upper plate until ~200 km of oceanic crust has been subducted. Plate convergence rate is applied at 2500 km on the right (upper) plate (red arrow). **C**: Initial temperature distribution.

conditions of the model are built during the initial stage of kinematic convergence. During this period, the oceanic subduction is kinematically prescribed using internal kinematic constrains (5 cm/yr until 200 km of convergence is accommodated). With ongoing convergence, the upper plate decouple from the lateral sides of the box; this zones accommodate hot mantle upwellings and are therefore the location where oceanic ridges spontaneously develop. After this model initialization step, the internal kinematic constrain is removed and the model is driven by internal, buoyancy forces. Thus, the obtained thermo-mechanical state is employed as the

initial condition for a self-driven, retreating subduction and continental collision. The subduction and collision rates, which are not in steady state, are controlled by the contribution of slab pull, crustal buoyancy, and dissipative forces. We employ an additional 20 km thick layer of sticky air (η_{air} = 10^{18} Pa s, ρ_{air} = 1 kg/m^3) in order to mimic the effect of a free surface and enable the development of topography (Crameri *et al.* , 2012).

The thermal structure of the oceanic lithosphere was calculated from the half space cooling model for a given plate age (Turcotte & Schubert, 2002) using a slab age of 70 Ma and a diffusivity of 10^{-6} m^2 s^1. The initial continental geotherm is defined as a linear temperature variation from the model surface (T=293 K) to the lithosphere–asthenosphere boundary (T=1617.6 K), the left and right sides of the model domain are insulating boundaries. The geothermal gradient in the asthenospheric mantle below the lithosphere is 0.5 K/km (Fig. 3.2C).

In order to initiate subduction a weak zone was imposed on the right ocean–upper plate transition. The weak zone cuts through the whole lithospheric mantle with an angle of ~30° and is characterized by weak plastic strength (1 MPa) and wet olivine rheology (Ranalli, 1995). Despite the fact that subduction initiation can be modelled in a geologically more relevant manner (e.g., Nikolaeva *et al.* , 2010), the use of such a weak zone remains useful for our specific setup.

3.4 Numerical model results

After a stage of pre-imposed model initiation, subduction and subsequent collision are solely driven by the buoyancy of the lithosphere slab. The upper Adriatic plate is decoupled from Africa (e.g., Platt *et al.* , 1989) and free to move, whereas the lower plate is fixed to the left boundary. This setup is thus consistent with palaeomagnetic evidence that the lower (European) continental plate has remained nearly stationary since the Late Cretaceous (Dewey *et al.* , 1989).

3.4.1 Rollback subduction, collision, and slab breakoff

After an initial stage of kinematically imposed subduction initiation, oceanic lithosphere sinks spontaneously at the ocean-upper plate (Adria) continental margin. Self-sustaining retreating subduction occurs in all our simulations: slab rollback causes the migration of the trench and exerts a suction force to the overriding plate, while the subduction-induced mantle flow maintains the upper plate highly coupled with the retreating slab (Fig. 3.3) (e.g., Faccenda *et al.* , 2009; Dal Zilio *et al.* , 2018a; Dal Zilio, 2018).

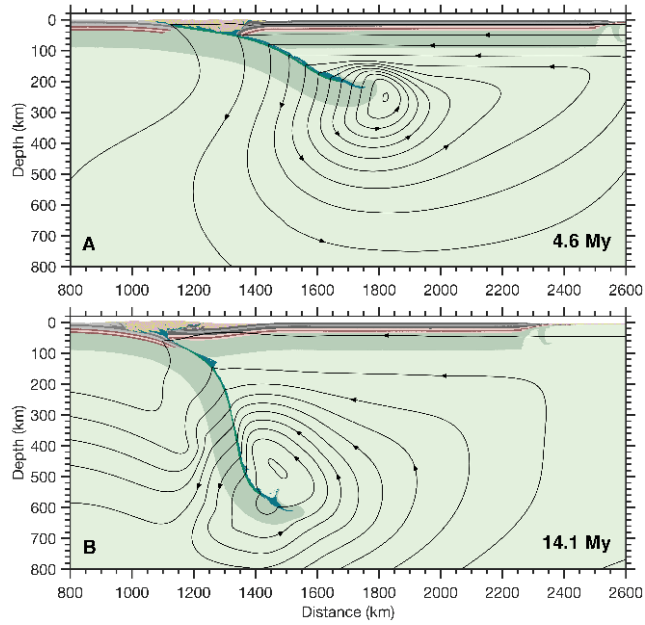


Figure 3.3.: Thermomechanical evolution of a spontaneously bending oceanic plate and evolution at key stages of mantle-lithosphere interaction. Composition of the reference model after 4.6 My (**A**) and 14.1 My (**B**). The superimposed stream function display the effect of subduction-induced trench suction and return flow in mantle, which maintain the upper plate coupled with the retreating slab.

Slab necking occurs at a relatively shallow depth of approximately 250 km during the stage of slab steepening. Breakoff occurs at the ocean–continent transition a few million years after the collision stage initiated (Fig. 3.4). Slab breakoff and subsequent rebound produces a sharp topographic signal, with an exhumation of ~5 km recorded above the orogen. Such exhumation, defined as the total

displacement of rocks with respect to the surface, is thus controlled by the rate of erosion and the rate of removal of overburden by tectonic processes. The topographic response is relatively rapid (~5 My) and produces an average uplift rate of 0.8 mm/yr, predominantly above the lower continental plate, and consistent with the observations (Schlunegger & Kissling, 2015).

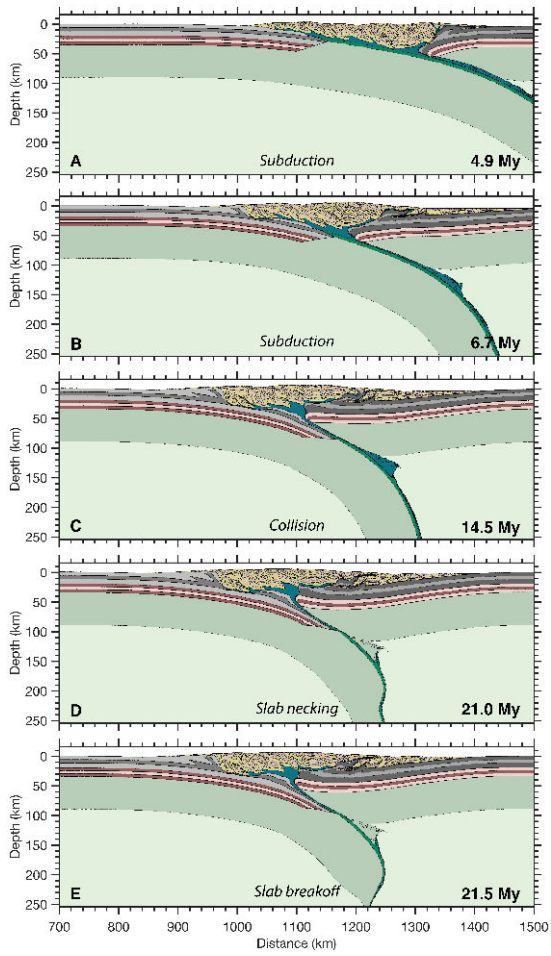


Figure 3.4.: Long-term evolution of subduction (**A–B**), collision (**C**), slab necking (**D**), and slab breakoff (**E**). The early phases of the models consist of oceanic plate consumption and ocean closure. The collisional regime is greatly affected by the buoyant and rheologically weak materials entering the subduction channel from above. The final structure is that of a *coupled* collision system (e.g., Faccenda *et al.* , 2009).

3.4.2 Post slab breakoff evolution of the orogen

Our numerical experiments indicate that the removal of the oceanic lithospheric load during slab breakoff is responsible for a stress redistribution within the lithosphere. Release of the gravitational stresses during breakoff is followed by the unbending of the remaining slab and a localized increase of stress in the lower plate related to the positive buoyancy of the subducted continental crust. However, our numerical simulations show that the vertical slab pull force—offered by the remaining slab—remains the dominant driving force in the collisional system (Fig. 3.5).

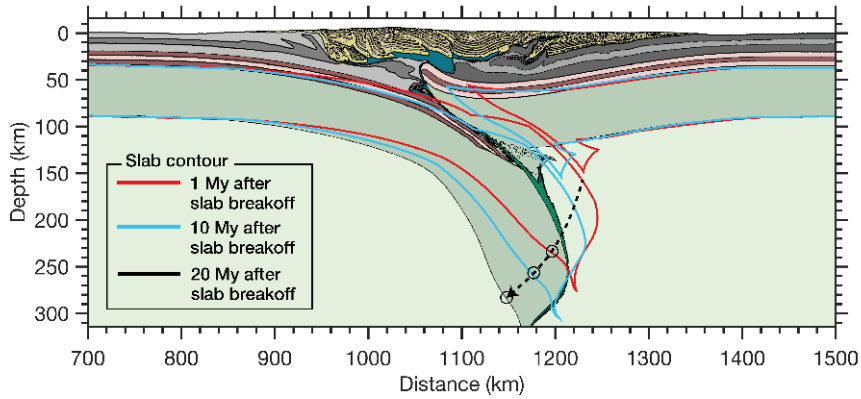


Figure 3.5.: Post-collisional evolution with superimposed outlines of the slab geometries 1 and 10 My after slab breakoff. Compositional map shows the final structure 20 My after slab breakoff. Evolution of the orogen is driven by slow slab rollback and delamination of crustal material at all levels of lower plate.

Following the rapid transient visco-elastic rebound (Gerya *et al.* , 2004; Duretz *et al.* , 2011), the resulting flexural bending provokes the migration of the whole orogen towards the foreland basin (Fig. 3.6). The ongoing rollback collision triggers crustal delamination, shortening at shallower crustal levels, and uplift of the frontal part of the orogen and in the foreland basin. At deeper crustal levels, extrusion and stacking of buoyant crustal materials occur on the downgoing plate, while the remaining slab continues to subduct at a low, but detectable, sinking rate (Fig. 3.5). In addition, heating of the slab decreases the flexural strength and increases the curvature of the subducted plate, thus inducing large-scale extension.

The final convergence rate is relatively small (2–3 mm/yr; Fig. 3.7), in agreement with continuous GPS measurements (Calais *et al.* , 2002). The uplift rate is ~0.6

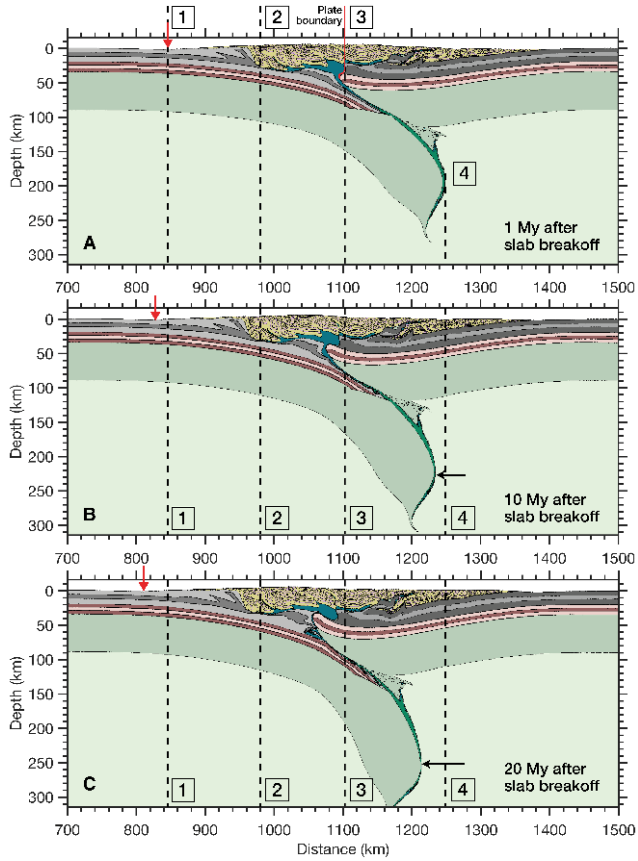


Figure 3.6.: Post-collisional evolution at 1 My (**A**), 10 My (**B**), and 20 My (**C**) after slab breakoff. (**1**): Location of northern front of orogen at the surface. Red arrows indicate the position of the orogenic piedmont. (**2**): Location of northern edge of the accretionary wedge and the upper crust at 20 km depth; (**3**): Surface location of plate boundary (solid red line), (**4**): Position of the slab tip.

mm/yr in the core of the orogen and ~0.2–0.3 mm/yr in the foreland basin, with an average exhumation of 2 km in 10 My, thus confirming analyzes of Alpine thermo-chronometric ages (Fox *et al.* , 2015). The orogenic volume is mostly accommodated on the lower continental plate, with a maximum topography greater than 5 km in height. Finally, at *ca.* 20 Myr after slab breakoff, crustal shortening and rock uplift propagate through the continental interiors, similarly to the main shortening observed in the Jura thrust belt over the last 10 Ma (e.g., Burkhard, 1990), thus resulting in a widening of the orogenic belt above the lower continental plate. Interestingly, our numerical experiments suggest that, when the post breakoff

remaining slab tip is less than 160 km deep, the vertical slab pull force decreases significantly.

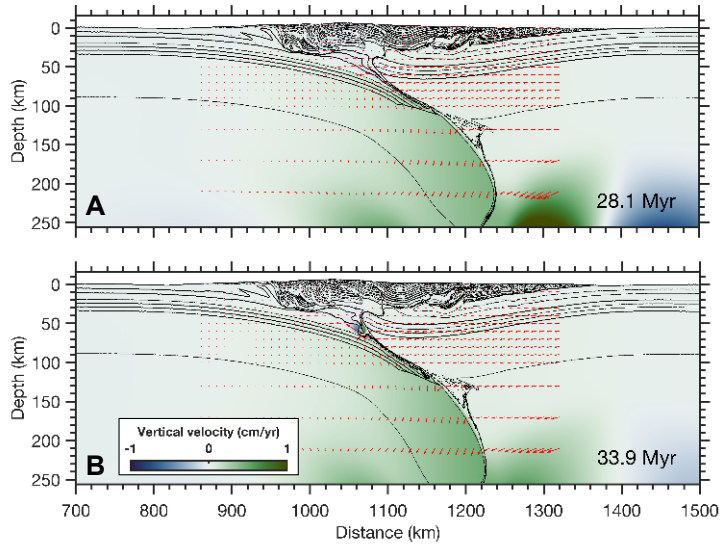


Figure 3.7.: Vertical velocity field in color overlain by arrows indicating velocities at 28.1 (~7 My after slab breakoff) and 33.9 (~13 My after slab breakoff). The inferred velocity fields show how the vertical sinking of the post breakoff remaining slab translates into horizontal convergence of the upper plate and uplift in the core of the orogen.

3.4.3 Regional stresses and seismicity distribution

The seismic cycle simulation shows a wide domain subjected to brittle faulting (Fig. 3.8). Seismogenic deformation in the orogenic wedge is largely driven by extensional stresses resulting from the development of retreating collision (Fig. 3.9). On the other hand, overthrusting of the orogenic wedge on the upper plate cause compressional stresses and, in turn, in a sequence of seismogenic thrusts at the front and beneath the retro-foreland basin (Fig. 3.8).

Deep earthquakes beneath the foreland basin extend into the lower crust and their distribution correlates well with the flexural bending of the downgoing plate. Flexural bending transfers stresses into the lithosphere beneath the foreland basin and leads to a compressional component in the shallower domains and an extensional domain at deeper crustal levels (Fig. 3.8 and 3.9). The rheological differences

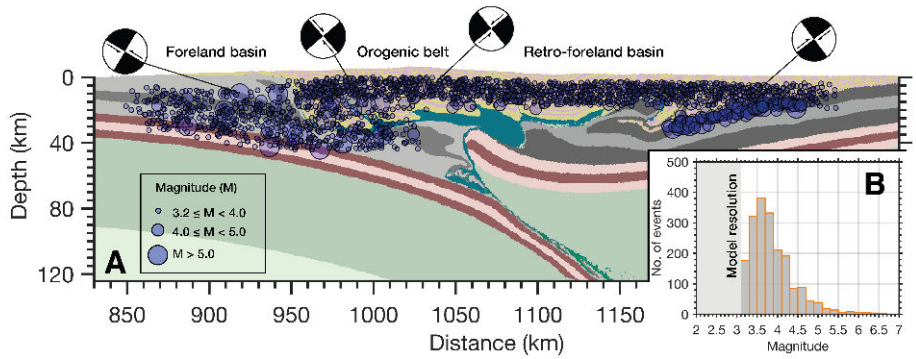


Figure 3.8.: Short-term seismicity pattern of the reference model. **A**: Composition shows a broad orogen marked by nappe stacking in the core of the orogen, crustal delamination beneath the foreland basin and crustal shortening in the retro-foreland basin. The spatial evolution of seismicity and the inferred focal mechanisms display a broad pattern of different style of faulting, which are consistent with the local tectonic regime. **B**: Histograms of all events and the corresponding magnitude.

between the lower crust and the brittle upper crust explain the peculiar rheological characteristics of the downgoing plate (Fig. 3.10). These results illustrate how the long-term tectonic evolution and crustal properties affect the architecture of the orogen and thereby their short-term spatial distribution of seismicity.

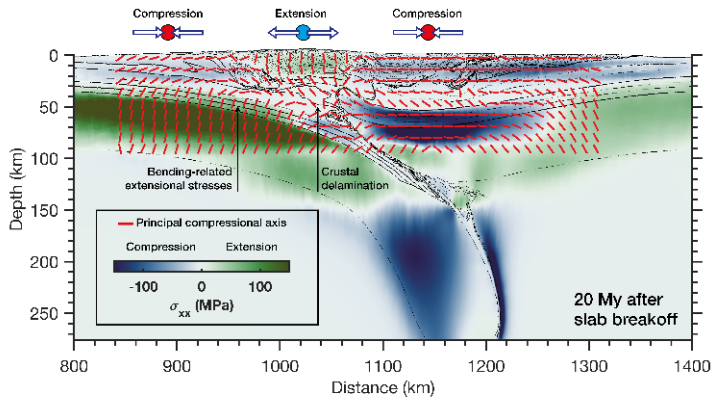


Figure 3.9.: Analysis of the coupled collision reference model and rheological behavior of rocks at 41.5 My (20 My after slab breakoff). Color scale corresponds to the magnitude of normal stress (σ_{xx}). Red axes indicate orientations of maximum (compression) principal stresses. The inferred stress axes show a broad pattern of different tectonic regimes, which are consistent with the style of faulting and focal mechanisms shown in Fig. 3.8.

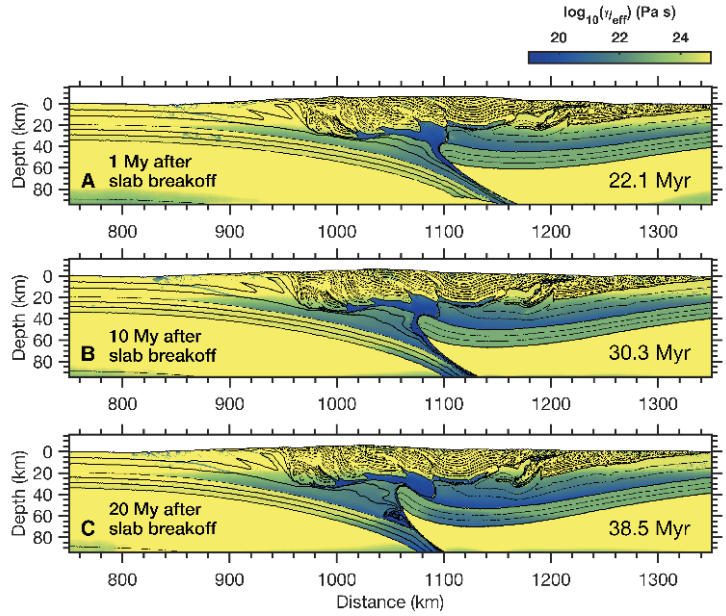


Figure 3.10.: Viscosity field at 1 My (**A**), 10 My (**B**), and 20 My (**C**) after slab breakoff. The rheological differences between the deeper lower crust and the brittle high strength shallow crust illustrate how the long-term tectonic evolution and crustal properties affect the architecture of the orogen and thereby their short-term spatial distribution of seismicity.

3.5 Discussion and Conclusions

Over the last decades, the evolution of the Alpine orogen has mainly been discussed in a kinematic framework (Handy *et al.* , 2010; Schmid *et al.* , 1996). This concept considers the kinematic relative movements between the colliding plates as the major driver of orogenesis, while the vertical forces—exerted by the buoyant crustal root and the subducted slab—have generally been neglected. In contrast, our study demonstrates that the dynamic forces, provided by a SRO model, can potentially explain the construction of an orogen with a pronounced topography and a stack of crustal material even in the absence of any convergence or of hard collision between two continental plates. Moreover, the kinematic concept based on the relative movements between the colliding plates is consistent neither with the current seismic regime nor with first-order isodynamic mass and force balancing approximations, which call for a different geodynamic model.

Our numerical experiments indicate that a rheologically "soft" collision regime facilitated by rollback mechanics can lead to the subduction of continental material. If the crust remains coupled to the downgoing slab, a large buoyancy force is generated. When these deep crustal domains are warmed up, they decouple from the downgoing slab and are subjected to buoyant extrusion and delamination. According to our results, the propagation of the foreland front, coeval with a pervasive crustal delamination—ductile at depth and brittle at shallower levels—suggest a predominant importance of the vertical slab load force. This is accomplished through a self-driven slab rollback, where the sinking rate of the slab is conditioned by the delamination of the crust from the mantle lithosphere as a consequence of bending-related extensional stresses, suction force, and heating of the deep crust. Most importantly, these processes create a positive feedback where delamination of buoyant crustal material from the subducting plate increases the relative importance of the vertical slab load, thus promoting further down warping of the plate. Also, this mechanism not only localizes the extensional stresses at the Moho but also within the crust, with the consequence of intra-crustal seismicity at both shallow and deep crustal levels. We also point out that the retreating collisional regime found in this SRO model is a distinct and dissimilar feature compared to previously investigated post-subduction collisional orogeny models, which are usually characterized by a fixed position of the overriding plate (e.g., Warren *et al.* , 2008; Faccenda *et al.* , 2009; van Hunen & Allen, 2011; Pusok *et al.* , 2018).

In natural convergent margins other aspects may play a relevant role, such as the three dimensionality or magmatism. Magmatism likely affects the distribution of the differential forces and is lacking in our numerical experiments (e.g., Menant *et al.* , 2016). Also, the lateral, third dimension is absent in our numerical model, which does not allow analyzing the role of transtensional/transpressional deformation (e.g., Magni *et al.* , 2017; Pusok *et al.* , 2018). However, while the direct application to the Alpine case may not be warranted at local smaller scale, slab rollback, crustal delamination, surface deformation, and post-orogenic reorganization should be consistent emerging features of interactions between large-scale geodynamic processes and shallow tectonic deformation, analogous to what we present here (Lister *et al.* , 2001; Brun & Faccenna, 2008).

Despite the along-strike variability of the Alpine belt, the results of this study have several important implications at the orogenic scale of the Central Alps. Based on our novel numerical experiments, supported by a chronological pattern of crustal deformation (Schlunegger & Kissling, 2015) and on seismic tomography (Fry *et al.* , 2010), we argue that a SRO model for the European Alps is capable to explain (1) the stacking of nappes, (2) the growth of the buoyant crustal root, (3) the evolution of the Molasse foreland basin, and (4) the current extensional seismicity pattern. This is what we refer to as *Slab Rollback Orogeny* model and it contrasts with the previously published view on the collisional development of the Alps mainly because in our physics-based numerical model, crustal uplift, nappe stacking, and the buildup of topography are solely driven by ongoing rollback and conditioned by the mechanical strength of the subducting slab. In light of these results, while the Himalayas (e.g., Avouac, 2015) and possibly the Andes (e.g., Oncken *et al.* , 2006) serve as much better examples where mountain building processes are driven by the horizontal push of the subducting plate, the understanding of the geologic history of the Central Alps does require an alternative view.

Acknowledgments

This study was funded by the Swiss National Science Foundation Swiss Alp-Array SINERGIA. Numerical simulations were performed on ETH cluster Euler. This paper benefited from discussions with Giacomo Pozzi, Kosuke Ueda, and Alberto Ceccato. Figures were made using perceptually uniform colormaps (Crameri, 2018).

4

Bimodal seismicity in the Himalaya controlled by fault friction and geometry

This chapter is published as:

Dal Zilio L., van Dinther, Y., Gerya, T. V., and Avouac, J. P.

Bimodal seismicity in the Himalaya controlled by fault friction and geometry

Nature communications 10.1 (2019): 48.

4.1 Abstract

There is increasing evidence that the Himalayan seismicity can be bimodal: blind earthquakes (up to $\mathrm{M_w}$~7.8) tend to cluster in the downdip part of the seismogenic zone, whereas infrequent great earthquakes ($\mathrm{M_w}$ 8+) propagate up to the Himalayan frontal thrust. To explore the causes of this bimodal seismicity, we developed a two-dimensional, seismic cycle model of the Nepal Himalaya. Our visco-elasto-plastic simulations reproduce important features of the earthquake cycle, including interseismic strain and a bimodal seismicity pattern. Bimodal seismicity emerges as a result of relatively higher friction and a non-planar geometry of the Main Himalayan Thrust fault. This introduces a region of large strength excess that can only be activated once enough stress is transferred upwards by blind earthquakes. This supports the view that most segments of the Himalaya might produce complete ruptures significantly larger than the 2015 $\mathrm{M_w}$ 7.8 Gorkha earthquake, which should be accounted for in future seismic hazard assessments.

4.2 Introduction

On 25 April 2015, an earthquake with moment magnitude $\mathrm{M_w}$ 7.8 struck the Nepal Himalaya (Avouac *et al.* , 2015; Galetzka *et al.* , 2015; Wang & Fialko, 2015), rupturing a 50-km-wide segment of the Main Himalayan Thrust (MHT) fault (Fig. 4.1a). The 2015 Gorkha earthquake has a similar location as the 1833 earthquake, with estimated magnitude $\mathrm{M_w}$ 7.6–7.7, which also caused significant damage in Kathmandu (Bilham, 1995; Mugnier *et al.* , 2017). The geometry of the MHT is relatively well known in their hypocentral region from various geological and geophysical campaigns (Lavé & Avouac, 2000; Nábělek *et al.* , 2009; Ader *et al.* , 2012). In particular, geodetic data (SAR, InSAR and GPS) and the detailed location of the Gorkha seismic sequence have provided new constraints on the geometry of the MHT (Elliott *et al.* , 2016; Duputel *et al.* , 2016). This information allows us to investigate the relation between interseismic strain and seismicity—given the MHT geometry—and contribute to an ongoing debate on how the Himalayan wedge is deforming. Some authors claim that the location of the front of the high topography could be explained by a mid-crustal ramp along the MHT (Pandey *et al.* , 1995; Lavé & Avouac, 2001; Herman *et al.* , 2010). Conversely, others have argued for active out-of-sequence thrusting at the front of the high Himalaya (Wobus *et al.* , 2005; Whipple *et al.* , 2016). Understanding how and where stresses build up in the Himalaya is important, because evaluating the balance between the interseismic strain accumulation and the elastic strain released during seismic events could potentially improve the seismic hazard assessment in central Nepal following the 2015 earthquake (Bollinger *et al.* , 2016).

It has long be noticed that the seismicity in the Himalaya is bimodal (Ni & Barazangi, 1984; Baranowski *et al.* , 1984; Pandey *et al.* , 1995). Partial (blind) earthquakes (up to $\mathrm{M_w}$~7.8) tend to cluster and repeatedly rupture the deeper portion of the MHT, whereas sporadic great earthquakes ($\mathrm{M_w}$>8) completely unzip the entire width of the seismogenic zone (Fig. 4.1a). The partial ruptures are generally characterised by 10–15 km focal depths and clustered along the front of the Himalaya. They seem to occur in the vicinity of the mid-crustal ramp (Pandey *et al.* , 1995). The $\mathrm{M_w}$ 7.8 Gorkha earthquake is the largest known event in that category. On the other hand, paleoseismological field studies found evidence for

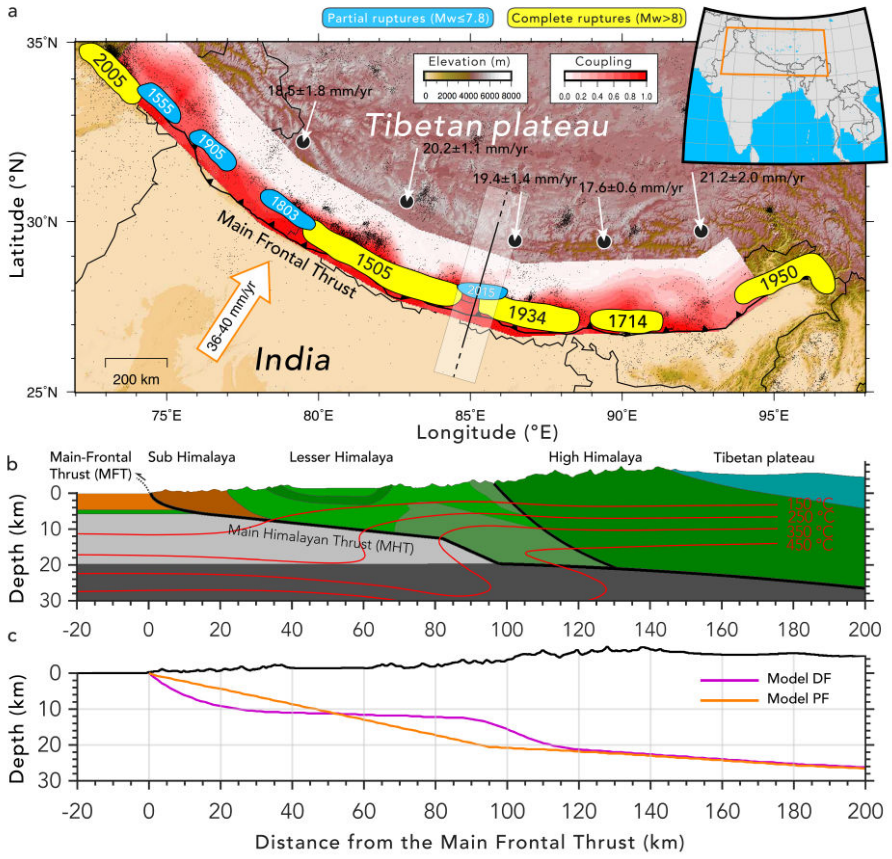


Figure 4.1.: Seismotectonic context, model setup, and fault geometries. **a**, Topographic relief, coupling mode, and historical seismicity. The white arrows show the long-term shortening across the arc. The interseismic coupling is shown as shades of red (Stevens & Avouac, 2015). A coupling value of 1 means the area is fully locked, while a value of 0 means fully creeping. Coloured patches indicate the supposed rupture zones since 1505 (Bilham, 1995; Sapkota *et al.* , 2013; Hetényi *et al.* , 2016a): blue patches display blind ruptures of large ($M_w \leq 7.8$) earthquakes, whereas yellow patches indicate surface ruptures of great ($M_w > 8$) events. Black line indicates the cross-section utilised for the numerical model setup. **b**, Zoom of the initial reference setup (model EF) and temperature. The numerical setup represents the geological cross section of the Nepal Himalaya constrained from the mainshock and aftershocks of the Gorkha sequence (Elliott *et al.* , 2016). **c**, Additional fault geometries employed in the numerical experiments: model DF, from Duputel *et al.* (2016), and a planar fault geometry (Model PF).

surface ruptures at the Himalayan frontal fault (Main Frontal Thrust, MFT), probably associated with great (M_w>8) events (Lavé *et al.* , 2005; Kumar *et al.* , 2010; Hetényi *et al.* , 2016a; Sapkota *et al.* , 2013; Bollinger *et al.* , 2016). The 1934 M_w 8.4 Bihar Nepal (Sapkota *et al.* , 2013; Bollinger *et al.* , 2016) and the 1950 M_w 8.7 Assam earthquake (Chen & Molnar, 1977)—the largest intracontinental earthquake ever recorded—probably fall in that category. On the basis of these observations, the mechanism driving bimodal behaviour remains poorly understood. One potential explanation is that the MHT consists of along-dip subsegments that rupture—either independently or jointly with neighbouring segments during larger earthquakes—with a non-periodic or even chaotic behaviour arising from stress transfers. This segmentation may partly be controlled by rheological (Huc *et al.* , 1998) and geometrical complexities such as local non-planarity (Hubbard *et al.* , 2016; Qiu *et al.* , 2016; Mugnier *et al.* , 2017). There is also growing evidence that fault frictional properties are also an influential and perhaps determining factor that affect the spatial extent, size, and timing of megathrust ruptures (Kaneko *et al.* , 2010). Dynamic simulations over multiple earthquake cycles with a linear slip-weakening friction law show that a large event that ruptures the entire fault is preceded by a number of small events with various rupture lengths (Duan & Oglesby, 2005). These results are in keeping with dynamic modelling of the seismic cycle based on rate-and-state friction, which produce partial ruptures even in the case of a planar fault with uniform frictional properties (Michel *et al.* , 2017). However, how complete ruptures relate to partial ruptures and the geometry and mechanical properties of the MHT, has not yet been investigated quantitatively.

Here we report use a novel two-dimensional (2D) numerical approach (Methods section) to explore the seismic rupture pattern on the MHT over many earthquake cycles (Fig. 4.1b). The geometry and mechanical properties of our model are defined based on constraints from structural geology and geophysical campaigns (Nábělek *et al.* , 2009) and new insights gained from studies of the Gorkha sequence (Avouac *et al.* , 2015; Elliott *et al.* , 2016; Mugnier *et al.* , 2017; Duputel *et al.* , 2016). The temperature distribution is based on a thermokinematic model derived from thermochronological and thermobarometric data (Herman *et al.* , 2010). The model is kinematically driven using a boundary condition that translates into a convergence rate of 38 mm yr^{-1} across the collisional system. The reference geometry of the

MHT (Fig. 4.1b) is inferred from Elliott *et al.* (Elliott *et al.* , 2016) and denoted as Model EF. It is comprised of three segments to reflect the ramp-flat-ramp geometry: a shallow ~30° dipping ramp between the surface and 5-km-depth constrained by structural sections; a flat portion with a shallow angle reaching, finally, a steeper mid-crustal ramp (Cattin & Avouac, 2000). Uncertainties regarding the geometry of the MHT still exist, and relatively gentle variation in geometry have also been proposed (Duputel *et al.* , 2016). We therefore also perform numerical experiments considering this alternative, smoother fault model (Model DF; Fig. 4.1c). To test the sensitivity of the model to the fault geometry, we consider a simple planar fault as well (Model PF; Fig. 4.1c). For each of the three fault geometries adopted, we execute a parameter study of the fault frictional properties by testing values of effective static fault friction (that is, static friction (μ_s) including pore-fluid pressure: $\mu_{eff} = \mu_s\ (1-\lambda)$) between 0.06 and 0.2. This range is consistent with the results of a compilation of previously published data (Avouac, 2015). A detailed description of the numerical technique, model setup, modelling procedure and limitations is given in the Methods section.

4.3 Methods

4.3.1 Seismo-Thermo-Mechanical methodology

The two-dimensional (2D) seismo-thermo-mechanical (STM) code uses an implicit, conservative finite difference scheme on a fully staggered Eulerian grid in combination with a Lagrangian marker-in-cell technique (Gerya & Yuen, 2007). The code solves for the conservation of mass for an incompressible material, momentum and energy. The advection of transport properties including viscosity, plastic strain and temperature is performed with the displacement of Lagrangian markers. The following three mechanical equations are solved to obtain the horizontal and vertical velocities, v_x and v_z, and pressure P (defined as the mean stress):

$$\frac{\partial v_x}{\partial x} + \frac{\partial v_z}{\partial z} = 0 \tag{4.1}$$

$$\frac{\partial \sigma'_{xx}}{\partial x} + \frac{\partial \sigma'_{xz}}{\partial z} - \frac{\partial P}{\partial x} = \rho \frac{Dv_x}{Dt} \tag{4.2}$$

$$\frac{\partial \sigma'_{zz}}{\partial z} + \frac{\partial \sigma'_{zx}}{\partial x} - \frac{\partial P}{\partial z} = \rho \frac{Dv_z}{Dt} - \rho g \tag{4.3}$$

where ρ is density, σ'_{ij} are deviatoric stress tensor components, and g = 9.81 m/s^2 is the vertical component of the gravitation acceleration. The momentum equations include the inertial term to stabilize high-coseismic slip rates at low time steps. A time step of 1 year, however, reduces our formulation to a virtually quasi-static one. Ruptures during the resulting events hence represent the occurrence of rapid threshold-exceeding slip during which permanent displacement and stress drop occur along a localised interface. The energy equation describes the balance of heat in a continuous medium and relates temperature changes due to internal heat generation, as well as with advective and conductive heat transport (Gerya, 2010). The Lagrangian form of energy equation solves for the temperature T:

$$\rho C_p \frac{DT}{Dt} = \frac{\partial}{\partial x_i}\left(k \frac{\partial T}{\partial x_i}\right) + H_\mathrm{r} + H_\mathrm{s} \tag{4.4}$$

where C_p is isobaric heat capacity, k is thermal conductivity, H_r is radioactive heat production and H_s is shear heat production during non-elastic deformation, as follow:

$$H_\mathrm{r} = \mathrm{cst.}; \tag{4.5}$$

$$H_\mathrm{s} = \sigma'_{ij}\ \dot{\varepsilon}_{ij,\ vp}; \tag{4.6}$$

where H_r is a constant value for each rock type, $\dot{\varepsilon}_{ij,\ vp}$ is the visco-plastic component of the deviatoric strain rate tensor.

4.3.2 Rheological model

The fundamental equations 4.1–4.4 are solved using constitutive relations that relate deviatoric stresses and strain rates in a nonlinear visco-elasto-plastic manner:

$$\dot{\varepsilon}_{ij} = \frac{1}{2G}\frac{D\sigma'_{ij}}{Dt} + \frac{1}{2\eta}\sigma'_{ij} + \begin{cases} 0 & \text{for } \sigma'_{II} < \sigma_{yield} \\ \chi \frac{\partial \sigma'_{II}}{\partial \sigma'_{ij}} = \chi \frac{\partial \sigma'_{ij}}{2\sigma'_{II}} & \text{for } \sigma'_{II} = \sigma_{yield} \end{cases} \tag{4.7}$$

where G is shear modulus and η is effective viscosity. $D\sigma'_{ij}/Dt$ is the objective co-rotational time derivative solved using a time explicit scheme (Gerya, 2010) and $\sigma_{II} = \sqrt{{\sigma'_{xx}}^2 + {\sigma'_{xz}}^2}$ is the second invariant of the deviatoric stress tensor, and χ is a plastic multiplier connecting plastic strain rates and stresses. Introducing a visco-plastic viscosity(η_{vp}), we can rewrite equation 4.7 as:

$$\sigma'_{ij} = 2\eta_{vp} Z \dot{\varepsilon}_{ij} + \sigma_{ij}(1 - Z) \tag{4.8}$$

where Z is the visco-elasticity factor:

$$Z = \frac{G\Delta t_{comp}}{G\Delta t_{comp} + \eta_{vp}} \tag{4.9}$$

where Δt_{comp} is the computational time step.

The plastic behaviour is taken into account assuming a non-associative Drucker-Prager yield criteria (Prager & Drucker, 1952). Plastic flow is evaluated at each Lagrangian marker if σ'_{II} reaches the local pressure dependent yield strength σ_{yield}:

$$\sigma_{yield} = C + \mu_{eff} P \tag{4.10}$$

where C is the cohesion.

An important component in the yield criterion is the friction coefficient. Following the approach in van Dinther *et al.* (2013b), we apply a strongly rate-dependent friction formulation (Ampuero & Ben-Zion, 2008), in which the effective friction coefficient

μ_{eff} depends on the visco-plastic slip velocity $V = (\sigma_{yield}/\eta_m)\Delta x$, in which η_m is the local viscosity from the previous time step and Δx is the Eulerian grid size:

$$\mu_{eff} = \mu_s(1-\gamma) + \mu_s \frac{\gamma}{1+\frac{V}{V_c}} \tag{4.11}$$

$$\gamma = 1 - (\mu_d/\mu_s) \tag{4.12}$$

where μ_s and μ_d are static and dynamic friction coefficients, respectively, V_c is the characteristic velocity, namely the velocity at which half of the friction change has occurred, and γ represents the amount of slip velocity-induced weakening if $\gamma = 1-(\mu_d/\mu_s)$ is positive, or strengthening if γ is negative.
When plastic yielding condition is locally reached we require a constant second invariant of deviatoric stresses (assuming the absence of elastic deformation)

$$\text{if} \quad \sigma'_{II} = \sigma_{yield} : \left\{ \quad \frac{D\sigma'_{II}}{Dt} = 0, \quad \dot{\varepsilon_{ij}}^{elastic} = 0 \right\} \tag{4.13}$$

then the stress components are similarly (i.e., isotropically) corrected so that

$$\sigma'_{ij} = \sigma'_{ij} \cdot \frac{\sigma_{yield}}{\sigma'_{II}} \tag{4.14}$$

Accordingly, the local viscosity-like parameter η_{vp} decreases to weaken the material and to localise deformation

$$\eta_{vp} = \eta \frac{\sigma'_{II}}{\eta\chi + \sigma'_{II}} \tag{4.15}$$

where

$$\chi = 2(\dot{\varepsilon_{II}} - \dot{\varepsilon_{II}}^{viscous}) = 2(\dot{\varepsilon_{II}} - \frac{1}{2\eta}\sigma'_{II}) \tag{4.16}$$

and

$$\dot{\varepsilon_{II}} = \sqrt{\dot{\varepsilon_{xx}}^2 + \dot{\varepsilon_{xz}}^2} \tag{4.17}$$

Finally the visco-plastic viscosity η_{vp} is corrected during plastic deformation:

$$\eta_{vp} = \frac{\sigma_{yield}}{2\dot{\varepsilon_{II}}} \tag{4.18}$$

On the other hand, if the plastic yielding condition is not satisfied, this means that the material is under elastic and/or viscous deformation (i.e., diffusion and/or dislocation creep), therefore $\eta_{vp} = \eta$.

4.4 Model setup

4.4.1 Model configuration and boundary conditions

The initial 2D model setup consists in a 1000 x 250 km computational domain (Fig. 5.2). The visco-elasto-plastic thermomechanical parameters of these lithologies are based on a range of laboratory experiments and are listed in Table 4.1. The models use a grid resolution of 1491 x 404 nodes with variable grid spacing. This allow a high resolution of 200 m in the area subjected to largest deformation. More than 35 million Lagrangian markers carrying material properties were used in each experiment. Velocity boundary conditions are free slip with the exception of the permeable lower boundary along which infinity-like external free slip and external constant temperature conditions are imposed implying free slip and constant temperature condition to be satisfied at 1000 km below the bottom of the model (Burg & Gerya, 2005).

The free surface boundary condition atop the crust is implemented by using a "sticky-air" layer (Schmeling *et al.* , 2008) with low density (1 kg/m^3) and viscosity (10^{17} Pa s). A prescribed convergence rate of 38 mm yr^{-1} is imposed on the left boundary, as inferred from several GPS campaigns (Wang *et al.* , 2001). This allows the subducting Indian plate to converge underneath the Asian upper plate. The model accounts for shear heating (see Methods, eq. 6) and for solid–solid phase transitions, such as the process of eclogitization, which has been shown to be an important component of the overall buoyancy budget of the underthrusting Indian lower crust (Hetényi *et al.* , 2007). These phase transitions are parameterised as a function of thermodynamic state variables (P, T, V) and composition by using polynomials to interpolate the reaction boundary (Faccenda & Dal Zilio, 2017).

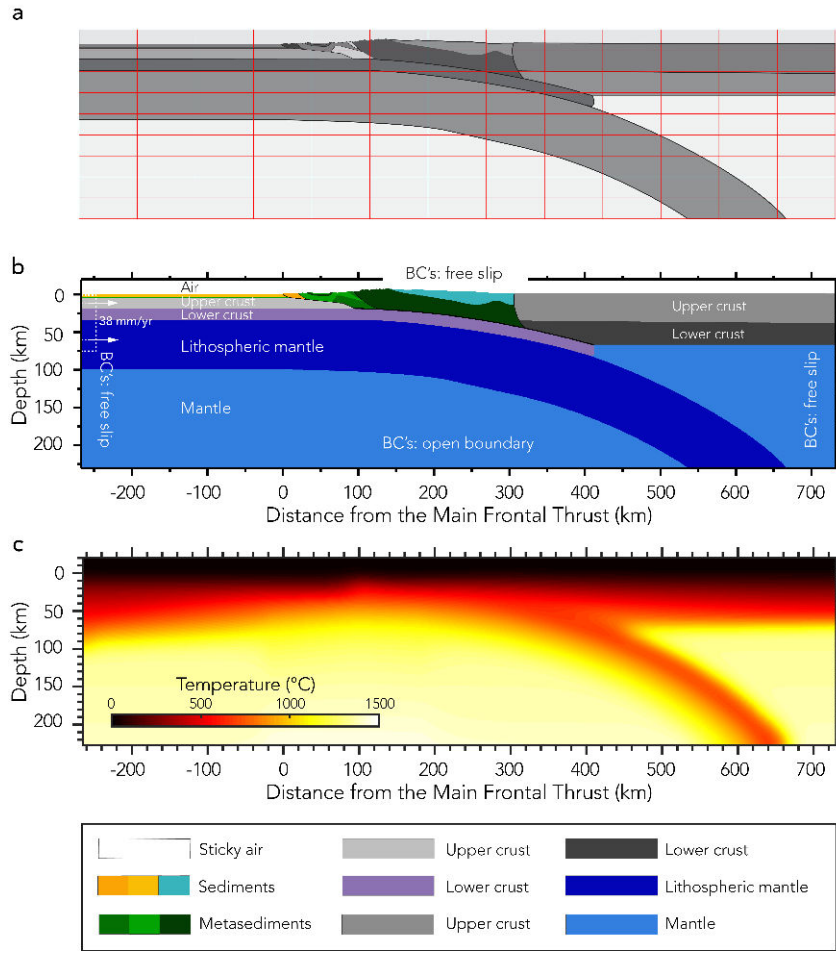


Figure 4.2.: Initial model configuration, depicting the (**a**) initial geometry, (**b**) composition including mechanical boundary conditions, and (**c**) temperature distribution for the entire modelling domain. Horizontal distance is from the Main Frontal Thrust. Bottom figurations clarify different rock types.

4.4.2 Initial geometry

Our proposed initial geometry of the India–Asia collision is based on the crustal data (Laske *et al.* , 2001) and geophysical constraints (Nelson *et al.* , 1996; Brown *et al.* , 1996; Nábělek *et al.* , 2009), and is also consistent with geomorphic and geologic structural constraints (Lemonnier *et al.* , 1999; Lavé & Avouac, 2000; Hetényi *et al.* , 2007; Ader *et al.* , 2012; Avouac, 2015; Elliott *et al.* , 2016). The initial setup

Material	*Flow law*	ρ_0 ($kg\ m^{-3}$)	E_a ($kJ\ mol^{-1}$)	V_a (J/bar)	n	η_0 ($Pa^n\ s$)	Hr ($\mu W m^{-3}$)	G (GPa)	μ_s
Fault rock (MHT–fault)	Wet Qz[a]	2750[b]	154[b]	0.8[b]	2.3[b]	1.97 x 10^{17} [b]	2.5[a]	20[k]	0.06–0.2[f,i,j]
Sediments (Ganga Plain)	Wet Qz[b]	2600[h]	154[b]	1.2[b]	2.3[b]	1.97 x 10^{17} [b]	2.25[a,e]	25[g,k]	0.35
Metasediments (Himalayan wedge)	Wet Black Hills Qz[c]	2700[c]	223[c]	0.8[b]	2.3[b]	1.97 x 10^{17} [b]	2.2[f]	25[g,k]	0.45[l]
Tethyan sediments (Tibetan Plateau)	Wet Qz[b]	2750[b,e]	154[b]	0.8[b]	2.3[b]	1.97 x 10^{17} [b]	1.0[a,e]	25[g,k]	0.50[m]
Upper cont. crust (India)	Granite[d]	2670[e]	190[c]	0.8[b]	3.3[c]	1.97 x 10^{17} [b]	2.25[a,e]	25[g,k]	0.60[m]
Lower cont. crust (India)	Diabase[d]	2900[d,e]	276[c]	0.8[b]	3.0[c]	1.25 x 10^{21} [b]	0.4[a,e]	25[g,k]	0.60[m]
Upper cont. crust (Eurasia)	Wet Qz[b]	2670[e]	154[b]	0.8[b]	2.3[b]	1.97 x 10^{17} [b]	1.00[a,e]	25[g,k]	0.50[m]
Lower cont. crust (Eurasia)	Dry–Mar Diabase[c]	2775[e]	238[c]	0.8[b]	4.7[b]	4.8 x 10^{22} [b]	1.50[a,e]	25[g,k]	0.60[n]
Mantle (India/Eurasia)	Olivine[b,d]	3300[b,h]	532[b]	0.8[b]	3.5[b]	3.98 x 10^{16} [b]	0.0022[h]	67[g,k]	0.60[n]

Table 4.1.: Thermo-mechanical visco-elasto-plastic parameters and flow laws corresponding to the adopted lithologies are based on a range of laboratory experiments, previously used data sets, and geological and geophysical constraints. ρ_0 is the reference density, E_a is the activation energy, V_a is the activation volume, n is the stress exponent, η_0 is the reference viscosity, Hr is the radiogenic heat production, G is the shear modulus, and μ_s is the static friction coefficient. Other properties for all rock types: cohesion C = 10 MPa [i], specific heat capacity C_p = 1000 J kg^{-1} K^{-1}, thermal conductivity K = 2.5 $Wm^{-1}K^{-1}$ [a], thermal diffusivity κ = 10^{-6} m^2 s^{-2} [a]; thermal expansion α_ρ= 2.4x10^{-5} K^{-1} [a] and compressibility β_ρ=2x10^{-11} MPa^{-1} [a].

References: *a*) Bollinger *et al.* (2006); *b*) Ranalli (1995); *c*) Gleason & Tullis (1995); *d*) Burg & Podladchikov (1999); *e*) Hetényi *et al.* (2007); *f*) Herman *et al.* (2010); *g*) van Dinther *et al.* (2013b); *h*) Turcotte & Schubert (2002); *i*) Cattin & Avouac (2000); *j*) Bollinger *et al.* (2004); *k*) Gillespie *et al.* (1992); *l*) Hirose & Bystricky (2007); *m*) Di Toro *et al.* (2011); *n*) Del Gaudio *et al.* (2009).

consists of a ~600-km-long Indian plate (on the left, Fig. 5.2) underthrusting the fixed overriding Asian plate (on the right) and the Himalayan wedge. The Indian upper crust is made of a thick layer of sediments (4-km-thick) and crystalline rocks (16-km-thick), overlying a 16-km-thick lower crust and a 65-km-thick lithospheric mantle. On the other side, the Eurasian plate is made of a very thick upper crust (36-km-thick) and lower crust (30-km-thick) due to crustal shortening and thickening. The tectonic architecture of the Himalayan wedge is instead more complicated, since it represents the impingement of the Indian continental margin on the Eurasian plate. The Himalayan fold-and-thrust belt is here divided into four lithotectonic units: the Sub-Himalaya, the Lesser Himalayan, the Higher Himalaya and the Tibetan Plateau. The geometry of the MHT across the Himalaya has been

derived from geophysical observations and surface geology. The frontal part of the fault system is well constrained from balanced cross sections across the Siwalik fold-and-thrust belt and some gravity and magnetotelluric data (Lavé & Avouac, 2000; Hetényi *et al.* , 2006). These data show that the MFT, the MBT and the intervening thrust faults all root into a 5–7 km deep décollement at the top of the underthrusted Indian basement. The décollement probably extends beneath the front of the Higher Himalaya, as indicated from a zone of high conductivity that has been interpreted as sediments dragged along the décollement (Lemonnier *et al.* , 1999). This décollement constitutes the sole of the Himalayan wedge and is usually called Main-Himalayan-Thrust (MHT) fault. The décollement extends beneath the Lesser Himalaya at depth of 7–12 km, and connects with a midcrustal ramp (12–22 km depth) beneath southern Tibet. This midcrustal ramp has been proposed in a number of previous studies (Cattin & Avouac, 2000; Avouac, 2003; Bollinger *et al.* , 2004) and is in agreement with recent slip inversions after the Gorkha event (Elliott *et al.* , 2016). This deeper ramp then roots into a shallow north-dipping shear zone of aseismic deformation, coinciding with the deeper portion of the MHT imaged from various seismological experiments (Nelson *et al.* , 1996; Nábělek *et al.* , 2009). This complicated 2D geometry is then transferred into the computational domain by using GeoMAC (Geo-Mapping And Converting tool), a C–based tool that allows for resampling and converting drawings into material properties. Hence, GeoMAC converts 2D vector drawings based on geological profiles, seismic data, tomography models and other geophysical constraints, by assigning material phases to Lagrangian markers inside the large-scale tectonic shapes.

4.4.3 Friction properties on the Main Himalayan Thrust

Several constraints indicate that the friction on the MHT is low (Avouac, 2015). For instance, recent thermometric and thermochronological data from the central Nepal suggest that the shortening across the range has been taken up primarily by thrusting along the Main Himalayan Thrust fault, with negligible internal shortening of the Himalayan wedge (Herman *et al.* , 2010). These data thus suggest that

friction along the MHT is ~0.07, which is in agreement with the observed pattern of erosion and the present morphology of the Himalayan range (Avouac, 2015; Lavé & Avouac, 2001). Also, given the slope of the Himalayan wedge and the dip angle of the MHT beneath the Lesser Himalaya, the effective basal friction on the flat portion of the MHT is inferred to be smaller than 0.12 (Cattin & Avouac, 2000). This is in keeping with previous numerical models, which require a basal effective friction less than 0.13. This value is consistent with the previous analysis of Davis *et al.* (Davis *et al.* , 1983) that, considering the whole Himalayan wedge (which has a steeper slope), results in a larger effective basal friction of 0.25. Another constrain comes from relationship between the topographic elevation and the cutoff in the microseismic activity, which is used to infer the shear stress on the fault. Since the décollement lies at a depth of ~10 km and the inferred shear stresses cannot exceed 35 MPa, this corresponds to a friction of ~0.1 (Bollinger *et al.* , 2004).

4.4.4 Temperature distribution

The thermal structure of both Indian shield and Asia (Fig. 5.2c) are calculated from the steady-state continental geotherm (Turcotte & Schubert, 2002). The initial thermal gradient is set using values of 273 K at the top and 1617 K at the bottom of the lithosphere, whereas within the mantle was quasi-adiabatic (0.5 K/km). The thermal structure within central Nepal is computed using the thermokinematic model proposed in Bollinger Bollinger *et al.* (2006) and updated in Herman *et al.* (2010). The formal inversion suggests a radiogenic production of 2.2 $\mu W m^{-3}$ for the Higher and Lesser Himalayan units and a value of 0.8 $\mu W m^{-3}$ for the middle and lower crust of India (Herman *et al.* , 2010), which are used for the corresponding lithologies of our numerical model. This latter was obtained from a formal inversion of the large data set of thermochronological and thermobarometric data available from central Nepal. The topography is assumed to be steady state. The model fits the data and shows a transition from brittle to ductile rheologies at a temperature of about 400–450°C, corresponding to about 18-km-depth on the Main Himalayan Thrust.

4.5 Modelling procedure

The STM modelling approach adopted for this study comprises two steps. Prior to the first modelling stage, we define the initial geometry, rock properties, temperature distributions, and the boundary conditions. During the first stage, which utilises a time step of 100 years, the stress builds up and all the physical properties iterate up to reach a isostatic equilibrium. Stress build up occurs as the strain is accumulated. Differential loading due to rheological discontinuities, tectonic asperities, temperature, and viscosity distribution causes heterogeneous stress localisation in the Himalayan wedge (Fig. 4.3). In the second modelling stage, the time step progressively decreases to approach a final value of 1 year, while the inertia term and rate-dependent friction are activated. During the seismic cycle, when the maximum strength is locally reached, the instability is fed through the feedback of decreasing viscosities. This increases slip velocities, which decreases the slip rate-dependent friction and strength, and in turn decreases viscosities even further. Spontaneous rupture propagation occurs because stresses are increased ahead of the rupture front to balance the dropping stresses within the rupture and to thereby maintain a static equilibrium. Finally, healing of strength occurs as slip velocities decrease.

4.6 Modelling limitations

General limitations of our modelling approach are discussed in previous studies, in which the STM models have been applied to subduction (van Dinther *et al.* , 2013b) and collision zones (Dal Zilio *et al.* , 2018b). In nature, earthquake ruptures occur within a three-dimensional, geometrically complex fault system with various scales of downdip and along-strike variations in its seismogenic behaviour. The lateral, third dimension is absent in our numerical model. That means that our two-dimensional plane strain model ignores lateral variations in interseismic stress buildup and rupture propagation. Compared to nature our model produces unrealistically long seismic events because of the large time step (i.e., 1 yr). This means that a simulated event or earthquake refers to the occurrence of rapid threshold-

exceeding slip during which permanent displacement and stress drop occur along a localised interface. On the other hand, the presented results generally demonstrate a satisfactory agreement with a wide range of long- and short-term natural observations in the Himalaya. Events in our numerical model have reasonable downdip extension, similar behaviour and comparable surface displacement. However, is important to stress that our incompressible inertial formulation does not account for the full inertial dynamics. Also, we acknowledge that modelling pressure and shear waves might impact part of our results. In spite of these limitations, our simulations mostly cover new ground, as yet unexplored, not only as far as the bimodal seismicity is concerned but also how short-term seismic processes are related to the long-term interseismic deformation.

4.7 Results

4.7.1 Consistency with interseismic deformation

An important goal in Himalayan studies over the past decades has been to refine the Himalayan convergence rate (Bilham *et al.* , 1997; Bettinelli *et al.* , 2006), because this is responsible for the productivity of Himalayan earthquakes (Bilham *et al.* , 2001; Avouac, 2015). We emulate the observed velocity field by imposing a convergence rate of 38 mm yr^{-1}. The model produces about 19–20 mm/yr of convergence across the Himalaya, a value consistent with the long term geological rate, while the residual convergence rate is dissipated by deformation distributed outside the domain shown in Figure 4.1b. The model fits the geodetic measurements of interseismic strain remarkably well (Fig. 4.3a). All three fault geometries yield predictions in good agreement with uplift rates measured from spirit-levelling (Jackson & Bilham, 1994), inSAR (Grandin *et al.* , 2012), and horizontal velocity measured from GPS (Ader *et al.* , 2012) (Fig. 5.5). However, we note that model EF agrees particularly well with the data, in terms of both horizontal and vertical velocities.

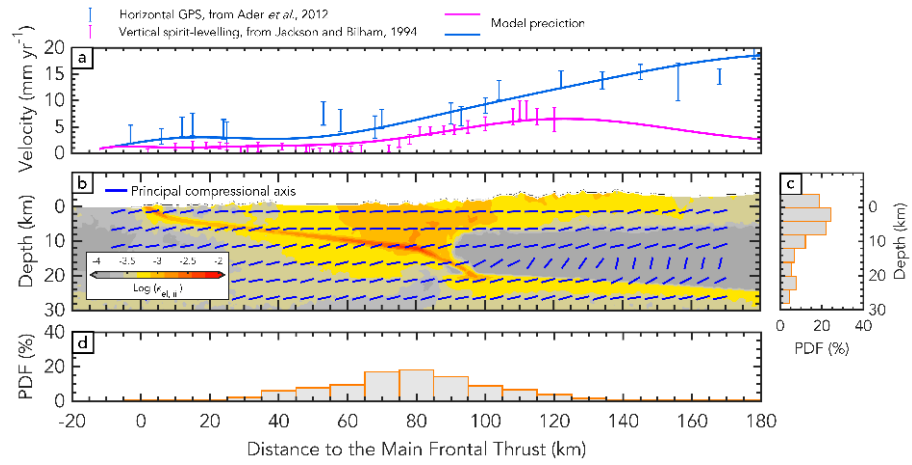


Figure 4.3.: Interseismic behaviour computed in the 2D model (Model EF). **a**, Observed vs. synthetic present-day velocity fields. Observed field (error bars) is shown in blue (horizontal GPS, Ader *et al.* , 2012)) and violet (spirit-levelling, Jackson & Bilham, 1994) bars, respectively. Solid lines show the corresponding horizontal and vertical modelling prediction. **b**, Elastic strain regime across the Himalaya inferred over an interseismic period of 350 yr and orientation of principal compressional axes (blue bars). Histograms in (**c**) and (**d**) show the vertical and horizontal off-megathrust faulting distributions, respectively.

The mid-crustal ramp operates as a geometric asperity during interseismic periods where elastic strain builds up and accounts for as much as two thirds of the convergence rate (Fig. 4.3b).

At greater depth the higher temperature favours the transition from frictionally unstable velocity-weakening behaviour to stable (velocity-strengthening) visco-plastic creep (Fig. 5.6). Visco-plastic strain rates show a sub-horizontal shear zone in the middle-lower crust, which corresponds to the aseismic creep along the MHT. Distributed viscous deformation also occurs in the vicinity of the kink along the MHT ramp-flat geometry (Fig. 4.3b). Another constraint on the simulated tectonic deformation comes from the off-megathrust events. The model shows that anelastic strain off the MHT tends to cluster beneath the topographic front of the Higher Himalaya (Fig. 4.3c,d). In fact, most of these events concentrate in a narrow zone near the edge of the mid-crustal ramp, which correlates well with the microseismicity observed over the past decades (Pandey *et al.* , 1995). This off-megathrust earthquake activity also shows a cut-off beneath the Higher Himalaya, which corresponds to the region where the viscous deformation is dominant and the axes of principal compressional stresses (σ_1) become (sub-)vertical.

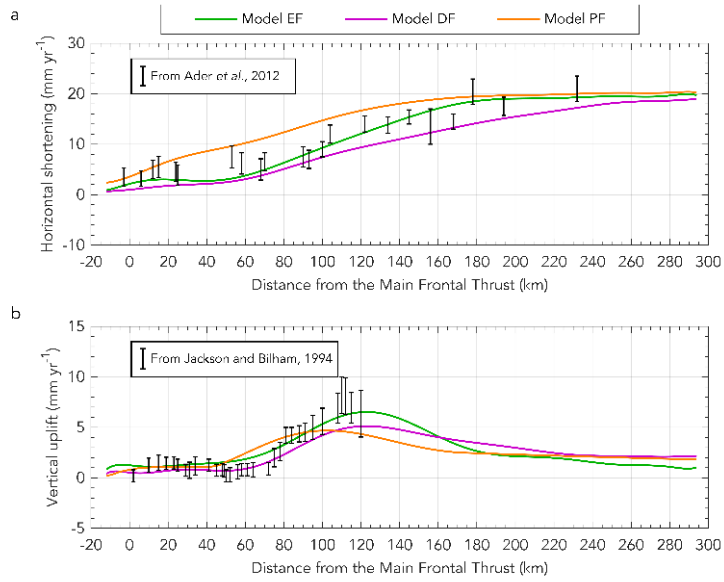


Figure 4.4.: Observed and synthetic present-day velocity fields for the Himalaya and southern Tibetan plateau. Black error bars indicate the horizontal and vertical observed fields. Synthetic fields are shown in orange, green and blue for the three MHT geometries employed. The models are driven by a background convergence rate of 38 mm yr^{-1} (Wang *et al.* , 2001).

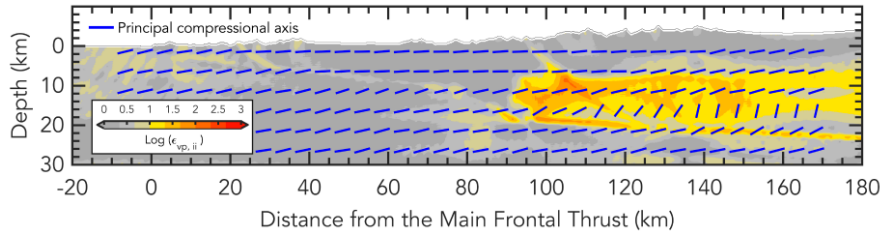


Figure 4.5.: Visco-plastic component of strain computed over the long-term interseismic deformation. It shows a sub-horizontal shear zone that closely follows the midcrustal reflector imaged by the INDEPTH experiment (Zhao *et al.* , 1993).

4.7.2 Bimodal earthquake behaviour of the reference model

Despite the 2D limitations, the reference model produces a rich earthquake behaviour, similar to that of natural faults. The spatiotemporal evolution of slip velocity of the reference model shows how coseismic slip events are released on the MHT-fault (Fig. 4.6a). Although the whole seismogenic zone is interseismically nearly fully locked, most of the simulated earthquakes nucleate and propagate only in

the lower edge of the locked Main Himalayan Thrust, whereas only a few events unzip the whole flat-and-ramp system. The largest events tend to have similar size and recur quasi periodically every ~1250 yr. Between them, a range of smaller events occurs, which release only small fraction of the accumulated strain energy. Using a rupture width–moment magnitude scaling law (Wells & Coppersmith, 1994), the moment magnitude of partial ruptures is estimated to $\mathrm{M_w}$~7.4–7.8 (Fig. 4.6b). Such cluster of differently-sized partial ruptures leads up to a final complete failure of the MHT. These complete ruptures are the largest events with an estimated moment magnitude in the order of $\mathrm{M_w}$~8.3–8.4 (Fig. 4.6b).

To investigate the physical mechanism behind this behaviour, we analyse the spatiotemporal evolution of the stress and yield strength on the MHT. For example, event E9 (Fig. 4.6a) ruptures only the lower edge of the seismogenic zone and then event E18 is capable of propagating up to the surface. Our analysis indicates that the partial rupture event E9 nucleates close to the downdip limit of the seismogenic zone, before the mid-crustal ramp, where the stress build-up due to tectonic loading is fastest (Fig. 4.6c). The rupture propagation causes a local stress drop (Fig. 4.6d), unzipping only part of the seismogenic zone as it is stopped as a result of a large initial strength excess—that is, difference between stress and yield strength. For this event, we further estimate the slip resulting from the occurrence of such rupture. Our results indicate that event E9 produces ~5–6 m of coseismic slip (Fig. 4.6e), mainly on the deeper flat portion of the MHT, between 10 and 15 km depth.

When only the downdip edge of the locked zone is unzipped, stress is transferred to the neighbouring updip region by a static stress transfer. Then the next downdip event nucleates sooner than expected from the average recurrence periods, with this new rupture being generally larger than the previous one. This occurs because the strength excess decreases in the frontal part of the MHT, as a result of the stress transfer and the ongoing tectonic loading. Consequently, partial ruptures contribute significantly to build up stresses to a critical level on the updip limit of the MHT, as for example before event E18 (Fig. 4.6f). Once strength excess is low throughout the MHT, a complete event eventually propagates through the whole ramp-flat-ramp fault system and leads to a large stress drop (Fig. 4.6g). These complete ruptures results in slip larger than 8 m (Fig. 4.6h), which is consistent with estimates from paleoseismic investigations (Lavé *et al.* , 2005; Kumar *et al.*

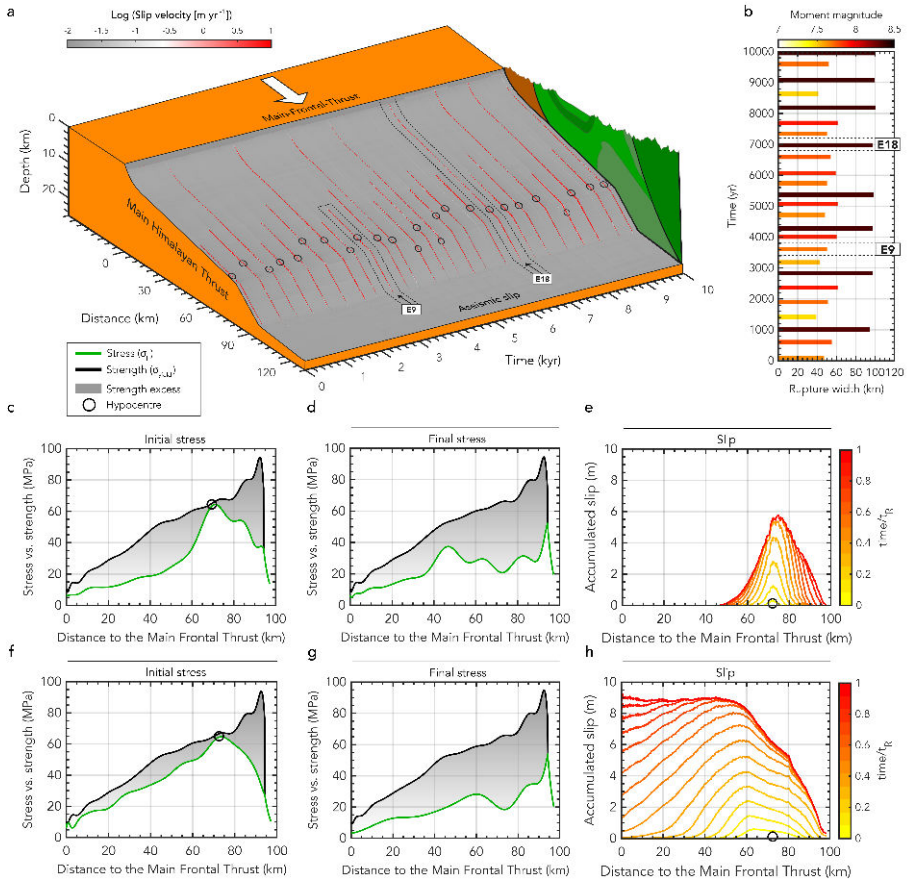


Figure 4.6.: Megathrust behaviour computed in the 2D model (EF) over 10,000 yr. **a**, Spatiotemporal evolution of slip on the MHT for the reference model. Red lines show slip during the simulated earthquakes. Note that hypocenters (black circles) are typically located in the lower edge of the flat segment, just before the mid-crustal ramp. **b**, Time evolution of downdip rupture width. Colorbar indicates the corresponding moment magnitude. **c-d**, Along megathrust profiles of initial (**c**) and final (**d**) stress vs. strength for the partial rupture event E9. **e**, Contours of accumulated coseismic slip throughout event E9. **f-g**, Along megathrust profiles initial (**f**) and final (**g**) stress vs. strength for the complete rupture event E18. **h**, Contours of accumulated coseismic slip throughout event E18.

, 2010; Bollinger *et al.* , 2006). Then a new cycle of partial ruptures begins, with an initial period of quiescence or small events activity (Fig. 4.6). This is exactly what our model shows in Figure 4.6: temporal evolution of the MHT displays a bimodal seismicity-dominated regime. Notably, rupture events are triggered by stress build-up near the downdip end of the locked fault zone, as is observed in nature (Bollinger *et al.* , 2004). Also, the model reproduces a realistic earthquake

sequence of irregular moment magnitude main shocks, including events similar to the 2015 Gorkha earthquake.

This bimodal pattern of large strength excess, low stress drop partial ruptures leading to infrequent low strength excess, high stress drop complete ruptures is also observed when analyzing their non-dimensional stress (S) parameter—that is, the ratio between the average strength excess before an event and the average coseismic static stress drop (Das & Aki, 1977; Herrendörfer *et al.* , 2015) (Fig. 4.8a-c). In terms of this S parameter, complete ruptures thus have relatively low values, while partial ruptures have relatively high values. When studying the kinematic slip evolution of each event, we observe both pulse- and crack-like ruptures (Fig. 5.7). In a pulse-like mode, the local slip duration—also known as rise time—is much shorter than the total duration of the event (Heaton, 1990). On the contrary, shear cracks have an extended slip duration, even after the rupture has reached the surface, in which the rise time scales with final rupture width. Our models thus show that slip-pulses and shear-cracks coexist along the same interface. They occur at marked points in time in relation to the stress state of the interface as defined by the S parameter. Large strength excess, prior to the event, leads to partial ruptures with relatively high S parameter that are pulse-like. These self-healing pulses could be the result of a strongly slip rate-dependent friction formulation that rapidly heals the fault for low characteristic slip velocities (Cochard & Madariaga, 1994). Conversely, relatively low S parameters are observed for complete ruptures that are crack-like. The hypothesis of a different rupture style for each event type is also supported by the identified mechanism of recurrent updip stress transfer toward a critical level (Burridge & Knopoff, 1967; Herrendörfer *et al.* , 2015) combined with results from dynamic rupture simulations that relate the fault stress state (S parameter) and rupture styles (Gabriel *et al.* , 2012). However, due to a low temporal resolution (Δ_t =1 yr) and missing wave-mediated stress transfer, we cannot be sure that the actual stress states at the MHT are such that both crack- and pulse-like ruptures are feasible. In spite of these potential pitfalls, our models show similar features to those observed during the Gorkha earthquake. In particular, the 2015 main-shock was a pulse-like rupture with slip on any given portion of the fault occurring over a short fraction (~10 s) of the total ~70 s duration of the earthquake source (Galetzka *et al.* , 2015).

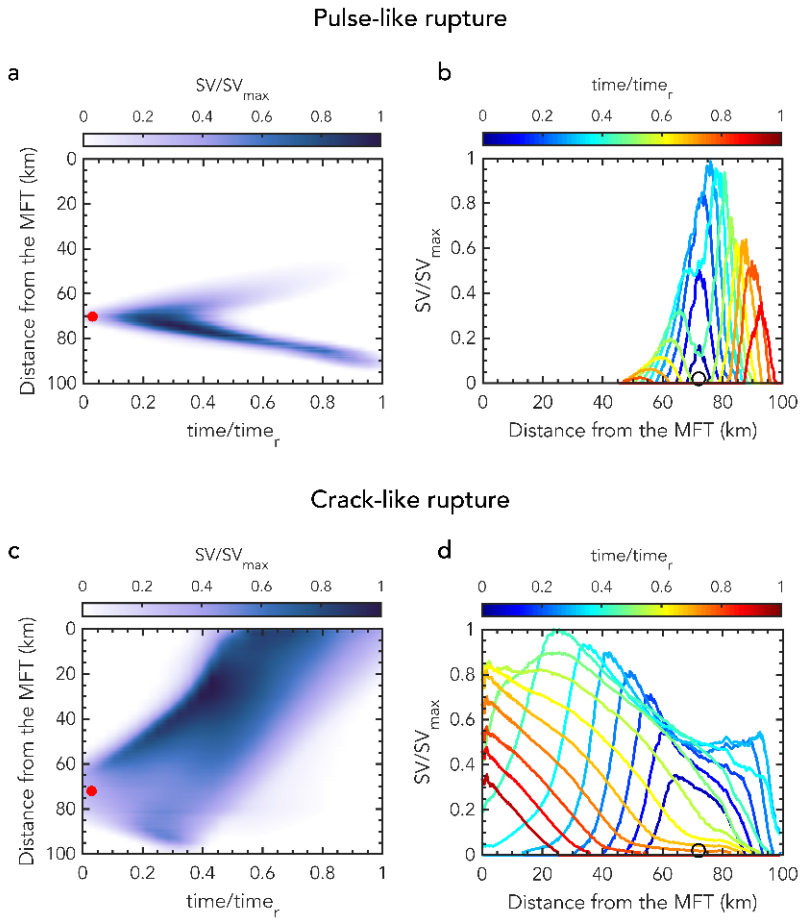


Figure 4.7.: Examples of pulse-like (**a,b**) and crack-like ruptures styles (**c,d**) along the downdip width of the MHT (0–100 km). To compare the rupture styles, the time is scaled by the total rupture time (time$_r$), whereas the slip velocity is scaled by the maximum slip velocity (SV$_{max}$). Evolution of slip velocity through time (left column, panels **a** and **c**) and along the fault (right column, panels **b** and **d**). Full circle indicates the hypocenter. Pulse-like rupture is characterised by a significant self-healing during the rupture propagation. In contrast, a crack-like rupture shows a continuous slip, almost until the end of the rupture.

A particular feature of the Himalayan wedge is the seismic–aseismic transition zone, which seems to coincide with the mid-crustal ramp beneath the front of the high Himalaya (Pandey *et al.* , 1995; Ader *et al.* , 2012). However, the feedback between the geometry and the rheological behaviour of the mid-crustal ramp are difficult to ascertain on the basis of natural observations alone. When a rupture occurs in our simulations, it generally expands upwards from the locked edge,

but not much downwards. This occurs because the zone of aseismic slip acts as an efficient barrier to downdip propagation of ruptures. This self-consistent feature of our models as an effect of the temperature increase with depth, which in turn decreases the viscosity of rocks. Also, our models show that all hypocentre locations fall in a narrow zone near the edge of the mid-crustal ramp (Fig. 4.6a), indicating a pivotal role of this crustal asperity in localising the strain both on and off the megathrust (Fig. 4.3b). Thus, our results suggest that both the geometric-structural and the thermal-rheological strength of the mid-crustal ramp control the downdip rupture width on the MHT.

4.7.3 Effect of fault friction and geometry on seismic ruptures

In our simulations we identify frictional properties and geometry of the MHT as key parameters that influence the emergence of the observed bimodal earthquake pattern. To examine the role of the three MHT fault geometries considered in this study, we first analyse the relation between the S parameter and rupture width of all events when a bimodal seismicity pattern is observed (μ_s=0.16 and γ=0.7; Fig. 4.8a–c). Results from the reference model EF (Fig. 4.8a) indicate that the S parameter decreases with increasing rupture width. Most importantly, we find that this ramp-flat-ramp geometry results in a rupture-width gap between 60–65 km and 90–95 km. A very similar trend is also observed in Model DF (Fig. 4.8b). Pulse-like partial ruptures are confined to a critical width of 60–65 km, whereas large crack-like events propagate through the whole seismogenic zone. Consequently, models EF and DF result in a bimodal distribution of rupture widths. On the other hand, results from the simple planar fault (Fig. 4.8c) indicate that the S parameter decreases linearly with increasing rupture width. This means that the larger the event, the higher the stress released and the resulting S parameter is lower. Although this model displays a wide spectrum of rupture widths, the general pattern does not indicate any bimodal distribution.

We then analyse the average downdip stress vs. strength distribution for the three fault geometries adopted (Fig. 4.8d–f). In general, these profiles suggest that, the steeper the fault dips in the updip region of the MHT, the higher would be

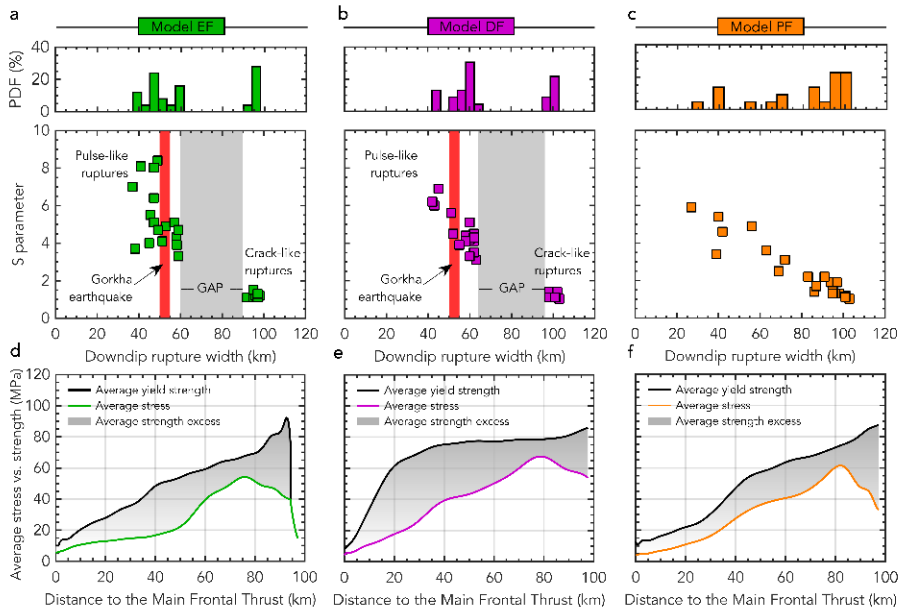


Figure 4.8.: Impact of the three fault geometries on the rupture patterns. Relationship between S parameter and rupture width for models adopting a realistic ramp-flat-ramp fault geometry inferred from Elliott *et al.* (2016) (**a**), Duputel *et al.* (2016) (**b**), which also indicate the dominance of different rupture styles (pulse- vs. crack-like ruptures), and a planar fault geometry (**c**). **d-f**, Along megathrust profiles of the average stress vs. strength for the three fault geometries adopted: model EF (**d**), DF (**e**), and PF (**f**). Our simulations also indicate that, for each partial rupture, the S parameter is generally higher than in dynamic rupture simulationsGabriel *et al.* (2012). This results from the large amount of slip velocity-induced weakening (γ; see Methods section), which is motivated by laboratory experiments at coseismic slip rates (Di Toro *et al.* , 2011).

the pressure-dependent fault strength. This, together with a relatively higher fault friction, increases the fault strength even further. Consequently, the strength excess also increases, and a higher pre-stress is thereby necessary to reach a critical level at which eventually a crack-like event ruptures the entire megathrust. As in the case of model EF (Fig. 4.8d), and even more clearly on model DF (Fig. 4.8e), the strength excess in the shallower region of the MHT is notably high. This behaviour arises because when the model accounts for a ramp-and-flat fault geometry, the far-field tectonic loading is not fast enough to bring the pre-stress up to a critical state in the upper edge of the MHT. Most of the simulated earthquakes are thus capable of rupturing only a fraction of the seismogenic zone. Then, the static stress distribution left over from these previous partial ruptures contribute significantly to increase the stress state in the updip limit of the MHT. On the other hand, the planar

fault geometry (Model PF) maintains a relatively low strength excess throughout the seismogenic zone (Fig. 4.8f), thereby allowing the propagation of frequent complete ruptures.

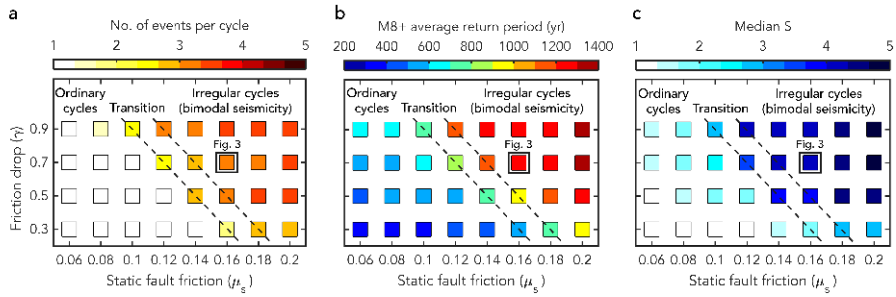


Figure 4.9.: Effect of frictional properties on the seismic behaviour of model EF. Average (**a**) number of events per cycle, (**b**) recurrence time of complete ruptures (M_w>8 events), and (**c**) median of the S parameter. Dashed black lines indicate the transition from ordinary cycles to irregular cycles (bimodal seismicity).

We then explore the effect of static fault friction (μ_s), and of the maximum friction drop from static to dynamic friction coefficient ($\gamma = 1 - \mu_d/\mu_s$) on the resulting bimodal pattern of large earthquakes. Our model produces distinctly different rupture patterns within a narrow range of frictional parameters (Fig. 4.9). In fact, an increase of both the static fault friction and friction drop leads to an increase of the number of events per cycle (Fig. 4.9a), the average recurrence interval between the largest events (Fig. 4.9b), and the median S parameter values (Fig. 4.9c).

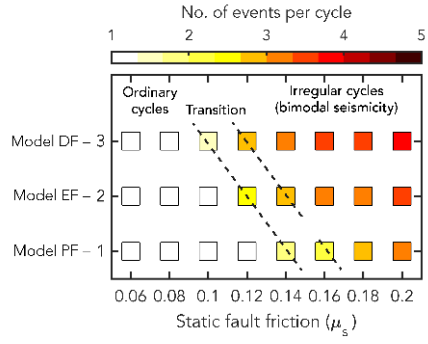


Figure 4.10.: Influence of static fault friction and geometry of the MHT on the number of events per cycle. Dashed line roughly indicates the transition between ordinary cycles and irregular cycles. Black frames indicate reference models and figures.

As illustrated in Figure 4.9, this corresponds to a transition from ordinary (unimodal) cycles to irregular cycles, which display a bimodal seismicity (see also Fig. 5.9). In contrast, the spatiotemporal evolution of the model with a lower static fault friction (μ_s=0.1) shows a more ordinary recurrence pattern of quasi-periodic large events (Fig. 4.11). These events mostly nucleate near the edge of the mid-crustal ramp, propagate both up- and downwards, and typically activate the whole flat-and-ramp system. These ruptures break the entire locked zone of the MHT in a crack-like style, and lead to significant stress drops. Consequently, this model is related to a low median S value (Fig. 4.9c). Thus, these results indicate that the maximum friction drop (γ) can significantly affect the recurrence interval of complete ruptures (Fig. 4.9b) and the average S parameter (Fig. 4.9c), but it cannot prevent the genesis of bimodal seismicity for relatively higher fault friction ($\mu_s \geqslant 0.16$).

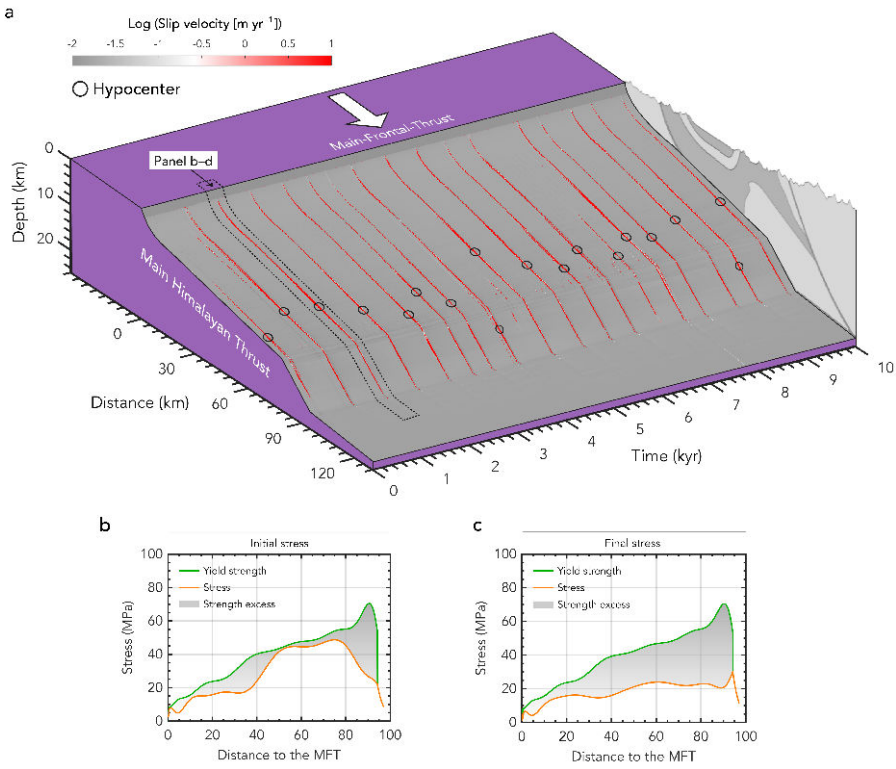


Figure 4.11.: MHT–fault behaviour adopting a lower fault friction (μ_s=0.1). **a**, Spatiotemporal evolution of slip on the MHT. Red lines show slip during the simulated earthquakes. **b-c**, Along interface profiles of (**b**) initial and (**c**) final second invariant of the deviatoric stress tensor and strength of the event highlighted in (**a**).

4.8 Discussion and conclusions

Our simulations show that it is probably incorrect to assume that earthquakes known to have occurred along the Himalayan front over history (Bilham, 2004) are representative of the greatest possible earthquakes. Along many segments, the large historical events probably represent partial ruptures with magnitude significantly lower than what complete ruptures would produce. In our model, the same segment of the MHT can in principle produce a sequence of partial ruptures similar to the Gorkha earthquake and occasionally much larger events, similar to the 1934 $\mathrm{M_w}$ 8.4 event or even larger. This is confirmed by moment conservation calculations at the scale of the Himalayan arc, which require $\mathrm{M_w}$~9 earthquakes with a 800–1000 years return period (Stevens & Avouac, 2016). Our models indicate that a great earthquake ($\mathrm{M_w}$>8) can occur at the same location as a $\mathrm{M_w}\leq$7.8 earthquake, and that it may strike sooner than would be anticipated from considerations of renewal time from plate convergence rates. While we cannot rule out the plausible presence of along-strike heterogeneities given the lack of the third-dimension, our models show that the combined effects of fault geometry and frictional properties in controlling the along-dip bimodal behaviour of the MHT could potentially hold for the entire Himalayan arc. In support of this claim, recent pattern of interseismic coupling on the MHT along the entire Himalayan arc do not indicate any aseismic barrier that could affect the seismic segmentation of the arc and limit the along-strike propagation of seismic ruptures (Stevens & Avouac, 2015) (Fig. 4.1a).

For a finite range of static fault friction (μ_s=0.06–0.2), our model exhibits a large spectrum (250–1500 yr) of recurrence time of great earthquakes. It also shows that an indication for the temporal proximity of such a $\mathrm{M_w}$>8 earthquake can come from the maximum updip limit of the prior, partial earthquake, which provides an indication for a likely critically stressed MHT (Fig. 4.6a). Our results indicate that an average recurrence time of ~600 yr leads to coseismic slip of 8–10 m in order to release the elastic strain accumulated during such interseismic periods. However, partial ruptures account only for an average slip of 4–6 m, in agreement with the average slip of moderate ($\mathrm{M_w}\leq$7.8) Himalayan earthquakes such as the Gorkha earthquake (Elliott *et al.* , 2016).

Finally, it appears that the static stress change due to partial ruptures is the major factor introducing irregularity in the seismic cycle. This is the main reason that could explain why the model obeys neither the slip- nor time-predictable behaviour at any given point on the fault (Fig. 4.12), since it does not incorporate a fixed threshold shear stress for slip to occur. This is because, after each earthquake, the stress on the ruptured area drops to a low level, approximately determined by the rate-dependent friction formulation evaluated at the coseismic slip rate.

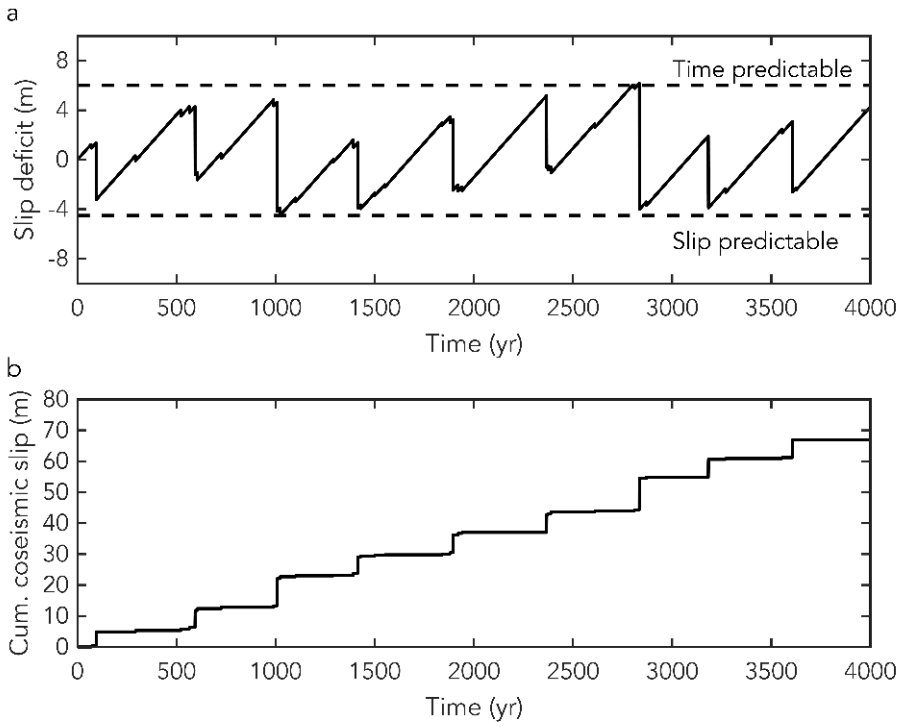


Figure 4.12.: An example of long-term fault behaviour computed in the 2D model (Model EF shown in Fig. 4.1). **a**, Time evolution of slip deficit of the MHT. Dashed lines illustrate that the model is neither time nor slip predictable. **b**, Cumulative coseismic slip against time.

To conclude, this seismo-thermo-mechanical model constrained by observations provides physical explanations to understand the behaviour of the seismic cycle in the Himalaya. It shows that frictional properties and non-planar geometry of the MHT control a variety of phenomena, such as the bimodal seismicity, the relative persistence of along-dip variations of seismic ruptures and the variable recurrence time of large ($M_w \leq 7.8$) and great ($M_w > 8$) earthquakes. Based on

our numerical experiments, we postulate that large crack-like earthquakes on the MHT may release stress inherited from former pulse-like partial ruptures. These very large events account for the bulk of the deformation that is transferred to the most frontal structures in the Sub-Himalaya. If this scenario is in fact correct, it has consequences for the assessment of seismic moment where only rupture length and surface slip are known, as is the case for all palaeoseismic ruptures inferred from slip on the MFT (Lavé *et al.* , 2005; Sapkota *et al.* , 2013; Bollinger *et al.* , 2016; Kumar *et al.* , 2010). Because a heterogeneous strain condition is likely to prevail throughout the Himalaya, our results may provide an answer to the long-standing difficulties in explaining the source of the stored stresses needed to drive large (>8–10 m) paleoseismic surface ruptures recorded on the MFT (Kumar *et al.* , 2010; Mugnier *et al.* , 2013). The risk of such extreme earthquakes may have been underestimated because of the evidence that these events might only exist in geological records given their millenary return period (Stevens & Avouac, 2016). Seismicity catalogues might also give the false impression that they include the largest possible earthquakes. This might be related to the magnitude gap separating $\mathrm{M_w}$ 8+ events from the dominant mode formed by the smaller partial ruptures, which make up the bulk of the seismicity.

In light of our modelling results, the updip arrest of the 2015 Gorkha earthquake calls for special attention. That fault patch, updip of the Gorkha rupture, stayed locked in the post-seismic period (Gualandi *et al.* , 2017). The stress level was increased by the Gorkha earthquake (Galetzka *et al.* , 2015), making that patch more likely to fail in the next large rupture of the MHT in that area. The nearly 800-km-long stretch between the 1833/2015 ruptures and the 1905 $\mathrm{M_w}$ 7.8 Kangra earthquake is also a well-identified seismic gap with no large earthquake for over 500 years (Avouac *et al.* , 2015). The MHT is clearly locked there (Ader *et al.* , 2012; Stevens & Avouac, 2015) and its deficit of slip may exceed ~10 m. The last large earthquake in that area occurred in 1505, and could have exceeded $\mathrm{M_w}$ 8.5 (Bilham & Ambraseys, 2005). These factors make this area a prime location for a future complete rupture of the MHT. Continued geodetic monitoring of the Himalayan arc in the coming years will help to provide new constraints and to ascertain these speculations.

Acknowledgements

This study was funded by the SNF 2-77090-14 project Swiss-AlpArray SINERGIA. We gratefully acknowledge A.A. Gabriel, E. Kissling, J.-P. Ampuero, L. Bollinger, R. Jolivet, G. Hetényi, R. Almeida, S. Barbot, and the STM-group for comments. V.L. Stevens kindly provided the coupling data. We are grateful to J. Singer for providing us with a basic GMT script to plot Fig. 4.1a. Numerical simulations were performed on ETH cluster Euler.

Author Contributions

L.D.Z. designed the study and model setup, carried out and analysed the numerical experiments and wrote the paper. Y.v.D. and T.V.G. developed the STM methodology and analysed the results. J.P.A. contributed to the concept development. All authors discussed the results and commented on the paper.

5

Segmentation of the Main Himalayan Thrust inferred from geodetic observations of interseismic coupling

A similar version of this chapter is under review as:
Dal Zilio L., Jolivet, R., and van Dinther, Y.
Segmentation of the Main Himalayan Thrust inferred from geodetic observations of interseismic coupling

5.1 Abstract

Mapping the distribution of locked segments along subduction megathrusts is essential for improving quantitative assessments of seismic hazard. Previous geodetic studies suggest the Main Himalayan Thrust (MHT) is homogeneously locked (or coupled) along its complete length over a down-dip extent of ~100 km. However, an increasing number of seismological and geophysical observations suggests the MHT is structurally segmented along strike. Furthermore, coupling appears to vary significantly in subduction zones worldwide, hence the MHT appears as a striking anomaly. Here, we use a recent compilation of geodetic data and a fully Bayesian approach to show that coupling is highly heterogeneous along the MHT, thus reconciling all observations available. Our probabilistic estimate of interseismic coupling along the entire MHT highlights four large, highly-coupled patches separated by three potential barriers of low coupling. Locked patches overlap with estimated rupture areas of historical large earthquake over the past centuries. The coincident spatial variability in coupling, seismicity, prominent active topography, and complexity in earthquake history, suggests a structural segmentation of the Himalayan imposed by inherited tectonic structures from the India-Eurasia collision. This correlation implies that inherited tectonic structures may influence how stress builds up along the MHT and thus may influence the location and size of large Himalayan earthquakes and the growth of the Himalaya.

5.2 Introduction

Seismic hazard assessments have important implications for society, providing a basis for building codes, risk assessments, and public policies to mitigate earthquake risk (Shaw *et al.* , 2018). In this regard, the magnitude ($\mathbf{M}_\mathrm{w}$) 7.8 Gorkha–Nepal earthquake of 2015 was a dramatic reminder of the importance of understanding seismic hazard in the Himalayas (Bilham, 2015) (Fig. 5.1). This densely populated region has been struck by some of the largest continental earthquakes, including the $\mathbf{M}_\mathrm{w}$ 6.9 Sikkim 2011, and $\mathbf{M}_\mathrm{w}$ 7.6 Kashmir 2005 earthquakes. It is also known to have produced larger historical earthquakes of magnitude larger than 8, such as the $\mathbf{M}_\mathrm{w}$ 8.5 Assam 1950 and the $\mathbf{M}_\mathrm{w}$ 8.2 1934 Nepal-Bihar earthquakes (Chen & Molnar, 1990; Sapkota *et al.* , 2013).

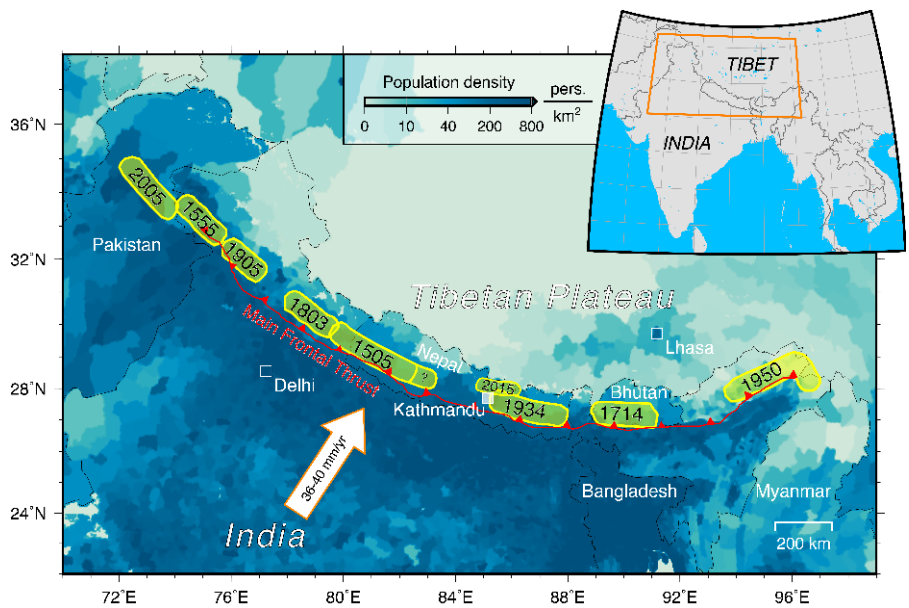


Figure 5.1.: **Great earthquakes in the Himalayas since 1500 A.D.** Yellow rupture areas of magnitude >7.5 and larger events are schematic and represent the published along-arc extent estimates (Bilham & England, 2001; Bilham, 2009; Kumar *et al.* , 2010; Bollinger *et al.* , 2014; Berthet *et al.* , 2014). Population density data from Ciesin (2005). Inset locates main map. Modified after Hetényi *et al.* (2016a).

In subduction zones, tectonic shortening imposed by plate motion on locked, seismogenic plate boundary faults leads to elastic stress increase, which is ul-

timately released by earthquakes (Lay, 2015). Geodetic observations allow to derive spatial variations of strain rates induced by interseismic locking of the main boundary faults. It consists of a mosaic of the plate boundary fault, which is used to map which portions of a plate boundary fault are locked versus those that slip aseismically. In the Himalayas, most large earthquakes have ruptured the Main Himalayan Thrust (MHT), the main plate boundary between the Indian and Eurasian plates. Interseismic strain results from tectonic shortening (~20 mm yr^{-1} across the Himalayas) imposed on a locked interface, the MHT, between those converging plates. The recent development of a large scale, dense network of GNSS stations (Kreemer *et al.* , 2014) allows to quantify the degree of fault locking and its spatial distribution on the MHT. Fault locking is referred to as coupling, defined as the ratio of the deficit of slip rate in the interseismic period divided by the long-term slip rate imposed by tectonic shortening. This ratio varies from 0 for a portion of the MHT that slips aseismically at a rate equal to the plate convergence rate to 1 for a fully locked fault.

Many models derived from geodetic data suggest interseismic coupling on subduction megathrusts worldwide is spatially heterogeneous, defining locked patches where stress increases more rapidly surrounded by segments that slip aseismically (Chlieh *et al.* , 2008; Moreno *et al.* , 2011). Megathrust earthquakes occur to first order on these interseismically locked patches (Loveless & Meade, 2011). Conversely, previously published models in the Himalayan region indicate that the entire MHT is uniformly locked from the surface to beneath the front of the high range over a width of 100 ±20 km (Ader *et al.* , 2012; Stevens & Avouac, 2015). Therefore, the MHT appears to be an anomaly with respect to subduction megathrusts worldwide. In addition, a fully locked MHT does not correlate with the variable size along strike and location of large (M7+) Himalayan earthquakes (Fig. 5.1). Furthermore, a recent and detailed GPS velocity solution over Bhutan highlights local variations in coupling over a small fraction of the MHT with aseismic slip at shallow depth (Marechal *et al.* , 2016).

Micro and moderate seismicity throughout the Himalayan arc varies significantly with some well defined active regions, highlighting a potential segmentation of the arc from a seismological point of view (Arora *et al.* , 2012). This lateral variation in seismic productivity may result from variations in fault geometry, rheology, frictional

properties along the fault interface or structural complexities (Mugnier *et al.* , 2017; Hubbard *et al.* , 2016; Bilham *et al.* , 2017; Dal Zilio *et al.* , 2019a). Recent studies also propose that the structure and seismicity may be influenced by the prolongation of subsurface ridges visible in the Indo-Gangetic Plains into the Himalaya (Arora *et al.* , 2012), a northward prolongation evidenced by the arc-parallel gravity anomalies (Hetényi *et al.* , 2016b). A segmentation in the seismic productivity or in the structure of the MHT would have important implications for the estimation of the return period and maximum magnitude of major earthquakes. Several studies suggest that a historical event near 1100 AD could have reached magnitude 9 along the Himalayan front (Kumar *et al.* , 2010; Le Roux-Mallouf *et al.* , 2016). Such large M9+ events are also required in the Himalayas to balance the moment deficit derived from geodetic strain measurements (Stevens & Avouac, 2016). If the degree of locking is high all along the MHT, a large M9+ earthquakes could dynamically propagate easily, while a segmented megathrust introduces rupture barriers and thus promotes laterally smaller earthquakes (Hubbard *et al.* , 2016; Grandin *et al.* , 2015; Mugnier *et al.* , 2017).

Considering a potential segmentation of the arc suggested by seismological and morphological features, we should question whether the current coupling models (Ader *et al.* , 2012; Stevens & Avouac, 2015) along the MHT are biased by the ill-posed nature of interseismic slip inversions. Because of the non-uniqueness of the solution, (ad hoc) smoothing constraints are often used to regularize slip inversions, effectively smoothing the resulting coupling map over regions with limited data (Loveless & Meade, 2011). In addition, estimates of coupling usually do not include uncertainties, which complicates any quantitative assessment of the overall strain budget. It therefore appears necessary to quantify the influence of regularization of the inverse problem on the distribution of coupling and to derive uncertainties only driven by data uncertainties and modeling assumptions.

In this chapter, we use 255 GPS-derived velocities spanning the 1990s to 2015 and levelling measurements between 1977 and 1990 (Kreemer *et al.* , 2014; Jackson & Bilham, 1994). We derive a probabilistic estimate of fault coupling along the MHT using AlTar, a Bayesian solver using elements of Markov Chain Monte Carlo (MCMC) sampler and tempering (Jolivet *et al.* , 2015; Minson *et al.* , 2013; Duputel *et al.* , 2014). Such probabilistic estimate does not rely on any spatial smoothing.

Furthermore, it provides full posterior probability distributions of coupling made of the ensemble of plausible models that fit the observations and are consistent with prior constraints. We consider a uniform prior PDF of coupling along the MHT, meaning we consider all spatial distributions of coupling are *a priori* equally probable. In addition, we assume 10% uncertainties on the prediction of the forward model due to variable elastic structure of the Himalayan crust (see Fig. 5.2–5.3, and Methods). We then propagate both data and prediction uncertainties and our modeling assumptions into *a posteriori* model uncertainties to evaluate what is allowed and what is not allowed by the GPS data. We generate 360'000 models corresponding to the posterior distribution of geodetic coupling given measured interseismic velocities.

5.3 Methods

5.3.1 Geodetic Observations

To assess the extent of interseismic coupling, we use an updated set of GPS-derived velocities spanning the 1990s to 2015. It was recently used to estimate the width of coupling across the MHT through a series of two-dimensional transects (Lindsey *et al.* , 2018) (Fig. 5.2). These velocities are from a number of published studies and combined into a consistent reference frame by reducing the best-fitting pole of rotation between overlapping sites in each data set (Kreemer *et al.* , 2014). Velocities for stations within China were combined with the reprocessed, updated velocity field (Zheng *et al.* , 2017). To better resolve the pattern of coupling we also include levelling measurements from the Survey of Nepal collected between 1977 and 1990 (Jackson & Bilham, 1994). Levelling data provide measurements of interseismic uplift rate. As pointed out by Ader *et al.* (2012), uncertainties on the levelling data are low with respect to those on the GPS-derived vertical rates and help constrain well the pattern of coupling locally.

Following the approach of Stevens & Avouac (2015), our fault model considers the total length of the arc of roughly 2000 km, from $73°$E to $96°$E (Fig. 5.2). The dip angle is set to 10° as in previous studies (Stevens & Avouac, 2015; Ader *et al.* ,

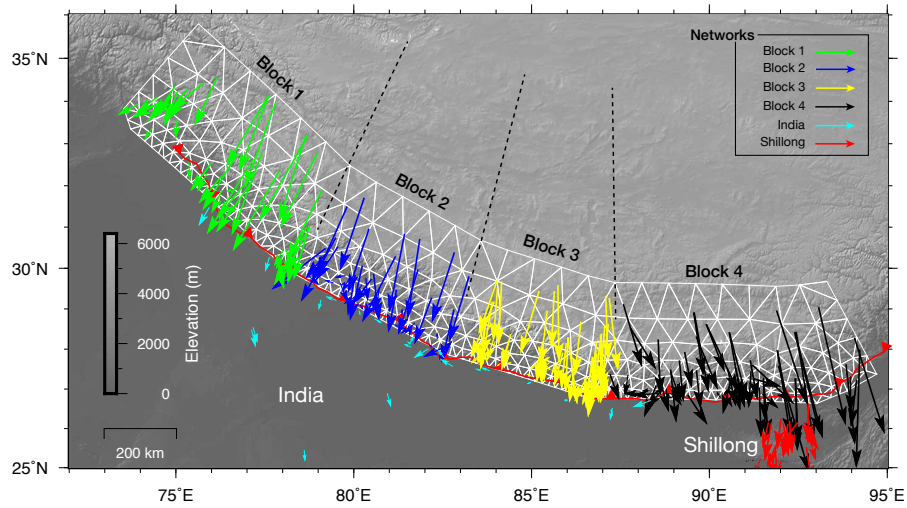


Figure 5.2.: Top view of the fault and GPS network employed in this study. The red line shows the surface trace of the Main Frontal Thrust. White triangular mesh is the fault discretization used in this model. Dashed black lines are the boundaries between different regions of uniform long term slip rate. GPS network is divided in the following subnetworks: block-1 (green), block-2 (blue), block-3 (yellow), block-4 (black), India (light blue), and Shillong (red).

2012). Due to the arcuate and irregular shape, we divide the fault geometry into four planar sub-faults blocks. These sub-faults are discretized in 353 triangles with variable size, smaller near the surface and larger down-dip. As estimates of the extent of plate coupling depend on the direction and rate of the plate convergence, we set a specific convergence rate and azimuth for each sub-fault based on plate motion models and regional geodetic measurements (see Table 5.1).

Longitude	Slip rate (mm/yr)	Reference
76.0	13.3	Thakur *et al.* (2014)
82.0	19.0	Mugnier *et al.* (2004)
85.8	18.2	Bollinger *et al.* (2014)
90.3	20.8	Berthet *et al.* (2014)

Table 5.1.: Long term slip rates from geomorphic studies used in this study.

We also assume that the otherwise rigidly moving India plates is fragmenting around the eastern end of the Himalayan arc where there is evidence for internal deformation (Vernant *et al.* , 2014). To account for this deformation, we consider two distinct blocks and related subnetworks: India and the Shillong block south

of the eastern Himalaya (Fig. 5.2). The elastostatic Green's functions of each sub-fault and block, relating unit slip on each patch to surface displacements at the data locations, are thus computed assuming a different long-term convergence rate and azimuth. The inversion solves for the poles of rotation with respect to India, as well as the coupling pattern.

We predict the response to subsurface fault slip at each data (GPS and levelling) location assuming a stratified semi-infinite elastic medium (Simons *et al.* , 2002; Zhu & Rivera, 2002). Our elastic space consists of 3 layers with elastic properties following roughly the average properties of the crust in the region (Pandey *et al.* , 1995) (Fig. 5.3). This 1D model was determined from the study of quarry blasts and from the distribution of apparent velocity of the first arriving phases generated by microseismic events occurring from a few kilometres to regional distance within the extent of the lesser Himalaya. Although the structure of the range is not one-dimensional, this simple model was found to be consistent with ray tracing modelling. It is also consistent with computed crustal thickness and velocity in the Lesser Himalaya determined from deep seismic profiling (Hirn *et al.* , 1984). Most of the microseismicity activity observed from 1985 to 1993 has occurred within the Lesser Himalaya where the velocity model has been constrained (Pandey *et al.* , 1995).

5.3.2 Bayesian analysis

We consider the forward problem **d = Gm**, where **d** is the vector containing the horizontal component of the GPS-derived velocities and of the vertical displacement of the levelling-derived measurements, **m** is the vector of model parameters, and **G** is the matrix of the response to slip on the faults at the data points and the geometric transformations in GPS and levelling data.

We solve the inverse problem to infer the distribution of model parameters (**m**) consistent with our data (**d**). The solution to this inverse problem is non-unique and large uncertainties on the parameters are expected. Therefore, instead of deriving a single model, we explore all the potential solutions using a Bayesian approach to derive the posterior PDF of our model given our set of data, **p(m|d)** (Minson *et al.* ,

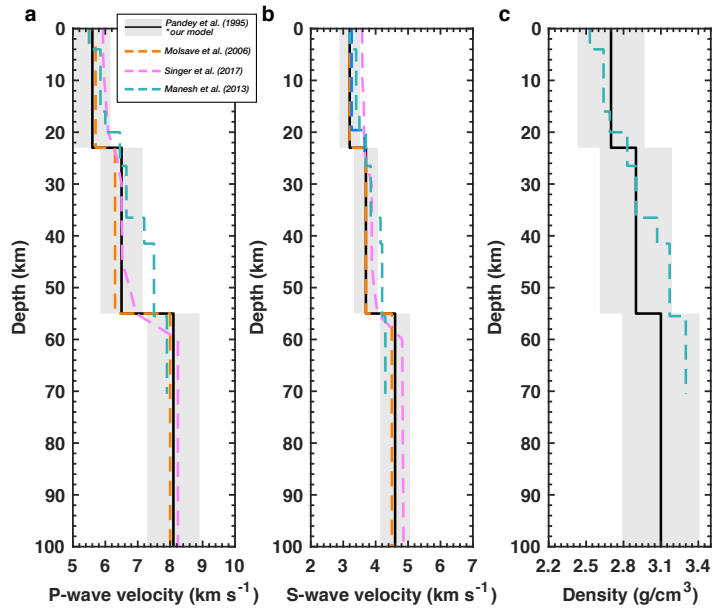


Figure 5.3.: Earth model: (**a**) P-wave velocity, (**b**) S-wave velocity and (**c**) Density used in this study for Green's function (GF) calculations. The layered model used in this study for Green's function (GF) calculations is plotted as a solid black line (Pandey *et al.* , 1995). Dashed lines refer to the other models used to constrain the uncertainties on model prediction (Mahesh *et al.* , 2013; Monsalve *et al.* , 2006; Singer *et al.* , 2017). Grey areas are the standard deviation of the probability density function, representing our confidence level on the elastic properties, as used to build the model prediction error ($\mathbf{C_p}$).

2013). We thus derive a probabilistic estimate of the degree of fault locking along the MHT. Following Bayes's theorem, we write the posterior PDF as:

$$\mathbf{p(m|d)} = p(\mathbf{m})\, exp\,[-\frac{1}{2}(\mathbf{d}-\mathbf{Gm})^T\,\mathbf{C}_\chi^{-1}\,(\mathbf{d}-\mathbf{Gm})]; \tag{5.1}$$

where **p(m)** is the prior PDF of the model that describes our state of knowledge before acquiring data, **d** is the data vector, **G** the Green's functions matrix, and **m** is the vector of model parameters. $\mathbf{C}_\chi$ is the covariance matrix in the data space, defined as the sum of the data covariance matrix $\mathbf{C_d}$, (i.e., measurement error matrix) and the prediction error matrix, $\mathbf{C_p}$, which describes uncertainties in our elastic model for the crust:

$$\mathbf{C}_\chi = \mathbf{C_d} + \mathbf{C_p}. \tag{5.2}$$

We account for prediction uncertainties due to inaccuracies in this layered elastic model using the approach of Duputel *et al.* (2014). The uncertainty on the elastic structure, presented as grey standard deviation in Fig. 5.3, is estimated by comparing previously published models across the all Himalayan region. We need a careful description of errors in order to not overfit the data and produce reasonable estimates of coupling uncertainties on each portion of the megathrust. Considering the variability and uncertainties on the 1D velocity models (Fig. 5.3) we include 10% uncertainty on the elastic properties of each layer of the elastic half-space. Previous studies have shown that not including the prediction errors when sampling for posterior PDF of coupling may lead to biased results (Jolivet *et al.* , 2015).

The solution of the inverse problem is the posterior ensemble of all plausible interseismic coupling models (**m**) that fit the GPS data (**d**) and that are consistent with our prior hypotheses. We test two different prior hypothesis: (1) a uniform PDF assuming no prior knowledge on the model parameters and (2) a heavily-constrained (that is, binary) prior. To sample the posterior PDF we use AlTar, a parallel Markov Chain Monte Carlo (MCMC) algorithm based on the Cascading Adaptive Transitional Metropolis in Parallel (CATMIP) formalism (Minson *et al.* , 2013). Using multiple MCMC chains in parallel, AlTar initially samples the prior PDF, **p(m)**, and then slowly increases the information brought by the data until it samples the posterior PDF. The implementation is accelerated by Graphic Processing Units (GPUs), allowing us to run thousands of chains in parallel. We generate 360'000 models corresponding to the posterior information on geodetic coupling given measured interseismic velocities. We perform a series of Bayesian inversions and we find that this number of models is enough to reach a convergence towards a constant posterior probability density function. Our final solution consists of an ensemble of models that are statistically distributed according to the posterior PDF.

5.4 Results

5.5 Interseismic coupling distribution

The posterior mean coupling model shows remarkable spatial variations in interseismic coupling, both down-dip and along-strike the MHT (Fig. 5.4a). We infer discrete highly-coupled segments along the fault extending throughout the arc. Coupling is high at the front, where the MFT reaches the surface and the resolution resulting from observations is highest. Down-dip, coupling tapers to negligible values around 100–120 km from the Main Frontal Thrust. From west to east, we observe a large lateral variability in geodetic coupling. Four large (*ca.* 300–450 km) and discrete highly-coupled segments (>0.8) are separated by three relatively smaller (*ca.* 100 km) regions with lower coupling (<0.3). These lateral variations of coupling raise two fundamental questions. First, are these variations a robust feature driven by the data? Second, what difference between our approach and previously published methods leads to the emergence of these low coupling segments along the MHT?

We interrogate the posterior PDF of coupling to assess the robustness of our estimate by considering the local marginals of coupling (nodes 1–6 in Fig. 5.4a). Marginal PDFs for nodes 2, 4, and 6 show a >75% probability that fault coupling exceeds 0.8. On the other hand, for node 1 and 5, we infer a 68% probability that fault coupling is lower than 0.4, confirming a high probability of low coupling. In contrast, the shape of the cumulative distribution function of coupling on node 3 suggests a wider range of probable values, not far from the initial prior distributions (i.e., uniform probability of coupling) but still tending towards lower values of coupling. This similarity of prior and posterior distributions suggests the data are less informative to derive fault coupling along this limited section of the model. Although our inversions include larger covariances compared to previous studies (Ader *et al.* , 2012; Stevens & Avouac, 2015), observed vs. predicted horizontal GPS displacements (Fig. 5.4b) and residuals (Fig. 5.5) from our mean model show a good agreement with the geodetic measurements.

However, it is important to note that the regions with lower coupling are where the MHT has a slightly different azimuth and convergence rate, and where the

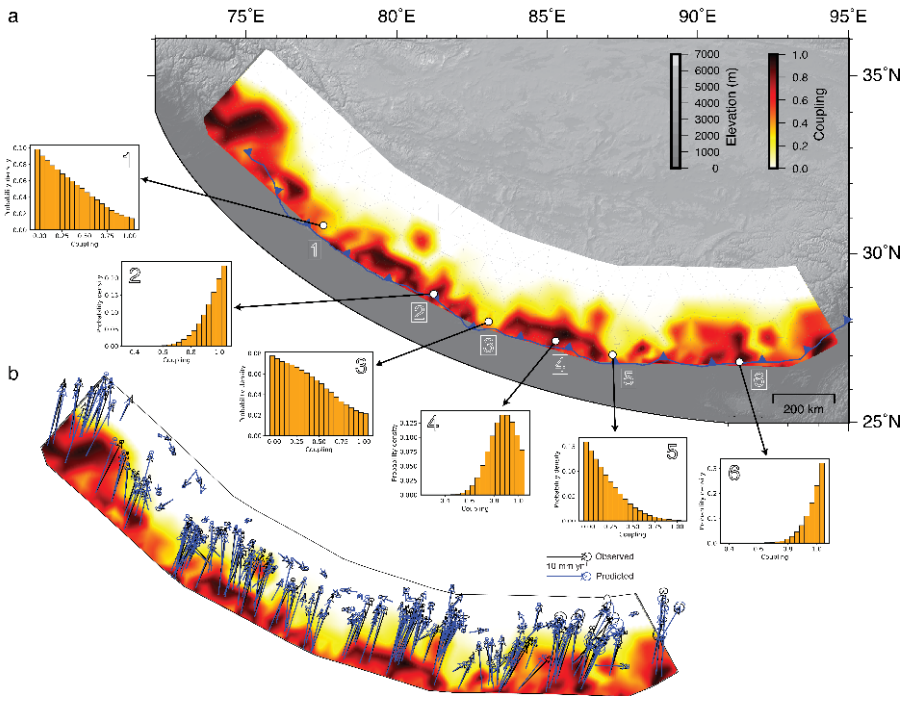


Figure 5.4.: **Posterior mean coupling model of the Himalayan megathrust**. **a,** The resulting posterior mean model accounts for data uncertainties and 10% of prediction uncertainties (see Methods for details). Coupling values are inverted at each triangle knot. For each of the histograms, orange bars are the marginal probability densities at discrete nodes of the fault model. Thin grey lines represent the fault mesh. Solid blue line shows the surface trace of the Main Frontal Thrust. **b,** Same posterior mean model with the GPS displacement and model predictions plotted as black and blue arrows, respectively.

GPS data are less dense (see Methods for details). To check the reliability of our results we perform another test in which we assume a uniform fault with a constant convergence rate along-strike. Despite small variations, these results are very similar and the regions with low coupling are still easily detectable (see Fig. 5.6). These results thus provide strong evidence that the observed megathrust segmentation is consistent with the data and the given the posterior uncertainties.

For comparison, instead of assuming a uniform non-informative prior, we consider a highly-constrained prior PDF distribution. In particular, we assume that the MHT is highly-coupled from the surface to 18-km-depth and with negligible coupling at depths greater than 20 km. To do so, we consider a tight Gaussian prior PDF with a standard deviation of 10%, centered on 1 from the surface to 18-km-depth (i.e., fully locked) and on 0 for depths greater than 20 km (i.e., fully creeping). All

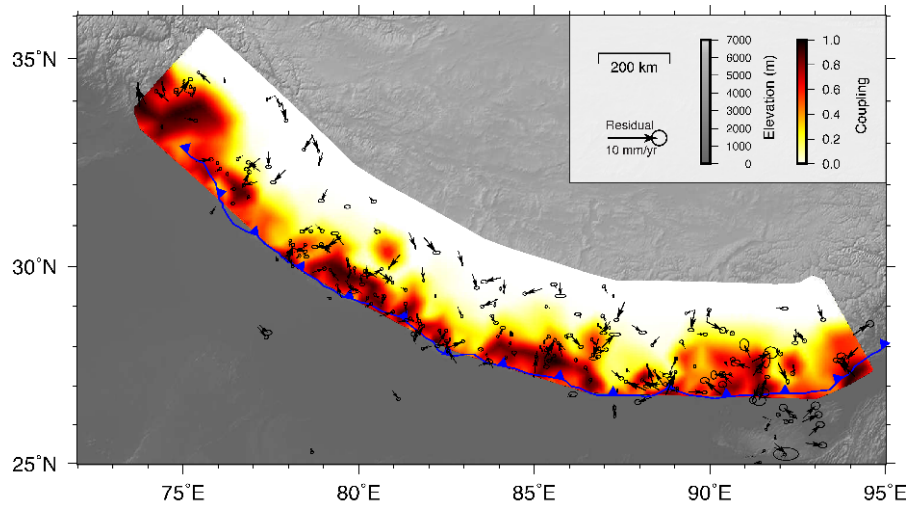


Figure 5.5.: Posterior mean coupling model of the Himalayan megathrust shown in Fig. 5.4 and residuals to the GPS data, with uncertainty ellipses. Ellipses show the uncertainties at the 67% confidence level.

other assumptions and hypothesis are kept identical to our preferred model. This strong assumption is based on previous geodetic studies using GPS campaign and leveling measurements (Bollinger *et al.* , 2004), a few continuous GPS stations (Bettinelli *et al.* , 2006), and a recent physics-based forward model of the Himalayan seismic cycle (Dal Zilio *et al.* , 2019a). Also, the location of the down-dip end of the locked fault zone is consistent with the seismicity pattern observed in Nepal Himalaya (Cattin & Avouac, 2000), and the postseismic deformation following the 2015 $\mathrm{M_w}$ 7.8 Gorkha earthquake (Gualandi *et al.* , 2017). By assuming that the MHT is locked from the surface to a certain depth, these previous studies found a satisfying fit to the data with a fault dipping about 10° to the north and a down-dip end of the locked part of the fault about 100 km along dip from its surface trace.

The posterior mean model suggests the MHT is highly-coupled from its surface expression along the Himalayan foothills to beneath the front of the high range about 100 km to the north (see Fig. 5.7). In general, coupling is nearly binary (1-to-0), with a sharp transition between the coupled and creeping zones, similarly to what has been observed in previous studies (Ader *et al.* , 2012; Stevens & Avouac, 2015). This distribution of coupling is actually very close to the prior PDF we have considered. Strikingly, residuals are of the same order of magnitude as in our

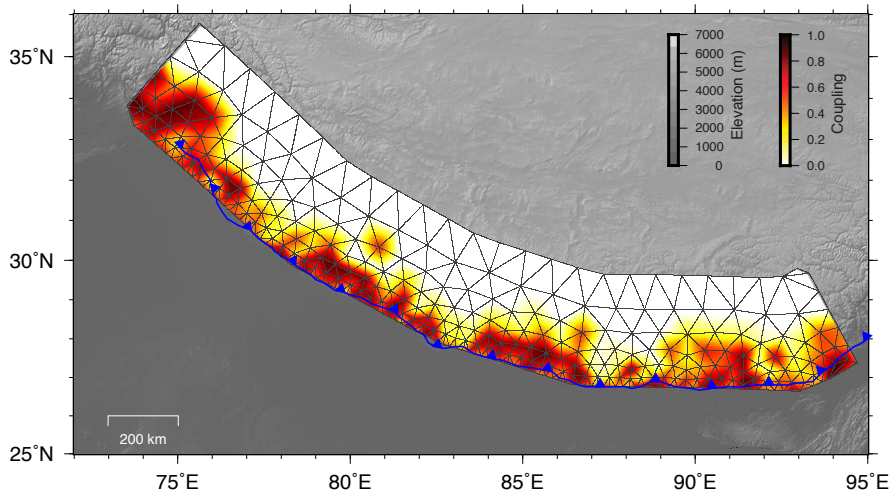


Figure 5.6.: Posterior mean coupling model assuming a homogeneous convergence rate. The resulting posterior mean coupling model is obtained assuming a constant convergence rate along-strike, with no along-strike blocks (see Fig. 5.2). Thin black lines represent the fault parametrization. Solid blue line shows the surface trace of the Main Frontal Thrust.

preferred model with uniform prior. This leads to the conclusion that both models, the one assuming a heavily constrained prior and the one with a uniform prior, fit the data almost equally well and are both possible. However, examination of marginal posterior PDFs suggest that the model derived from highly-constrained prior is only a subset of potential models. As shown by marginal PDFs of coupling on node 1, 3, and 5 (Fig. 5.7), models with high coupling are not excluded, but they are less probable than low coupled models given the available data. Homogeneous coupling along the MHT thus results mainly from a strong prior assumption, which may derive from smoothing of the solution. On the other hand, relaxing this hypothesis reveals a complex distribution of coupling and this complex distribution is more probable given the available data as shown by the posterior uncertainties directly translated from the data.

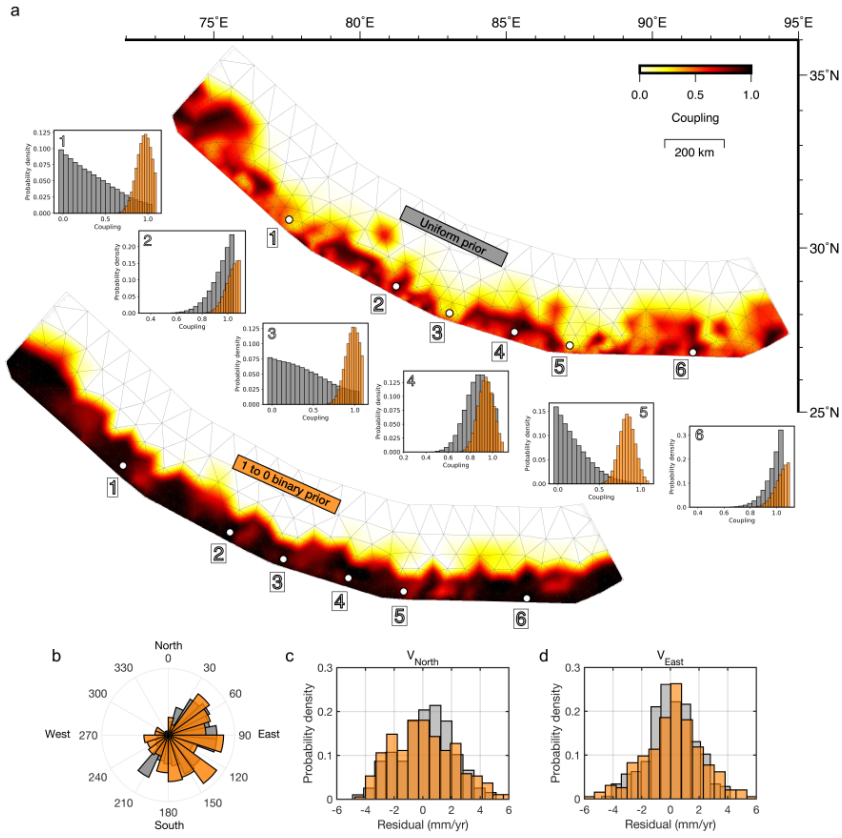


Figure 5.7.: Comparison of coupling models, probability density functions and residuals of the GPS data. **a,** Top: posterior mean solution shown in Fig. 5.4 assuming a uniform prior. Bottom: posterior mean solution of model incorporating a strongly constrained 0-to-1 binary prior. Histograms indicate the marginal probability densities at discrete 6 nodes of the fault of models with uniform prior (grey) and binary prior (orange). **b,** Rosetta histograms showing the orientation of the residuals of the two models. **c–d,** Probability density distributions of residuals on both north and east velocity components.

5.6 Discussion

5.6.1 Segmentation of the Himalayan megathrust and seismicity

The spatial variability of interseismic coupling is an important factor to consider in interpreting relationships with the slip distribution of historical ruptures (Fig. 5.8). Along-strike, low coupling regions around nodes 1, 3, and 5 (Fig. 5.4a) coincide

with three subsurface Indian basement ridges in the Indo-Gangetic plains: The Delhi-Haridwar ridge (DHR), the Faizabad ridge (FR), and the Munger-Saharsa ridge (MSR). These subsurface basement ridges extend northward across the Himalayan foothills and they might have affected the development of the arcuate shape and the morphology of the Himalayan arc. They have been detected first from basin thickness changes (Gahalaut & Kundu, 2012), and they are confirmed by the analysis of anomalous transient geomagnetic variations and arc-parallel gravity anomalies (Hetényi *et al.* , 2016b; Arora *et al.* , 2012). They typically include oblique to transverse synclines, folds, fracture zones or faults athwart the strike of the Himalaya, and they are associated with normal faulting and strike-slip seismicity (Valdiya, 1976). Details of the origin and nature of the lineaments, however, remain mostly obscure at present although it is believed that more extensive structures are in tectonic continuation from the Indian shield (Valdiya, 1976).

The subduction of these major tectonic structures is likely related to a segmentation in the seismic behavior of the MHT. Despite uncertainties, the rupture extent of major and great Himalayan earthquakes for past two hundred years appears to correlate with the regions of ridge subduction and the pattern of coupling (Fig. 5.8b). For example, the eastern edge of the 1905 Kangra earthquake rupture appears to approximately coincide with the Delhi–Hardwar ridge (Gahalaut & Kundu, 2012; Wallace *et al.* , 2005). The western edge of the 1803 rupture, though not well constrained, abuts the Delhi–Hardwar ridge (Rajendran & Rajendran, 2005). The 1934 Nepal Bihar earthquake rupture propagated eastward until or into the Munger–Saharsa ridge (Hough & Roger, 2008). However, it should be noted that an error of about 50 km could exist in the estimation of the rupture extent and rupture dimensions, and in the northward extrapolation of the ridges under the Himalayan region (Gahalaut & Kundu, 2012).

Recorded M≥4.5 earthquakes (USGS catalogue) suggest a segmentation of the Himalayan arc (Fig. 5.8c). Cumulative seismic moment released shows along-strike variations with less seismic moment released in the three regions corresponding to the subsurface ridges. In particular, the cumulated effect of all smaller events does not reach that of a single M6 event. Furthermore, low seismicity across the Faizabad ridge has been evidenced by a dense seismic network in Nepal (Ader *et al.* , 2012). Relocated microseismic activity (Mahesh *et al.* , 2013; Ader *et al.*

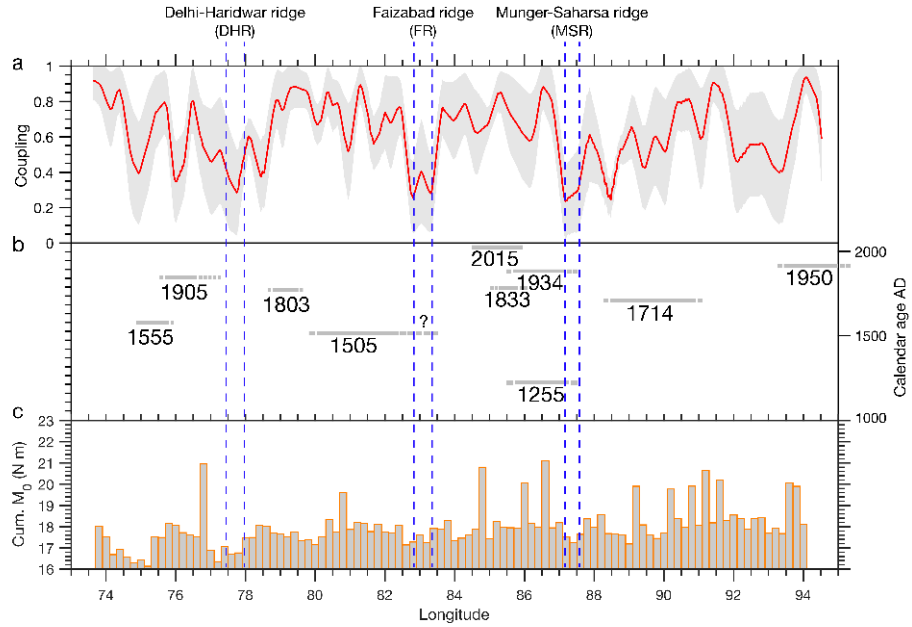


Figure 5.8.: **Comparison between along-strike variability of coupling, lateral extension of historical M>7.5 earthquakes, location of the subsurface ridges, and cumulative seismic moment released. a,** arc-parallel coupling profile at 45-50 km from the Main-Frontal-Thrust, derived from the posterior mean coupling model shown in Fig. 5.4. Shaded grey area represents the corresponding 2-σ deviation. Blue dashed lines indicate the location of the subsurface ridges in the Indo-Gangetic plains at the Main Frontal Thrust: **DHR** – Delhi Hardwar ridge; **FR** – Faizabad ridge; **MSR** – Munger–Saharsa ridge. **b,** Known major and great earthquakes in the Himalaya. The lateral extension of the 1555, 1505, and 1255 earthquakes is speculative. The medieval event in Bhutan is after Hetényi *et al.* (2016a). The 1905 Kangra earthquake rupture is after Wallace *et al.* (2005). Other instrumentally recorded events on this diagram are the 1905 M7.9 Kangra earthquake, the 1934 M8.0 Bihar earthquakes, and the 2015 M7.8 and M7.3 events in the Kathmandu region. **c,** Lateral variation of cumulative seismic moment released of M>4.5 earthquakes across the Himalayan belt (USGS catalog). The seismicity is defined within 250 km north of the Main Frontal Thrust.

, 2012), which extends over two regions from 77°E and 81°E and from 81°E to 87°E, respectively, follow the down-dip edge of the highly-coupled patches quite well (Fig. 5.9). East of Bhutan, in Arunachal Pradesh, there is a seismically active band that extends into the orogen. Also, the cluster of seismicity extending into the Himalayan orogen at 77.5–78°E turns northward as a possible continuation of the Delhi-Haridwar ridge.

Most of this background seismicity does not occur on the MHT itself, but rather within a 5–10 km size volume around the down-dip end of the locked fault zone (Avouac, 2015). Assuming that the instrumental record is representative of the long-

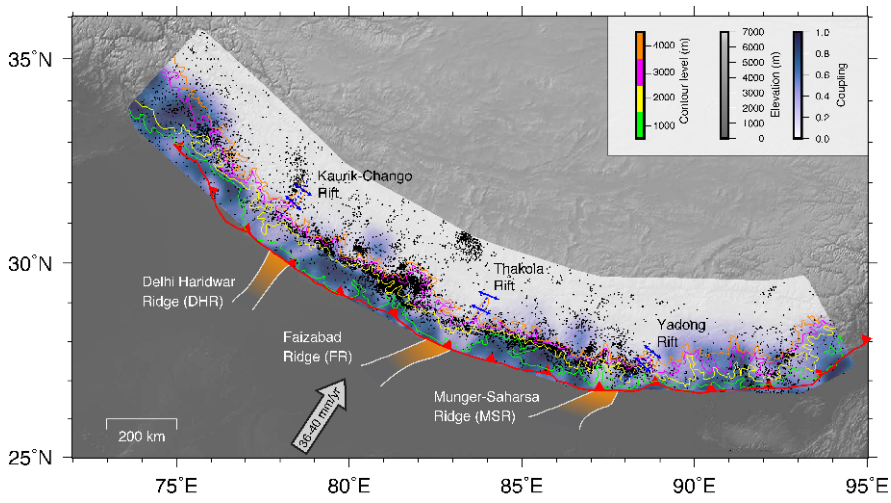


Figure 5.9.: Comparison between topography, interseismic coupling, and (micro-)seismicity. Seismicity within Nepal is from an NSC catalog (Ader *et al.* , 2012). Seismicity between ~77°E and 81°E is from Mahesh *et al.* (2013), and the remainder is from National Earthquake Information Center (NEIC). Solid coloured lines show the topography contour lines. Dashed blue lines indicate the location of the Kaurik-Chango, Thakola, and Yadong rifts. Orange patches indicate the location of the subsurface ridges beneath the Indo-Gangetic Plains. The Main Frontal Thrust is outlined in red.

term seismicity, such spatial variability in seismic moment released suggests that stressing rates are lower where the ridges are subducting, which coincides with low coupling along the MHT. Where the MHT is locked, stress builds up faster and thus results in higher microseismic activity. Conversely, regions with low coupling may be associated with lower stress build up and lower microseismic activity (Bollinger *et al.* , 2004).

5.6.2 Coupling vs. topography

Assuming that coupling is stable over geological times, the resulting pattern of strain should influence the construction of topography locally. To first order, topography contour lines show how the Himalaya rise abruptly at a distance of about 120-150 km from the Main Frontal Thrust (Fig. 5.10a). Notably, the down-dip end of the highly-coupled section of the MHT is spatially coincident with the abrupt rise in topography. This confirms that the down-dip limit of the brittle-ductile transition

is located where the shear stress accumulation is the highest, and drops under topography greater than 3500 m of elevation (Bollinger *et al.* , 2004). To second order, we identify frontal topography cusps where the subsurface ridges subduct under the arc, especially in the case of the FR and MSR, as highlighted by the position of the 2000 m contour line with respect to the Main Frontal Thrust. These cusps could have formed during earlier episodes of subduction when the ridges were subducting at that location about 10 million years ago (Gahalaut & Kundu, 2012). In addition, the largest across-strike graben of the Himalayan belt, the Kaurik-Chango Rifts, the Thakola Rifts and the Yadong Rifts, lie in the prolongation of the three ridges (Fig. 5.10a). In particular, normal faulting earthquakes continuously occur along N-S fault planes in the Kaurik-Chango Rift (Gahalaut & Arora, 2012), where the eastern limit of the 1905 Kangra earthquake is located. Possibly, the Kaurik-Chango Rift keeps this part of the Himalayan seismic belt in a dilated (or low stress) state so that earthquake ruptures along the MHT do not extend through it. It should be noted, however, that the assumption of a linear extension in the trend of these ridges below the Himalaya is uncertain and that the ridges may in fact deviate from their extrapolated linear trend.

A link between topography and coupling suggests a long-term influence of the seismic behavior of the megathrust and topography building. One possibility to reconcile the segmentation of topography and that of coupling is to consider the topographic effects of ridge subduction. In subduction zones, seafloor observations (Singh *et al.* , 2011) and numerical experiments (Ruh *et al.* , 2016) suggest that subduction of large topographic structures (e.g., seamounts) result in a bulge above the underthrusting seamount and normal faults within the overriding plate. If this holds for the Himalayan orogen, the long-term passage of these three basement ridges could explain the topography cusps and the arc-perpendicular normal faults. This is speculative but possible. More in general, the correlation between the pattern of interseismic coupling and the topography suggests that segmentation and effective frictional properties vary little in time, while irrecoverable strain of the Himalayan wedge is small during the interseismic period. If a significant amount of permanent deformation were present, the long-term convergence rate predicted by the geodetic data would be higher than the convergence rate used to infer the pattern of coupling on the MHT. All together, these results demonstrate

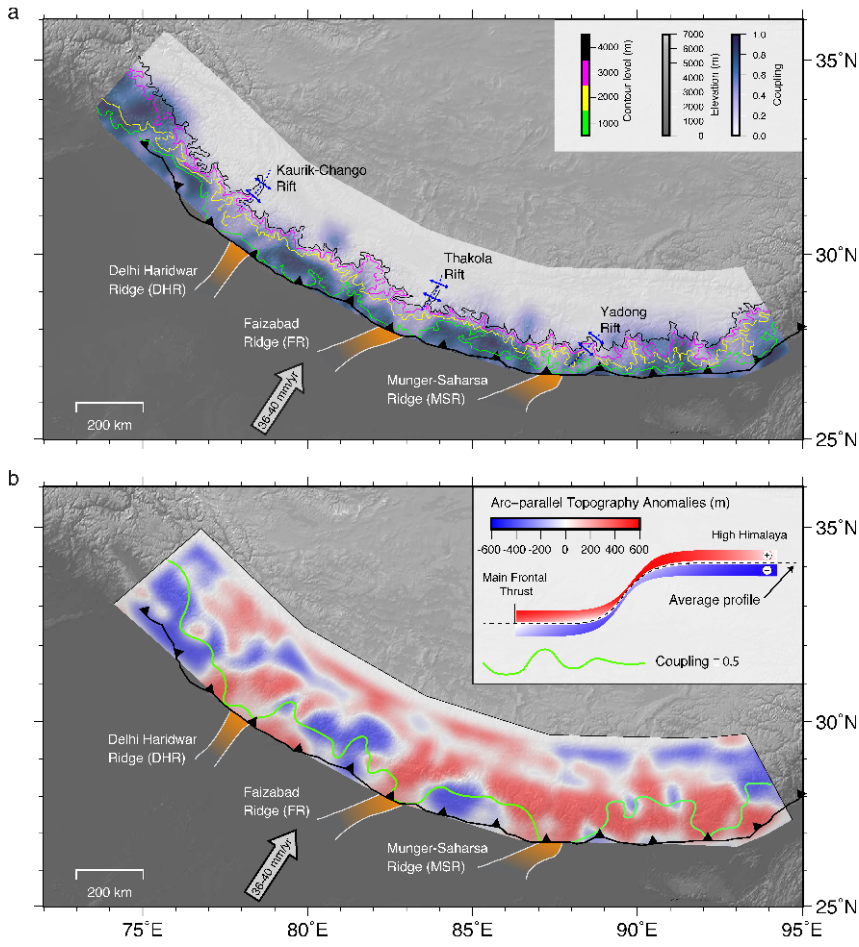


Figure 5.10.: **Interseismic coupling vs. topography. a,** Comparison between the present-day topography and coupling distribution inferred from the posterior mean coupling model shown in Fig. 5.4. Blue colormap displays the interseismic coupling pattern. Solid coloured lines show the topography contour lines. Dashed blue lines indicate the location of the Kaurik-Chango, Thakola, and Yadong rifts. **b,** Arc-Parallel Topography Anomalies after smoothing with a 30-km radius circle (Hetényi *et al.* , 2016b). Green line depicts the contour line of coupling≡0.5. Orange patches indicate the location of the subsurface ridges beneath the Indo-Gangetic Plains. The Main Frontal Thrust fault is outlined in black.

that the Himalayas is a highly three-dimensional mountain range. Yet, it has been described by several two-dimensional cross-sectional models (Bettinelli *et al.* , 2006; Bilham *et al.* , 1997; Lindsey *et al.* , 2018). The 2D approximation is likely a poor approximation as these models are inefficient to describe geodetic

observations resulting from ongoing plate convergence and/or spatially variable tectonic heterogeneities.

To investigate lateral variations in collisional structure we also compare (i) the Arc-Parallel Topography Anomalies (Hetényi *et al.* , 2016b), which define the topography differences from the average arc-perpendicular profile, (ii) the 0.5 contour line of coupling, and (iii) the location of the three subsurface ridges (Fig. 5.10). The variation of the Arc-Parallel Topography Anomalies exceed 500 m with a number of alternating negative and positive patches throughout the arc. Remarkably, the higher values at the front of the range are located where the coupling is low and the three subsurface ridges come across the Main Frontal Thrust. The western boundary near 76.5°E, aligned with the Delhi-Haridwar ridge (DHR), is visible in the topography anomalies. The middle boundary near 82.5°E, aligned with the Faizabad ridge (FR), as well as the eastern end of the Munger-Saharsa ridge (MSR) near 87.5°E, are also visible in the topography anomalies. This latter is certainly a major boundary in (or of) the India plate (Hetényi *et al.* , 2016b). The correlation between the Arc-Parallel Topography Anomalies and coupling suggests that regions with strongly positive Arc-Parallel Topography Anomalies are likely more aseismic, as already observed in subduction zones (Song & Simons, 2003).

To conclude, we propose that inherited structures along the Himalayan arc induce a zonation of interseismic coupling along the plate interface. Regardless of uncertainties, our first probabilistic estimate of interseismic coupling along the MHT suggests that the Himalayan megathrust is segmented by regions of low coupling. These low-coupled patches overlap with inherited structures. Despite competing hypotheses, the segmentation of the orogen into these blocks is also confirmed in the along-strike rupture extension of historical earthquakes. Large earthquakes of the past millennium do not propagate across the segment boundaries defined by lower plate inherited structure (Hetényi *et al.* , 2016b; Gahalaut & Arora, 2012). Therefore, the here identified low-coupled patches potentially set three boundaries for the lateral extent of potential megathrust earthquakes. From a general agreement between previous results (Ader *et al.* , 2012; Stevens & Avouac, 2015), geodetic data, and geological constraints, our results confirm that the fraction of anelastic deformation in the highly-coupled regions might be within uncertainties of the geodetic data (≤10%).

These new findings also highlight important targets for future studies, which will be essential to question how these segment boundaries control interseismic strain accumulation. Further GPS campaigns should assist in answering this challenging but crucial question. By the same token, these new results are of practical importance to seismic hazard analysis where effort is spent attempting to place limits on the probable lateral extension of future earthquakes across the whole Himalayan region.

Acknowledgements

This study was funded by the SNSF 2-77090-14 project Swiss-AlpArray SINERGIA (L.D.Z.) and the E.R.C. Starting Grant GEO-4D (R.J.). Numerical simulations were performed on ENS cluster Euler, Paris. We thank J.-P. Avouac, G. Hetény, M. Simons, L. Bollinger, C. Pranger, A. Gualandi, K. Wang, and S. Michel for constructive comments and discussions. We are grateful to G. Hetény for providing us with GMT scripts to plot Fig. 5.1 and the Arc-Parallel Topography Anomalies (Hetényi *et al.* , 2016b).

6

Conclusions and perspectives

6.1 Thesis conclusions

Recent earthquakes in collisional orogens, e.g., the 2015 $\mathrm{M_w}$ 7.8 Gorkha and the 2016 $\mathrm{M_w}$ 6.2 Central Italy events, killed thousands of people and caused billions of dollars of property loss. As these regions are usually densely populated, understanding the physical processes controlling earthquakes in collisional orogens is of utmost importance. Exploring the dynamics of mountain building processes requires an in-depth, quantitative and physical understanding of how orogenic systems operated in the past and present. Moreover, addressing which long-term regimes of seismic activity are characteristic for different parts of these systems could potentially improve our ability to assess seismic risk factors. One increasingly important tool to improve our understanding is numerical modeling. However, integration of diverse observations and disciplines requires multiple approaches operating at different spatiotemporal scales. Accordingly, this thesis applied different methods to address different, albeit related goals.

In the first part, I validated and applied seismo-thermo-mechanical models in continent-continent collision settings. This approach allowed me to investigate the relative contribution of tectonic and kinematic processes to seismic behavior of mountain belts (Chapter 2), and how self-driven subduction controls mountain building processes and related seismicity (Chapter 3). After obtaining general insights into the seismic behavior of mountain belts, I extended the STM methodology by developing a modeling approach that includes various geological and geophysical constraints in the design of accurate, and more realistic, present-day model setups. The development, validation and application represents one of the key novel contributions of this thesis. This opened a clear avenue to bridge the gap between physics-based models and observations and gain a grip on how well

models fit different constraints (Chapter 4). In the last part of this thesis (Chapter 6), an inverse modeling based on a Bayesian formulation was used to propose an interseismic coupling model of the Himalayan megathrust, which benefits from an objective weighting of the various datasets by combining observational errors and modeling uncertainties.

6.2 Application of the STM approach in collisional orogens

The role of plate convergence rate in seismic behavior of mountain belts

Maximum earthquake magnitude and the rate of seismic activity differ among orogenic mountain belts. These variations are generally attributed to factors such as tectonic structures and stress-strain distributions. In Chapter 2, I showed that the seismic behavior of continent-continent orogenic belts is controlled by the plate convergence rate (Dal Zilio *et al.* , 2018b). I analysed this using a tectonically realistic seismo-thermo-mechanical modeling approach (van Dinther *et al.* , 2013b,a) that, for the first time, considers the long-term and self-consistent collisional orogeny and the short-term seismic cycle.

Analysis of the physical processes involved during continent-continent collision shows cycles of spontaneous earthquake-like ruptures on non-predefined faults, with physically consistent emergence as complex rupture events, both on- and off-megathrust. These synthetic events lead to a Gutenberg–Richter frequency–magnitude distribution, which is a key observational feature of seismicity that is typically not reproduced in seismic cycle models. These Gutenberg–Richter distributions suggest an inverse, linear relationship between plate convergence rate and the slope of this power law, the "*b* value", which is commonly used to describe the relative occurrence of large and small events. These results indicate a positive, linear relationship between $\mathrm{M}_{\mathrm{max}}$ and plate convergence rate. Collisional orogens with high convergence rates are thus manifested by pervasive seismicity, high magnitude of earthquakes and relatively low *b* values. In contrast, decreasing convergence rates lead to relatively larger amounts of smaller earthquakes (i.e., increasing *b* value) and lower maximum magnitudes. Moreover, seismicity is ob-

served to migrate from the main thrust into the orogenic wedge as convergence rate decreases. This more distributed form of brittle deformation is also accompanied by a larger contribution of ductile deformation, thereby reducing seismic hazard for slower convergent margins. These models explain how high convergence rates reduce the average temperature of the orogen, which increases the brittle portion of the crust at the expense of the ductile portion. The rheological feedback mechanism proposed in this chapter suggests that for high collision rates the brittle strength is larger and, in turn, increases the capacity of seismogenic faults to store and release elastic strain energy. Lastly, the applicability of this approach to simulate seismicity in collisional margins is demonstrated by a good agreement with the observed seismicity patterns within the Alps, Apennines, Zagros and Himalaya.

Slab rollback orogeny model: A test-of-concept

The applicability of the STM methodology to natural problems was significantly extended by investigating the effect of self-driven subduction dynamics on mountain building processes (Chapter 3, Dal Zilio *et al.* , 2019b). A relevant improvement of the model presented in this chapter concerns the slab dynamics: subduction and subsequent collision are self-driven by the buoyancy of the lithospheric slab and the respective crust, initially oceanic then continental, without imposing any kinematic boundary conditions.

This model reproduced the self-consistent stages of oceanic subduction, continent-continent collision, spontaneous slab breakoff and subsequent evolution of the orogen. Notably, the retreating collisional regime found in this model is a distinct and dissimilar feature compared to previously investigated post-subduction collisional orogeny models, which are usually characterized by a fixed position of the overriding plate. The subsequent evolution of the orogen shows interesting geodynamic features of the collisional zone, including a slow, but persistent, flexural bending of post-collisional residual slab and crustal delamination. In particular, evolution of the orogenic front and foreland basin, nappe stacking of the crustal root, and widening of the orogen were found to be solely driven by the flexural bending of the remaining slab. The impact of this flexural bending on the seismicity pattern

was also very distinctive, as it implies the occurrence of extensional forces at work in the orogen and beneath the foreland basin.

Thus, this mechanism — also known as *Slab Rollback Orogeny* model — supports the emerging hypothesis that the buoyancy forces, provided from the post-breakoff remaining slab, exert a first-order control on the migration and deformation of the orogen (Kissling & Schlunegger, 2018). This mechanism, recently applied on the central European Alps (Schlunegger & Kissling, 2015), contradicts nearly all models of orogeny that are based on the concept of horizontal convergence and subsequent collision of two continental plates. In light of these results, we proposed that the Central Alps does require an alternative mountain building concept. These results also stress the importance of large-scale, self-consistent driving forces on the tectonic and related seismic evolution of collisional orogens.

6.3 Development of observationally constrained models

A key contribution of this thesis is the methodological advancement of the STM modeling approach to overcome its generic and simple model setups. Although geodynamic modeling is a practical tool to address and understand fundamental geoscientific questions, results obtained from these models are often generic and difficult to compare to a specific geological setting. On the other hand, instantaneous modeling approach have been used over the last years to study the dynamics of plate tectonics and mantle flow. These models showed high accuracy of initial model setups, but they are not dynamically consistent and require a careful analysis of the physical parameters to constrain the thermal structure and the density distribution.

In this thesis I addressed the limitations of the generic STM model setups and combined the advantages of both geodynamic modeling and instantaneous modeling simulations through the development of GeoMAC (Geo-Mapping And Converting tool). The development of this tool allowed me to sample and convert geological cross sections into lithologies with laboratory-based material properties, by including a large number of input data, such as geological profiles, seismic data, tomography models and other geophysical constraints. Through the use

of this tool, I designed initial model configurations that include accurate shapes of tectonic nappes and corresponding rheologies, slab geometries, fault patterns and related morphology, topography and temperature distributions. This approach demonstrated the importance of combining field geological and geophysical data to explore, for example, the anatomy of a megathrust over multiple seismic cycles.

6.4 Exploring the potential of GeoMAC

Bimodal seismicity of large Himalayan earthquakes: Influence of fault friction and geometry

In Chapter 4, I explored part of the potential of this new tool by investigating the seismicity pattern in the Nepal Himalaya. In particular, I explored the conditions that could explain the bimodal seismicity ($\mathrm{M_w}$≤7.8 vs. $\mathrm{M_w}$ 8+ earthquakes) of large Himalayan earthquakes. By employing geodetic data, combined with geological and geophysical analysis, I designed a high-resolution model of the present-day lithospheric structure and geometry of the Nepal Himalayan wedge and the Main Himalayan Thrust.

This model consistently reconciled a suite of independent observations from both interseismic and seismic crustal deformation. In particular, it suggested that the bimodal behavior of megathrust earthquakes results from a relatively higher friction and a non-planar geometry of the Himalayan megathrust (Dal Zilio *et al.* , 2019a). These advanced models illuminate two puzzling features of the Himalayan seismic hazard: how great earthquakes ($\mathrm{M_w}$ 7+) can re-rupture regions that have already ruptured in recent smaller earthquakes, and how large earthquakes ($\mathrm{M_w}$ 8+) may occasionally propagate up to the surface, driven by residual strain accumulated over many centuries of smaller earthquakes. The model presented in this chapter illuminates new research directions for improving our physical understanding of seismic rupture on megathrust, and provided new ways to assess a region's seismic hazard.

Puzzling features of Northern Apennines tectonics and seismicity explained by slab retreat and crustal delamination

The potential impact of the models presented in this thesis is further demonstrated in Appendix A by ETH student Mario D'Acquisto, who I supervised during his MSc thesis. By combining the insights gained from self-driven retreating collisional regimes (Chapter 3) and accurate present-day model setups (Chapter 4), we studied the complex geodynamic system of the Northern Apennines fold-and-thrust belt. A major effort was put in developing the model setup, which was built from an exceptional number of geological and geophysical constraints. This allowed us to design a high-resolution model of the present-day Northern Apennines. The main outcome from this model is related to the self-consistent dynamics of the subducting slab, which resulted in spontaneous protrusion and lithospheric delamination in the mantle wedge. Most importantly, these results showed how the negative buoyancy of the subducting slab controls the migration of the orogen. It also controlled the crustal tectonics and related seismicity, which is characterized by two different, adjacent tectonic domains: extension and uplift in the core of the orogen and active shortening and subsidence in the largely buried frontal part. The success of these models in reproducing some major features of the Northern Apennines tectonics and in describing the influence of key physical parameters in such a complex tectonic setting paves the way for future applications of the methodology in other settings.

6.5 Inverse modeling: Bayesian sampling method

Interseismic coupling on the Himalayan megathrust

A variety of enigmatic features of how megathrust segmentation can influence the extent of earthquake rupture led me to investigate the spatial variability of interseismic coupling along the Main Himalayan Thrust (Chapter 5). In collaboration with Prof. Romain Jolivet (ENS, Paris), I proposed a new interseismic coupling model obtained from the joint inversion of multiple data sets (GPS and leveling

data) in a fully Bayesian framework. In particular, using a careful description of uncertainties on the data and on the elastic stratification on the forward model, I derived the first probabilistic estimate of the interseismic coupling along the Himalayan megathrust (Dal Zilio *et al.* , 2019c). This approach allowed me to quantify the population of plausible coupling models that could fit the geodetic data, while accounting for forward problem uncertainties. The goal of this chapter was not only to obtain a trustworthy coupling distribution, but also a realistic estimate of uncertainties.

Results obtained from these models contradict previously published results, since they suggest a heterogeneous coupling of the megathrust interface, both along-strike and down-dip. In particular, potential barriers of low coupling separating discrete and large highly-coupled patches are inferred. Notably, these highly-coupled patches coincide with areas where historical large earthquakes propagated over the past centuries. As this Bayesian approach does not use any form of unphysical regularization, the inferred distribution of low-coupling zones depends only on the data used as input. Based on these results, it is likely that these low-coupling patches are substantial enough to act as barriers for dynamic ruptures.

The advances proposed in this chapter represent the next generation of source inversion models that are more resistant to over-fitting of data. Moreover, they provide a physical basis for the relative weighting between different data sets, and include a more realistic description of uncertainty in the inferred source model parameters.

6.6 Future perspectives

The full potential of this STM methodology is not yet reached, and rooms for improvements and further investigations are still widely open. From my perspective, there are three main areas of research associated with the seismo-thermo-mechanical methodology that could be pursued. These include (1) further numerical development of the STM methodology, aimed at improving the accuracy of physical processes, (2) application to several unresolved issues in mountain building processes and related seismicity, and (3) the extension of the STM methodology in

three-dimensions. Each of these avenues is briefly discussed below to illustrate the wide range of problems that one could attempt to tackle using this methodology.

Numerical developments

The most crucial limitation observed in this thesis concerns the too long duration of the coseismic phase and the resulting absence of distinct inertial dynamics. In this thesis this unfortunately had to be sacrificed, but improvements have been made by former group member Dr. Robert Herrendörfer. The key contribution of his PhD thesis was the methodological advancement of the STM modeling approach to overcome its physical and numerical limitations in 2D. He developed and implemented an invariant reformulation of rate-and-state friction (RSF) to investigate earthquake cycles along mature and spontaneously forming faults in a visco-elasto-plastic continuum (Herrendörfer *et al.* , 2018). This STM-RSF approach resolves a wide range of time scales during earthquake cycles through the implementation of an adaptive time stepping scheme. In particular, he demonstrated that this method is capable of resolving the dynamic time of an earthquake cycle, including dynamic rupture propagation. However, so far this STM-RSF approach has only been applied in a relatively simple model setup on the time scale of multiple earthquake cycles.

Merging the models presented in this thesis with the recent developments of this numerical framework remains a non-trivial challenge and a promising future research direction to truly bridge geodynamic and seismic time scales. An adequate completion of these numerical developments would improve our physical understanding of the cause-effect relationships between the long-term tectonic evolution of collisional orogens and short-term seismicity. Most importantly, successfully executed applications of this approach could also trigger a snowball effect with large impact on the geodynamic and seismological communities and ultimately influence the seismic hazard community.

Potential applications

The presented results give insights into the interplay between earthquakes, the seismic cycle, and the long-term mountain building processes. Some of these results have posed the basis for further research that need to be done in order to better understand these complex geological systems. One potential application is to investigate afterslip phenomena in a more accurate manner, and validate them against postseismic GPS velocities. One example of a unique and intriguing observation comes from the 2015 $\mathrm{M_w}$ 7.8 Gorkha–Nepal earthquake, which ruptured the lower edge of the interseismically locked portion of the Main Himalayan Thrust (MHT) and was followed by distributed postseismic deformation in the Himalaya and southern Tibet. A number of studies have documented and analyzed the postseismic deformation following the Gorkha earthquake (e.g., Gualandi *et al.* , 2017) and have disagreed on the processes responsible for transient postseismic deformation. Some inferred that the deformation was due to afterslip downdip of the coseismic rupture (Wang & Fialko, 2018) and others suggested a visco-elastic relaxation as the dominant process (Zhao *et al.* , 2017). Although cumulative 1.5-year postseismic displacements can be fit to afterslip downdip of the rupture in a kinematic inversion, the afterslip distribution invoked extends >100 km downdip from the coseismic rupture with nearly uniform slip, a behavior that is normally not predicted by simple stress-driven forward models. Coupling the newly developed STM-RSF approach with the model presented in Chapter 4, which accounts for realistic distribution of temperatures, non-linear rheologies, stresses, and megathrust geometry, has the potential to get new insights on the causative processes at depth. In particular, this would allow for focused testing of the elastic rebound in the shallow crust, aseismic afterslip surrounding the coseismic rupture areas, and viscoelastic relaxation in the lower crust and upper mantle.

Another long-standing issue in the Himalaya stems from the poorly constrained spatial and temporal relationships between permanent and transient vertical deformation, leading to an unresolved causal relationship between the two. A physics-based, rheologically consistent STM-RSF model accounting for a realistic present-day setup of the Himalayan wedge would allow to resolve all stages of the seismic cycle with a wide spectrum of slip processes. This could provide a new under-

standing of how the main fault in the Himalayan mountain range operates over the long-term. It could also highlight the role for the Himalayan megathrust and/or other faults in the growth of Earth's highest mountains, both during individual earthquakes and at longer interseismic periods.

Modeling seismic cycles in three-dimensions

Another important numerical improvement is the extension to three dimensions in order to capture lateral propagation possibilities, triggering, and complexities. During my PhD, the 3D version of the STM code was simultaneously developed by PhD student Casper Pranger (ETH Zürich), with the focus on flexibility, stability, and accuracy. At the same time, this code incorporates new ideas that more efficiently solve for the new component of seismic wave propagation. The 3D STM modeling method is in its infancy and still requires substantial benchmarking and validation.

Benchmarking the new 3D code has the highest priority, since the execution of future tasks — each requiring a considerable time investment — depends on it. Specifically, these benchmarks consist of a set of exercises to prove that the code fulfills its specification in simulating dynamic earthquake ruptures and sequences of earthquakes and aseismic slip (Harris *et al.* , 2018; Jiang & Erickson, 2018). From my perspective, once the 3D code is finalized and benchmarked, I would like to explore the physical mechanisms influencing the along-strike megathrust segmentation on lateral rupture propagation. This goal has very important implications for both hazard assessment and understanding earthquake physics, because if seismicity is not random, key characteristics of large earthquakes can be forecast through analysis of physical properties.

The Himalayan–Tibetan belt represents an ideal example to test different hypothesis. In fact, lateral variations along the Himalayan arc are suggested by an increasing number of studies and carry important information about the orogen's segmentation (e.g., Hetényi *et al.* , 2016b). Recent studies suggest that the geometry of the Himalayan megathrust varies significantly along strike (e.g., Hubbard *et al.* , 2016) and that the intersection of Indian basement and the Main Frontal thrust coincides with at least three major subsurface ridges (e.g., Arora *et al.* , 2012),

which may play a role in segmenting the range. To provide answers within our lifetimes, extensive 3D numerical studies are needed in order to extrapolate results. This will allow for the evaluation of the effectiveness and behavior of physical parameters in generating megathrust segmentation observed both interseismically (Chapter 5, Dal Zilio *et al.* , 2019c) and coseismically (Chapter 4, Dal Zilio *et al.* , 2019a). However, performance estimates of the envisioned 3D models currently indicate that only modeling part of the Himalayan arc is feasible at present due to the tremendous computational costs associated with larger model setups.

On the side of applications, using the distinct advantages of these 3D models could ultimately result in covering weak spots in current hazard assessment approaches. This means that such models can enhance our capabilities of estimating hazard off known faults. Moreover, these new depth-wise 3D models can potentially contribute to improve understanding of seismic hazard in densely populated areas such as the Alps and Apennines (e.g., AlpArray Working Group[1]: Hetényi *et al.* , 2018) and Himalaya (e.g., Namaste project[2]: Karplus & Velasco, 2015).

On the longer term, organizing seismotectonic information for major plate boundaries is crucial for understanding the spectrum of expected behavior of a fault zone after a major event has occurred (and indeed beforehand), and is the foundation of any framework for better communication of time-dependent earthquake hazards to affected communities (Jordan & Jones, 2010). From a personal point of view, these research efforts will provide a wealth of new insights in the next years and will create important synergies between the communities of geodynamics, seismotectonics and earthquake physics. A successful execution of these tasks will thus bridge the existing gap between geodynamics and seismology and thereby ignite new research in both communities and at their cross-roads.

1 **AlpArray** is a **European** initiative to advance our understanding of orogenesis and its relationship to mantle dynamics, plate reorganizations, surface processes and seismic hazard in the Alps-Apennines-Carpathians-Dinarides orogenic system. The initiative integrates present-day Earth observables with high-resolution geophysical imaging of 3D structure and physical properties of the lithosphere and of the upper mantle, with focus on a high-end seismological array.

2 Following the April 25, 2015 Gorkha magnitude 7.8, a collaborative team from different universities deployed an NSF rapid-funded aftershock array of 45 seismic stations (41 broadband and short-period seismometers, 14 strong motion sensors) across the Main Himalayan Thrust (MHT) fault where the large earthquakes occurred. The array, known as the Nepal Array Measuring Aftershock Seismicity Trailing Earthquake (**NAMASTE**) remained in place for 11 months, allowing for a unique data set right over the active Himalayan thrust system.

A

Tectonics and seismicity in the Northern Apennines driven by slab retreat and crustal delamination

A similar version of this appendix is under review as:
D'Acquisto, M., Dal Zilio L., van Dinther, Y., Molinari, I., Kissling, E., and Gerya, T. V.
Tectonics and seismicity in the Northern Apennines driven by slab retreat and crustal delamination

A.1 Abstract

Understanding how long-term subduction dynamics relates to short-term seismicity and shallow tectonics is a challenging but crucial topic in seismotectonics. We attempt to address this in the context of the Northern Apennines orogenic belt, which displays characteristic tectonic and seismogenic behaviors on a wide range of spatiotemporal scales. We use a visco-elasto-plastic seismo-thermo-mechanical (STM) modeling approach with a realistic 2D setup based on available geological and geophysical data. Subduction dynamics and seismicity are simulated together and are driven solely by slab pull, in accordance with regional geodynamics. Our numerical experiments suggest that lower crustal rheology and lithospheric mantle temperatures modulate the crustal tectonics of the Northern Apennines. Results indicate that the observed spatial distribution of the upper crustal tectonic regimes requires buoyant and highly ductile material beneath the suture zone. This allows protrusion of the asthenosphere in the lower crust, lithospheric delamination, and slab retreat. The resulting horizontal velocities and principal stress axis orientations agree with observations, thus suggesting that slab delamination and retreat are compatible with regional deformation. Our simulations successfully reproduce the presence of seismicity in the thrust front and on normal faults in the interior of the range. Slab temperatures and lithospheric mantle stiffness distinctly affect the

cumulative seismic moment released by and the spatial distribution of upper crustal earthquakes. The properties of deep, sub-crustal material are thus shown to influence model shallow seismicity, even though the upper crust is largely mechanically decoupled from the lithospheric mantle. Our simulations therefore highlight the important effect of deep crustal rheologies and self-driven subduction dynamics in controlling the shallow, brittle deformation and related seismicity during an ongoing orogeny.

A.2 Introduction

The Northern Apennines are a tectonically and seismically active orogen located where the continental part of the Adriatic plate underthrusts the Tyrrhenian domain of the European plate (Fig. A.1). It results from asymmetrically eastward slab retreat and trench migration in a northwest-directed subduction zone (Faccenna *et al.* , 2004), and is characterized by the ongoing migration of two opposing tectonic regimes (Devoti *et al.* , 2008; Carminati & Doglioni, 2012). The frontal area is an active thrust belt with tectonic convergence at a rate of 2–3 mm yr^{-1} (Bennett *et al.* , 2012). Most of it is subsiding at rates of ~4–5 mm yr^{-1} (but locally as fast as 9 mm yr^{-1}) and is buried by the foreland basin sediments of the Po Plain (Devoti *et al.* , 2008, 2011; Serpelloni *et al.* , 2013). Buried thrusts produce earthquakes from the surface of the plain to a depth of 20 km and at 20–35 km depth beneath the most external, northeastern part of the range (Chiarabba *et al.* , 2005). In the mountains further south and west the thrust belt is inactive and is dissected by normal faults (Doglioni *et al.* , 1996; Collettini *et al.* , 2006), which results in internal extension (at ~2–3 mm yr^{-1}), and modest uplift (up to ~1 mm yr^{-1}) (Bennett *et al.* , 2012; Devoti *et al.* , 2011; Serpelloni *et al.* , 2013). Previous studies invoked lithospheric delamination as the main mechanism controlling the regional tectonics and seismicity (Chiarabba *et al.* , 2014; Benoit *et al.* , 2011). Such a mechanisms would imply that the local buoyancy structure and lithospheric ductility play a crucial role in the dynamics of the orogen. Therefore, the dynamics of the orogen might be explained by internal driving forces and rheological structure.

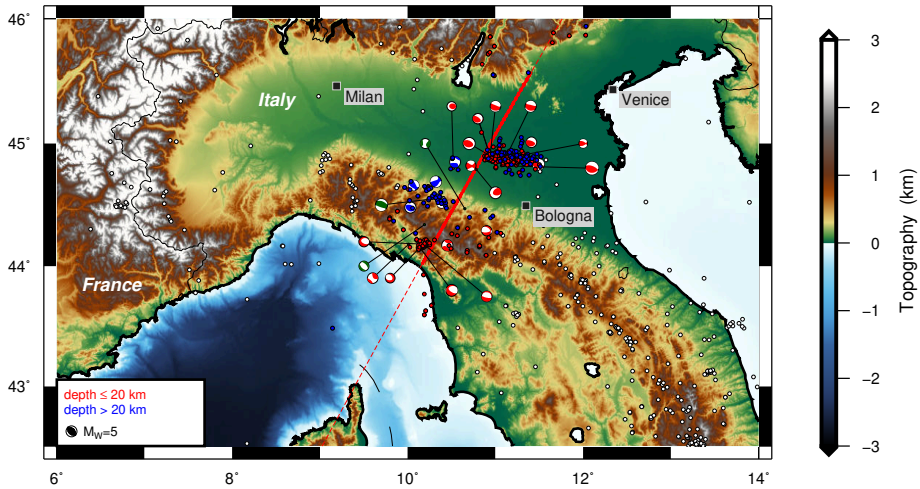


Figure A.1.: Topographic map of the northern Apennines and surroundings, showing in red the trace of the reference profile (thick line) and its continuation (thin, dashed). Also shown are earthquake locations and select focal mechanisms within 25 km of the profile. The radius of the latter scales linearly with magnitude. Hypocenter locations with no mechanism were determined by Chiarabba *et al.* (2014) on the basis of INGV recordings of earthquakes occurred between 28 February 2005 and 31 December 2014. Focal mechanisms are from an updated version (covering from 1977 to 2015) of a compilation of CMT solutions in the Italian region (Pondrelli *et al.* , 2006).

The tectonics and seismicity of the area have been the subject of renewed interest following the 2012 Emilia-Romagna earthquakes (Fig. A.1). That seismic sequence which had two main shocks of $\mathrm{M_w}$ 5.9 and 5.7, respectively, and activated part of the external thrust front complex (Scognamiglio *et al.* , 2012; Tertulliani *et al.* , 2012). Historical seismicity includes several earthquakes similarly located on blind thrusts in the plain and at the base of the mountain range. These events have a maximum estimated $\mathrm{M_w}$ of 6.1. The middle and external parts of the range, further to the southwest, are also seismically active. Earthquakes there are related to shallow normal faults and extensionally reactivated thrusts. Among them is the largest known event in the area, the $\mathrm{M_w} \approxeq 6.5$ Lunigiana-Garfagnana earthquake of 1920 (Rovida *et al.* , 2016).

Studies of observed seismicity and surface deformation have illustrated the earthquake source mechanisms and active structures in the Apennines belt (e.g., Tizzani *et al.* , 2013; Cheloni *et al.* , 2016; Pezzo *et al.* , 2014; Stramondo *et al.* , 2014). However, it is difficult to obtain a full picture of the seismicity and tectonics of the area and its relationship with the deep structure and geodynamics of the

orogen. This is due to the relatively low strain rates (~10^{-6} yr^{-1}, Chiaraluce *et al.* , 2005) and resulting relatively low magnitudes ($M_w \leq 6.5$, Rovida *et al.* 2016) and long (>160 yr) recurrence time of the largest earthquakes (Mantovani *et al.* , 2015). The reasonably well-known internal structure and surface observations of active deformation of the Northern Apennines can be used as a starting point to shed light onto the long-term dynamics and large-scale structure of the area and its influence on tectonics and short-term seismicity.

The link between lithospheric–scale structure and geodynamics and the resulting crustal tectonics has already been the subject of several observational studies. For instance, maximum earthquake size in subduction zones was suggested to correlate with convergence rate and lithospheric age (and thus temperature and slab pull) (e.g., Ruff & Kanamori, 1980). Furthermore, greater coupling between the slab and the rest of the subducting plate at the ocean floor was observed to correspond to less energy release via shallow megathrust earthquakes and more intermediate and deep seismicity (Conrad *et al.* , 2004; Bilek *et al.* , 2005). This is thought to reflect the effect of strength and structural integrity of the subducting plate on the localization of seismogenic brittle deformation. However, statistical correlations are often weak (e.g., Heuret *et al.* , 2011). Furthermore, such studies are often limited by the short observational period compared to the recurrence times of earthquakes and by the difficulty of studying systems governed by multiple, interacting processes occurring at tens to hundreds of kilometers of depth and across various spatio-temporal scales. Modeling is thus needed to reveal the physical processes connecting deep and shallow deformation over different time scales (e.g., Corbi *et al.* , 2017; Dal Zilio *et al.* , 2018b).

To investigate the mechanisms controlling the regional tectonics and to address the limitations of existing research in considering long time periods and linking small-scale tectonics and seismicity to large-scale dynamics and structure, this study uses a seismo-thermo-mechanical (STM) modeling approach slip (van Dinther *et al.* , 2013b). This can simulate long-term elastic deformation of the lithosphere, dislocation creep and mantle flow together with short-term brittle-plastic failure and fault slip associated with accumulated elastic stress release, ensuring that faults can be loaded tectonically by velocities and stresses resulting from slab pull. Our model setup is thus based on the hypothesis that lithospheric dynamics driven

by slab pull (i.e., with no imposed shortening or extension) can largely explain the active tectonics and seismicity of the modeled retreating subduction/collision system.

We performed a series of numerical experiments in order to both investigate the retreating subduction/collision system and to identify a set of best-fit model parameters allowing to approximate the present-day spatial distribution of compressional and extensional normal stresses and of surface velocities. This is achieved by varying the rheology of the lower crust and the temperature of the slab, the asthenospheric wedge and of the lowermost crust of Adria. Once the location of present-day tectonic regimes is broadly reproduced, the resulting seismogenic ruptures and surface displacement are analyzed in comparison with observations. Subsequently, we study how these short-term features are affected by slab pull and lithospheric rheology.

A.3 Methodology and setup

A.3.1 Seismo-thermo-mechanical modeling

The STM modeling method was developed, described, and first applied by van Dinther *et al.* (2013b). This code is based on a finite-difference, marker-in-cell geodynamic code that solves the momentum, continuity equation and temperature equations (Gerya & Yuen, 2007; Gerya, 2010).

In the STM method, the rheological relation between deviatoric stress σ'_{ij} and strain rate $\dot{\varepsilon}_{ij}$ consists of Maxwell viscoelasticity and brittle-plastic yielding with strength σ_{yield}:

$$\dot{\varepsilon}'_{ij} = \frac{1}{2\eta}\sigma'_{ij} + \frac{1}{2G}\frac{D\sigma'_{ij}}{Dt} + \begin{cases} 0 & \text{for } \sigma'_{II} < \sigma_{yield} \\ \chi \frac{\partial \sigma'_{\mathrm{II}}}{\partial \sigma'_{ij}} = \chi \frac{\sigma'_{ij}}{2\sigma'_{\mathrm{II}}} & \text{for } \sigma'_{\mathrm{II}} = \sigma_{yield} \end{cases}, \tag{A.1}$$

where G is the shear modulus, $\frac{D}{Dt}$ the objective co-rotational time derivative, $\sigma'_{\mathrm{II}} = \sqrt{\sigma'^2_{xx} + \sigma'^2_{xz}}$ the second invariant of the deviatoric stress tensor, and χ a plastic multiplier which connects strain rates to stresses during yielding (Gerya & Yuen,

2007). Non-plastic effective viscosity η is computed as a function of stress according to a non-linear flow law with dependence on pressure P and temperature T:

$$\eta = \frac{\sigma'^{\,1-n}_{\mathrm{II}}}{2A_D} \exp\left(\frac{E_a + PV_a}{RT}\right), \tag{A.2}$$

with R the universal gas constant, n the exponential coefficient, A_D the pre-exponential factor, E_a and V_a the activation energy and volume (Ranalli, 1995).

The yield strength is defined by the Drucker-Prager criterion

$$\sigma_{yield} = C + \mu_{eff} P, \tag{A.3}$$

with compressive strength C and effective friction coefficient $\mu_{eff} = \mu(1-\lambda)$, where μ is the internal friction coefficient of the material and λ is the pore fluid pressure factor, i.e. the ratio $\frac{P_{fluid}}{P}$ between fluid pressure P_{fluid} and total pressure P. When σ'_{II} exceeds the yield criterion, the effective viscoplastic viscosity η_{vp}, otherwise equal to η, becomes $\eta \frac{\sigma'_{\mathrm{II}}}{\eta\chi + \sigma'_{\mathrm{II}}}$. To allow the spontaneous nucleation and propagation of rupture events, friction depends on slip rate V as

$$\mu = \mu_s - (\mu_s - \mu_d)\frac{V}{V_c + V}, \tag{A.4}$$

where static and dynamic friction coefficients μ_s and μ_d, respectively, and characteristic velocity V_c.

In our models, μ_d is set to 30% of μ_s after Di Toro *et al.* (2011) and V_c is 4.4 mm yr^{-1} following van Dinther *et al.* (2013b). The slip velocity (V) is computed as

$$V = 2\,\dot{\varepsilon}_{\mathrm{II},vp}\,\Delta x, \tag{A.5}$$

where Δx is grid size, and $\dot{\varepsilon}_{\mathrm{II},vp}$ is visco-plastic strain rate invariant.

A.3.2 Model setup and observational constraints

Figure A.2 presents our reference model setup based on a geological profile and geophysical data such as seismic tomography, reflection seismology and receiver functions. Following the approach of Dal Zilio *et al.* (2019a), the setup image is

used to assign the material parameters according to the initial geometry through the use of the GeoMAC tool.

We design the initial configuration on the basis of a geological and structural profile of Molli *et al.* (2010). We selected this profile because it synthesizes various geological and geophysical observations into a schematic yet detailed cross-section extending to middle crustal depths. The Adriatic lower crust follows the lithospheric mantle downwards and represents the low-velocity zone identified at moderate depths (35–55 km) beneath the middle and southwestern side of the range, above the Adriatic mantle (Di Stefano *et al.* , 2009). Moho geometry follows a cut through the model of Spada *et al.* (2013a) and includes two distinct and partly overlapping segments (Adriatic and Tyrrhenian), in accordance with the receiver function study of Bianchi *et al.* (2010). The lithosphere-asthenosphere boundary is 100–120 km deep beneath the southern Po Plain and northernmost Apennines and around 70 km deep beneath the eastern coast of the Ligurian sea (Panza *et al.* , 2003). In accordance with the teleseismic tomography of Benoit *et al.* (2011), a sub-vertical slab of lithospheric Adriatic mantle extends down to 400 km depth.

The reference set of material properties corresponding to each rock type is shown in Table A.1. Three different lower crustal rheologies are tested, as their ductility is expected to control the style of deformation. Following Faccenda *et al.* (2009) and Ranalli (1995), these are mafic granulite, plagioclase, and wet quartzite.

The model temperature field is initialized on the basis of a self-consistent simulation of retreating subduction with a generic initial geometry. The initial temperature field accounts for model geometry and includes a cold accretionary crustal wedge, a hot asthenospheric wedge, and a lithosphere-asthenosphere boundary at around 1300 $^{\circ}\mathrm{C}$. The maximum depths of earthquake hypocenters, relocated and personally provided by Chiarabba *et al.* (2014), are used as a broad indicator of the location of the thermally determined brittle-plastic transition, keeping in mind that seismicity has been observed beneath the Apennines in hotter areas than normally expected (Pasquale *et al.* , 2010). The isotherms in the asthenospheric mantle follow an adiabatic thermal gradient of $\sim$0.5 $^{\circ}\mathrm{C\,km^{-1}}$ (Katsura *et al.* , 2010). The top of the crustal basement has a temperature of around $200\ ^{\circ}\mathrm{C}$, in accordance with the thermal model inverted by Pasquale *et al.* (2013). For the initial thermal setup, temperature contours are designed with 100 $^{\circ}\mathrm{C}$) intervals. These isotherms are then

interpolated to the entire temperature field using the biharmonic splines method. To explore possible range of temperatures, we also test alternative versions of the temperature field. In particular, we vary the isotherms in the poorly constrained areas that might control the large-scale tectonic regime: (i) the subducted slab and (ii) the deep suture area between Adriatic and Tyrrhenian lithospheres (Fig. A.3).

A.3.3 Model settings

The boundary conditions used are free-slip on all boundaries and zero lateral P gradient at the four corners (with $P = 0$ at one point at the top). Lateral boundaries are zero-heat-flux, while the top has fixed T (0 °C) and the bottom a fixed T gradient

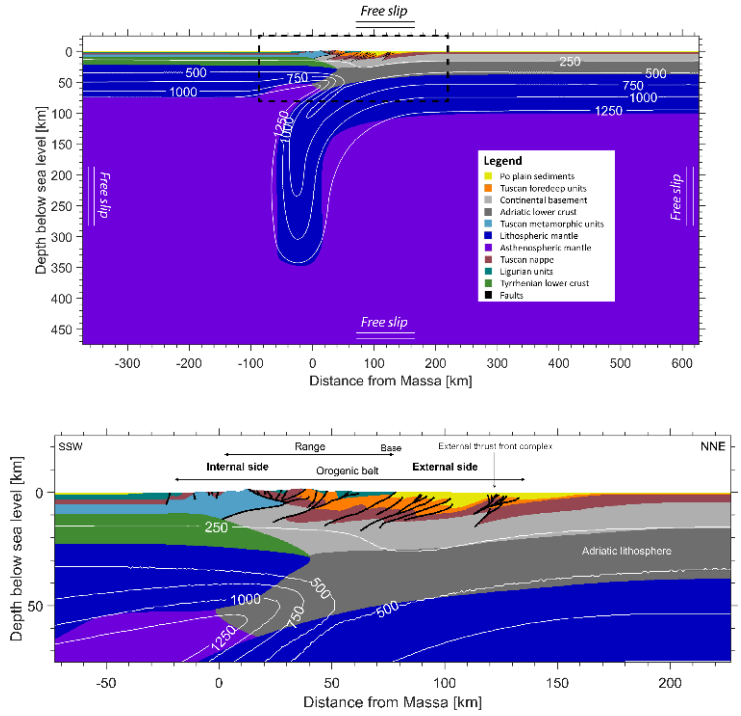


Figure A.2.: Reference model setup showing the distribution of the different rock types, as well as the isotherms of the reference temperature setup (with values in °C) and the velocity boundary conditions. (a) Full setup. (b) Zoom on the area outlined in (a), showing the details of the lithospheric setup. The labels and arrows show the location of the whole orogen and of the mountain range and identify the two lithospheric domains. Horizontal distance is measured northeastwards along the profile trace, starting from the city of Massa.

Table A.1.: Initial rheological and other physical parameters for each material type in the reference model. For all materials, $\rho = \rho_0[1-\alpha(T-298)][1+\beta(P-0.1MPa)]$ and $\mu_d = 0.3\mu_s$. All rock types (faults included) have $\alpha = 3\cdot10^{-5}$ °C, $\beta = 10^{-5}$ MPa^{-1}, and $C_p = 1000$ J Kg^{-1}. Air has $\alpha = 0$ °C^{-1}, $\beta = 0$ MPa^{-1}, and $C_p = 3.3310^6$ J kg^{-1}. The static friction coefficient μ_s is 0.3 on faults, 0.8 in the mantle, 0.6 in other rock types and 0 in air. The pore fluid pressure parameter λ is 0.4 in the mantle and lower crusts, 0.6 elsewhere. In the formulas for k, P and T are in SI units.

Quantity Units	η_0 $Pa^n \cdot s$	n –	E_a kJ	V_a $\frac{J}{bar}$	G GPa	C MPa	μ_s –	λ –	ρ_0 $\frac{kg}{m^3}$	k $\frac{W}{°Cm}$	H_r $\frac{nW}{m^3}$
Sticky air	$1.00\cdot10^{17}$	1.0	0.00	0.0	700	0	0	0	1	200	0
Po Plain sediments	$1.97\cdot10^{17}$	2.3	154	0.6	50	3	0.6	0.6	2800	$\left[0.64+\frac{807}{T+77}\right]$ $e^{4\cdot10^{-6}P}$	1500
Tuscan foredeep units	$1.97\cdot10^{17}$	2.3	154	0.8	50	5	0.6	0.6	2800	$\left[0.64+\frac{807}{T+77}\right]$ $e^{4\cdot10^{-6}P}$	1500
Continental basement	$1.97\cdot10^{17}$	2.3	154	1.2	50	10	0.6	0.6	2900	$\left[0.64+\frac{807}{T+77}\right]$ $e^{4\cdot10^{-6}P}$	1000
Adriatic lower crust											
Mafic granulite	$1.13\cdot10^{21}$	4.2	445	0	120	5	0.6	0.4	2900	$\left[1.18+\frac{474}{T+77}\right]$ $e^{4\cdot10^{-6}P}$	250
Plagioclase (An75)	$4.80\cdot10^{22}$	3.2	238	0	25	5	0.6	0.4	3000	$\left[1.18+\frac{474}{T+77}\right]$ $e^{4\cdot10^{-6}P}$	250
Wet quartzite	$1.97\cdot10^{17}$	2.3	154	0	10	5	0.6	0.4	3000	$\left[1.18+\frac{474}{T+77}\right]$ $e^{4\cdot10^{-6}P}$	250
Tuscan metamorphics	$2.80\cdot10^{22}$	3.2	238	0.8	50	26	0.6	0.6	2900	$\left[1.18+\frac{474}{T+77}\right]$ $e^{4\cdot10^{-6}P}$	250
Mantle (lithosphere)	$3.98\cdot10^{16}$	3.5	532	0.8	50	5	0.8	0.4	3300	$\left[0.73+\frac{1293}{T+77}\right]$ $e^{4\cdot10^{-6}P}$	22
Mantle (asthenosphere)	$3.98\cdot10^{16}$	3.5	532	0.8	50	5	0.8	0.4	3300	$\left[0.73+\frac{1293}{T+77}\right]$ $e^{4\cdot10^{-6}P}$	22
Tuscan nappe	$1.97\cdot10^{17}$	2.3	154	1.2	50	19	0.6	0.6	2850	$\left[0.64+\frac{807}{T+77}\right]$ $e^{4\cdot10^{-6}P}$	1000
Ligurian units	$1.97\cdot10^{17}$	2.3	154	1.2	50	4	0.6	0.6	2800	$\left[0.64+\frac{807}{T+77}\right]$ $e^{4\cdot10^{-6}P}$	1000
Tyrrhenian lower crust	$1.25\cdot10^{21}$	4.2	154	0.8	50	5	0.6	0.4	2800	$\left[1.18+\frac{474}{T+77}\right]$ $e^{4\cdot10^{-6}P}$	250
Faults	$5.01\cdot10^{25}$	4.0	154	0.8	12	1	0.3	0.6	2900	$\left[1.73+\frac{1293}{T+77}\right]$ $e^{4\cdot10^{-6}P}$	22

(2.413 °C km^{-1}) at the bottom. A 25-km-thick weak "sticky air" layer ($\sigma_{yield} = 0$, $\rho = 1$ kg m^{-3}, $\eta = 10^{17}$ Pa s) was placed at the top to approximate a free surface (Crameri *et al.* , 2012; Schmeling *et al.* , 2008). The models have a variable spatial resolution, from 250 m in the area of interest to 5 km at the edges and bottom. To minimize boundary effects, the model space extends vertically for 500 km and horizontally for 1000 km.

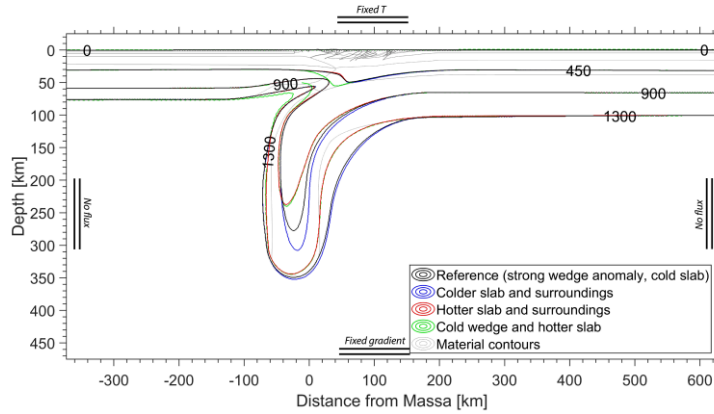


Figure A.3.: Contours of different interpolated temperature setups used in the models. For each setup, the same isotherms are shown. Each color corresponds to a different temperature setup. Boundary conditions are also shown. The thin grey lines, shown as a spatial reference, are material contours.

A.3.4 Modeling procedure

Models are run in two phases: (i) long-term, with timestep $\Delta t = 200$ yr, and (ii) short-term, with $\Delta t = 1$ yr. The long-term phase allows the model to develop self-consistent stresses and velocities and attain isostatic equilibrium. Once the stress configuration and crustal velocities are broadly consistent with present-day observations, the timestep size is progressively reduced to 1 yr. Then the model is run the for $20{,}000$ years in the short-term phase, during which seismogenic ruptures and surface velocities are recorded.

A.3.5 Evaluation of model seismicity

Seismic events are recognized in the models by the rupture detection algorithm of Dal Zilio *et al.* (2019a). The thresholds for seismogenic ruptures are a stress drop greater than 0.5 MPa, after Allmann & Shearer (2009), and a velocity of $4 \times 10^{-9}\,\mathrm{m\,s^{-1}}$. The moment magnitude M_w is computed according to the empirical scaling law

$$M_w = a + b \log_{10}(W), \tag{A.6}$$

where W is rupture width and $a = 4.1356$, $b = 1.6949$ are empirical coefficients (Wells & Coppersmith, 1994). Markers within a seismogenic event that rupture at the earliest time define the hypocentral region.

A.4 Results and analysis

A.4.1 Lithospheric and crustal dynamics

The present-day distribution of velocities and stresses in the study area of the northern Apennines can be broadly reproduced by our reference model, which combining high temperatures in the mantle wedge and lowermost crust with ductile lower crustal rheologies (Figs. A.3 and A.4a). This allows mantle material to protrude laterally at relatively high velocity (~20 mm yr^{-1}) into the lower crust. As a result, a hot, low-viscosity, increasingly weak channel forms above the Adriatic lithospheric mantle. The overlying upper crust, which forms the mountain range, is therefore decoupled from the slab and under extensional normal stresses. While the lithospheric mantle of Adria is partially delaminated, the area of the upper crust in front of the protruding material, including the Po Plain, is under compression.

The use of the weakest (wet quartzite) rheology for the lower crust in the reference model produces two adjacent, active tectonic regimes in the upper crust: extension and uplift throughout the range, compression and subsidence in the foreland (Fig. A.4b). This is in agreement with present-day observations and requires high temperatures in the mantle wedge and lowermost crust. In contrast, the use of the strongest (mafic granulite) rheology, produces a rheological coupling of the slab to the upper crust, regardless of temperatures. This leads to tectonic regimes opposite to the observed in the study area, with thrusting and subsidence in the range and extension and uplift in the Po plain (Fig. A.5a). On the other hand, the intermediate (plagioclase) rheology of the lower crust allows for wedge protrusion and lithospheric delamination only when the lower crust is brought to temperatures of over $450°C$. However, normal stresses in the range are partially compressional, the deep area 20–35 km beneath the base of the mountain range is not entirely

compressional, and the foreland past the external thrust front undergoes intense extension and uplift (Fig. A.5b).

Our further modeling attempts to produce realistic tectonic regimes with less ductile lower crust, such as by imposing a zone of eclogitic material or a localized shear zone at the deep suture between the two lithospheric domains, did not lead to compression throughout the Po plain without significant changes in the defined initial crustal and lithospheric geometry.

A.4.2 Seismicity and surface displacement

We analyze the short-term behavior of the reference model in terms of surface displacement and seismicity.

A.4.3 Surface velocities

Horizontal model velocities show a similar trend to GPS measurements by Devoti *et al.* (2011) with respect to stable Eurasia (Fig. A.6). Model velocities are lower by a roughly constant offset of $1.5 - 2$ mm yr^{-1}, probably due to the northwestward drift of the Adriatic plate in observations. Horizontal velocities in the plain and in the most external and internal parts of the range are in good agreement with most of the velocity data from Bennett *et al.* (2012). Model velocities describe horizontal shortening between the base of the range and the external buried thrust front as well as extension in the middle and external side of the chain. Vertical model velocities in the Apennines are compatible with some GPS observations (especially those by Bennett *et al.* 2012). In general, however, GPS data do not show consistent uplift in the mountain range like the models do. In the foreland, furthermore, the modeled subsidence peak is relatively low in amplitude (less than 5 mm yr^{-1}) and extends across the whole plain.

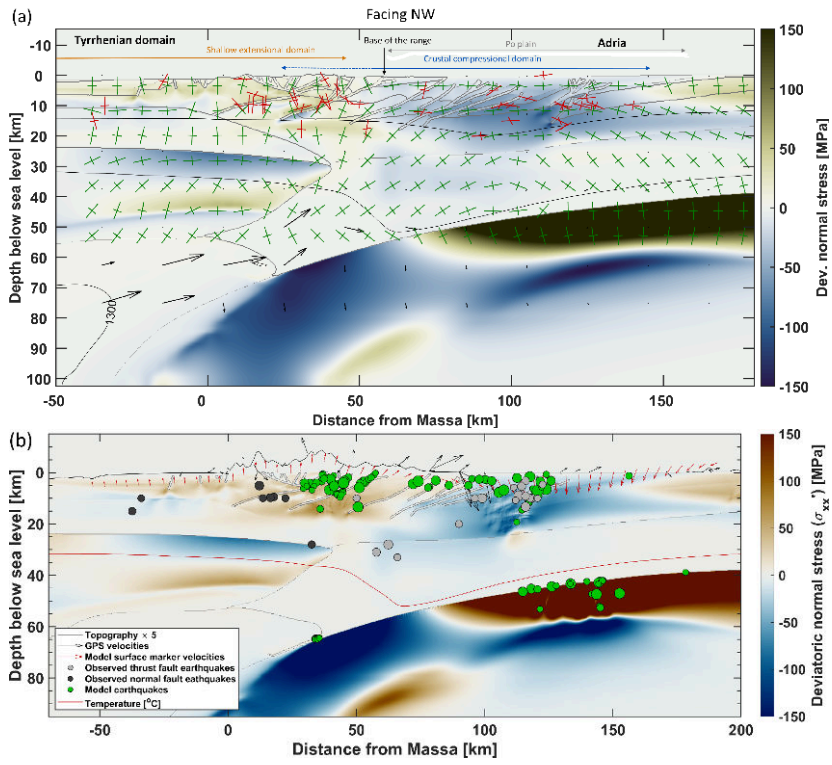


Figure A.4.: Deformation features of the reference model in comparison with observations. (a): deviatoric normal stresses, principal stress axes, and velocity vectors in the reference model. (b): deviatoric normal stresses, earthquake hypocentres surface velocities. Slab delamination-retreat and wedge protrusion lead to horizontal compression in the external part of the orogenic belt and extension in the internal part, in agreement with observations. Observed stress axes, velocities, and hypocentres are projected onto the profile from within 40 km of horizontal distance. The compressional (long) and extensional (short) principal stress axes are shown in brown for the model and in cyan for World Stress Map observations (Heidbach *et al.* , 2016). In (a), velocities are in 50,000:1 scale with respect to the plot axes: a length of 1 km in the reference frame of the axes corresponds to 20 mm yr^{-1}. In (b), the topography is vertically exaggerated and velocity arrows represent the average yearly displacement in 500,000:1 scale. Observed earthquake hypocenters with $M_w \geq 3.5$ are selected from an updated version of the CMT catalog of Pondrelli *et al.* (2006) and shown with diameter proportional to M_w. Deeper earthquakes are observed in the compressional regime (at 50–60 km horizontal distance, 25–35 km depth) and not reproduced in the model.

A.4.4 Seismicity and stresses

Crustal stresses in the reference model are extensional underneath the Apennines and compressional throughout the Po Plain (Fig. A.4b). Average shear stresses σ'_{xy} reach their highest magnitudes in the middle of the Po plain, in the external

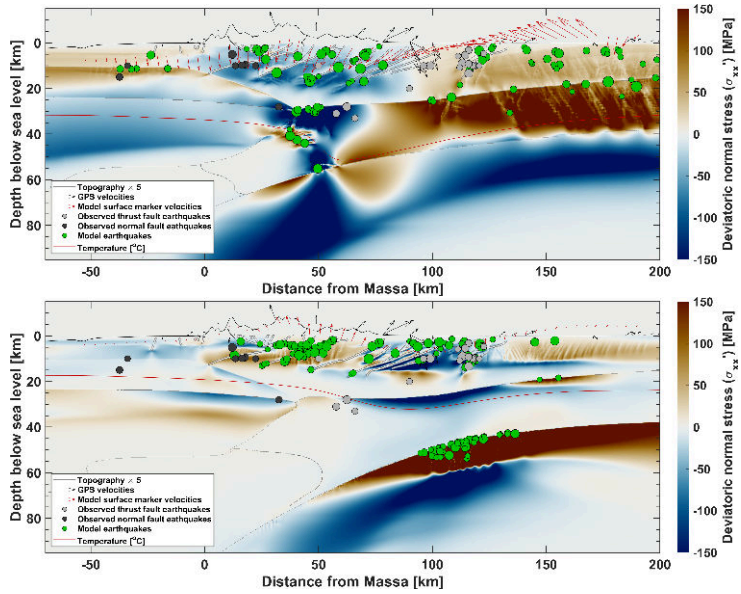


Figure A.5.: Comparison with observations of the deformation features of different models. (a): mafic granulite lower crusts and the same temperature setup as the reference model (hot mantle wedge, cold slab). The resulting pattern of tectonic regimes is opposite as what is observed in the Northern Apennines, with thrust-related seismicity and subsidence in the mountain range and with seismogenic extension and uplift in the plain. (b): plagioclase lower crusts and a hot lithosphere and slab. Lithospheric delamination-retreat and wedge protrusion are occurring. However, the mountain range is partly compressional and the external Po plain intensely extensional and uplifting, and the Moho geometry has deformed significantly from the initial setup. Observed topography, observed and modeled velocity arrows, observed earthquake hypocenters and model stresses and material contours are shown as in Fig. A.4b.

thrust front. In this area, on both the prescribed faults and off-fault ruptures, most of the modeled seismic moment release occurs.

Modeled earthquakes also occur on thrusts around the base of the range, which produce fewer earthquakes than the external thrust front itself (Fig. A.4b). This is in agreement with both instrumentally observed and historical seismicity, which tend to cluster on the external thrust front complex.

Extensional crustal seismicity in the reference model is focused in the middle of the range and is absent in its most internal part (distance along the profile $x < 25$ km). This is in agreement with earthquake locations observed tens of kilometers to the southeast and with the proposed source of the $\mathrm{M_w} \approxeq 6.5$ Lunigiana-Garfagnana earthquake of 1920 (Rovida *et al.* , 2016). Nevertheless, it should be noted that several earthquakes have been observed instrumentally along our reference profile

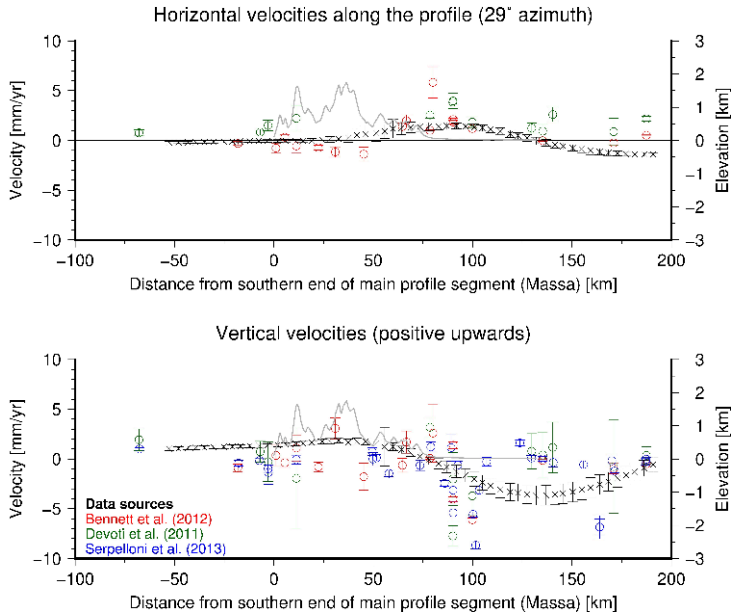


Figure A.6.: Average horizontal and vertical velocities of markers placed at the surface of the reference model. Only time periods between major seismogenic ruptures are considered. Published GPS velocities are shown for comparison, color-coded on the basis of the source paper and projected from within 40 km of the profile. Note that velocities from Bennett *et al.* (2012) are relative to the centroid of the regional GPS network used, whereas Devoti *et al.* (2011) take stable Eurasia as the reference frame and Serpelloni *et al.* (2013) use a global reference frame (ITRF2008). Vertical bars show an uncertainty of one standard deviation (1σ). Topography is outlined in light gray for orientation purposes.

at $x < 25$ km (Chiarabba *et al.* , 2005). The largest seismogenic ruptures in the model have a corresponding M_w of 6.65.

Reference model seismicity also includes events in the lithospheric mantle, at the top of the Adriatic slab. These occur on spontaneously formed normal faults located in the external hinge area of the bending slab (Fig. A.4b). Overall, the depth distribution of model earthquake hypocenters is bimodal, with a peak in the upper crust and one in the bending slab, and no events in the lower crust (Fig. A.7). Conversely, the cluster of instrumentally observed earthquakes located underneath the external thrust front only includes focal locations at middle- to -lower crustal depths (25-45 km).

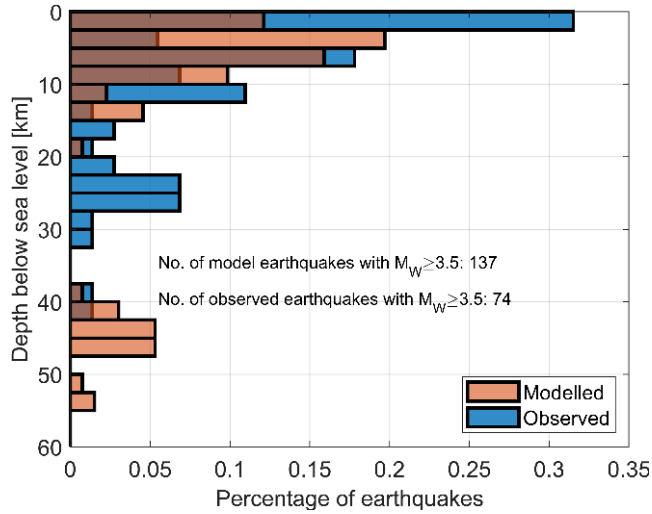


Figure A.7.: Depth distribution of earthquakes in the reference model. The relative depth distribution is compared with that of events in the updated instrumental seismicity catalog of Chiarabba *et al.* (2005) within 25 km of horizontal distance from the profile.

A.4.5 Slab pull controlling the distribution of seismicity

In a novel development, we directly link slab pull and seismogenic ruptures in the same simulation. To this end, we perform two numerical experiments to explore the importance of slab pull in driving the dynamics of the northern Apennines. In these experiments, we use alternative temperature setups (Appendix A.3.2 and Fig. A.3) with different isotherms in and around the slab, thus altering its buoyancy. This also allows us to explore the effect of different mantle temperatures on model dynamics, which is important given the lack of knowledge of the deep thermal conditions in the study area. Higher temperatures, corresponding to less negative buoyancy of the slab and thus to less slab pull, increase the intensity of crustal deformation (Fig. A.3) . Conversely, lower temperatures increase slab pull and reduce deformation. This occurs despite the absence of strong mechanical coupling between the upper crust and the slab (Fig. A.3). The effect of slab temperatures on deformation is manifested in the total seismic moment released and seismic rates (Fig. A.8). In fact, the hotter slab reduces the moment released in both crustal regimes to around 20% of its value in the reference model. The seismic rate in the crust is also reduced, though unevenly in the two regimes. The mountain range

under extensional stresses thus attains a considerably lower seismic rate than the active thrust belt.

The different magnitude of the effect of slab temperatures on seismic moment release and on seismic rates is consistent with the distribution of model stresses and seismicity. In particular, the reference model has a higher proportion of smaller earthquakes with respect to larger ones in the extensional regime than in the compressional ones. Furthermore,$|\sigma_{xx}|$ and σ'_{II} are larger in the compressional regime. Therefore, the seismic rate in the extensional regime is more susceptible to weaker driving forces, as even a small reduction in crustal stresses stops the small extensional earthquakes from occurring. The influence of slab temperatures on crustal deformation is also evident in the surface velocities: the hotter, more buoyant slab increases horizontal and vertical velocities, while the hotter slab has the opposite effect. Based on our results, we can conclude that the lateral distribution of relative earthquake frequency and seismic moment release in the studied migrating orogen is critically controlled by the slab pull driving this system.

A.4.6 Effect of lithospheric mantle stiffness on seismicity

The impact of the properties of the lithospheric mantle on shallow tectonics is evaluated by varying its elastic stiffness. A higher shear modulus G in the lithospheric mantle leads to a stiffer, more rigid slab, which generally reduces slab bending and lithospheric delamination. As a consequence, less crustal deformation occurs. Therefore, less seismic moment is released in the crust, especially in the compressional domain (Fig. A.9). Model surface velocities are also affected. In particular, the upward component of velocity decreases by up to 1 mm yr^{-1} (for $G = 90$ GPa) in the external part of the mountain range (thus reducinguplift) and in the adjacent $\sim$ 50 km of the plain (which amounts to faster subsidence). Despite a general negative trend, the change in total seismic moment released with increasing slab G is variable. This could be due to a trade-off between two processes: on one hand, the lithospheric mantle undergoes less bending in response to the unchanged dynamic load. This forces the deformation due to ductile, hot mantle wedge and lower crust protrusion to localize to a greater extent in the crust, rather than in the bending

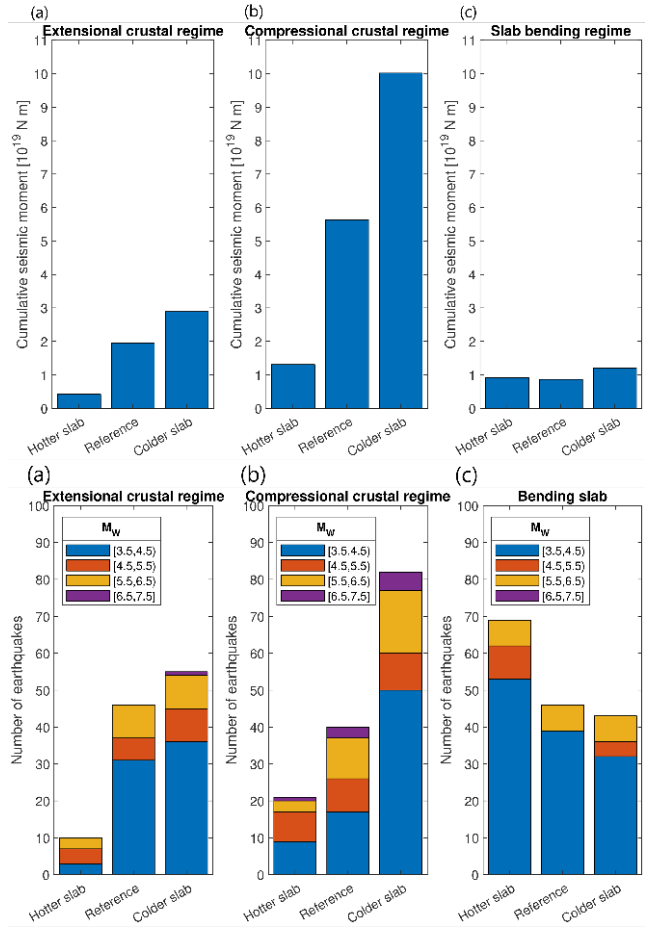


Figure A.8.: Comparison of the total released seismic moment M_0 (a-c), and number of earthquakes (d-f) in models with different temperatures in and around the slab. The isotherms corresponding to the different temperature setups used are shown in Fig. A.3. Increasing slab pull increases the seismic moment released in both the extensional and compressional regimes of the upper crust. It also increases the seismic rate in the crust and lowers it in the mantle. The two crustal regimes and the lithospheric mantle slab are selected manually. Only earthquakes with $M_w \geq 3.5$ are considered.

and downwelling of lithospheric mantle. On the other hand, greater stiffness slows down slab bending and thus overall deformation. Such influence of slab stiffness on seismicity highlights the importance of complex interactions between different subsurface regions. Furthermore, it highlights that small changes in stresses and displacements due to properties of material at sub-crustal depths (greater than 40 km) contribute to determining the lateral distribution and abundance of earthquakes.

A.4.7 Effect of rock strength on earthquake distribution

We also investigate the influence of the yield strength parameters on model tectonics. Yield strength is expected to strongly affect local stresses and the specific distribution for seismicity, while varying relatively little the overall stress and velocity pattern. To sum up, we find that both bulk rock strength and fault friction (which determines fault strength) do influence the intensity and distribution of simulated seismicity. In particular, increasing or decreasing the bulk strength, either uniformly throughout the model or through the pore fluid pressure in specific rock types, accordingly increases or decreases the seismic moment M_0 released. The effect on total seismic rate in the different regimes is not uniform. This is because the various regimes and combinations of model parameters produce different distributions of the M_0 release in earthquakes of different magnitudes. Fault friction, instead, affects seismic M_0 release in a less consistent way. Both decreasing and increasing fault friction reduce the M_0 released in the extensional regime. Conversely, the effect of increasing friction on M_0 release in the compressional regime is monotonic. This implies that the lateral distribution of the intensity of seismicity, in terms of M_0 release, is significantly affected by fault friction, because of the different stress loading regimes active in different areas in the model.

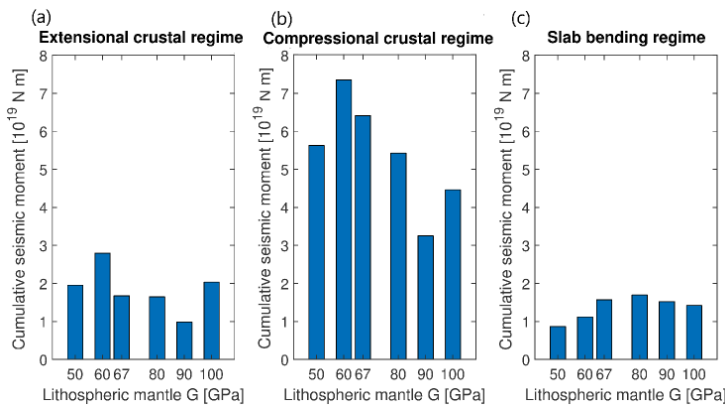


Figure A.9.: Comparison of the total seismic moment M_0 in models with different shear modulus G in the lithospheric mantle. Slab stiffness affects the lateral distribution of crustal seismicity. The two crustal regimes in (a) and (b) and the bending lithospheric mantle hinge regime in (c) are considered separately and selected manually, looking at the distribution of ruptures in space. Only earthquakes with $M_w \geq 3.5$ are considered.

Overall, the strength of bulk rock and of predefined faults determine the specific lateral distribution of seismicity across the model. However, the magnitude of the impact of strength, especially of bulk rock, on seismic moment release is not dominant with respect to the effect of the temperature and stiffness of the lithospheric mantle (Appendices A.4.5 and A.4.6). Therefore, our simulations suggest that the elastic and thermal properties of deep material, in the particular geodynamic setting of the northern Apennines, can be of comparable importance in controlling crustal seismicity as the mechanical strength of the crust. This is a significant result, given that rock and fault strength are usually paid much more attention than any deep properties when studying seismicity on complex fault systems.

A.5 Discussion

A.5.1 Surface deformation and GPS observations

The horizontal components of model velocities delineate moderate surface extension in the external part of the range and shortening in the adjacent Po plain foreland, in agreement with GPS observations by Devoti *et al.* (2011). Vertical model velocities delineate the pattern of uplift in the mountain range and subsidence in the foreland generally observed for the Northern Apennines. Maximum earthquake magnitudes are also realistic. Furthermore, upward model velocities are in agreement with exhumation rates estimated near the southwestern end of our reference profile (~0.7 mm yr^{-1} on average, 1.8 mm yr^{-1} maximum; Balestrieri *et al.* (2003)). However, GPS observations show a roughly even mix of uplift and subsidence in the mountain range (Fig. A.6). This suggest that either localized deformation overprints the slow uplift signal, or that broad tectonic uplift has recently ceased.

The downward velocities produced in the models form a broad peak more than 100 km wide. Conversely, in GPS observations directly along the profile, subsidence in the Po plain is focused in the vicinity of the range and reaches rates of 8 mm yr^{-1} or more. However, results from the geodetic study of Serpelloni *et al.* (2013)

are in better agreement with the subsidence rates produced in the model. In particular, their best-fit smoothed spline along a line ~50 km to the southeast of our profile defines an 80-km-wide peak beginning with an amplitude of less than 4 mm yr^{-1}. This suggests that subsidence in the eastern part of the Po Plain might be compatible with a lithospheric-scale velocity field dominated by lithospheric delamination and slab flexure and retreat, as proposed by Carminati *et al.* (2003). The lack of a lithospheric delamination-retreat signal in the observed vertical velocities could result from slab retreat and flexure being significantly slower or currently absent altogether to the northwest of the lithospheric tear proposed by Piccinini *et al.* (2014). Alternatively, shallow crustal processes such as fault creep and sediment deposition might mask the signal of lithospheric delamination-retreat.

A.5.2 Geodynamics

Our results show that lithospheric and asthenospheric dynamics driven only by the buoyancy anomalies of a slab and mantle wedge can lead to peculiar crustal tectonics in agreement with the key observations from the northern Apennines. In particular, two regimes are produced, which respectively combine modest uplift with horizontal extension and subsidence with compression. This characteristic pattern is explained in the models as the result of lithospheric deformation due to wedge protrusion and lithospheric delamination-retreat (Figs. A.4a and A.4b). The tectonic regimes resulting from this flow pattern are coupled and move together as a result of continued wedge protrusion. This is consistent with the observed northeastward migration of both the external thrust front and of the locus of extension over the past 30 Ma (Patacca *et al.* , 1990; Carminati & Doglioni, 2012; Faccenna *et al.* , 2004). Producing delamination-retreat in the models requires the presence of very ductile and buoyant material at the suture with the Tyrrhenian-Ligurian domain. Such material properties are obtained in the models through wet quartzite rheology for the Adriatic lower crust together with high temperatures. The importance of ductile lower crustal material decoupling the upper crust and lithospheric mantle, shown by the models (Figs. A.4b, A.5a and A.5b), is consistent with previous research. In particular, Benoit *et al.* (2011) explain the deep structure and magmatism of

the Northern Apennines in terms of delamination of the lithospheric mantle, which requires rheological weakness of the lower or middle crust. Furthermore, the rheology of Adriatic middle-lower lithosphere was inferred to control the orogen's tectonic style (Chiarabba *et al.* , 2014).

The ductile lower crust and resulting asthenospheric wedge protrusion in the models could not reproduce the thrust-related seismicity observed beneath the external part of the mountain range. This supports the idea that ductile deformation beneath the Tyrrhenian Moho is not occurring in the western sector of the Northern Apennines, while crustal underplating is likely taking place. Such an interpretation of regional tectonics was proposed by Thomson *et al.* (2010) from thermochronological observations and supported by Chiarabba *et al.* (2014). Nevertheless, the models indicate that ductility of deep material at the Tyrrhenian-Adriatic suture and ongoing lithospheric mantle retreat are needed to obtain realistic stress distribution pattern through solely local stresses and axis-parallel deformation.

A.5.3 Seismicity

Extensional seismicity in the models occurs on major faults—including reactivated thrusts—underneath the crest of the range, while compressional crustal seismicity is focused on the external thrust front complex. This is in agreement with observations.

The moderately deep seismicity (deeper than 20 km) observed underneath both the base of the range and the external thrust front is not reproduced in the models (Figs. A.4b and A.7). This suggests that the models might not be fully capable to capture the rheological and geological structure of the orogen. In particular, a high-viscosity and brittle lower crust in the Adriatic foreland seems to be present.

Seismicity in the models is sensitive to multiple physical parameters, delineating a complex non-linear system. The different models highlight the importance of a sufficiently ductile lower crust and mantle wedge in allowing a realistic velocity and stress distribution (Figs. A.4b and A.5). They also show how significantly slab pull affects crustal seismicity, particularly the seismic rate in the extensional regime and the seismic moment release in both the extensional and compressional regimes (Figs. A.8b and A.9). This suggest that the structure of the Northern Apennines

orogen probably includes a significantly cold and negatively buoyant subducting slab and a distinctly hot mantle wedge. The lack of observed earthquakes in the mantle, produced in the models through slab bending (Figs. A.4b and A.7), suggests that the lithospheric mantle in the models is either not strong or not ductile enough. However, it is possible that the regional seismic velocity models used to locate earthquake hypocenter systematically underestimate deep velocities and thus event depths. If so, at least some of the deeper earthquakes recorded there could indeed be located immediately below the Adriatic Moho.

A.5.4 Implications of deeper processes on upper crustal seismicity

The significance of results and conclusions from our numerical study may potentially go beyond the specific setting of the Northern Apennines. This study in particular shows the importance of long-term, large-scale dynamics on determining short-term tectonic regimes. It also shows the influence of deep temperatures, strength and stiffness on the specific distribution of crustal seismicity. This should be taken into account in numerical studies of seismogenic ruptures on fault networks through physics-based earthquake simulators (e.g. Dieterich & Richards-Dinger, 2010). Our simulations show that such parameters affect the stress loading and brittle rupturing pattern in a geometrically complex system of predefined faults and therefore alter the partitioning of earthquakes between different model regions. Tectonic loading in such complex fault systems is not a simple boundary condition adding uniform relative displacement and strain. Instead, it can be spatially complex and needs to be modeled self-consistently to be able to correctly reproduce the presence of seismicity in certain areas. Overall, both long- and short-term dynamics, and therefore the lower crustal rheologies and deep temperatures and material parameters that affect them, are needed for a complete physics-based probabilistic seismic hazard assessment of a complex region.

This study also implies that evidence of certain styles of lithospheric deformation can be used to constrain compatible crustal structure responsible for observed seismicity. Conversely, given an accurate, realistic rheological-structural model of the

crust, present-day observations can point towards plausible long-term lithospheric and asthenospheric flow patterns (Baumann & Kaus, 2015).

The sensitivity to various model parameters of the spatial distribution of earthquake epicenters shows that any attempt to understand the relationship between seismicity and lithospheric-scale geodynamics through modeling needs to accurately constrain the physical characteristics of the system. Importantly, rock stiffness and strength at depth and fault friction are shown to have far-reaching effects on the distribution of seismic rates. This influence is likely to hold for a variety of tectonic settings involving lithospheric-scale deformation, particularly in asymmetric patterns. Rupture simulations that assume a homogeneous, randomly or uniformly stressed, elastic background material and faults with relatively simple initial stress distributions are likely to be limited in their ability to approximate realistic earthquake distributions corresponding to complex fault systems.

A.5.5 Limitations

This study shows that STM modeling can partly reproduce the observed seismically active tectonic regimes in a system in which deformation is driven by buoyancy forces. This methodology can be applied to a variety of tectonic regimes in complex and diverse geodynamic settings. However, the limitations of our numerical methodology need to be considered. Two major limitations are the purely slip rate–dependent friction and the coarse temporal resolution. Both of these have been recently addressed in a newer version of the numerical code, which is yet to be tested on large-scale models (Herrendörfer *et al.* , 2018). Short-term model characteristics such as the duration of seismic events as well as their specific frequency and size may thus be affected, but the long-term stress regimes and resulting large-scale distribution of events in the extensional and compressional domains are likely to be robust. Another major limitation is the 2D model geometry. This allows a relatively simple model setup procedure and short run times, but implies the assumption of lateral homogeneity of the system, which is unrealistic for a real-world orogen.

A.6 Conclusions

We investigated the link between lithospheric-scale geodynamic deformation and relatively short-term tectonics through seismo-thermo-mechanical numerical modeling and comparisons with seismic catalogs and GPS observations. The results show that a large-scale dynamic regime driven by negative slab buoyancy can broadly reproduce the distinct adjacent, coupled, active extensional and compressional regimes of the Northern Apennines. The presence of high temperatures and a ductile rheology (here, wet quartzite lower crust) at the deep boundary between the two lithospheric domains in the area is crucial in reproducing a realistic deformation field. The ductile lower crustal material and the adjacent asthenospheric wedge protrudes upward and northwards as the slab sinks and retreats. It thus decouples the upper crust from the lithospheric mantle, which delaminates from the rest of the lithosphere. Substantial slab pull cotrols critically both the formation and the seismic activity of the two adjacent compressional and extensional tectonics domains of the orogen. Our models thus suggest that slab sinking and delamination-retreat allowed by lower crustal deformation are consistent with the tectonic configuration of the orogen (Chiarabba *et al.* , 2014; Benoit *et al.* , 2011). The surface velocity field produced in the simulations is coherent with the observed trends in horizontal displacements and with the rough location of the hinge between subsidence and uplift. However, the models have a more consistent uplift signal and a wider subsidence peak than observed in the westernmost sector of the orogen.

The success of STM modeling in reproducing some major features of the regional tectonics of the Northern Apennines and in describing the complex influence of key physical parameters on such tectonics paves the way for further applications of the methodology in other settings. The different combinations of parameters illustrate a complex system in which the temperature of the slab and surroundings controls the driving force through slab pull. Therefore, lower temperatures increase the intensity of upper crustal deformation. Other material properties and features such as strength, elastic stiffness, and slab temperatures also influence the specific features of crustal tectonics. The seismic rates in the different crustal regimes is unevenly affected, and therefore the lateral distribution of seismicity is altered. This is the case with the same imposed fault network geometry and despite the

overall dynamic and stress pattern being unchanged. The broader implication is that research aiming to model the distribution in time and space of seismogenic ruptures in complex fault systems should consider the effect of geodynamics and physical properties on the loading pattern of on- and off-fault rocks.

Bibliography

Aagaard, Brad T, Knepley, Matthew G, & Williams, Charles A. 2013. A domain decomposition approach to implementing fault slip in finite-element models of quasi-static and dynamic crustal deformation. *Journal of Geophysical Research: Solid Earth*, **118**(6), 3059–3079.

Ader, Thomas, Avouac, Jean-Philippe, Liu-Zeng, Jing, Lyon-Caen, Hélène, Bollinger, Laurent, Galetzka, John, Genrich, Jeff, Thomas, Marion, Chanard, Kristel, Sapkota, Soma Nath, *et al.* . 2012. Convergence rate across the Nepal Himalaya and interseismic coupling on the Main Himalayan Thrust: Implications for seismic hazard. *Journal of Geophysical Research: Solid Earth (1978–2012)*, **117**(B4).

Allmann, Bettina P, & Shearer, Peter M. 2009. Global variations of stress drop for moderate to large earthquakes. *Journal of Geophysical Research: Solid Earth*, **114**(B1).

Amitrano, David. 2003. Brittle-ductile transition and associated seismicity: Experimental and numerical studies and relationship with the b value. *Journal of Geophysical Research: Solid Earth (1978–2012)*, **108**(B1).

Ampuero, J-P, & Ben-Zion, Y. 2008. Cracks, pulses and macroscopic asymmetry of dynamic rupture on a bimaterial interface with velocity-weakening friction. *Geophysical Journal International*, **173**(2), 674–692.

Arora, BR, Gahalaut, VK, & Kumar, Naresh. 2012. Structural control on along-strike variation in the seismicity of the northwest Himalaya. *Journal of Asian Earth Sciences*, **57**, 15–24.

Avouac, Jean-Philippe. 2003. Mountain building, erosion, and the seismic cycle in the Nepal Himalaya. *Advances in Geophysics*, **46**, 1–80.

Avouac, Jean-Philippe. 2015. Mountain building: From earthquakes to geologic deformation. *Treatise on Geophysics,*, **6**, 381–432.

Avouac, Jean-Philippe. 2015b. From geodetic imaging of seismic and aseismic fault slip to dynamic modeling of the seismic cycle. *Annual Review of Earth and Planetary Sciences*, **43**, 233–271.

Avouac, Jean-Philippe, Meng, Lingsen, Wei, Shengji, Wang, Teng, & Ampuero, Jean-Paul. 2015. Lower edge of locked Main Himalayan Thrust unzipped by the 2015 Gorkha earthquake. *Nature Geoscience*.

Balestrieri, M. L., Bernet, M., Brandon, M. T., Picotti, V., Reiners, P., & Zattin, M. 2003. Pliocene and Pleistocene Exhumation and Uplift of Two Key Areas of the Northern Apennines. *Quaternary International*, **101-102**(Jan.), 67–73.

Baranowski, Jean, Armbruster, John, Seeber, Leonardo, & Molnar, Peter. 1984. Focal depths and fault plane solutions of earthquakes and active tectonics of the Himalaya. *Journal of Geophysical Research: Solid Earth*, **89**(B8), 6918–6928.

Barba, Salvatore, Finocchio, Debora, Sikdar, Elena, & Burrato, Pierfrancesco. 2013. Modelling the interseismic deformation of a thrust system: seismogenic potential of the Southern Alps. *Terra Nova*, **25**(3), 221–227.

Battaglia, Maurizio, Murray, Mark H, Serpelloni, Enrico, & Bürgmann, Roland. 2004. The Adriatic region: An independent microplate within the Africa-Eurasia collision zone. *Geophysical Research Letters*, **31**(9).

Baumann, TS, & Kaus, Boris JP. 2015. Geodynamic inversion to constrain the non-linear rheology of the lithosphere. *Geophysical Journal International*, **202**(2), 1289–1316.

Beaumont, Christopher, Ellis, Susan, Hamilton, Juliet, & Fullsack, Philippe. 1996. Mechanical model for subduction-collision tectonics of Alpine-type compressional orogens. *Geology*, **24**(8), 675–678.

Bechtold, Michel, Battaglia, M, Tanner, DC, & Zuliani, D. 2009. Constraints on the active tectonics of the Friuli/NW Slovenia area from CGPS measurements and three-dimensional kinematic modeling. *Journal of Geophysical Research: Solid Earth*, **114**(B3).

Beller, S, Monteiller, V, Operto, S, Nolet, G, Paul, A, & Zhao, L. 2017. Lithospheric architecture of the South-Western Alps revealed by multiparameter teleseismic full-waveform inversion. *Geophysical Journal International*, **212**(2), 1369–1388.

Benedetti, Lucilla, Tapponnier, Paul, King, Geoffrey CP, Meyer, Bertrand, & Manighetti, Isabelle. 2000. Growth folding and active thrusting in the Montello region, Veneto, northern Italy. *Journal of Geophysical Research: Solid Earth*, **105**(B1), 739–766.

Bennett, R. A., Serpelloni, E., Hreinsdóttir, S., Brandon, M. T., Buble, G., Basic, T., Casale, G., Cavaliere, A., Anzidei, M., Marjonovic, M., Minelli, G., Molli, G., & Montanari, A. 2012. Syn-Convergent Extension Observed Using the RETREAT GPS Network, Northern Apennines, Italy: NORTHERN APENNINES DEFORMATION. *Journal of Geophysical Research: Solid Earth*, **117**(B4).

Benoit, Margaret H., Torpey, Megan, Liszewski, Kelly, Levin, Vadim, & Park, Jeffrey. 2011. P and S Wave Upper Mantle Seismic Velocity Structure beneath the Northern Apennines: New Evidence for the End of Subduction. *Geochemistry, Geophysics, Geosystems*, **12**(6).

Berger, Antoine, Jouanne, François, Hassani, Riad, & Mugnier, Jean Louis. 2004. Modelling the spatial distribution of present-day deformation in Nepal: how cylindrical is the Main Himalayan Thrust in Nepal? *Geophysical Journal International*, **156**(1), 94–114.

Berthet, Théo, Ritz, Jean-François, Ferry, Matthieu, Pelgay, Phuntsho, Cattin, Rodolphe, Drukpa, Dowchu, Braucher, Régis, & Hetényi, György. 2014. Active tectonics of the eastern Himalaya: New constraints from the first tectonic geomorphology study in southern Bhutan. *Geology*, **42**(5), 427–430.

Bettinelli, Pierre, Avouac, Jean-Philippe, Flouzat, Mireille, Jouanne, François, Bollinger, Laurent, Willis, Pascal, & Chitrakar, Gyani Raja. 2006. Plate motion of India and interseismic strain in the Nepal Himalaya from GPS and DORIS measurements. *Journal of Geodesy*, **80**(8-11), 567–589.

Bianchi, I., Park, J., Piana Agostinetti, N., & Levin, V. 2010. Mapping Seismic Anisotropy Using Harmonic Decomposition of Receiver Functions: An Application to Northern Apennines, Italy. *Journal of Geophysical Research: Solid Earth*, **115**(12), 1–14.

Bilek, Susan L., Conrad, Clinton P., & Lithgow-Bertelloni, Carolina. 2005. Slab Pull, Slab Weakening, and Their Relation to Deep Intra-Slab Seismicity: SLAB PULL AND SLAB WEAKENING. *Geophysical Research Letters*, **32**(14), n/a–n/a.

Bilham, Roger. 1995. Location and magnitude of the 1833 Nepal earthquake and its relation to the rupture zones of contiguous great Himalayan earthquakes. *Current Science*, **69**(2), 101–128.

Bilham, Roger. 2004. Earthquakes in India and the Himalaya: tectonics, geodesy and history. *Annals of Geophysics*, **47**(2-3).

Bilham, Roger. 2009. The seismic future of cities. *Bulletin of Earthquake Engineering*, **7**(4), 839.

Bilham, Roger. 2015. Seismology: raising kathmandu. *Nature Geoscience*, **8**(8), 582.

Bilham, Roger, & Ambraseys, Nicholas. 2005. Apparent Himalayan slip deficit from the summation of seismic moments for Himalayan earthquakes, 1500–2000. *Current Science*, **88**(10), 1658–1663.

Bilham, Roger, & England, Philip. 2001. Plateau 'pop-up'in the great 1897 Assam earthquake. *Nature*, **410**(6830), 806.

Bilham, Roger, Larson, Kristine, Freymueller, Jeffrey, Jouanne, F, LeFort, P, Leturmy, P, Mugnier, JL, Gamond, JF, Glot, JP, Martinod, J, *et al.* . 1997. GPS measurements of present-day convergence across the Nepal Himalaya. *Nature*, **386**(6620), 61–64.

Bilham, Roger, Gaur, Vinod K, & Molnar, Peter. 2001. Himalayan seismic hazard. *Science*, **293**(5534), 1442–1444.

Bilham, Roger, Mencin, David, Bendick, Rebecca, & Bürgmann, Roland. 2017. Implications for elastic energy storage in the Himalaya from the Gorkha 2015 earthquake and other incomplete ruptures of the Main Himalayan Thrust. *Quaternary International*, **462**, 3–21.

Bollinger, L, Avouac, JP, Cattin, R, & Pandey, MR. 2004. Stress buildup in the Himalaya. *Journal of Geophysical Research: Solid Earth (1978–2012)*, **109**(B11).

Bollinger, L, Henry, Pierre, & Avouac, JP. 2006. Mountain building in the Nepal Himalaya: Thermal and kinematic model. *Earth and Planetary Science Letters*, **244**(1), 58–71.

Bollinger, L, Tapponnier, Paul, Sapkota, SN, & Klinger, Y. 2016. Slip deficit in central Nepal: omen for a repeat of the 1344 AD earthquake? *Earth, Planets and Space*, **68**(1), 12.

Bollinger, Laurent, Sapkota, Soma Nath, Tapponnier, Paul, Klinger, Yann, Rizza, Magali, Van Der Woerd, Jerome, Tiwari, DR, Pandey, R, Bitri, Adnand, & Bes de Berc, S. 2014. Estimating the return times of great Himalayan earthquakes in eastern Nepal: Evidence from the Patu and Bardibas strands of the Main Frontal Thrust. *Journal of Geophysical Research: Solid Earth*, **119**(9), 7123–7163.

Bragato, PL, & Slejko, D. 2005. Empirical ground-motion attenuation relations for the eastern Alps in the magnitude range 2.5–6.3. *Bulletin of the Seismological Society of America*, **95**(1), 252–276.

Bressan, G, Bragato, PL, & Venturini, C. 2003. Stress and strain tensors based on focal mechanisms in the seismotectonic framework of the Friuli–Venezia Giulia region (Northeastern Italy). *Bulletin of the Seismological Society of America*, **93**(3), 1280–1297.

Brown, LD, Zhao, Wenjin, Nelson, KD, Hauck, M, *et al.* . 1996. Bright spots, structure, and magmatism in southern Tibet from INDEPTH seismic reflection profiling. *Science*, **274**(5293), 1688.

Brun, Jean-Pierre, & Faccenna, Claudio. 2008. Exhumation of high-pressure rocks driven by slab rollback. *Earth and Planetary Science Letters*, **272**(1-2), 1–7.

Burg, J-P, & Gerya, TV. 2005. The role of viscous heating in Barrovian metamorphism of collisional orogens: thermomechanical models and application to the Lepontine Dome in the Central Alps. *Journal of Metamorphic Geology*, **23**(2), 75–95.

Burg, J-P, & Podladchikov, Yu. 1999. Lithospheric scale folding: numerical modelling and application to the Himalayan syntaxes. *International Journal of Earth Sciences*, **88**(2), 190–200.

Bürgmann, Roland, & Dresen, Georg. 2008. Rheology of the lower crust and upper mantle: Evidence from rock mechanics, geodesy, and field observations. *Annual Review of Earth and Planetary Sciences*, **36**.

Burkhard, Martin. 1990. Aspects of the large-scale Miocene deformation in the most external part of the Swiss Alps (sub-Alpine molasse to Jura fold belt). *Eclogae Geologicae Helvetiae*, **83**(3), 559–583.

Burridge, R, & Knopoff, Leon. 1967. Model and theoretical seismicity. *Bulletin of the seismological society of america*, **57**(3), 341–371.

Calais, E, Nocquet, J-M, Jouanne, F, & Tardy, M. 2002. Current strain regime in the Western Alps from continuous Global Positioning System measurements, 1996–2001. *Geology*, **30**(7), 651–654.

Capitanio, FA, Stegman, DR, Moresi, Louis-Noel, & Sharples, Wendy. 2010. Upper plate controls on deep subduction, trench migrations and deformations at convergent margins. *Tectonophysics*, **483**(1), 80–92.

Caporali, Alessandro, Neubauer, Franz, Ostini, L, Stangl, G, & Zuliani, David. 2013. Modeling surface GPS velocities in the Southern and Eastern Alps by finite dislocations at crustal depths. *Tectonophysics*, **590**, 136–150.

Carminati, Eugenio, & Doglioni, Carlo. 2012. Alps vs. Apennines: the paradigm of a tectonically asymmetric Earth. *Earth-Science Reviews*, **112**(1), 67–96.

Carminati, Eugenio, Doglioni, Carlo, & Scrocca, Davide. 2003. Apennines Subduction-Related Subsidence of Venice (Italy). *Geophysical Research Letters*, **30**(13).

Cattin, R, & Avouac, JP. 2000. Modeling mountain building and the seismic cycle in the Himalaya of Nepal. *Journal of Geophysical Research*, **105**(B6), 13389–13407.

Champagnac, JD, Molnar, P, Anderson, RS, Sue, C, & Delacou, B. 2007. Quaternary erosion-induced isostatic rebound in the western Alps. *Geology*, **35**(3), 195–198.

Cheloni, D, D'Agostino, N, D'Anastasio, E, & Selvaggi, G. 2012. Reassessment of the source of the 1976 Friuli, NE Italy, earthquake sequence from the joint inversion of high-precision levelling and triangulation data. *Geophysical Journal International*, **190**(2), 1279–1294.

Cheloni, D., Giuliani, R., D'Agostino, N., Mattone, M., Bonano, M., Fornaro, G., Lanari, R., Reale, D., & Atzori, S. 2016. New Insights into Fault Activation and Stress Transfer between En Echelon Thrusts: The 2012 Emilia, Northern Italy, Earthquake Sequence. *Journal of Geophysical Research: Solid Earth*, **121**(6), 4742–4766.

Cheloni, Daniele, D'Agostino, Nicola, & Selvaggi, Giulio. 2014. Interseismic coupling, seismic potential, and earthquake recurrence on the southern front of the Eastern Alps (NE Italy). *Journal of Geophysical Research: Solid Earth*, **119**(5), 4448–4468.

Chen, Wang-Ping, & Molnar, Peter. 1977. Seismic moments of major earthquakes and the average rate of slip in central Asia. *Journal of Geophysical Research*, **82**(20), 2945–2969.

Chen, Wang-Ping, & Molnar, Peter. 1990. Source parameters of earthquakes and intraplate deformation beneath the Shillong Plateau and the northern Indoburman ranges. *Journal of Geophysical Research: Solid Earth*, **95**(B8), 12527–12552.

Chen, Wang-Ping, & Yang, Zhaohui. 2004. Earthquakes beneath the Himalayas and Tibet: Evidence for strong lithospheric mantle. *Science*, **304**(5679), 1949–1952.

Chen, Yen-Ling, Hung, Shu-Huei, Jiang, Juen-Shi, & Chiao, Ling-Yun. 2016. Systematic correlations of the earthquake frequency-magnitude distribution with the deformation and mechanical regimes in the Taiwan orogen. *Geophysical Research Letters*.

Chiarabba, C, Jovane, L, & DiStefano, R. 2005. A new view of Italian seismicity using 20 years of instrumental recordings. *Tectonophysics*, **395**(3), 251–268.

Chiarabba, C., Giacomuzzi, G., Bianchi, I., Agostinetti, N. P., & Park, J. 2014. From Underplating to Delamination-Retreat in the Northern Apennines. *Earth and Planetary Science Letters*, **403**, 108–116.

Chiaraluce, L., Barchi, M., Collettini, C., Mirabella, F., & Pucci, S. 2005. Connecting Seismically Active Normal Faults with Quaternary Geological Structures in a Complex Extensional Environment: The Colfiorito 1997 Case History (Northern Apennines, Italy). *Tectonics*, **24**(1), TC1002.

Chlieh, Mohamed, Avouac, Jean-Philippe, Sieh, Kerry, Natawidjaja, Danny Hilman, & Galetzka, John. 2008. Heterogeneous coupling of the Sumatran megathrust constrained by geodetic and paleogeodetic measurements. *Journal of Geophysical Research: Solid Earth*, **113**(B5).

Ciesin, Ciat. 2005. Gridded population of the world version 3 (GPWV3): population density grids. *Palisades, NY: Socioeconomic Data and Applications Center (SEDAC), Columbia University*.

Cochard, Alain, & Madariaga, Raúl. 1994. Dynamic faulting under rate-dependent friction. *pure and applied geophysics*, **142**(3-4), 419–445.

Collettini, C., De Paola, N., Holdsworth, R. E., & Barchi, M. R. 2006. The Development and Behaviour of Low-Angle Normal Faults during Cenozoic Asymmetric Extension in the Northern Apennines, Italy. *Journal of Structural Geology*, **28**(2), 333–352.

Conrad, Clinton P., Bilek, Susan, & Lithgow-Bertelloni, Carolina. 2004. Great Earthquakes and Slab Pull: Interaction between Seismic Coupling and Plate–Slab Coupling. *Earth and Planetary Science Letters*, **218**(1), 109–122.

Corbi, F, Funiciello, F, Moroni, M, Dinther, Y, Mai, Paul Martin, Dalguer, LA, & Faccenna, C. 2013. The seismic cycle at subduction thrusts: 1. Insights from laboratory models. *Journal of Geophysical Research: Solid Earth*, **118**(4), 1483–1501.

Corbi, Fabio, Herrendoerfer, Robert, Funiciello, Francesca, & Van Dinther, Ylona. 2017. Controls of seismogenic zone width and subduction velocity on interplate seismicity: insights from analog and numerical models. *Geophysical Research Letters*.

Coward, Mike, & Dietrich, Dorothee. 1989. Alpine tectonics—an overview. *Geological Society, London, Special Publications*, **45**(1), 1–29.

Crameri, F. 2018. *Scientific colour-maps*.

Crameri, F, Schmeling, H, Golabek, GJ, Duretz, T, Orendt, R, Buiter, SJH, May, DA, Kaus, BJP, Gerya, TV, & Tackley, PJ. 2012. A comparison of numerical surface topography calculations in geodynamic modelling: An evaluation of the 'sticky air'method. *Geophysical Journal International*, **189**(1), 38–54.

D'agostino, N, Avallone, A, Cheloni, D, D'anastasio, E, Mantenuto, S, & Selvaggi, G. 2008. Active tectonics of the Adriatic region from GPS and earthquake slip vectors. *Journal of Geophysical Research: Solid Earth*, **113**(B12).

Dal Zilio, L, van Dinther, Y, Gerya, T, & Avouac, J-P. 2019a. Bimodal seismicity in the Himalaya controlled by fault friction and geometry. *Nature communications*, **10**(1), 48.

Dal Zilio, L, Kissling, E, & Gerya, T. 2019b. Slab rollback orogeny model for the evolution of the Central Alps: seismo-thermo-mechanical test. *(in review)*.

Dal Zilio, L, Jolivet, R, & van Dinther, Y. 2019c. Segmentation of the Main Himalayan Thrust inferred from geodetic observations of interseismic coupling. *(in review)*.

Dal Zilio, Luca. 2018. Subduction-driven Earth machine. *Nature Geoscience*, **11**(4), 229–229.

Dal Zilio, Luca, Faccenda, Manuele, & Capitanio, Fabio. 2018a. The role of deep subduction in supercontinent breakup. *Tectonophysics*, **746**, 312–324.

Dal Zilio, Luca, van Dinther, Ylona, Gerya, Taras V, & Pranger, Casper C. 2018b. Seismic behaviour of mountain belts controlled by plate convergence rate. *Earth and Planetary Science Letters*, **482**(1), 81–92.

Dalguer, Luis A. 2012. Numerical algorithms for earthquake rupture dynamic modeling. *The Mechanics of Faulting: From Laboratory to Real Earthquakes*, 93–124.

Das, Shamita, & Aki, Keiiti. 1977. A numerical study of two-dimensional spontaneous rupture propagation. *Geophysical Journal of the Royal Astronomical Society*, **50**(3), 643–668.

Davis, Dan, Suppe, John, & Dahlen, FA. 1983. Mechanics of fold-and-thrust belts and accretionary wedges. *Journal of Geophysical Research: Solid Earth*, **88**(B2), 1153–1172.

Del Gaudio, P, Di Toro, G, Han, R, Hirose, T, Nielsen, S, Shimamoto, T, & Cavallo, A. 2009. Frictional melting of peridotite and seismic slip. *Journal of Geophysical Research: Solid Earth*, **114**(B6).

Den Hartog, SAM, Niemeijer, AR, & Spiers, CJ. 2012. New constraints on megathrust slip stability under subduction zone P–T conditions. *Earth and Planetary Science Letters*, **353**, 240–252.

Devoti, Roberto, Riguzzi, Federica, Cuffaro, Marco, & Doglioni, Carlo. 2008. New GPS Constraints on the Kinematics of the Apennines Subduction. *Earth and Planetary Science Letters*, **273**(1-2), 163–174.

Devoti, Roberto, Esposito, Alessandra, Pietrantonio, Grazia, Pisani, Anna Rita, & Riguzzi, Federica. 2011. Evidence of Large Scale Deformation Patterns from GPS Data in the Italian Subduction Boundary. *Earth and Planetary Science Letters*, **311**(3), 230–241.

Dewey, JF, Helman, ML, Knott, SD, Turco, E, & Hutton, DHW. 1989. Kinematics of the western Mediterranean. *Geological Society, London, Special Publications*, **45**(1), 265–283.

Di Stefano, R., Kissling, E., Chiarabba, C., Amato, A., & Giardini, D. 2009. Shallow Subduction beneath Italy: Three-Dimensional Images of the Adriatic-European-Tyrrhenian Lithosphere System Based on High-Quality P Wave Arrival Times. *Journal of Geophysical Research: Solid Earth*, **114**(5), 1–17.

Di Toro, Giulio, Han, Raehee, Hirose, Takehiro, De Paola, Nicola, Nielsen, Stefan, Mizoguchi, Kazuo, Ferri, Fabio, Cocco, Massimo, & Shimamoto, Tosihiko. 2011. Fault lubrication during earthquakes. *Nature*, **471**(7339), 494–498.

Dieterich, James H., & Richards-Dinger, Keith B. 2010. Earthquake Recurrence in Simulated Fault Systems. *Pages 233–250 of:* Savage, Martha K., Rhoades, David A., Smith, Euan G. C., Gerstenberger, Matthew C., & Vere-Jones, David (eds), *Seismogenesis and Earthquake Forecasting: The Frank Evison Volume II*. Pageoph Topical Volumes. Basel: Springer Basel.

Doglioni, C., Harabaglia, P., Martinelli, G., Mongelli, F., & Zito, G. 1996. A Geodynamic Model of the Southern Apennines Accretionary Prism. *Terra Nova*, **8**(6), 540–547.

Doglioni, C, Barba, S, Carminati, E, & Riguzzi, F. 2011. Role of the brittle–ductile transition on fault activation. *Physics of the Earth and Planetary Interiors*, **184**(3), 160–171.

Doglioni, C, Carminati, E, Petricca, P, & Riguzzi, F. 2015. Normal fault earthquakes or graviquakes. *Scientific reports*, **5**.

Doin, Marie-Pierre, & Henry, Pierre. 2001. Subduction initiation and continental crust recycling: the roles of rheology and eclogitization. *Tectonophysics*, **342**(1-2), 163–191.

Duan, Benchun, & Oglesby, David D. 2005. The dynamics of thrust and normal faults over multiple earthquake cycles: Effects of dipping fault geometry. *Bulletin of the Seismological Society of America*, **95**(5), 1623–1636.

Duputel, Zacharie, Agram, Piyush S, Simons, Mark, Minson, Sarah E, & Beck, James L. 2014. Accounting for prediction uncertainty when inferring subsurface fault slip. *Geophysical Journal International*, **197**(1), 464–482.

Duputel, Zacharie, Vergne, Jérôme, Rivera, Luis, Wittlinger, Gérard, Farra, Véronique, & Hetényi, György. 2016. The 2015 Gorkha earthquake: A large event illuminating the Main Himalayan thrust fault. *Geophysical Research Letters*, **43**(6), 2517–2525.

Duretz, Thibault, Gerya, Taras V, & May, Dave A. 2011. Numerical modelling of spontaneous slab breakoff and subsequent topographic response. *Tectonophysics*, **502**(1-2), 244–256.

Elliott, JR, Jolivet, R, González, PJ, Avouac, J-P, Hollingsworth, J, Searle, MP, & Stevens, VL. 2016. Himalayan megathrust geometry and relation to topography revealed by the Gorkha earthquake. *Nature Geoscience*.

Evans, Brian, & Goetze, Christopher. 1979. The temperature variation of hardness of olivine and its implication for polycrystalline yield stress. *Journal of Geophysical Research: Solid Earth*, **84**(B10), 5505–5524.

Faccenda, M, Minelli, G, & Gerya, TV. 2009. Coupled and decoupled regimes of continental collision: Numerical modeling. *Earth and Planetary Science Letters*, **278**(3-4), 337–349.

Faccenda, Manuele, & Dal Zilio, Luca. 2017. The role of solid–solid phase transitions in mantle convection. *Lithos*, **268**, 198–224.

Faccenda, Manuele, Gerya, Taras V, & Chakraborty, Sumit. 2008. Styles of post-subduction collisional orogeny: influence of convergence velocity, crustal rheology and radiogenic heat production. *Lithos*, **103**(1), 257–287.

Faccenna, Claudio, Piromallo, Claudia, Crespo-Blanc, Ana, Jolivet, Laurent, & Rossetti, Federico. 2004. Lateral Slab Deformation and the Origin of the Western Mediterranean Arcs. *Tectonics*, **23**(1), TC1012.

Feldl, Nicole, & Bilham, Roger. 2006. Great Himalayan earthquakes and the Tibetan plateau. *Nature*, **444**(7116), 165–170.

Fisher, Ronald Aylmer. 1950. Contributions to mathematical statistics.

Fox, Matthew, Herman, Frédéric, Kissling, Edi, & Willett, Sean D. 2015. Rapid exhumation in the Western Alps driven by slab detachment and glacial erosion. *Geology*, **43**(5), 379–382.

Fry, Bill, Deschamps, Frédéric, Kissling, Edi, Stehly, Laurent, & Giardini, Domenico. 2010. Layered azimuthal anisotropy of Rayleigh wave phase velocities in the European Alpine lithosphere inferred from ambient noise. *Earth and Planetary Science Letters*, **297**(1-2), 95–102.

Gabriel, A-A, Ampuero, J-P, Dalguer, Luis A, & Mai, Paul Martin. 2012. The transition of dynamic rupture styles in elastic media under velocity-weakening friction. *Journal of Geophysical Research: Solid Earth*, **117**(B9).

Gahalaut, VK, & Arora, BR. 2012. Segmentation of seismicity along the Himalayan Arc due to structural heterogeneities in the under-thrusting Indian plate and overriding Himalayan wedge. *Episodes*, **35**(4), 493–500.

Gahalaut, VK, & Kundu, Bhaskar. 2012. Possible influence of subducting ridges on the Himalayan arc and on the ruptures of great and major Himalayan earthquakes. *Gondwana Research*, **21**(4), 1080–1088.

Galetzka, John, Melgar, Diego, Genrich, Joachim F, Geng, Jianghui, Owen, Susan, Lindsey, Eric O, Xu, Xiaohua, Bock, Yehuda, Avouac, J-P, Adhikari, Lok Bijaya, *et al.* . 2015. Slip pulse and resonance of the Kathmandu basin during the 2015 Gorkha earthquake, Nepal. *Science*, **349**(6252), 1091–1095.

Galli, Paolo, Galadini, Fabrizio, & Pantosti, Daniela. 2008. Twenty years of paleoseismology in Italy. *Earth-Science Reviews*, **88**(1-2), 89–117.

Gardner, JK, & Knopoff, Leon. 1974. Is the sequence of earthquakes in Southern California, with aftershocks removed, Poissonian? *Bulletin of the Seismological Society of America*, **64**(5), 1363–1367.

Gerya, T. 2010. *Introduction to Numerical Geodynamic Modelling*. Cambridge University Press.

Gerya, Taras. 2011. Future directions in subduction modeling. *Journal of Geodynamics*, **52**(5), 344–378.

Gerya, Taras V., & Yuen, David A. 2003. Characteristics-based marker-in-cell method with conservative finite-differences schemes for modeling geological flows with strongly variable transport properties. *Physics of the Earth and Planetary Interiors*, **140**(4), 293 – 318.

Gerya, Taras V, & Yuen, David A. 2007. Robust characteristics method for modelling multiphase visco-elasto-plastic thermo-mechanical problems. *Physics of the Earth and Planetary Interiors*, **163**(1), 83–105.

Gerya, Taras V, Yuen, David A, & Maresch, Walter V. 2004. Thermomechanical modelling of slab detachment. *Earth and Planetary Science Letters*, **226**(1-2), 101–116.

Gillespie, PA, Walsh, JJ t, & Watterson, J. 1992. Limitations of dimension and displacement data from single faults and the consequences for data analysis and interpretation. *Journal of Structural Geology*, **14**(10), 1157–1172.

Gleason, Gayle C, & Tullis, Jan. 1995. A flow law for dislocation creep of quartz aggregates determined with the molten salt cell. *Tectonophysics*, **247**(1), 1–23.

Grandin, Raphaël, Doin, Marie-Pierre, Bollinger, Laurent, Pinel-Puysségur, Béatrice, Ducret, Gabriel, Jolivet, Romain, & Sapkota, Soma Nath. 2012. Long-term growth of the Himalaya inferred from interseismic InSAR measurement. *Geology*, **40**(12), 1059–1062.

Grandin, Raphaël, Vallée, Martin, Satriano, Claudio, Lacassin, Robin, Klinger, Yann, Simoes, Martine, & Bollinger, Laurent. 2015. Rupture process of the Mw= 7.9 2015 Gorkha earthquake (Nepal): insights into Himalayan megathrust segmentation. *Geophysical Research Letters*, **42**(20), 8373–8382.

Grenerczy, Gyula, Sella, Giovanni, Stein, Seth, & Kenyeres, Ambrus. 2005. Tectonic implications of the GPS velocity field in the northern Adriatic region. *Geophysical Research Letters*, **32**(16).

Gualandi, Adriano, Avouac, Jean-Philippe, Galetzka, John, Genrich, Joachim F, Blewitt, Geoffrey, Adhikari, Lok Bijaya, Koirala, Bharat Prasad, Gupta, Ratnamani, Upreti, Bishal Nath, Pratt-Sitaula, Beth, *et al.* . 2017. Pre-and post-seismic deformation related to the 2015, Mw 7.8 Gorkha earthquake, Nepal. *Tectonophysics*, **714**, 90–106.

Gulia, Laura, & Wiemer, Stefan. 2010. The influence of tectonic regimes on the earthquake size distribution: A case study for Italy. *Geophysical Research Letters*, **37**(10).

Gutenberg, Beno, & Richter, Charles F. 1944. Frequency of earthquakes in California. *Bulletin of the Seismological Society of America*, **34**(4), 185–188.

Handy, Mark R, Schmid, Stefan M, Bousquet, Romain, Kissling, Eduard, & Bernoulli, Daniel. 2010. Reconciling plate-tectonic reconstructions of Alpine Tethys with the geological–geophysical record of spreading and subduction in the Alps. *Earth-Science Reviews*, **102**(3-4), 121–158.

Hanks, Thomas C, & Kanamori, Hiroo. 1979. A moment magnitude scale. *Journal of Geophysical Research*, **84**(B5), 2348–2350.

Harris, Ruth A, Barall, Michael, Aagaard, Brad, Ma, Shuo, Roten, Daniel, Olsen, Kim, Duan, Benchun, Liu, Dunyu, Luo, Bin, Bai, Kangchen, *et al.* . 2018. A suite of exercises for verifying dynamic earthquake rupture codes. *Seismological Research Letters*, **89**(3), 1146–1162.

Heaton, Thomas H. 1990. Evidence for and implications of self-healing pulses of slip in earthquake rupture. *Physics of the Earth and Planetary Interiors*, **64**(1), 1–20.

Heidbach, Oliver, Rajabi, Mojtaba, Reiter, Karsten, & Ziegler, Moritz. 2016. *World Stress Map 2016*.

Herak, Davorka, Herak, Marijan, & Tomljenović, Bruno. 2009. Seismicity and earthquake focal mechanisms in North-Western Croatia. *Tectonophysics*, **465**(1-4), 212–220.

Herman, Frédéric, Copeland, Peter, Avouac, Jean-Philippe, Bollinger, Laurent, Mahéo, Gweltaz, Le Fort, Patrick, Rai, Santaman, Foster, David, Pêcher, Arnaud, Stüwe, Kurt, *et al.* . 2010. Exhumation, crustal deformation, and thermal structure of the Nepal Himalaya derived from the inversion of thermochronological and thermobarometric data and modeling of the topography. *Journal of Geophysical Research: Solid Earth*, **115**(B6).

Herrendörfer, R, Gerya, T, & Dinther, Y. 2018. An Invariant Rate- and State-Dependent Friction Formulation for Viscoeastoplastic Earthquake Cycle Simulations. *Journal of Geophysical Research: Solid Earth*, **123**(6), 5018–5051.

Herrendörfer, Robert, Van Dinther, Ylona, Gerya, Taras, & Dalguer, Luis Angel. 2015. Earthquake supercycle in subduction zones controlled by the width of the seismogenic zone. *Nature Geoscience*, **8**(6), 471–474.

Hetényi, György, Cattin, Rodolphe, Vergne, Jérôme, & Nábělek, John L. 2006. The effective elastic thickness of the India Plate from receiver function imaging, gravity anomalies and thermomechanical modelling. *Geophysical Journal International*, **167**(3), 1106–1118.

Hetényi, György, Cattin, Rodolphe, Brunet, Fabrice, Bollinger, Laurent, Vergne, Jérôme, Nábělek, John L, & Diament, Michel. 2007. Density distribution of the India plate beneath the Tibetan plateau: Geophysical and petrological constraints on the kinetics of lower-crustal eclogitization. *Earth and Planetary Science Letters*, **264**(1), 226–244.

Hetényi, György, Roux-Mallouf, Le, Berthet, Théo, Cattin, Rodolphe, Cauzzi, Carlo, Phuntsho, Karma, Grolimund, Remo, *et al.* . 2016a. Joint approach combining damage and paleoseismology observations constrains the 1714 AD Bhutan earthquake at magnitude 8±0.5. *Geophysical Research Letters*, **43**(20).

Hetényi, György, Cattin, Rodolphe, Berthet, Théo, Le Moigne, Nicolas, Chophel, Jamyang, Lechmann, Sarah, Hammer, Paul, Drukpa, Dowchu, Sapkota, Soma Nath, Gautier, Stéphanie, *et al.* . 2016b. Segmentation of the Himalayas as revealed by arc-parallel gravity anomalies. *Scientific reports*, **6**, 33866.

Hetényi, György, Molinari, Irene, Clinton, John, Bokelmann, Götz, Bondár, István, Crawford, Wayne C, Dessa, Jean-Xavier, Doubre, Cecile, Friederich, Wolfgang, Fuchs, Florian, *et al.* . 2018. The AlpArray Seismic Network: A large-scale European experiment to image the Alpine orogen. *Surveys in Geophysics*, 1–25.

Heuret, Arnauld, Lallemand, Serge, Funiciello, Francesca, Piromallo, Claudia, & Faccenna, Claudio. 2011. Physical characteristics of subduction interface type seismogenic zones revisited. *Geochemistry, Geophysics, Geosystems*, **12**(1).

Hinderer, Matthias, Kastowski, Martin, Kamelger, Achim, Bartolini, Carlo, & Schlunegger, Fritz. 2013. River loads and modern denudation of the Alps—a review. *Earth-science reviews*, **118**, 11–44.

Hirn, Alfred, Lepine, Jean-Claude, Jobert, Georges, Sapin, Martine, Wittlinger, Gérard, Zhong Xin, Xu, En Yuan, Gao, Xiang Jing, Wang, Ji Wen, Teng, Shao Bai, Xiong, Pandey, M. R., & Tater, J. M. 1984. Crustal structure and variability of the Himalayan border of Tibet. *Nature*, **307**(01), 23 EP –.

Hirose, Takehiro, & Bystricky, Misha. 2007. Extreme dynamic weakening of faults during dehydration by coseismic shear heating. *Geophysical Research Letters*, **34**(14).

Hough, Susan E, & Roger, Bilham. 2008. Site response of the Ganges basin inferred from re-evaluated macroseismic observations from the 1897 Shillong, 1905 Kangra, and 1934 Nepal earthquakes. *Journal of Earth System Science*, **117**(2), 773–782.

Houlie, Nicolas, Woessner, Jochen, Giardini, Domenico, & Rothacher, Markus. 2018. Lithosphere strain rate and stress field orientations near the Alpine arc in Switzerland. *Scientific reports*, **8**(1).

Hubbard, Judith, Almeida, Rafael, Foster, Anna, Sapkota, Soma Nath, Bürgi, Paula, & Tapponnier, Paul. 2016. Structural segmentation controlled the 2015 Mw 7.8 Gorkha earthquake rupture in Nepal. *Geology*, **44**(8), 639–642.

Huc, Mireille, Hassani, Riad, & Chéry, Jean. 1998. Large earthquake nucleation associated with stress exchange between middle and upper crust. *Geophysical research letters*, **25**(4), 551–554.

Ito, Keisuke, & Kennedy, George C. 1971. An experimental study of the basalt-garnet granulite-eclogite transition. *The structure and physical properties of the Earth's crust*, **14**, 303–314.

Jackson, James. 2002. Faulting, flow, and the strength of the continental lithosphere. *International Geology Review*, **44**(1), 39–61.

Jackson, Michael, & Bilham, Roger. 1994. Constraints on Himalayan deformation inferred from vertical velocity fields in Nepal and Tibet. *Journal of Geophysical Research*, **99**, 13–897.

Jiang, J, & Erickson, B A. 2018. Advancing Simulations of Sequences of Earthquakes and Aseismic Slip [SEAS]. *Oral Presentation at 2018 SCEC Annual Meeting*.

Jolivet, R, Simons, M, Agram, PS, Duputel, Z, & Shen, Z-K. 2015. Aseismic slip and seismogenic coupling along the central San Andreas Fault. *Geophysical Research Letters*, **42**(2), 297–306.

Jordan, Thomas H, & Jones, Lucile M. 2010. Operational earthquake forecasting: Some thoughts on why and how. *Seismological Research Letters*, **81**(4), 571–574.

Jouanne, F., Awan, A., Madji, A., Pêcher, A., Latif, M., Kausar, A., Mugnier, J. L., Khan, I., & Khan, N. A. 2011. Postseismic deformation in Pakistan after the 8 October 2005 earthquake: Evidence of afterslip along a flat north of the Balakot-Bagh thrust. *Journal of Geophysical Research: Solid Earth*, **116**(B7).

Kamer, Yavor, & Hiemer, Stefan. 2015. Data-driven spatial b value estimation with applications to California seismicity: To b or not to b. *Journal of Geophysical Research: Solid Earth*, **120**(7), 5191–5214.

Kameyama, Masanori, Yuen, David A, & Karato, Shun-Ichiro. 1999. Thermal-mechanical effects of low-temperature plasticity (the Peierls mechanism) on the deformation of a viscoelastic shear zone. *Earth and Planetary Science Letters*, **168**(1-2), 159–172.

Kaneko, Yoshihiro, Avouac, Jean-Philippe, & Lapusta, Nadia. 2010. Towards inferring earthquake patterns from geodetic observations of interseismic coupling. *Nature Geoscience*, **3**(5), 363–369.

Karato, Shun-ichiro, Riedel, Michael R, & Yuen, David A. 2001. Rheological structure and deformation of subducted slabs in the mantle transition zone: implications for mantle circulation and deep earthquakes. *Physics of the Earth and Planetary Interiors*, **127**(1-4), 83–108.

Karplus, M, & Velasco, A. 2015. RAPID: Collaborative Research: Nepal Array Measuring Aftershock Seismicity Trailing Earthquake (NAMASTE). *National Science Foundation*.

Katayama, Ikuo, & Karato, Shun-ichiro. 2008. Low-temperature, high-stress deformation of olivine under water-saturated conditions. *Physics of the Earth and Planetary Interiors*, **168**(3), 125–133.

Katsura, Tomoo, Yoneda, Akira, Yamazaki, Daisuke, Yoshino, Takashi, & Ito, Eiji. 2010. Adiabatic Temperature Profile in the Mantle. *Physics of the Earth and Planetary Interiors*, **183**(1), 212–218.

Kay, Robert W, & Kay, S Mahlburg. 1993. Delamination and delamination magmatism. *Tectonophysics*, **219**(1-3), 177–189.

Kissling, Edi. 1993. Deep structure of the Alps—what do we really know? *Physics of the Earth and Planetary Interiors*, **79**(1-2), 87–112.

Kissling, Edi. 2009. Deep structure and tectonics of the Valais: And the rest of the Alps. *Bulletin fuer Angewandte Geologie*, **13**(2), 3–10.

Kissling, Edi, & Schlunegger, Fritz. 2018. Rollback orogeny model for the evolution of the Swiss Alps. *Tectonics*, **37**(4), 1097–1115.

Kreemer, Corné, Blewitt, Geoffrey, & Klein, Elliot C. 2014. A geodetic plate motion and Global Strain Rate Model. *Geochemistry, Geophysics, Geosystems*, **15**(10), 3849–3889.

Krystopowicz, Neil J, & Currie, Claire A. 2013. Crustal eclogitization and lithosphere delamination in orogens. *Earth and Planetary Science Letters*, **361**, 195–207.

Kumar, Senthil, Wesnousky, Steven G, Jayangondaperumal, R, Nakata, T, Kumahara, Y, & Singh, Vimal. 2010. Paleoseismological evidence of surface faulting along the northeastern Himalayan front, India: Timing, size, and spatial extent of great earthquakes. *Journal of Geophysical Research: Solid Earth*, **115**(B12).

Lapusta, N, & Barbot, S. 2012. Models of earthquakes and aseismic slip based on laboratory-derived rate and state friction laws. *The Mechanics of Faulting: From Laboratory to Real Earthquakes*, 153–207.

Lapusta, Nadia, & Liu, Yi. 2009. Three-dimensional boundary integral modeling of spontaneous earthquake sequences and aseismic slip. *Journal of Geophysical Research: Solid Earth*, **114**(B9).

Laske, G, Masters, G, & Reif, C. 2001. CRUST2. 0: a new global crustal model at 2× 2 degrees. *Institute of Geophysics and Planetary Physics, The University of California, San Diego, website http://mahi. ucsd. edu/Gabi/rem. dir/crust/crust2. html*.

Lavé, J, & Avouac, J-Ph. 2000. Active folding of fluvial terraces across the Siwaliks Hills, Himalayas of central Nepal. *Journal of Geophysical Research: Solid Earth*, **105**(B3), 5735–5770.

Lavé, J, & Avouac, JP. 2001. Fluvial incision and tectonic uplift across the Himalayas of central Nepal. *Journal of Geophysical Research: Solid Earth*, **106**(B11), 26561–26591.

Lavé, Jérôme, Yule, D, Sapkota, S, Basant, K, Madden, C, Attal, M, & Pandey, R. 2005. Evidence for a great Medieval earthquake (~1100 AD) in the central Himalayas, Nepal. *Science*, **307**(5713), 1302–1305.

Lay, Thorne. 2015. The surge of great earthquakes from 2004 to 2014. *Earth and Planetary Science Letters*, **409**, 133–146.

Le Fort, Patrick. 1975. Himalayas: the collided range. Present knowledge of the continental arc. *American Journal of Science*, **275**(1), 1–44.

Le Roux-Mallouf, Romain, Ferry, Matthieu, Ritz, Jean-François, Berthet, Théo, Cattin, Rodolphe, & Drukpa, Dowchu. 2016. Paleoseismic evidence for two major historical earthquakes in Bhutan: new insight for rupture segmentation along the Himalayan arc. *Page 7105 of: EGU General Assembly Conference Abstracts*, vol. 18.

Lemonnier, Carole, Marquis, Guy, Perrier, Frédéric, Avouac, Jean-Philippe, Chitrakar, Gyani, Kafle, Basantha, Sapkota, Som, Gautam, Umesh, Tiwari, Dilliram, & Bano, Maksim. 1999. Electrical structure of the Himalaya of Central Nepal: high conductivity around the mid-crustal ramp along the MHT. *Geophysical Research Letters*, **26**(21), 3261–3264.

Li, Zhong-Hai, Liu, Mian, & Gerya, Taras. 2016. Lithosphere delamination in continental collisional orogens: A systematic numerical study. *Journal of Geophysical Research: Solid Earth*, **121**(7), 5186–5211.

Lindsey, Eric O, Almeida, Rafael, Mallick, Rishav, Hubbard, Judith, Bradley, Kyle, Tsang, Louisa LH, Liu, Yixiang, Burgmann, Roland, & Hill, Emma M. 2018. Structural Control on Down-dip Locking Extent of the Himalayan Megathrust. *Journal of Geophysical Research: Solid Earth*.

Lippitsch, Regina, Kissling, Edi, & Ansorge, Jörg. 2003. Upper mantle structure beneath the Alpine orogen from high-resolution teleseismic tomography. *Journal of Geophysical Research: Solid Earth*, **108**(B8).

Lister, GS, Forster, Margaret A, & Rawling, Timothy J. 2001. Episodicity during orogenesis. *Geological Society, London, Special Publications*, **184**(1), 89–113.

Lomnitz, Cinna. 1989. Comment on "Temporal and magnitude dependence in earthquake recurrence models" by CA Cornell and SR Winterstein. *Bulletin of the Seismological Society of America*, **79**(5), 1662–1662.

Loveless, John P, & Meade, Brendan J. 2011. Spatial correlation of interseismic coupling and coseismic rupture extent of the 2011 Mw= 9.0 Tohoku-oki earthquake. *Geophysical Research Letters*, **38**(17).

Lu, Gang, Kaus, Boris JP, & Zhao, Liang. 2011. Thermal localization as a potential mechanism to rift cratons. *Physics of the Earth and Planetary Interiors*, **186**(3-4), 125–137.

Maggi, Alessia, Jackson, JA, Mckenzie, Dan, & Priestley, Keith. 2000. Earthquake focal depths, effective elastic thickness, and the strength of the continental lithosphere. *Geology*, **28**(6), 495–498.

Magni, Valentina, Allen, Mark B, van Hunen, Jeroen, & Bouilhol, Pierre. 2017. Continental underplating after slab break-off. *Earth and Planetary Science Letters*, **474**, 59–67.

Mahesh, P, Rai, SS, Sivaram, K, Paul, Ajay, Gupta, Sandeep, Sarma, Rajagopala, & Gaur, VK. 2013. One-dimensional reference velocity model and precise locations of earthquake hypocenters in the Kumaon–Garhwal Himalaya. *Bulletin of the Seismological Society of America*, **103**(1), 328–339.

Malinverno, Alberto, & Ryan, William BF. 1986. Extension in the Tyrrhenian Sea and shortening in the Apennines as result of arc migration driven by sinking of the lithosphere. *Tectonics*, **5**(2), 227–245.

Mantovani, Enzo, Viti, Marcello, Babbucci, Daniele, Tamburelli, Caterina, Cenni, Nicola, Baglione, Massimo, & D'Intinosante, Vittorio. 2015. Present Tectonic Setting and Spatio-Temporal Distribution of Seismicity in the Apennine Belt. *International Journal of Geosciences*, **06**(Mar.), 429.

Marechal, Anais, Mazzotti, Stephane, Cattin, Rodolphe, Cazes, Gael, Vernant, Philippe, Drukpa, Dowchu, Thinley, Kinzang, Tarayoun, Alizia, Roux-Mallouf, Le, Thapa, Bal Bahadur, *et al.* . 2016. Evidence of interseismic coupling variations along the Bhutan Himalayan arc from new GPS data. *Geophysical Research Letters*, **43**(24).

Marzocchi, W, Sandri, L, Heuret, A, & Funiciello, F. 2016. Where giant earthquakes may come. *Journal of Geophysical Research: Solid Earth*, **121**(10), 7322–7336.

Marzocchi, Warner, & Sandri, Laura. 2003. A review and new insights on the estimation of the b-value and its uncertainty. *Annals of geophysics*.

McCaffrey, Robert. 2008. Global frequency of magnitude 9 earthquakes. *Geology*, **36**(3), 263–266.

Menant, Armel, Sternai, Pietro, Jolivet, Laurent, Guillou-Frottier, Laurent, & Gerya, Taras. 2016. 3D numerical modeling of mantle flow, crustal dynamics and magma genesis associated with slab roll-back and tearing: The eastern Mediterranean case. *Earth and Planetary Science Letters*, **442**, 93–107.

Metois, Marianne, D'Agostino, Nicola, Avallone, Antonio, Chamot-Rooke, Nicolas, Rabaute, Alain, Duni, Llambro, Kuka, Neki, Koci, Rexhep, & Georgiev, Ivan.

2015. Insights on continental collisional processes from GPS data: Dynamics of the peri-Adriatic belts. *Journal of Geophysical Research: Solid Earth*, **120**(12), 8701–8719.

Michel, Sylvain, Avouac, Jean-Philippe, Lapusta, Nadia, & Jiang, Junle. 2017. Pulse-like partial ruptures and high-frequency radiation at creeping-locked transition during megathrust earthquakes. *Geophysical Research Letters*, **44**(16), 8345–8351.

Minson, SE, Simons, M, & Beck, JL. 2013. Bayesian inversion for finite fault earthquake source models I—Theory and algorithm. *Geophysical Journal International*, **194**(3), 1701–1726.

Molli, Giancarlo, Crispini, Laura, Malusà, Marco G., Mosca, Pietro, Piana, Fabrizio, & Federico, Laura. 2010. Geology of the Western Alps-Northern Apennine Junction Area: A Regional Review. *Journal of the Virtual Explorer*, **36**.

Molnar, Peter. 1979. Earthquake recurrence intervals and plate tectonics. *Bulletin of the Seismological Society of America*, **69**(1), 115–133.

Molnar, Peter, & Tapponnier, Paul. 1975. Cenozoic tectonics of Asia: effects of a continental collision. *science*, **189**(4201), 419–426.

Monsalve, G, Sheehan, A, Schulte-Pelkum, V, Rajaure, S, Pandey, MR, & Wu, F. 2006. Seismicity and one-dimensional velocity structure of the Himalayan collision zone: Earthquakes in the crust and upper mantle. *Journal of Geophysical Research: Solid Earth*, **111**(B10).

Moreno, M, Melnick, Daniel, Rosenau, M, Bolte, John, Klotz, Jan, Echtler, H, Baez, J, Bataille, K, Chen, J, Bevis, M, *et al.* . 2011. Heterogeneous plate locking in the South–Central Chile subduction zone: Building up the next great earthquake. *Earth and Planetary Science Letters*, **305**(3-4), 413–424.

Moreno, Marcos, Rosenau, Matthias, & Oncken, Onno. 2010. 2010 Maule earthquake slip correlates with pre-seismic locking of Andean subduction zone. *Nature*, **467**(09), 198 EP –.

Mugnier, J-L, Gajurel, A, Huyghe, P, Jayangondaperumal, R, Jouanne, F, & Upreti, B. 2013. Structural interpretation of the great earthquakes of the last millennium in the central Himalaya. *Earth-Science Reviews*, **127**, 30–47.

Mugnier, Jean-Louis, Huyghe, Pascale, Leturmy, Pascale, & Jouanne, Franois. 2004. Episodicity and rates of thrust-sheet motion in the Himalayas (western Nepal).

Mugnier, Jean-Louis, Jouanne, François, Bhattarai, Roshan, Cortes-Aranda, Joaquim, Gajurel, Ananta, Leturmy, Pascale, Robert, Xavier, Upreti, Bishal, & Vassallo, Riccardo. 2017. Segmentation of the Himalayan megathrust around the Gorkha earthquake (25 April 2015) in Nepal. *Journal of Asian Earth Sciences*.

Nábělek, John, Hetényi, György, Vergne, Jérôme, Sapkota, Soma, Kafle, Basant, Jiang, Mei, Su, Heping, Chen, John, Huang, Bor-Shouh, *et al.* . 2009. Underplating in the Himalaya-Tibet collision zone revealed by the Hi-CLIMB experiment. *Science*, **325**(5946), 1371–1374.

Nelson, K Douglas, Zhao, Wenjin, Brown, LD, Kuo, J, *et al.* . 1996. Partially molten middle crust beneath southern Tibet: synthesis of project INDEPTH results. *Science*, **274**(5293), 1684.

Ni, James, & Barazangi, Muawia. 1984. Seismotectonics of the Himalayan collision zone: Geometry of the underthrusting Indian plate beneath the Himalaya. *Journal of Geophysical Research: Solid Earth*, **89**(B2), 1147–1163.

Nikolaeva, K, Gerya, TV, & Marques, FO. 2010. Subduction initiation at passive margins: Numerical modeling. *Journal of Geophysical Research: Solid Earth (1978–2012)*, **115**(B3).

Nishikawa, Tomoaki, & Ide, Satoshi. 2014. Earthquake size distribution in subduction zones linked to slab buoyancy. *Nature Geoscience*, **7**(12), 904–908.

Nocquet, J-M, & Calais, E. 2003. Crustal velocity field of western Europe from permanent GPS array solutions, 1996–2001. *Geophysical Journal International*, **154**(1), 72–88.

Oncken, Onno, Hindle, David, Kley, Jonas, Elger, Kirsten, Victor, Pia, & Schemmann, Kerstin. 2006. Deformation of the central Andean upper plate system—Facts, fiction, and constraints for plateau models. *Pages 3–27 of: The Andes*. Springer.

Pandey, MR, Tandukar, RP, Avouac, JP, Lave, J, & Massot, JP. 1995. Interseismic strain accumulation on the Himalayan crustal ramp (Nepal). *Geophysical Research Letters*, **22**(7), 751–754.

Panza, Giuliano F., Chimera, G., Pontevivo, A., Aoudia, A., & Raykova, R. 2003. The Lithosphere-Asthenosphere: Italy and Surroundings. *Episodes*, **26**(3), 169–174.

Pasquale, V, Chiozzi, P, & Verdoya, M. 2010. Tectonothermal processes and mechanical strength in a recent orogenic belt: Northern Apennines. *Journal of Geophysical Research: Solid Earth*, **115**(B3).

Pasquale, V., Chiozzi, P., & Verdoya, M. 2013. Evidence for Thermal Convection in the Deep Carbonate Aquifer of the Eastern Sector of the Po Plain, Italy. *Tectonophysics*, **594**, 1–12.

Patacca, E., Sartori, R., & Scandone, P. 1990. Tyrrhenian Basin and Apenninic Arcs; Kinematic Relations since Late Tortonian Times. *Pages 425–451 of: Memorie Della Societa Geologica Italiana*, vol. 45. Rome: Societa Geologica Italiana.

Peresan, Antonella, & Panza, Giuliano F. 2012. Improving earthquake hazard assessments in Italy: An alternative to “Texas Sharpshooting”. *Eos, Transactions American Geophysical Union*, **93**(51), 538–538.

Perfettini, Hugo, Avouac, Jean-Philippe, Tavera, Hernando, Kositsky, Andrew, Nocquet, Jean-Mathieu, Bondoux, Francis, Chlieh, Mohamed, Sladen, Anthony, Audin, Laurence, Farber, Daniel L, *et al.* . 2010. Seismic and aseismic slip on the Central Peru megathrust. *Nature*, **465**(7294), 78.

Pezzo, Giuseppe, Boncori, John Peter Merryman, Atzori, Simone, Piccinini, Davide, Antonioli, Andrea, & Salvi, Stefano. 2014. The 2013 Lunigiana (Central Italy) Earthquake: Seismic Source Analysis from DInSAR and Seismological Data, and Geodynamical Implications for the Northern Apennines. *Tectonophysics*, **636**(Dec.), 315–324.

Pfiffner, Othmar-Adrian, Schlunegger, Fritz, & Buiter, SJH. 2002. The Swiss Alps and their peripheral foreland basin: Stratigraphic response to deep crustal processes. *Tectonics*, **21**(2).

Piccinini, D., Piana Agostinetti, N., Saccorotti, G., Fiaschi, A., Matassoni, L., & Morelli, M. 2014. Orogen-Parallel Variability in 3D Seismicity Distribution, Northern Apennines (Italy): Evidence for a Slab Tear Fault? *Journal of Geodynamics*, **82**(Dec.), 110–117.

Platt, JP, Behrmann, JH, Cunningham, PC, Dewey, JF, Helman, M, Parish, M, Shepley, MG, Wallis, S, & Western, PJ. 1989. Kinematics of the Alpine arc and the motion history of Adria. *Nature*, **337**(6203), 158.

Poli, ME, & Renner, G. 2004. Normal focal mechanisms in the Julian Alps and Prealps: seismotectonic implications for the Italian-Slovenian border region. *Boll. Geof. Teor. Appl*, **45**, 51–69.

Pondrelli, S., Salimbeni, S., Ekström, G., Morelli, A., Gasperini, P., & Vannucci, G. 2006. The Italian CMT Dataset from 1977 to the Present. *Physics of the Earth and Planetary Interiors*, **159**(3), 286–303.

Pondrelli, Silvia, Ekström, Göran, & Morelli, Andrea. 2001. Seismotectonic re-evaluation of the 1976 Friuli, Italy, seismic sequence. *Journal of Seismology*, **5**(1), 73–83.

Prager, W, & Drucker, DC. 1952. Soil mechanics and plastic analysis or limit design, 0. *Appi. Math*, **10**(2), 157–165.

Pusok, Adina E, Kaus, Boris JP, & Popov, Anton A. 2018. The effect of rheological approximations in 3-D numerical simulations of subduction and collision. *Tectonophysics*, **746**, 296–311.

Qiu, Qiang, Hill, Emma M, Barbot, Sylvain, Hubbard, Judith, Feng, Wanpeng, Lindsey, Eric O, Feng, Lujia, Dai, Keren, Samsonov, Sergey V, & Tapponnier, Paul. 2016. The mechanism of partial rupture of a locked megathrust: The role of fault morphology. *Geology*, **44**(10), 875–878.

Rajendran, CP, & Rajendran, Kusala. 2005. The status of central seismic gap: a perspective based on the spatial and temporal aspects of the large Himalayan earthquakes. *Tectonophysics*, **395**(1-2), 19–39.

Rajendran, Kusala, Parameswaran, Revathy M, & Rajendran, CP. 2017. Seismotectonic perspectives on the Himalayan arc and contiguous areas: Inferences from past and recent earthquakes. *Earth-Science Reviews*, **173**, 1–30.

Ranalli, Giorgio. 1995. *Rheology of the Earth*. Springer.

Rosenberg, Claudio L, Schneider, S, Scharf, A, Bertrand, A, Hammerschmidt, K, Rabaute, A, & Brun, J-P. 2017. Relating collisional kinematics to exhumation processes in the Eastern Alps. *Earth-Science Reviews*.

Rovida, A, Camassi, R, Gasperini, P, & Stucchi, M. 2011. *Catalogo parametrico dei terremoti italiani*.

Rovida, Andrea, Locati, Mario, Camassi, Romano, Lolli, Barbara, & Gasperini, Paolo. 2016. CPTI15, the 2015 Version of the Parametric Catalogue of Italian Earthquakes. *Istituto Nazionale di Geofisica e Vulcanologia*.

Rudnick, Roberta L, & Fountain, David M. 1995. Nature and composition of the continental crust: a lower crustal perspective. *Reviews of geophysics*, **33**(3), 267–309.

Ruff, Larry, & Kanamori, Hiroo. 1980. Seismicity and the subduction process. *Physics of the Earth and Planetary interiors*, **23**(3), 240–252.

Ruh, Jonas B, Sallarès, Valentí, Ranero, César R, & Gerya, Taras. 2016. Crustal deformation dynamics and stress evolution during seamount subduction: High-resolution 3-D numerical modeling. *Journal of Geophysical Research: Solid Earth*, **121**(9), 6880–6902.

Sapkota, SN, Bollinger, L, Klinger, Y, Tapponnier, P, Gaudemer, Y, & Tiwari, D. 2013. Primary surface ruptures of the great Himalayan earthquakes in 1934 and 1255. *Nature Geoscience*, **6**(1), 71–76.

Schlunegger, Fritz, & Kissling, Edi. 2015. Slab rollback orogeny in the Alps and evolution of the Swiss Molasse basin. *Nature communications*, **6**.

Schmeling, H, Babeyko, AY, Enns, A, Faccenna, C, Funiciello, F, Gerya, T, Golabek, GJ, Grigull, S, Kaus, BJP, Morra, G, *et al.* . 2008. A benchmark comparison of spontaneous subduction models—Towards a free surface. *Physics of the Earth and Planetary Interiors*, **171**(1), 198–223.

Schmid, Stefan M, Pfiffner, OA, Froitzheim, N, Schönborn, G, & Kissling, E. 1996. Geophysical-geological transect and tectonic evolution of the Swiss-Italian Alps. *Tectonics*, **15**(5), 1036–1064.

Scholz, Christopher H. 2002. *The mechanics of earthquakes and faulting*. Cambridge university press.

Scholz, Christopher H. 2015. On the stress dependence of the earthquake b value. *Geophysical Research Letters*, **42**(5), 1399–1402.

Schorlemmer, Danijel, Wiemer, Stefan, & Wyss, Max. 2005. Variations in earthquake-size distribution across different stress regimes. *Nature*, **437**(7058), 539–542.

Schultz, RA. 1995. Limits on strength and deformation properties of jointed basaltic rock masses. *Rock Mechanics and Rock Engineering*, **28**(1), 1–15.

Scognamiglio, Laura, Margheriti, Lucia, Mele, Francesco Mariano, Tinti, Elisa, Bono, Andrea, De Gori, Pasquale, Lauciani, Valentino, Lucente, Francesco Pio, Mandiello, Alfonso Giovanni, Marcocci, Carlo, Mazza, Salvatore, Pintore, Stefano, & Quintiliani, Matteo. 2012. The 2012 Pianura Padana Emiliana Seimic Sequence: Locations, Moment Tensors and Magnitudes. *Annals of Geophysics*, **55**(4), 549–559.

Scordilis, EM. 2006. Empirical global relations converting M S and m b to moment magnitude. *Journal of seismology*, **10**(2), 225–236.

Seno, Tetsuzo. 2009. Determination of the pore fluid pressure ratio at seismogenic megathrusts in subduction zones: Implications for strength of asperities and Andean-type mountain building. *Journal of Geophysical Research: Solid Earth*, **114**(B5).

Serpelloni, E, Anzidei, M, Baldi, P, Casula, G, & Galvani, A. 2005. Crustal velocity and strain-rate fields in Italy and surrounding regions: new results from the analysis of permanent and non-permanent GPS networks. *Geophysical Journal International*, **161**(3), 861–880.

Serpelloni, Enrico, Faccenna, Claudio, Spada, Giorgio, Dong, Danan, & Williams, Simon DP. 2013. Vertical GPS ground motion rates in the Euro-Mediterranean region: New evidence of velocity gradients at different spatial scales along the Nubia-Eurasia plate boundary. *Journal of Geophysical Research: Solid Earth*, **118**(11), 6003–6024.

Shaw, Bruce E, Milner, Kevin R, Field, Edward H, Richards-Dinger, Keith, Gilchrist, Jacquelyn J, Dieterich, James H, & Jordan, Thomas H. 2018. A physics-based earthquake simulator replicates seismic hazard statistics across California. *Science advances*, **4**(8), eaau0688.

Sibson, Richard H. 1994. Crustal stress, faulting and fluid flow. *Geological Society, London, Special Publications*, **78**(1), 69–84.

Sieh, Kerry, Natawidjaja, Danny H, Meltzner, Aron J, Shen, Chuan-Chou, Cheng, Hai, Li, Kuei-Shu, Suwargadi, Bambang W, Galetzka, John, Philibosian, Belle, & Edwards, R Lawrence. 2008. Earthquake supercycles inferred from sea-level changes recorded in the corals of west Sumatra. *Science*, **322**(5908), 1674–1678.

Simons, Mark, Fialko, Yuri, & Rivera, Luis. 2002. Coseismic deformation from the 1999 M w 7.1 Hector Mine, California, earthquake as inferred from InSAR and GPS observations. *Bulletin of the Seismological Society of America*, **92**(4), 1390–1402.

Singer, J, Diehl, T, Husen, S, Kissling, E, & Duretz, T. 2014. Alpine lithosphere slab rollback causing lower crustal seismicity in northern foreland. *Earth and Planetary Science Letters*, **397**, 42–56.

Singer, Julia, Kissling, Edi, Diehl, Tobias, & Hetényi, György. 2017. The underthrusting Indian crust and its role in collision dynamics of the Eastern Himalaya in Bhutan: Insights from receiver function imaging. *Journal of Geophysical Research: Solid Earth*, **122**(2), 1152–1178.

Singh, Chandrani, Singh, Arun, & Chadha, RK. 2009. Fractal and b-value mapping in Eastern Himalaya and Southern Tibet. *Bulletin of the Seismological Society of America*, **99**(6), 3529–3533.

Singh, Satish C, Hananto, Nugroho, Mukti, Maruf, Robinson, David P, Das, Shamita, Chauhan, Ajay, Carton, Helene, Gratacos, Bruno, Midnet, Stephan, Djajadihardja, Yusuf, *et al.* . 2011. Aseismic zone and earthquake segmentation associated with a deep subducted seamount in Sumatra. *Nature Geoscience*, **4**(5), 308.

Song, Teh-Ru Alex, & Simons, Mark. 2003. Large trench-parallel gravity variations predict seismogenic behavior in subduction zones. *Science*, **301**(5633), 630–633.

Spada, M., Bianchi, I., Kissling, E., Agostinetti, N. Piana, & Wiemer, S. 2013a. Combining Controlled-Source Seismology and Receiver Function Information to Derive 3-D Moho Topography for Italy. *Geophysical Journal International*, **194**(2), 1050–1068.

Spada, M, Tormann, T, Wiemer, S, & Enescu, B. 2013b. Generic dependence of the frequency-size distribution of earthquakes on depth and its relation to the strength profile of the crust. *Geophysical research letters*, **40**(4), 709–714.

Stampfli, GM, Mosar, Jon, Marquer, D, Marchant, R, Baudin, Th, & Borel, G. 1998. Subduction and obduction processes in the Swiss Alps. *Tectonophysics*, **296**(1-2), 159–204.

Stein, Seth, Geller, Robert J, & Liu, Mian. 2012. Why earthquake hazard maps often fail and what to do about it. *Tectonophysics*, **562**, 1–25.

Stevens, VL, & Avouac, J-P. 2016. Millenary Mw>9.0 earthquakes required by geodetic strain in the Himalaya. *Geophysical Research Letters*, **43**(3), 1118–1123.

Stevens, VL, & Avouac, JP. 2015. Interseismic coupling on the main Himalayan thrust. *Geophysical Research Letters*, **42**(14), 5828–5837.

Stramondo, Salvatore, Vannoli, Paola, Cannelli, Valentina, Polcari, Marco, Melini, Daniele, Samsonov, Sergey, Moro, Marco, Bignami, Christian, & Saroli, Michele. 2014. X- and C-Band SAR Surface Displacement for the 2013 Lunigiana Earthquake (Northern Italy): A Breached Relay Ramp? *IEEE Journal of Selected Topics in Applied Earth Observations and Remote Sensing*, **7**(7), 2746–2753.

Stucchi, Max, Rovida, A, Capera, AA Gomez, Alexandre, P, Camelbeeck, T, Demircioglu, MB, Gasperini, P, Kouskouna, V, Musson, RMW, Radulian, M, *et al.* . 2013. The SHARE European earthquake catalogue (SHEEC) 1000–1899. *Journal of Seismology*, **17**(2), 523–544.

Sue, Christian, Thouvenot, François, Fréchet, Julien, & Tricart, Pierre. 1999. Widespread extension in the core of the western Alps revealed by earthquake analysis. *Journal of Geophysical Research: Solid Earth*, **104**(B11), 25611–25622.

Sue, Christian, Delacou, Bastien, Champagnac, Jean-Daniel, Allanic, Cécile, Tricart, Pierre, & Burkhard, Martin. 2007. Extensional neotectonics around the bend of the Western/Central Alps: an overview. *International Journal of Earth Sciences*, **96**(6), 1101–1129.

Tarantola, Albert, & Valette, Bernard. 1982. Generalized nonlinear inverse problems solved using the least squares criterion. *Reviews of Geophysics*, **20**(2), 219–232.

Tatar, Mohammad, Hatzfeld, Denis, Martinod, Joseph, Walpersdorf, Andrea, Ghafori-Ashtiany, Mohsen, & Chéry, Jean. 2002. The present-day deformation of the central Zagros from GPS measurements. *Geophysical Research Letters*, **29**(19).

Tertulliani, Andrea, Arcoraci, Luca, Berardi, Michele, Bernardini, Filippo, Brizuela, Beatriz, Castellano, Corrado, Mese, Sergio Del, Ercolani, Emanuela, Graziani, Laura, Maramai, Alessandra, Rossi, Antonio, Sbarra, Manuela, & Vecchi, Maurizio. 2012. The Emilia 2012 Sequence: A Macroseismic Survey. *Annals of Geophysics*, **55**(4).

Thakur, VC, Joshi, M, Sahoo, D, Suresh, N, Jayangondapermal, R, & Singh, A. 2014. Partitioning of convergence in Northwest Sub-Himalaya: estimation of late Quaternary uplift and convergence rates across the Kangra reentrant, North India. *International Journal of Earth Sciences*, **103**(4), 1037–1056.

Thatcher, Wayne. 1975. Strain accumulation and release mechanism of the 1906 San Francisco earthquake. *Journal of Geophysical Research*, **80**(35), 4862–4872.

Thatcher, Wayne. 2009. How the continents deform: The evidence from tectonic geodesy. *Annual Review of Earth and Planetary Sciences*, **37**.

Thomson, Stuart N., Brandon, Mark T., Reiners, Peter W., Zattin, Massimiliano, Isaacson, Peter J., & Balestrieri, Maria Laura. 2010. Thermochronologic Evidence for Orogen-Parallel Variability in Wedge Kinematics during Extending Convergent Orogenesis of the Northern Apennines, Italy. *Geological Society of America Bulletin*, **122**(7-8), 1160–1179.

Tinti, Stefano, & Mulargia, Francesco. 1987. Confidence intervals of b values for grouped magnitudes. *Bulletin of the Seismological Society of America*, **77**(6), 2125–2134.

Tizzani, P., Castaldo, R., Solaro, G., Pepe, S., Bonano, M., Casu, F., Manunta, M., Manzo, M., Pepe, A., Samsonov, S., Lanari, R., & Sansosti, E. 2013. New Insights into the 2012 Emilia (Italy) Seismic Sequence through Advanced Numerical Modeling of Ground Deformation InSAR Measurements. *Geophysical Research Letters*, **40**(10), 1971–1977.

Trumpy, R. 1980. An outline of the geology of Switzerland. *Page 104 of: 26th International Congress, section G*, vol. 10.

Trümpy, R. 2001. Why plate tectonics was not invented in the Alps. *International Journal of Earth Sciences*, **90**(3), 477–483.

Turcotte, D.L., & Schubert, G. 2002. *Geodynamics*. Cambridge University Press.

Utsu, Tokuji. 1966. A statistical significance test of the difference in b-value between two earthquake groups. *Journal of Physics of the Earth*, **14**(2), 37–40.

Uyeda, Seiya, & Kanamori, Hiroo. 1979. Back-arc opening and the mode of subduction. *Journal of Geophysical Research: Solid Earth*, **84**(B3), 1049–1061.

Valdiya, KS. 1976. Himalayan transverse faults and folds and their parallelism with subsurface structures of north Indian plains. *Tectonophysics*, **32**(3-4), 353–386.

van Dinther, Y. 2013. *Seismo-thermo-mechanical modeling of subduction zone seismicity*. Ph.D. thesis, ETH Zurich.

van Dinther, Y, Gerya, TV, Dalguer, LA, Corbi, F, Funiciello, F, & Mai, Paul Martin. 2013a. The seismic cycle at subduction thrusts: 2. Dynamic implications of geodynamic simulations validated with laboratory models. *Journal of Geophysical Research: Solid Earth*, **118**(4), 1502–1525.

van Dinther, Y, Gerya, TV, Dalguer, LA, Mai, Paul Martin, Morra, G, & Giardini, D. 2013b. The seismic cycle at subduction thrusts: Insights from seismo-thermo-mechanical models. *Journal of Geophysical Research: Solid Earth*, **118**(12), 6183–6202.

van Dinther, Y, Mai, Paul Martin, Dalguer, LA, & Gerya, TV. 2014. Modeling the seismic cycle in subduction zones: The role and spatiotemporal occurrence of off-megathrust earthquakes. *Geophysical Research Letters*, **41**(4), 1194–1201.

Van Heck, HJ, & Tackley, PJ. 2008. Planforms of self-consistently generated plates in 3D spherical geometry. *Geophysical Research Letters*, **35**(19).

van Hunen, Jeroen, & Allen, Mark B. 2011. Continental collision and slab break-off: a comparison of 3-D numerical models with observations. *Earth and Planetary Science Letters*, **302**(1-2), 27–37.

Vernant, Philippe, Bilham, R, Szeliga, W, Drupka, D, Kalita, S, Bhattacharyya, AK, Gaur, VK, Pelgay, P, Cattin, Rodolphe, & Berthet, Theo. 2014. Clockwise rotation of the Brahmaputra Valley relative to India: Tectonic convergence in the eastern Himalaya, Naga Hills, and Shillong Plateau. *Journal of Geophysical Research: Solid Earth*, **119**(8), 6558–6571.

Wallace, K, Bilham, R, Blume, F, Gaur, VK, & Gahalaut, V. 2005. Surface deformation in the region of the 1905 Kangra Mw= 7.8 earthquake in the period 1846–2001. *Geophysical Research Letters*, **32**(15).

Wang, Kang, & Fialko, Yuri. 2015. Slip model of the 2015 Mw 7.8 Gorkha (Nepal) earthquake from inversions of ALOS-2 and GPS data. *Geophysical Research Letters*, **42**(18), 7452–7458.

Wang, Kang, & Fialko, Yuri. 2018. Observations and modeling of coseismic and postseismic deformation due to the 2015 Mw 7.8 Gorkha (Nepal) earthquake. *Journal of Geophysical Research: Solid Earth*, **123**(1), 761–779.

Wang, Kelin. 2007. Elastic and viscoelastic models of crustal deformation in subduction earthquake cycles. *The seismogenic zone of subduction thrust faults*, 540–575.

Wang, Qi, Zhang, Pei-Zhen, Freymueller, Jeffrey T, Bilham, Roger, Larson, Kristine M, Lai, Xi'an, You, Xinzhao, Niu, Zhijun, Wu, Jianchun, Li, Yanxin, *et al.* . 2001. Present-day crustal deformation in China constrained by global positioning system measurements. *science*, **294**(5542), 574–577.

Warren, CJ, Beaumont, C, & Jamieson, Rebecca Anne. 2008. Modelling tectonic styles and ultra-high pressure (UHP) rock exhumation during the transition from oceanic subduction to continental collision. *Earth and Planetary Science Letters*, **267**(1-2), 129–145.

Wells, Donald L, & Coppersmith, Kevin J. 1994. New empirical relationships among magnitude, rupture length, rupture width, rupture area, and surface displacement. *Bulletin of the seismological Society of America*, **84**(4), 974–1002.

Whipple, Kelin X, Shirzaei, Manoochehr, Hodges, Kip V, & Arrowsmith, J Ramon. 2016. Active shortening within the Himalayan orogenic wedge implied by the 2015 Gorkha earthquake. *Nature Geoscience*, **9**(9), 711–716.

Wiemer, Stefan. 2001. A software package to analyze seismicity: ZMAP. *Seismological Research Letters*, **72**(3), 373–382.

Wiemer, Stefan, Giardini, Domenico, Fäh, Donat, Deichmann, Nicholas, & Sellami, Souad. 2009. Probabilistic seismic hazard assessment of Switzerland: best estimates and uncertainties. *Journal of Seismology*, **13**(4), 449.

Willett, Sean D. 2010. Late Neogene erosion of the Alps: A climate driver? *Annual Review of Earth and Planetary Sciences*, **38**, 411–437.

Wobus, Cameron, Heimsath, Arjun, Whipple, Kelin, & Hodges, Kip. 2005. Active out-of-sequence thrust faulting in the central Nepalese Himalaya. *Nature*, **434**(7036), 1008.

Yin, An, & Harrison, T Mark. 2000. Geologic evolution of the Himalayan-Tibetan orogen. *Annual Review of Earth and Planetary Sciences*, **28**(1), 211–280.

Zhao, Bin, Bürgmann, Roland, Wang, Dongzhen, Tan, Kai, Du, Ruilin, & Zhang, Rui. 2017. Dominant controls of downdip afterslip and viscous relaxation on the postseismic displacements following the Mw7. 9 Gorkha, Nepal, earthquake. *Journal of Geophysical Research: Solid Earth*, **122**(10), 8376–8401.

Zhao, Liang, Paul, Anne, Guillot, Stéphane, Solarino, Stefano, Malusà, Marco G, Zheng, Tianyu, Aubert, Coralie, Salimbeni, Simone, Dumont, Thierry, Schwartz, Stéphane, *et al.* . 2015. First seismic evidence for continental subduction beneath the Western Alps. *Geology*, **43**(9), 815–818.

Zhao, Liang, Paul, Anne, Malusà, Marco G, Xu, Xiaobing, Zheng, Tianyu, Solarino, Stefano, Guillot, Stéphane, Schwartz, Stéphane, Dumont, Thierry, Salimbeni, Simone, *et al.* . 2016. Continuity of the Alpine slab unraveled by high-resolution P wave tomography. *Journal of Geophysical Research: Solid Earth*, **121**(12), 8720–8737.

Zhao, Wenjin, Nelson, KD, Che, J, Quo, J, Lu, D, Wu, C, & Liu, X. 1993. Deep seismic reflection evidence for continental underthrusting beneath southern Tibet. *Nature*, **366**(6455), 557.

Zheng, Gang, Wang, Hua, Wright, Tim J, Lou, Yidong, Zhang, Rui, Zhang, Weixing, Shi, Chuang, Huang, Jinfang, & Wei, Na. 2017. Crustal Deformation in the India-Eurasia Collision Zone From 25 Years of GPS Measurements. *Journal of Geophysical Research: Solid Earth*, **122**(11), 9290–9312.

Zhu, Lupei, & Rivera, Luis A. 2002. A note on the dynamic and static displacements from a point source in multilayered media. *Geophysical Journal International*, **148**(3), 619–627.

Curriculum Vitae

Luca Dal Zilio
Swiss Federal Institute of Technology, ETH Zürich
Department of Earth Sciences, Institute of Geophysics, Zürich, Switzerland
email: *luca.dalzilio@erdw.ethz.ch*

■ Current position

2/19 – **Cecil and Sally Drinkward Fellow in Mechanical Engineering and Geophysics**
California Institute of Technology (Caltech), Pasadena, California

■ Education

2/15–1/19 **PhD student at Swiss Federal Institute of Technology (ETH) Zürich**
Thesis: *Cross-scale modeling of mountain building and the seismic cycle: From Alps to Himalaya*
Advisor: *Taras Gerya, Ylona van Dinther*

10/12–11/14 **MSc (cum laude) in Geology, University of Padova, Italy**
Thesis: *Subduction-induced break-up and drifting of continental plates*
Advisor: *Manuele Faccenda, Fabio Capitanio*

10/12–11/14 **BSc in Earth Sciences, University of Padova, Italy**
Thesis: *Preliminary study of the structural setting of the "Fadalto rumbles"*
Advisor: *Nereo Preto, Giulio Di Toro*

Scientific Community

Reviewer/Topic Editor, *Frontiers in Earth Science*
Blog Editor for the European Geosciences Union (EGU), Geodynamic Division
Book Reviewer: Times Higher Education (THE)
Journal Reviewer for *JGR: Solid Earth*, *Geophys. Res. Lett.* and *Earth-Science Reviews*, *EGU Solid Earth*, *Journal of Geodynamics*
International conference chair and convener:
AGU-2019: Seismic and Aseismic Slip on Seismogenic Faults
AGU-2019: Cross-Scale and Multi-Scale Building of the Himalaya
AGU-2019: Integrating Plate Interface Rheology and Seismicity with Subduction Zone
EGU-2019: Integrated approaches to bridge Long-term Tectonics and Earthquake cycles
EGU-2018: The Interplay between earthquakes and long-term Deformation

■ Advanced training course

2017: Probabilistic Seismic Risk Analysis and Management for Civil Systems
2016: Thermodynamics Applied to Earth Materials
2016: Crystalline Geology of the Alps
2015: Crustal Seismology
2015: Finite Element Modelling in Geosciences

■ Visiting researcher

7/17; 6/18 École Normale Supérieure (ENS), Paris, France
2018 Earth Observatory of Singapore (EOS), Singapore

■ Students

2018: MSc student: Julian Stypulkowski (*ETH Zürich*), co-supervisor.
2018: MSc student: Mario D'Acquisto (*ETH Zürich*), supervisor.
2016: PhD student: Eleonora Ficini (*Sapienza University, Rome*), co-supervisor.
2015: MSc student: Eleonora Ficini (*Sapienza University, Rome*), co-supervisor.

■ Grants / Awards / Supports

2019: Springer Nature Thesis Award
2019: Recipient of the annual EGU Best Blog article
2018: Early Postdoc Mobility fellowship, Swiss National Science Foundation
2018: Travel support for the *Workshop on Modeling Earthquake Source Processes* (Caltech)
2018: Cecil and Sally Drinkward Postdoctoral Fellowship at Caltech
2018: EGU Outstanding Student Poster (OSP) Award
2018: Best Geostory award by *Nature Geoscience journal*
2018: Nominated by ETH for the *Global Young Scientists Summit 2018*, Singapore (+ travel grant)
2017: Invited keynote speaker at TEDx event – *Earthquakes: prediction or prevention?*
2017: Proposal writer: AlpArray SINERGIA project 1-yr-extension PhD funded
2015: Swiss Nat. Science Found. – 3 years PhD Research, Project *SINERGIA (Swiss-AlpArray)*
2014: Proposal writer: Uni-Padua research: *Modelling linked to Plate Tectonics*, 3 months
2014: Cineca High Performance Computing, 50k/hours, SINDRICO project (co-PI; PI: M. Faccenda)
2013: Travel grant by European Geosciences Union (EGU) Summer School

■ Publications

[10] D'Acquisto, M., **Dal Zilio, L.**, van Dinther, Y., Molinari, I., Kissling, E., and Gerya, T. V. (2019). Tectonics and seismicity in the Northern Apennines driven by slab retreat and crustal delamination (*submitted*)

[9] **Dal Zilio, L.**, Jolivet, R., and van Dinther Y. (2019). Segmentation of the Main Himalayan Thrust inferred from geodetic observations of interseismic coupling (*in review*)

[8] **Dal Zilio, L.**, Kissling, E., Gerya, T., and van Dinther, Y. (2019). Slab rollback orogeny model for the evolution of the Central Alps: seismo-thermo-mechanical test. (*in review*)

[7] **Dal Zilio, L.**, van Dinther, Y., Gerya, T., and Avouac, J.P. (2018). Bimodal seismicity in the Himalaya controlled by fault friction and geometry. *Nature communications 10.1: 48.*

[6] **Dal Zilio, L.** (2018). Subduction-driven Earth machine. *Nature Geoscience, News and Views* 11, 229

[5] **Dal Zilio, L.**, van Dinther, Y., and Gerya, T. V., (2018). Seismic behaviour of mountain belts controlled by plate convergence rate. *Earth and Planetary Science Letters.* 482, 81–92.

[4] Ficini, E., **Dal Zilio, L.**, Doglioni, C., and Gerya, T. V., (2017). Horizontal mantle flow controls subduction dynamics. *Scientific Reports* 7.

[3] **Dal Zilio, L.**, Faccenda, M., and Capitanio, F. A., (2017). The role of deep subduction in supercontinent breakup. *Tectonophysics*.

[2] Faccenda, M., and **Dal Zilio, L.**, (2017). The role of solid–solid phase transitions in mantle convection. *Lithos* 268, 198-224.

[1] Meyzen, C.M., Massironi, M., Pozzobon. R., and **Dal Zilio, L.**, (2015). Are plumes on motionless plates analogues to Martian plume feeding the giant shield volcanoes? - Volcanism and Tectonism Across the Inner Solar System, *Geological Society of London*, v. 401.

■ Seminars

2019: University of Lausanne
University of Padova
United Nation (UNICEF), Geneva
University of California Los Angeles

2018: Earth Observatory of Singapore
Sapienza University of Rome
École Normale Supérieure, Paris

■ Invited talk

Dal Zilio, L. (2019). *The influence of tectonics on seismicity of mountain belts: A case study from the Himalayas.* CIG Crustal Deformation Modeling Workshop, Golden, Colorado.
Dal Zilio, L., Kissling, E., and Gerya, T. (2018) *Slab Rollback Orogeny Model: A test-of-concept.* AGU meeting, Washington D.C., USA.
Dal Zilio, L. (2018) *Modeling mountain building across time scales.* First AlpArray Science Meeting, Zürich, Switzerland.

■ Selected meeting presentations

2019:

Dal Zilio, L., Kissling, E., and Gerya, T. *Cross-scale modeling of Slab Rollback Orogeny Model: The Central Alps case* EGU meeting, Vienna (oral).

2018:

Dal Zilio, L., Kissling, E., and van Dinther Y. *Slab Rollback Orogeny Model: A test-of-concept.* AGU meeting, Washington D.C., USA (invited oral).
Dal Zilio, L., Jolivet, R., and van Dinther Y. *Interseismic coupling on the Main Himalayan Thrust: Bayesian modelling accounting for data and prediction uncertainties.* AGU meeting, Washington D.C., USA (oral).
Dal Zilio, L. *Modeling mountain building across time scales.* First AlpArray Science Meeting, Zürich, Switzerland (oral).
Dal Zilio, L., Jolivet, R. *Seismic and aseismic slip on the Main Himalayan Thrust: Bayesian modelling accounting for prediction uncertainties.* Himalaya-Karakorum-Tibet (HKT) workshop, Lausanne, Switzerland (oral).
Dal Zilio, L., van Dinther, Y., Gerya, T. and Avouac, J.-P. *Bimodal seismicity in the Himalaya controlled by fault friction and geometry.* EGU meeting, Vienna (poster).
Dal Zilio, L., Jolivet, R. and van Dinther, Y. *Interseismic coupling on the Main Himalayan Thrust: Bayesian modelling accounting for prediction uncertainties.* EGU meeting, Vienna (poster).

2017:

Dal Zilio, L., van Dinther, Y., Gerya, T. and Avouac, J.-P. *What controls the bimodal seismicity of large Himalayan earthquakes?* AGU meeting, New Orleans, USA (oral).
Dal Zilio, L., Jolivet, R. and van Dinther, Y. *Interseismic coupling and geometry of the Main Himalayan Thrust: A complementary approach.* AGU meeting, New Orleans, USA (poster).
Dal Zilio, L., van Dinther, Y., Gerya, T. and Avouac, J.-P. *Under the hood of the earthquake machine: Toward predictive modeling of the Himalayan seismic cycle.* NetherMod workshop, The Netherlands (poster).
Liao, J., **Dal Zilio, L.**, and Gerya, T. *Influence of slab rollback on the curvature of the Western Alps.* EGU meeting, Vienna (poster).
Dal Zilio, L., van Dinther, Y. and Gerya, T. *Seismic cycle in the Nepal Himalaya inferred from instantaneous modelling.* EGU meeting, Vienna (oral).

2016:

Dal Zilio, L., van Dinther, Y. and Gerya, T. *Seismic cycle in the Nepal Himalaya: Instantaneous Modeling*. AGU meeting, San Francisco (oral).

Dal Zilio, L., van Dinther, Y. and Gerya, T. *Plate convergence rate controls earthquake-size distribution of mountain belts*. AGU meeting, San Francisco (oral).

Dal Zilio, L., van Dinther, Y. and Gerya, T. *Plate convergence rate controls earthquake-size distribution of mountain belts*. GeoMod conference, Montpellier, France (oral).

Ficini, E., **Dal Zilio, L.**, Doglioni, C. and Gerya T. *Numerical modelling of subduction zones: A new beginning*. 35th Int. Geological Congress, Cape Town, South Africa (poster).

Dal Zilio, L., van Dinther, Y. and Gerya, T. *Convergence rate controls seismicity styles in collision orogens*. EGU meeting, Vienna (oral).

Dal Zilio, L., Faccenda M. and Capitanio, F.A. *The role of deep subduction in supercontinent breakup*. EGU meeting, Vienna (oral).

Ficini, E., **Dal Zilio, L.**, Doglioni, C. and Gerya T. *Numerical modelling of subduction zones: A new beginning*. EGU meeting, Vienna (poster).

2015:

Dal Zilio, L., van Dinther, Y. and Gerya, T. *The long-term seismic cycle in collisional margins: insights from Seismo-Thermo-Mechanical models*. AGU meeting, San Francisco (poster).

Dal Zilio, L., van Dinther, Y. and Gerya, T. *Seismo-Thermo-Mechanical modelling of collisional margins*. XIV Int. Workshop on Modelling of Mantle and lithosphere Dynamics, France (poster).

Dal Zilio, L., Faccenda M. and Capitanio, F.A. *Subduction-induced break-up and drifting of continental plates*. XIV Int. workshop on modelling of mantle and lithosphere dynamics, France (poster).

■ Media Coverage

Why massive earthquakes menace the Himalayas, *Nature Highlights*.

Devastating quakes are priming the Himalaya for a mega-disaster, *National Geographic*.

Waiting for the complete rupture, *ETH News*.

Faster tectonic-plate collisions spell bigger earthquakes, *Nature Highlights*.

Why are some earthquakes so much worse than others? *International Business Times*.

Earthquakes – Swiss study shines new light on the risks in the Alps, *Le News*.

Acknowledgments

First and foremost I would like to thank Taras Gerya for advising me during this PhD project. His remarkable knowledge and experience, his great explanations and even more importantly his constant confidence of success and infectious smile built a stable foundation for my work. I benefited very much over the last four years from his continuous supervision, helpful advice and enlightening discussions, as well as his attitude and enthusiasm for science. Thanks for opening the door of a stimulating and exciting environment.

I would like to express my sincere gratitude to my co-supervisor, Ylona van Dinther, who kept me under her wings throughout this PhD project. With thoughtful advice, Ylona guided me to roam and explore my own ideas, tackling major challenges that pushed me to find new limits. I am thankful for — and do not take for granted — the trust I was given as well as the understanding and unconditional support in difficult situations.

Many thanks to the rest of my committee: Edi Kissling, Stefan Wiemer, Romain Jolivet and Onno Oncken. Thanks for accepting to examine my thesis. I am glad to have found a committee of designated experts, who are willing to give feedback to my research. Special thanks goes to Romain for introducing me to inverse modeling and Python. I was inspired and also infected by his devotion. A special mention goes to Edi, for the financial support he provided during my PhD and, in particular, for great *scientific* discussions and never-ending passion for science. Thanks go to Paul Tackley as well, for kindly accepting to chair my PhD defence and for all the *non-scientific* discussions.

I would have never made it here without the unlimited, natural support of my former supervisors, Manuele Faccenda and Fabio Capitanio. Manuele, your unlimited support when I was in Padova helped me greatly to become the scientist I am today. Fabio, your creative and expressive nature have always been a source of inspiration. In my darkest moments you helped me to find a light — grazie!

I am deeply indebted to my office mates: Iris, Casper, and Robert. Working with them is as much an honor as it is a pleasure. To Iris, for sharing a deep, simple, yet fundamental enthusiasm. Thanks for never forgetting to teasing me when I was working too much. To Robert, for showing me that hard work and a good life with lots of extracurricular interests are not a contradiction. To Casper, for his profound knowledge on numerical modeling, his creativity, and his admirably independent way of thinking. A special thanks goes to my first master student, Mario D'Acquisto. I have been lucky to have supervised a motivated and hard-working student like Mario.

Particular thanks goes to my former colleagues from Padova: Giacomo, Alberto, Andrea, Chiara, and Matteo. Our academic paths have scattered us like beads off a broken necklace. Many things changed since then, but it doesn't matter. As I take the next step in my career, I will never forget where it all began.

It was an amazing experience to be part of the Earth Sciences department, which is a multicultural, positive, mixture of people. I hope it will always remain like it is. Many thanks to the current and former GFD members and H-floor colleagues: CJ, Jessica, Patrick, Filippo, Theo, Claudio, Daniela, Antoine, Marie, Maxim, Jie, Antonio, Tim, and Patrick.

I would like to thank Federica, who represents part of my past. Despite life brought us apart, I will never forget all the encouragements, support, and understanding that you, and your family, gave me — all the best for your future!

During ups and downs of my PhD I always had a great support from fabulous, charming and optimistic friends, who brought a lot of pleasure and light into my PhD life. Thanks to Emily, Diogo, Simon, and Leo for the great time together!

I would be nowhere without my friends. Old friends are the best mirror. Special thanks to the ladies and gentlemen from way back in time: Gabriela, Susy, Mirko, Fede, Matteo, and Beppe. I hope we will still hang out when we are old and clever. Thanks guys for always being there to listen, help out and lend support!

I would like to thank my family for all their love and encouragement, for raising me with a passion of science and for supporting me in all my pursuits. Grazie. On a more personal note I would like to thank Maria, my grandmother. Words cannot express my gratitude for everything you have done. This PhD is a testament to your faith in me, I hope I have made you proud. Thank you for accompanying me on this adventure.

One day, an extraordinary woman came into my life like a ray of sunshine on a summer's morning: silently, unnoticed at first, yet ever growing to fill all about me. Thanks Sarah for that who you are and how you make me feel; for your endless belief, support, care and inspiration; for all the collateral beauty of your personality that I keep open for myself, and for all the strength I feel next to you! I don't know what the future holds for you and me, but whatever our destiny has in store for us, I will never give up on loving you.